UNIVERSITY OF ZAGREB
FACULTY OF SCIENCE
DEPARTMENT OF PHYSICS

Petar Žugec

MEASUREMENT OF THE ^{58}Ni NEUTRON CAPTURE CROSS SECTION

DOCTORAL THESIS

Zagreb, 2014

SVEUČILIŠTE U ZAGREBU
PRIRODOSLOVNO MAMTEMATIČKI FAKULTET
FIZIČKI ODSJEK

Petar Žugec

MJERENJE UDARNOGA PRESJEKA ZA UHVAT NEUTRONA NA IZOTOPU ^{58}Ni

DOKTORSKI RAD

Zagreb, 2014

BASIC DOCUMENTATION CARD

University of Zagreb
Faculty of Science
Department of Physics

Doctoral Thesis

Measurement of the ^{58}Ni neutron capture cross section

Petar Žugec
Faculty of Science, Zagreb

The (n,γ) cross section of ^{58}Ni – of importance for the nuclear astrophysics, as well as for nuclear technologies – was measured at the neutron time-of-flight facility n_TOF at CERN. For the measurement, two C_6D_6 liquid scintillation detectors were used, specifically optimized to provide as low neutron sensitivity as possible. At n_TOF, the highly luminous white neutron beam covers 12 orders of magnitude in energy – from 10 meV to 10 GeV. It is produced by a pulsed beam of 20 GeV protons impinging on a massive Pb spallation target, yielding a total of 2×10^{15} neutrons per pulse. Through an evacuated beamline the neutrons are transported towards the experimental area at a distance of approximately 185 m from a spallation target. In the process the beam is collimated by the set of two collimators, while charged particles are removed by a sweeping magnet. The neutron flux is actively monitored during the measurement by means of a silicon based neutron beam monitor SiMon, relying on ^{6}Li$(n,t)\alpha$ reaction. The measurement is performed by detecting the prompt capture γ-rays from ^{58}Ni(n,γ) reaction. The kinetic energy of captured neutron is calculated from its time-of-flight, which is determined from a time-stamp of a detected γ-ray, relative to the start-signal caused by an intense γ-flash following every proton pulse hitting the spallation target. In order to calculate a capture yield from a measured data, the well-established Pulse Height Weighting Technique was applied. A capture yield was analyzed in the energy range between 27 meV and 400 keV. The resolved resonance region was analyzed up to 122 keV by means of a multilevel R-matrix code SAMMY. Within the resolved resonance region 51 capture resonances were identified and their parameters reported. By complementing these results with the data from the unresolved resonance region – analyzed by the specialized code SESH – the Maxwellian averaged cross sections (MACS) were calculated for the stellar temperatures of kT = 5–100 keV. The new results call for the revaluation of the cross section data presently available throughout the various evaluation libraries, while revealing a significant impact on the final ^{58}Ni abundance in the massive stars. In calculating the capture yield a significant effort has been paid to the clear identification of the separate background components. While the environmental and the so called empty-frame background are easily and regularly measured, the neutron background – caused by the neutrons elastically scattered off the sample itself – has been identified for the first time at n_TOF by means of the high-precision

GEANT4 simulations. The simulated results were extensively compared against the available experimental data, confirming that they may be used with high degree of confidence for reaching the new precision standards in analyzing the capture data from n_TOF.

Keywords: n_TOF, neutron time of flight, ^{58}Ni neutron capture cross section, GEANT4 simulations, neutron background

(147 pages, 87 references, original in English)

Supervisor: prof. dr. sc. Damir Bosnar, University of Zagreb

Committee:
1. izv. prof. dr. sc. Tamara Nikšić, University of Zagreb
2. prof. dr. sc. Damir Bosnar, University of Zagreb
3. dr. sc. Neven Soić, Senior research associate, Ruđer Bošković Institute, Zagreb

Thesis accepted: 2014

TEMELJNA DOKUMENTACIJSKA KARTICA

Sveučilište u Zagrebu
Prirodoslovno-matematički fakultet
Fizički odsjek

Doktorski rad

Mjerenje udarnoga presjeka za uhvat neutrona na izotopu ^{58}Ni

Petar Žugec

Prirodoslovno-matematički fakultet, Zagreb

Udarni presjek za uhvat neutrona na izotopu ^{58}Ni – od važnosti za nuklearnu astrofiziku i tehnologije vezane uz nuklearnu fiziku – mjeren je na n_TOF postrojenju neutronskog vremena proleta u CERN-u. Kao mjerni instrumenti korištena su dva C_6D_6 tekuća scintilacijska detektora, posebno optimizirana kako bi osigurali najnižu izvedivu neutronsku osjetljivost. Intenzivan snop neutrona s n_TOF postrojenja proteže se 12 redova veličine u energiji – od 10 meV do 10 GeV. Snop se proizvodi izlaganjem masivne olovne spalacijske mete pulsnom protonskom snopu energije 20 GeV, pri čemu se oslobađa približno 2×10^{15} neutrona po pulsu. Evakuirani cjevovod vodi snop prema eksperimentalnoj prostoriji udaljenoj približno 185 m od spalacijske mete. U međuvremenu snop se kolimira dvama kolimatorima i oslobađa nabijenih čestica snažnim magnetom. Tok neutrona aktivno se mjeri tijekom eksperimenta tzv. neutronskim monitorom snopa baziranim na siliciju, koji se oslanja na ^{6}Li$(n,t)\alpha$ reakciju. Mjerenja neutronskih uhvata provode se detekcijom trenutno emitiranih γ-zraka iz ^{58}Ni(n,γ) reakcije. Kinetička energija uhvaćenog neutrona računa se iz njegova vremena proleta, koje se određuje iz vremena detekcije γ-zrake s obzirom na početni signal izazvan snažnim γ-bljeskom uzrokovanim udarom protonskoga snopa o spalacijsku metu. U svrhu izračuna vjerojatnosti uhvata iz eksperimentalnih podataka, pojedinim događajima pridruženi su odgovarajući težinski faktori na temelju visine mjerenih signala. Vjerojatnost uhvata analizirana je u energijskom rasponu od 27 meV do 400 keV. Područje raspoznatljivih rezonanci analizirano je do 122 keV primjenom programskoga koda SAMMY koji koristi formalizam R-matrice za obradu podataka. Unutar ovog područja izdvojena je i parametrizirana 51 rezonanca u udarnome presjeku za uhvat neutrona. Nadopunivši ove rezultate podacima iz područja neraspoznatljivih rezonanci – analiziranog posebnim programskim kodom SESH – izračunati su maxwellovski usrednjeni udarni presjeci za zvjezdane temperature od kT = 5–100 keV. Najnoviji rezultati ukazuju na potrebu za ponovljenim vrednovanjem udarnih presjeka dostupnih u različitim bazama podataka. Rezultati također pokazuju značajan utjecaj na zastupljenost konačnog sadržaja ^{58}Ni u masivnim zvijezdama. Pri izračunu vjerojatnosti uhvata značajna pažnja posvećena je jasnoj identifikaciji izdvojenih doprinosa pozadinskim događajima. Pozadina uzrokovana prirodnim i induciranim zračenjem

iz eksperimentalnog okruženja te pozadina uzrokovana prolaskom neutronskog snopa kroz eksperimentalnu prostoriju lako se i redovito mjere. No tzv. neutronska pozadina uzrokovana raspršenjem neutrona na samome mjerenom uzorku po prvi put u povijesti n_TOF postrojenja jasno je identificirana GEANT4 simulacijama visoke preciznosti. Simulirani rezultati uspoređeni su s dostupnim eksperimentalnim podacima, čime je potvrđeno da se s pouzdanošću mogu koristiti za postizanje nove razine preciznosti u analizi mjerenja neutronskih uhvata s n_TOF postrojenja.

Ključne riječi: n_TOF, vrijeme proleta neutrona, udarni presjek za uhvat neutrona na ^{58}Ni, GEANT4 simulacije, neutronska pozadina

(147 stranica, 87 literaturnih navoda, izvornik na engleskome jeziku)

Mentor: prof. dr. sc. Damir Bosnar, Sveučilište u Zagrebu

Ocjenjivači:
1. izv. prof. dr. sc. Tamara Nikšić, Sveučilište u Zagrebu
2. prof. dr. sc. Damir Bosnar, Sveučilište u Zagrebu
3. dr. sc. Neven Soić, viši znanstveni suradnik, Institut Ruđer Bošković, Zagreb

Rad prihvaćen: 2014

This work is dedicated to Kosta.
I am indebted to him in more ways than I can put into words.

Acknowledgements

This work was performed under the supervision of prof. dr. sc. Damir Bosnar, to whom I am grateful for the skillful mentorship. Special thanks also goes to Nicola Colonna and Massimo Barbagallo of the n_TOF collaboration for their extensive help and indispensable cooperation. The note of appreciation, of course, must be paid to the whole n_TOF collaboration that made the experimental part of this work possible. The members of Laboratory for Advanced Computing at Faculty of Science, University of Zagreb, are recognized for providing us with the computer cluster used for running the simulations. Finally, my colleagues Bruno Klajn and Ivica Friščić are to be complemented for bearing with me through thick and thin of making this work.

Table of Contents

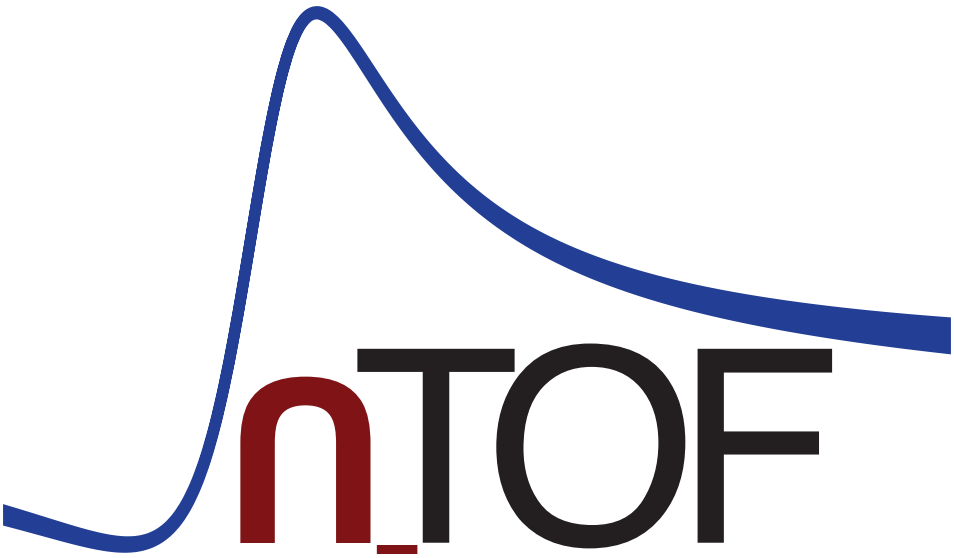
nTOF

1 Introduction

1.1 Motivation for the ^{58}Ni neutron capture measurement

The precise knowledge of the radiative neutron capture cross section of ^{58}Ni is required in the nuclear astrophysics framework, as well as in the nuclear technologies. Being an important constituent of structural materials widely used in nuclear technologies, through the neutron irradiation ^{58}Ni contributes to the long-term radiation hazard due to the production of the long-lived ^{59}Ni with a half-life of 7.5×10^4 years. In addition, the ^{58}Ni$(n,\gamma)^{59}$Ni$(n,\alpha)^{56}$Fe chain of reactions, which produces He in stainless steel alloys, contributes to the damaging of structural materials [1, 2].

Detailed neutron capture data are of essential importance for modeling the stellar nucleosynthesis of the elements heavier than iron. While the elements up to iron have been created by the charged particle reactions – some of them during the Big Bang nucleosynthesis, some of them during the later stellar nucleosynthesis made possible by the formation of the first stars – the production of the elements in the mass region above iron mostly occurs (directly or indirectly) through the neutron induced reactions, in particular the neutron captures. The slow neutron capture process (s-process) produces approximately half of the abundances of elements heavier than iron [3]. The other half is mainly produced by the rapid neutron capture process (r-process), characteristic of stellar environments with extremely high neutron flux, such as (super)novae or neutron stars collisions. Therefore, an attempt at a profound understanding of these processes is no less than an attempt at uncovering the origin of the matter in the universe. And though this quest has been capturing the imagination of humankind throughout its history, exposing this cosmic secret was made possible only in the 20th century by the dawn of the nuclear physics. In developing the s- and r-process models – which were over time brought into ever closer agreement with the experimental observations, gradually building the consistent and comprehensive description of the stellar evolution – it was found that the detailed neutron capture data on a wide range of isotopes play a central role in governing the final outcome and the accuracy of these models' results. And though the experimental neutron capture data are certainly desirable for all the isotopes found in nature – having at least the fundamental scientific value – the data on some of them are of distinct importance. Among these select isotopes are the so called branching points of the s-process – β-unstable nuclides characterized by a lifetime comparable to the mean time between two successive neutron captures within the stellar environment. Figure 1.1 illustrates the s-process path along the chart of nuclides starting from the primary ^{56}Fe seed, showing that it progresses through a series of neutron captures and β-decays. However, the development of the s-process is particularly sensitive to the branching points where the comparable probabilities for either of these

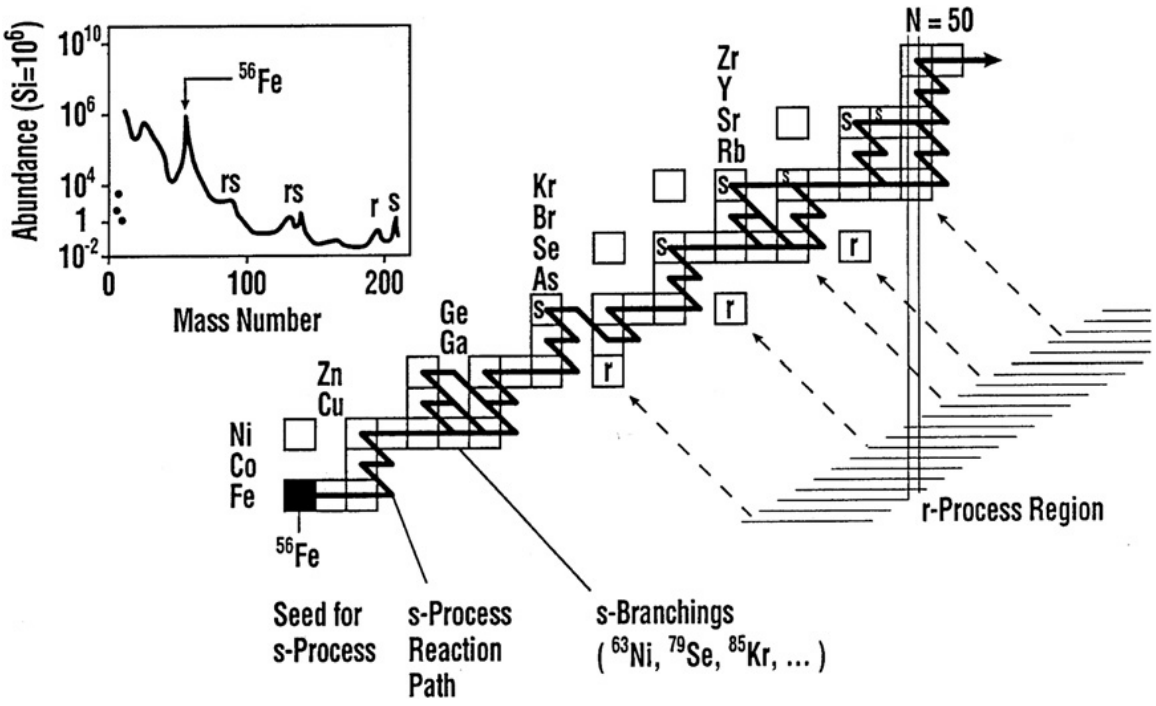

Figure 1.1 — Path of the *s*-process along the chart of nuclides, starting from the primary ^{56}Fe seed (adopted from Ref. [4]).

two outcomes compete and feed the different nucleosynthesis paths, governing the assumption of the other successive steps taken along the course of the nuclear evolution. One of such branching points – belonging to a nickel group – is ^{63}Ni, whose neutron capture cross section has recently been measured for the first time at the *neutron time of flight* facility n_TOF from CERN [5, 6].

Within the nuclear astrophysics framework, ^{58}Ni is important as the participant in the *s*-process, serving as the secondary seed with a much lower abundance (4.3% [7]) than that of the primary ^{56}Fe seed. In a course of the stellar evolution, *s*-process takes place during He- and C-burning at temperatures between 0.1 and 1 GK (kT = 8 to 90 keV) [4]. There are two principal *s*-process components contributing to the total solar system abundances in the mass region between iron and actinides – the *main* and *weak* component – with an additional contribution from the *strong* component related to the production of Pb and Bi. The main *s*-process takes place in the low-mass (1-5 $M_\odot$) asymptotic giant branch (AGB) stars, producing almost all the *s*-process related abundances above $A = 90$. This may be inferred by comparing the experimental observations with the main *s*-process model predictions for *s*-only isotopes, i.e. those produced exclusively by the *s*-process. Since the low-mass AGB stars are not able to ignite the inert C/O core, the *s*-process operates in the He-burning shell (Figure 1.2 illustrates the interior structure of a typical AGB star). Due to the mixing of material, following the thermal pulsing stages of the stellar evolution, ^{13}C is created by the $^{12}C(p,\gamma)^{13}N(\beta^+\nu)^{13}C$ reaction, fueling the $^{13}C(\alpha,n)^{16}O$ reaction which serves as the primary source of neutrons. At the later stage of the main *s*-process there is a marginal contribution to the neutron production from the $^{22}Ne(\alpha,n)^{25}Mg$ reaction. On the other hand, the weak *s*-process – which takes place in massive ($>8M_\odot$) stars during both He- and C- burning – is predominantly driven by the $^{22}Ne(\alpha,n)^{25}Mg$ reaction. ^{22}Ne itself is produced by the $^{14}N(\alpha,n)^{18}F(\beta^+\nu)^{18}O(\alpha,n)^{22}Ne$ reaction, with ^{14}N seed as a leftover

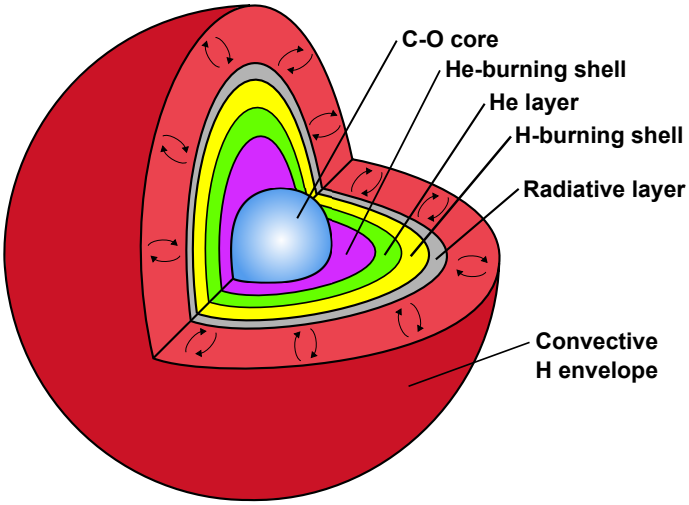

Figure 1.2 — Interior structure of a typical asymptotic giant branch (AGB) star.

from the previous CNO cycle active during H-burning. As Fig. 1.3 clearly shows, the model predictions from the combined main and weak *s*-process components successfully reproduce the observed solar abundances both below and above $A = 90$ [4]. ^{58}Ni isotope – contributing with 68% to the isotopic abundance of Ni – serves as the secondary seed for the *s*-process nucleosynthesis. It has been established that the solar Ni abundance comes both from the core-collapse supernovae [8] and the thermonuclear supernovae of type Ia [9]. Spectroscopic observations indicate that roughly 30% of the solar Ni abundance has been produced by the massive core-collapse stars, while 70% by the thermonuclear supernovae [10].

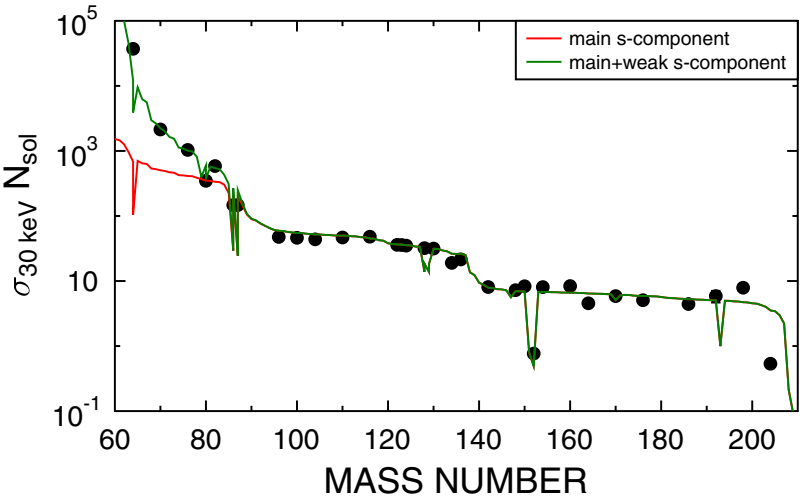

Figure 1.3 — Product of the average capture cross section and the solar *s*-process abundance. The results of the main and weak *s*-process model are compared against the observational data for *s*-only isotopes (adopted from Ref. [4]).

For calculation of the astrophysical reaction rates, the energy dependence of the radiative capture (n, γ) cross section must be known up to the several hundreds of keV in neutron energy. Several experimental datasets for the ^{58}Ni(n, γ) reaction are available in the Experimental nuclear reaction data library EXFOR [11], though only few extend over the full range of astrophysically relevant energies. A measurement has been performed recently at the Oak Ridge Electron Linear Accelerator (ORELA) by Guber et al. [12], yielding a globally lower cross section than adopted for evaluation throughout most of the evaluation libraries, including ENDF/B-VII.0 [13]. Among several measurements on which the ENDF/B-VII.0 evaluation is based, is the one performed by Perey et al. [14], relying on the use of C_6F_6 detectors, characterized by the neutron sensitivity higher than that of C_6D_6 counterparts used by Guber et al. A recent measurement by Rugel et al. [15] also indicates the global decrease in the capture cross section of ^{58}Ni, relative to the past evaluations. Taking into account these results – together with the high-resolution transmission measurement by Brusegan et al. [16] and the new thermal value from Raman et al. [17] – a renewed evaluation was adopted for the ENDF/B-VII.1 release [18]. The new high-resolution measurement from n_TOF facility [19] aims at solving the discrepancies between the past experimental results and set course for the future evaluations of the ^{58}Ni(n, γ) cross section.

1.2 Neutron interactions

Although the neutron capture is the central neutron induced reaction of interest to this work, for the successful design and execution of highly precise neutron related experiments one must be well acquainted with all categories of the neutron interactions. In fact, alongside the neutron capture, in this work both the elastic and inelastic neutron scattering will play a prominent role, being the major cause for the neutron induced background, which will be studied in detail. In addition, a specific inelastic (n, p) reaction has been found to contribute to the ^{nat}C measurements. Therefore, in the following section a few words are given on the general properties of the neutron induced reactions.

1.2.1 Overwiev

In principle, the neutrons are subjected to all four fundamental interactions – strong and weak nuclear, electromagnetic and gravitational. In practical applications of the relatively long-lived hadron with no electric charge, the strong interactions are most commonly exploited. By their very nature, the neutrons are also subject to the weak interactions. The prime example of these is a neutron decay – either the free neutron decay with a half-life of approximately 10 minutes, or a β-decay of neutrons bound inside the atomic nuclei. Though neutrons do not posses an overall electric charge, they do exhibit a magnetic moment, together with a spatial distribution of charge due to their composite quark content. Therefore, the electromagnetic interactions are fully within a domain of the neutron physics. Finally, for particles of finite mass the gravitational interaction also comes into play. Neutron stars present the best known example of the neutron-related gravitational effects.

The neutron interactions with matter may be categorized into four main groups:

- *Elastic neutron scattering.* During the elastic scattering the reaction partner – such as atomic nucleus – is not excited into a higher quantum state by the passage of neutron. However, there is a definite energy transfer, needed for the recoil of all involved particles. One of the very basic examples of applications relying on the elastic scattering is the neutron diffraction – a method used for investigating the atomic and magnetic structure of materials by means of the low energy (thermal or cold) neutrons. The other one is the neutron moderation, since the elastic scattering is the dominant mode of energy loss for the neutrons in the MeV energy region.
- *Inelastic neutron scattering.* During the inelastic scattering the reaction partner is left excited and/or changes its particle structure. Therefore, we consider reactions such as (n,p), (n,d), (n,t), (n,α) (...) and even the high energy hadron shower production also to fall within this category. In practical applications, inelastic scattering also plays a role in the neutron moderation and in condensed matter research.
- *Radiative neutron capture.* During the (n,γ) capture reaction the nucleus absorbs an incoming neutron and a compound nucleus is produced in a highly excited state above the neutron separation energy. The deexcitation promptly follows through the emission of the cascade of γ-rays, which is governed by the structure of nuclear states. The neutron capture data are indispensable for the nuclear astrophysics and also find their use in the design of the nuclear reactors and accelerator facilities. Specifically, they affect the selection of the structural materials, with purpose of optimizing the radiation protection within such facilities. Furthermore, in nuclear reactors special care must be taken not to introduce the unforeseen neutron poisons into the reactor core, that might hinder or even stop the nuclear chain reactions producing usable energy.
- *Neutron induced fission.* The incoming neutron destabilizes the heavy nucleus, causing it to undergo an induced fission – a fragmentation into lighter fragments, some of which also include secondary neutrons. The neutron induced fission finds its prominent place in the modern energy production industry.

All of the listed reactions are characterized by their respective energy differential cross sections: σ_{elastic}, $\sigma_{\text{inelastic}}$, σ_{capture}, σ_{fission}. The total cross section σ_{total}, measuring the probability for any reaction to occur within a given material, is given by the sum of the individual components:

$$\sigma_{\text{total}} = \sigma_{\text{elastic}} + \sigma_{\text{inelastic}} + \sigma_{\text{capture}} + \sigma_{\text{fission}} \tag{1.1}$$

1.2.2 Neutron capture

Following the neutron capture, the nucleus is left in highly excited state, above a neutron separation energy which is typically between 5 and 10 MeV, depending on the target nucleus. The excitation energy is equal to the sum of the neutron separation energy and the total kinetic energy of the neutron and nucleus in the center of mass reference frame prior to the capture reaction. Since there is a multitude of nuclear states between the excited one and the ground state, the deexcitation proceeds through the emission of γ-ray cascades (typical γ-ray multiplicities are between 2 and 3). While in the light

nuclei the average level spacing between the states is large, in heavy nuclei it may be of the order of only 0.1 MeV. Therefore, the level structure up to the neutron separation energy in the light nuclei consists only of a few states, while the structure in heavy nuclei consists of considerably more.

The most successful formalism describing the neutron capture is the R-matrix formalism, proposed by Wigner and Eisenbud [20, 21]. The most striking feature of the theory is the separation of space into the region outside the nucleus – where the incoming neutron is not affected by the nuclear forces due to their short range – and the region inside the nucleus, where the neutron capture takes place. Without going into further details, the original formulation of the R-matrix takes on the form:

$$R_{cc'} = \sum_{\lambda} \frac{\gamma_{\lambda c}\gamma_{\lambda c'}}{E_\lambda - E} \tag{1.2}$$

where c and c' denote the entrance and exit reaction channels, respectively, with the sum going over the compound nuclear states λ through which the reaction proceeds. E_λ is, therefore, the energy of these states, while $\gamma_{\lambda c}$ and $\gamma_{\lambda c'}$ are the so-called partial widths giving the probability for a decay of a state λ through the respective channel. In order to apply the R-matrix formalism, some approximations usually have to be made. One that is widely used – for example, by the multi-level R-matrix code SAMMY [22] discussed in Section 3.6 – is the Reich-Moore approximation, translating the R-matrix elements into:

$$R_{cc'} = \sum_{\lambda} \frac{\gamma_{\lambda c}\gamma_{\lambda c'}}{E_\lambda - E - i\Gamma_{\lambda\gamma}/2}\,; \qquad c, c' \neq \gamma \tag{1.3}$$

where the elements corresponding to the γ-channels have been neglected and only those pertaining to the particle channels have been kept. As a consequence, a decay into the eliminated γ-channels has been absorbed by the newly introduced total radiation widths $\Gamma_{\lambda\gamma}$. Extensive derivation of these expressions my be found in Refs. [22, 23].

1.3 Neutron production facilities

There are several major neutron production facilities presently operating around the world. They specialize in measurements of the neutron induced reactions, which are crucial in various fields of the fundamental scientific research, as well as in applied sciences [24, 25]. In fundamental sciences the detailed data on the neutron induced reactions are important for the nuclear astrophysics – in particular for the stellar nucleosynthesis [4, 26] – for the neutron-induced symmetry breaking [27, 28], for the study of the nuclear separation energies, excited states above the neutron separation energy, nuclear level densities [29–31], etc. In applied sciences these data play a prominent role in radioprotection, dosimetry, nuclear medicine and, above all, the energy production industry. At present, nuclear energy production relying on the nuclear fission suffers from the low efficiency, gradual depletion of uranium resources and the production of a high-level nuclear waste. For this reason the alternative technologies have been considered, among which the subcritical Accelerator Driven Systems (ADS) and Generation IV fast nuclear reactors stand apart as the most promising candidates [25]. Within Accelerator Driven Systems the nuclear reaction is sustained by the neutron irradiation of the nuclear fuel in sub-critical conditions. The safety advantages of this

design are evident. In addition, the fuel may be selected such that its residual nuclear waste is either stable or characterized by the much shorter half-life (hundreds of years) relative to the presently used option (millions of years for the uranium waste). On the other hand, Generation IV nuclear reactors rely on the more efficient burning of transuranic actinides, thus producing more energy while reducing the amount of nuclear waste. The new and highly precise data on the neutron induced reactions – in particular the capture, fission and inelastic reactions on actinides – are required for the development of Accelerator Driven Systems and/or Generation IV reactors.

Alongside the neutron time of flight facility n_TOF from CERN, described in Chapter 2, the major operational neutron production facilities around the world include:

- GELINA – Geel Electron Linear Accelerator at Geel, Belgium [32]
- ORELA – Oak Ridge Electron Linear Accelerator at Oak Ridge, Tennessee [33]
- SNS – Spallation Neutron Source at Oak Ridge, Tennessee [34]
- LANSCE – Los Alamos Neutron Science Center at Los Alamos, New Mexico [35]
- J-PARC – Japan Proton Accelerator Research Complex at Tokai, Japan [36]
- Gaerttner LINAC – Gaerttner Linear Accelerator Laboratory at Troy, New York [37]
- IPNS – Intense Pulsed Neutron Source at Lemont, Illinois [38]

All these are pulsed, white neutron sources. GELINA, ORELA and Gaerttner LINAC use the electron accelerator to produce neutrons via (γ, n) reaction, while the other listed facilities use the proton accelerator, relying on the spallation process induced by protons. The high energy of the primary particle beam – ranging from tens of MeV for electrons to 20 GeV for protons – makes these facilities highly efficient at the neutron production. After the moderation, the white neutron spectra extend several orders of magnitude in energy – from thermal to at least hundreds MeV. Due to the intense γ-flash released by the charged particle beams hitting the neutron production targets, the measurements must be performed at longer flight paths, in order for the detectors to recover from the initial pulse induced by the γ-flash. Thus, the neutron flight paths used throughout these facilities vary between approximately 10 m (e.g. at LANSCE) to 400 m (at GELINA). In addition, the longer flight paths allow for the greater neutron energy resolution, facilitating the study of the resolved resonance regions. Considering the time of flight technique – yielding the neutron energy E from its time of flight t along the path length L – from a nonrelativistic relation:

$$E = \frac{m_n L^2}{2t^2} \tag{1.4}$$

it may be easily shown that the relative energy resolution:

$$\frac{\Delta E}{E} = 2\sqrt{\left(\frac{\Delta L}{L}\right)^2 + \left(\frac{\Delta t}{t}\right)^2} \tag{1.5}$$

is improved by the use of long flight paths (large L and t) and by a small spread in neutron production time, i.e. small temporal and spatial spans Δt and ΔL. At smaller accelerator facilities the neutron beam may be produced by the nuclear reactions – e.g.

^{7}Li$(p,n)^{7}$Be. Though this sources lack in intensity when compared to the major facilities, they offer a lower background and the possibility to use the short flight paths. The activation measurements – with many practical applications – are specially well suited to this kind of conditions [4]. However, only the time of flight facilities offer the extraction of the detailed parameters describing the neutron induced reactions throughout the wide energy range.

1.4 Experimental techniques

One type of the detectors used for the neutron capture experiments consists of the Total Absorption Calorimeters. Nowadays, they are most commonly constructed as 4π arrays of separate BaF_2 modules. Their most striking feature is the very high γ-ray detection efficiency, with an efficiency of almost 100% for detecting a capture reaction. BaF_2 modules are used due to their high energy resolution, low background and very fast response, allowing for the excellent signal timing resolution. One such array, made of 40 BaF_2 crystals, is used at n_TOF [39] (see Section 2.4). Another example is a DANCE detector at LANSCE [40], made of 160 crystals, featuring a high segmentation which is beneficial for the rejection of background events – based on the activated crystals multiplicity – and reduction of the data rate per single module. In general, the high detection efficiency and the background rejection capabilities of segmented 4π arrays allow to perform measurements on the very small samples and/or the radioactive ones, which produce the high activity background that needs to be suppressed [4].

In spite of being able to overcome the background of uncorrelated γ-rays, Total Absorption Calorimeters do suffer from the sensitivity to the background of the scattered neutrons. This becomes a problem when dealing with samples characterized by much larger cross section for the neutron scattering than that for the neutron capture. To a certain degree, this background may be suppressed by placing the sample inside ^{6}Li [40, 41] or ^{10}B [39] loaded absorber shell. However, for nuclei with capture-to-scattering ratio exceeding several orders of magnitude – such as the neutron-magic or light nuclei – the large arrays no longer present the best available option for performing the capture measurements. In order to meet this challenge, Moxon-Rae detectors were developed, exhibiting both the low sensitivity to scattered neutrons and the low γ-ray detection efficiency [42]. The necessary requirement for this type of detectors is a detection efficiency proportional to the total energy released in the γ-cascades. In order to fulfill this condition, the response of the detector to individual γ-rays has to be modified – for example, by the off-line procedures. Furthermore, due to the requirement for the low neutron sensitivity, the material of Moxon-Rae detectors consists of the light, low neutron capture isotopes (^{2}H, ^{12,13}C, ^{19}F) which – as the γ-ray detection materials – exhibit a negligible photoelectric effect. Therefore, the energy deposition spectra acquired with such materials do not show the photo-peaks, creating further difficulties in reconstructing the energy of γ-rays and in bringing the deposited energy into a relation with the total cascade energy. For this reason the Pulse Height Weighting Technique (PHWT) was developed [43], consisting in the off-line manipulation of the detected signals by means of the appropriate weighing function, thus making the detection efficiency proportional to the total cascade energy and independent of the actual cascade path. The details on the Pulse Height Weighting Technique may be found in Section 3.3.

The PHWT was first applied on C_6F_6 detectors [43], however they were soon shown to exhibit large systematic uncertainties [44]. The challenge was met by replacing them with C_6D_6 (deuterated benzene) liquid scintillators, which have shown to be an appropriate choice and remain in use to the present day.

^{58}Ni falls into the category of isotopes characterized by the very low neutron capture-to-scattering ratio. Therefore, the set of two optimized C_6D_6 detectors was used for its neutron capture measurement, in accordance with the above considerations. It must be emphasized that the neutron scattering off ^{58}Ni produces such a background that not only the most neutron insensitive detectors had to be used, but also dedicated simulations of the neutron background had to be performed in order to identify and subtract its contribution from the measurements. The simulated results – accompanied by the experimental background data – constitute the first complete identification of the background present in the capture measurements from n_TOF [45].

Chapter 2 of this work describes the general features of the n_TOF facility at CERN. Chapter 3 presents the analysis of the experimental ^{58}Ni neutron capture data and investigates their results. Chapter 4 describes in detail the GEANT4 simulations of the neutron background used for completing the analysis of the ^{58}Ni capture data. Finally, Chapter 5 summarizes the most important aspects and results of this work.

2

n_TOF facility

2.1 CERN complex

The *neutron time of flight* facility n_TOF at CERN (European Organization for Nuclear Research [46]) has been in operation since 2001 [47]. The layout of CERN complex is shown if Fig. 2.1.

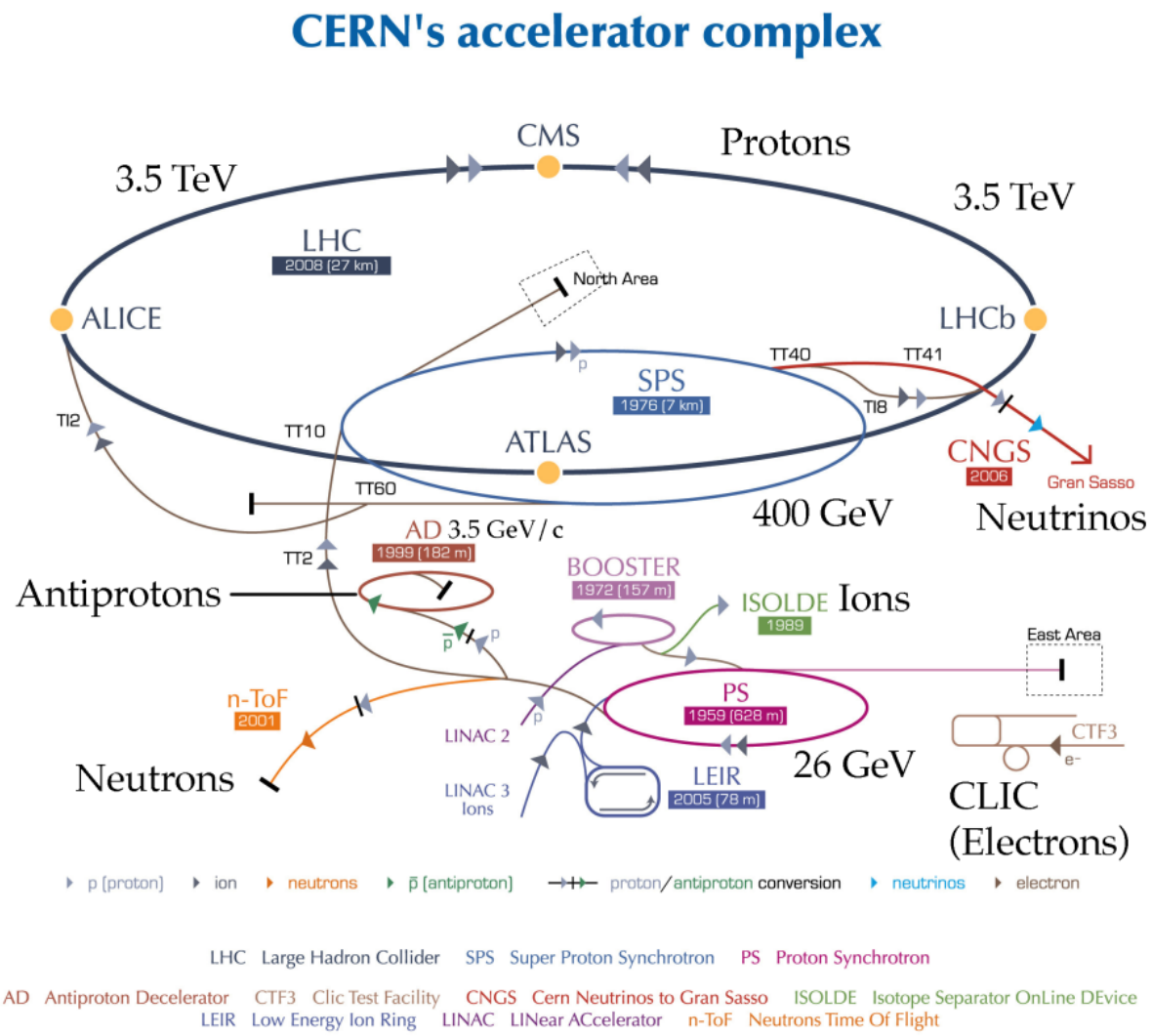

Figure 2.1 — Layout of CERN complex (adopted from Ref. [46]).

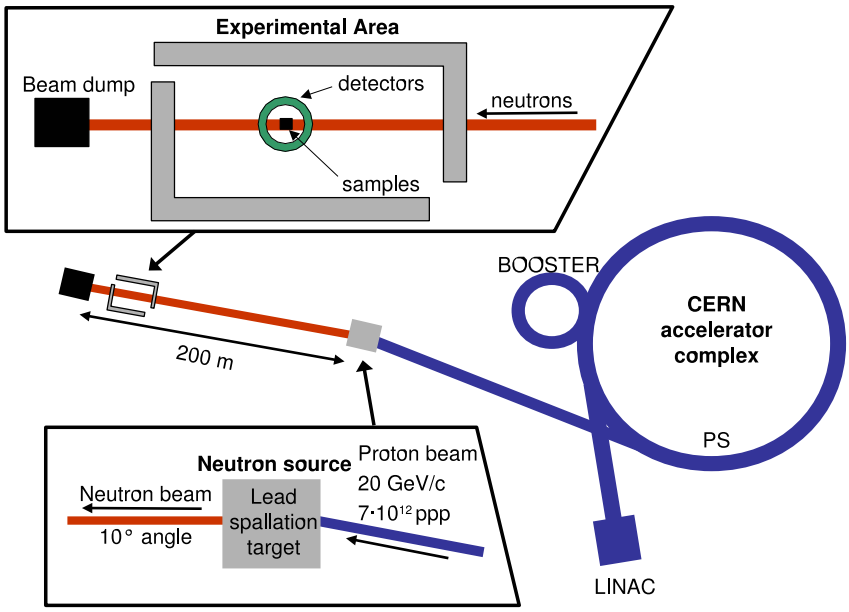

Figure 2.2 — Layout of n_TOF facility within CERN complex (adopted from Ref. [50]).

In essence, n_TOF is a pulsed neutron source coupled to 200 m long flight path, designed for the investigation of neutron induced nuclear reactions in the neutron energy range from several meV to several GeV. The closeup of the n_TOF facility is shown in Fig. 2.2.

2.2 Neutron production

At n_TOF the neutrons are produced through irradiation of the massive cylindrical Pb spallation target – 40 cm in length and 60 cm in diameter – by an intense proton beam provided by the CERN Proton Synchrotron. The beam delivers 20 GeV protons, operating in a pulsed mode with a repetition period in multiples of 1.2 s (with 0.8 Hz as the maximal repetition rate) and the pulse width of 7 ns. The very low average repetition rate of 0.4 Hz eliminates the problem of separate neutron bunches overlapping, while allowing for an efficient heat removal from the Pb target. The distribution of the protons delivered per pulse (ppp), as shown in Fig. 2.3, presents two delivery modes – so called *dedicated* and *parasitic* mode. While the dedicated component is centered at 8×10^{12} ppp, the less pronounced parasitic satellite provides the approximate delivery of 3×10^{12} ppp. The nominal delivery amounts to 7×10^{12} ppp.

During the proton induced spallation inside the Pb block, on average 300 neutrons are released per incident proton, yielding the total of 2×10^{15} neutrons per pulse – the so called neutron bunch. The initially fast neutrons are moderated by the Pb block itself, 1 cm layer of water from the cooling system and an additional 4 cm layer of borated water. The neutron flux covers 12 orders of magnitude in energy – from thermal (several meV) to several GeV. The use of borated water (H_2O + 1.28% H_3BO_3; mass fraction) as the neutron moderator is characteristic of n_TOF-Phase2, which started in 2008, following an upgrade of the spallation target. The initial run of the facility – known as n_TOF-Phase1 – lasted from 2001 to 2004, when the demineralized water was

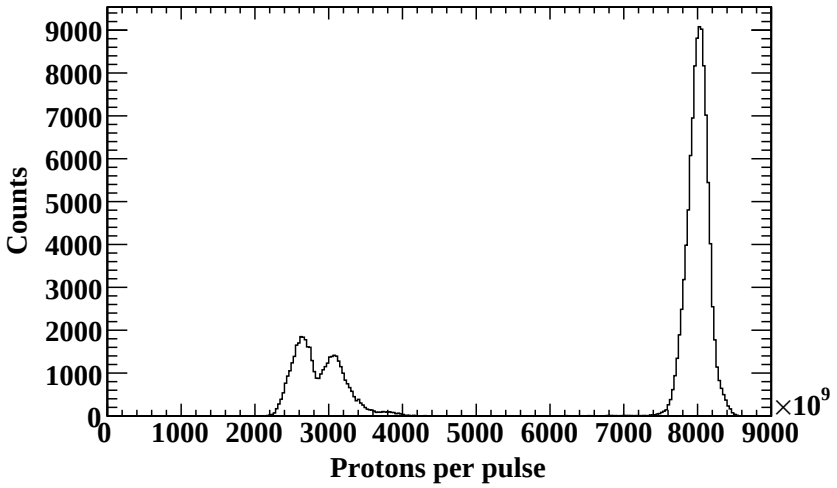

Figure 2.3 — Distribution of protons delivered per single pulse. The structure centered at 8×10^{12} protons per pulse represents the dedicated component, with the complementary satellite as the parasitic component.

used instead of borated one, resulting in a significantly higher outgoing flux of thermal neutrons. However, by the virtue of a highly neutron-absorbent $^{10}B(n,\alpha)$ reaction, the borated water suppresses the excessive production of 2.2 MeV γ-rays from the neutron capture on hydrogen, while still providing sufficiently high thermal component. By diverting the neutrons from $^{1}H(n,\gamma)$ reaction, neutron capture on ^{10}B helps in reducing the intensity of the initial γ-flash, that propagates to the experimental area and temporarily blinds the C_6D_6 detectors just before the arrival of every single neutron bunch.

An evacuated beamline – shown in Fig. 2.4 – is connected to the spallation target, leading toward the experimental area at a distance of approximately 185 m. The spallation products (neutrons, charged particles, γ-rays) not managing to enter the beamline are stopped by the massive concrete walls and 3.5 m thick iron shielding (not shown in Fig. 2.4), placed after the sweeping magnet for diverting the charged particles. The shielding was installed after the initial runs performed at the start of n_TOF facility operation, when the level of background in the experimental area was found to be two orders of magnitude higher than expected. Using the dedicated FLUKA simulations [48], the negative muon captures in the concrete walls were identified as the source of the background, causing the intense neutron emission from walls directly into the experimental area. These indications were confirmed by the dedicated measurements [49] and the iron shielding was empirically selected as the optimal means of attenuating the incident muon flux.

The filter station at 135 m from spallation target holds several filters exhibiting the so called black resonances for the neutron absorption. During the ^{58}Ni experimental campaign these were W (0.8 mm), Co (0.25 mm) and Al (30 mm) filters. By inserting the filters directly into the neutron beam, the beam is left completely devoid of neutrons within the energy range of black resonances, allowing to assess – within the energy range of black resonances – the level of background with the sample in place and to check the consistency with background measured without the sample [6].

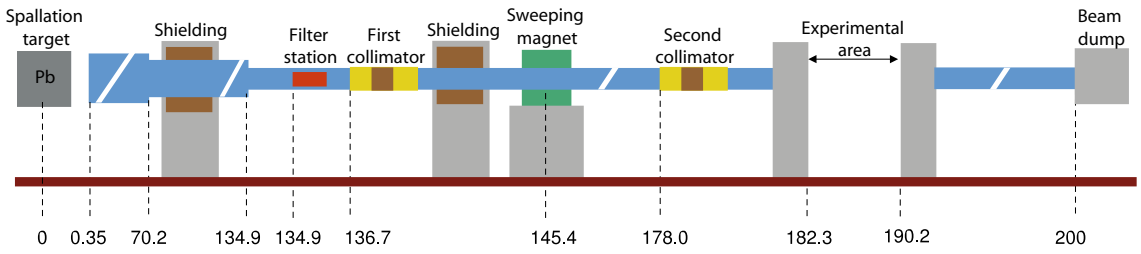

Figure 2.4 — Evacuated beamline leading from the spallation target to the experimental area. Distances are designated in meters (adopted from Ref. [50]).

The charged particles are removed from the neutron beam by a 1.5 T sweeping magnet placed at a distance of 145 m from the spallation target, and is shaped by a system of two collimators – one at 137 m, the other at 178 m from a spallation target. The aperture of the second collimator may be adjusted between 19 mm and 80 mm, corresponding to the so called *capture* and *fission* modes, respectively. Using the borated water as moderator, the total integrated (up to 1 GeV) neutron flux entering the experimental area amounts to 5.5×10^5 neutrons per bunch in capture mode or 1.2×10^7 neutrons per bunch in fission mode. ^{58}Ni capture measurement was performed with a second collimator in capture mode. The beamline ends at the beam dump placed behind the experimental area, effectively stopping the neutron beam and minimizing the neutron backscattering. Further details on the n_TOF facility may be found in Refs. [47, 50].

Alongside the number of neutrons produced and delivered per proton pulse, the n_TOF neutron beam is also characterized by the spatial profile and the resolution function. Both are well described in Ref. [50]. The beam profile near the entrance of the experimental area has been measured in the capture collimation mode, showing the Gaussian form contained within the diameter of approximately 4 cm. The profile in the fission collimation mode has been estimated from simulations, spanning the diameter of approximately 10 cm. If a sample of the diameter smaller than that of the beam itself is placed in the neutron beam, the beam interception factor has to be taken into account. It is the energy dependent fraction of the total evaluated neutron flux intercepted by the sample, with the energy dependence as a consequence of the neutron beam profile being energy dependent. Beam interception factor is described in greater detail in Section 3.5. Finally, the resolution function is introduced in order to describe the distribution of the measured time of flight t for a given neutron energy E, since not all the neutrons are produced simultaneously nor at a single point within a spallation target. The simulated distribution of released neutrons – as a function of the original neutron energy and the depth of origin inside the lead target [48, 51] – serves to evaluate and parametrize the resolution function. It was found that within a wide energy range from 1 eV to 1 MeV, the resolution function $R(t)$ may be described by the following analytical expression:

$$R(t) = A_1(t+\tau)^2 e^{-(t-\tau)/\Lambda} + A_2 e^{-A_3(t-t_0)\sqrt{E}} + A_4 e^{-A_5(t-t_0)\sqrt{E}} \tag{2.1}$$

where τ, Λ, A_1, A_2, A_3, A_4 and A_5 are all energy dependent parameters [50]. The parametrization of the resolution function will play a role during the analysis of the capture yield by means of the multi-level R-matrix code SAMMY [22], as described in Section 3.6.

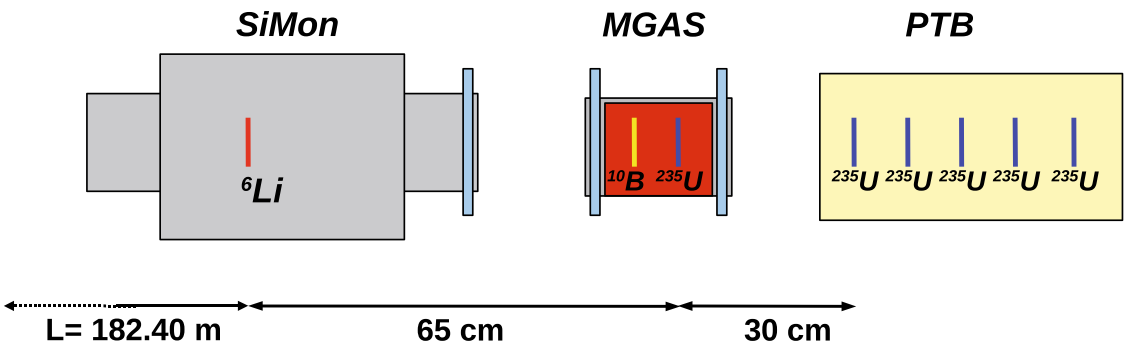

Figure 2.5 — Relative placement of the detectors used for measuring the neutron flux. L is the distance of the SiMon detector from the spallation target. PPAC detector is not shown because the measurements with PPAC were performed separately (adopted from Ref. [57]).

2.3 Neutron flux measurements

The neutron flux at n_TOF is measured by means of four different detectors, relying on different neutron induced reactions. These detectors are:

- SiMon – a silicon-based neutron beam monitor [52]
- MGAS – a Micromegas gas detector [53, 54]
- PTB – a calibrated fission chamber from Physikalisch Technische Bundesanstalt [55]
- PPAC – a set of Parallel Plate Avalanche Counters [56]

Relative placement of SiMon, MGAS and PTB detectors is shown in Fig. 2.5 (since the measurements with PPAC were performed separately, it is not included in Fig. 2.5). The used reactions include ^{6}Li(n,t), ^{10}B(n,α) and ^{235}U(n,f). Each of these reactions is characterized by a cross section standard within a limited energy range. Therefore, the measurements from different detectors were combined in order to obtain a unique evaluated neutron spectrum covering the wide energy range from thermal to 1 GeV. Table 2.1 lists the reactions employed by a given detector and their energy range considered for a reliable evaluation of the n_TOF neutron flux. Further details on the neutron flux measurements at n_TOF may be found in Refs. [50, 57].

Table 2.1 — List of the detectors used for the neutron flux measurements at n_TOF, together with the reactions they employ and the energy range used for a final determination of a unique energy dependence of the evaluated flux.

Detector	Reaction	Energy range
SiMon	^{6}Li(n,t)	30 meV – 100 keV
MGAS	^{10}B(n,α)	30 meV – 100 keV
	^{235}U(n,f)	100 keV – 1 MeV
PTB	^{235}U(n,f)	30 meV – 10 MeV
PPAC	^{235}U(n,f)	10 MeV – 1 GeV

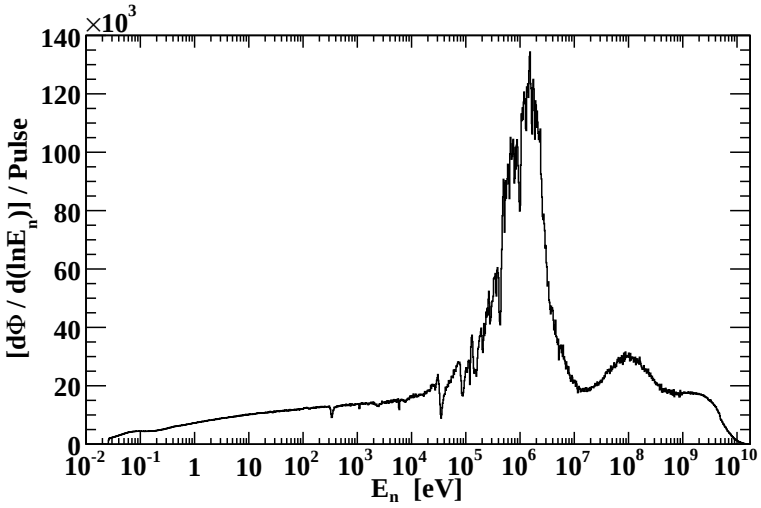

Figure 2.6 — Energy dependence of the evaluated neutron flux at n_TOF. Experimental data are available from thermal up to 1 GeV, while above 1 GeV the data were taken from the dedicated FLUKA simulations.

While the neutron flux measurements are available up to 1 GeV, the dedicated FLUKA [58–60] simulations were used to extend the evaluations up to 17 GeV, due to the extraordinary agreement between the simulated and experimental results below 1 GeV (see Ref. [57]). Though this extension is far from necessary for the analysis of ^{58}Ni capture data, the extended flux has been used for the neutron background simulations described in Chapter 4. The complete neutron flux from thermal to 17 GeV is shown in Fig. 2.6.

2.4 Detectors

For the capture measurements at n_TOF – performed by detecting the prompt γ-rays following the capture (n, γ) reactions – a set of two C_6D_6 (deuterated benzene) liquid scintillation detectors is used. One is a modified version of a detector available from Bicron, while the other one – denoted as FZK detector – was custom built at Forschungszentrum Karlsruhe [61]. The volumes of the scintillation liquids are 618 ml for Bicron and 1027 ml for FZK. These volumes must be kept low enough to provide sufficiently low detection efficiency so as to detect at most one γ-ray from a single capture reaction, which is a requirement set by the Pulse Height Weighting Technique applied during the analysis of the capture data (discussed in Section 3.3).

C_6D_6 detectors were specially optimized in order to exhibit as low neutron sensitivity as possible, which is a requirement specific to the low background neutron capture measurements. The neutron sensitivity issue and the neutron background present during the measurements are addressed in detail in Chapter 4. The two detectors, mounted face-to-face several cm upstream of the sample and perpendicular to the beamline, are shown in Fig. 2.7. In order to further minimize the neutron sensitivity of the experimental setup, the detector supports and sample exchanger were made of carbon fiber. In general, when the background of neutron captures caused by the scattered neutrons must be minimized, the carbon is preferred material due to its chemical stability, price, availability and, above all, very low neutron capture cross section.

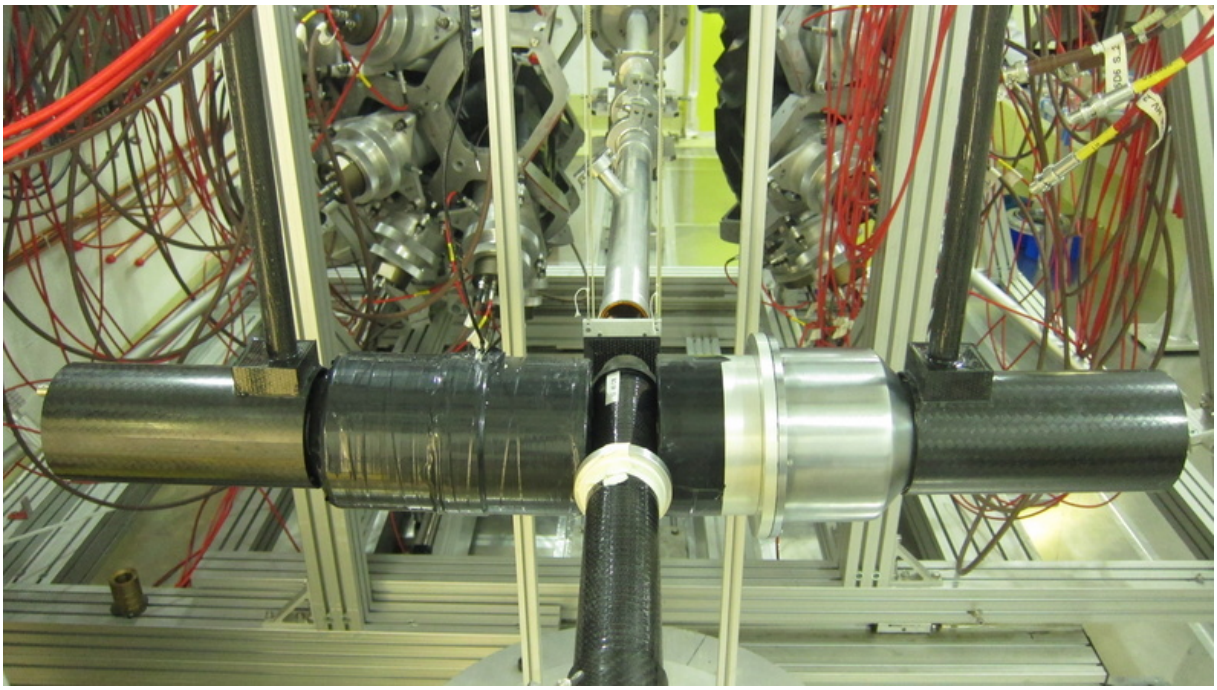

Figure 2.7 — C_6D_6 liquid scintillation detectors supported by carbon fiber housing. Left detector is FZK, while the right one is Bicron.

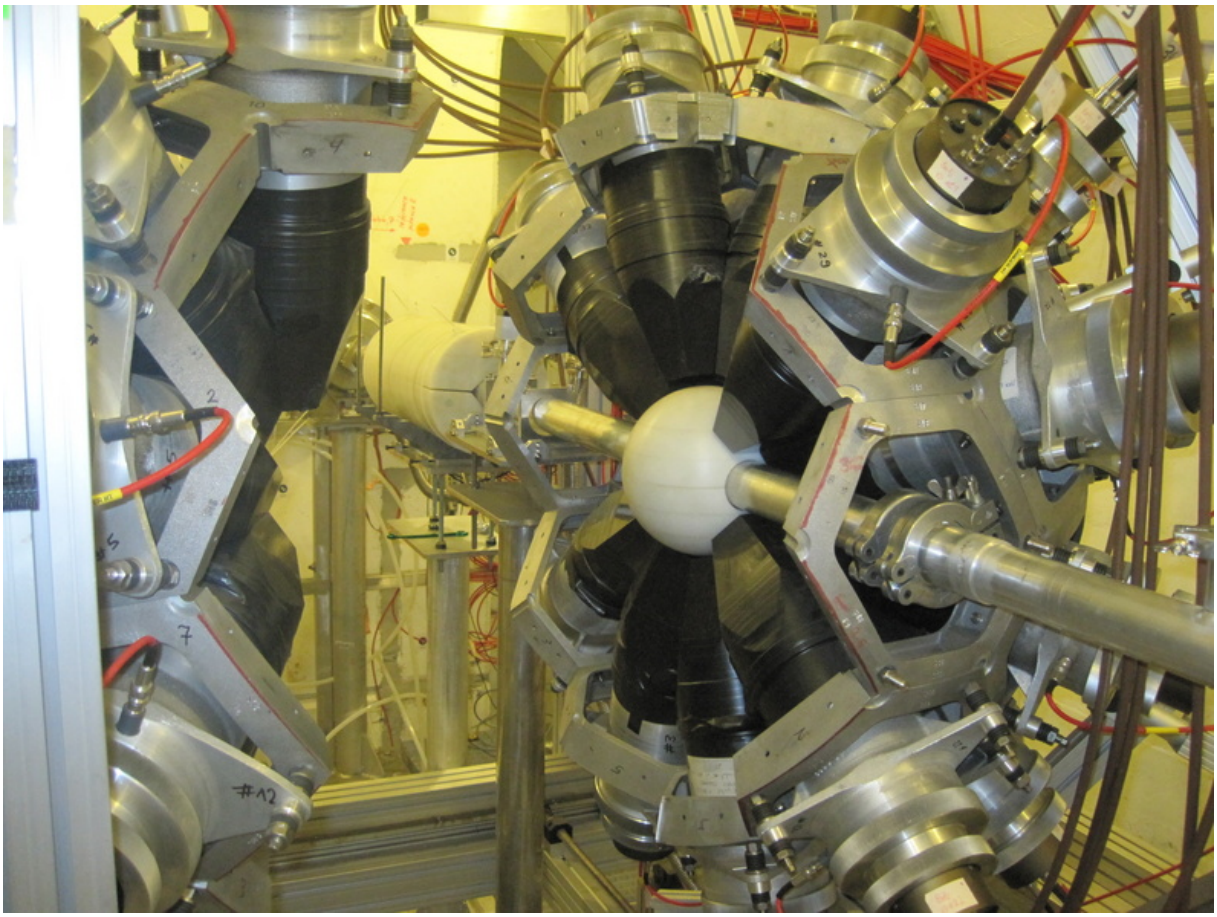

Figure 2.8 — Total Absorption Calorimeter (TAC) consisting of 40 BaF_2 scintillation crystals. The supporting honeycomb-structured ball is opened and the two hemispheres are disjointed. BaF_2 modules are wrapped in black tape. At the center is ^{10}B loaded neutron absorbing shell.

Another detector used at the n_TOF facility, though not employed within the ^{58}Ni campaign, is the TAC – a Total Absorption Calorimeter shown in Fig. 2.8 – consisting of 40 BaF_2 scintillating crystals placed in 4π-configuration around the target sample, covering 95% of a total solid angle [39]. Comprising 12 pentagonal and 28 hexagonal-shaped crystals – each one covering the same solid angle – the TAC is characterized by a high efficiency for capturing the detecting the whole γ-ray cascades. It features a good energy resolution and a rapid response. It is an experimental tool specially suited for measuring highly radioactive samples, even in small quantities due to the high detection efficiency and impressive background rejection capabilities.

2.5 Data acquisition system

A high-performance digital data acquisition system is used for recording the electronic signals from the detectors. The layout of this system is shown in Fig. 2.9. It employs 8-bit flash analog-to-digital converters (FADC) from Acqiris [62], operating at a sampling rate of 500 MHz. These units, commonly referred to as *digitizers*, allow storing the entire measured signals, one voltage point at the time. Thus the signals can be repeatedly accessed and analyzed at any later time. A memory buffer of 48 MB is used, corresponding to the waveform length of 96 ms, which allows to reach the neutron energy of 20 meV via the time of flight technique. The lower energy limit for the analysis of the capture data, however, is set by the energy range of the evaluated neutron flux, starting from 27 meV. Once digitized and stored, electronic signals can later be processed by specially developed and optimized algorithms. Further details on the data acquisition system adopted at n_TOF may be found in Ref. [63].

Figure 2.9 — Digital data acquisition system at n_TOF.

From the stored waveforms, the physical quantities such as the neutron time of flight and the energy deposited by the capture γ-rays (and/or other particles) are to be extracted. This is achieved by applying the specialized data analysis algorithms. First, the presence and the positions of voltage pulses – caused by the scintillations following the energy deposition inside the active volume of the detector – must be identified. An example of well isolated pulses from C_6D_6 detectors is shown in Fig. 2.10. For locating the pulses, the smoothed derivative of the signal is calculated, which allows for the easier pulse recognition, as the original voltage pulses are translated into strong bipolar pulses. Then the signal baseline is calculated, selecting the method best suited to the pulse's surroundings. If the pulse is far enough in time from the initial γ-flash – so that the strong leftover baseline perturbations have subsided (see Sections 1.3 and 2.2) – then the constant baseline level is calculated either from the given number of signal presamples (voltage points preceding the first pulse within the waveform) or from the portions of the signal in between the identified pulses. In case the pulse is superimposed on top of the baseline disturbance, the special iterative algorithms are applied, such as the ones described in Ref. [64]. From the baseline corrected signals, i.e. pulses, the actual physical parameters related to detected counts are to be extracted. If the detector has a well-defined pulse shape – as is the case with C_6D_6 detectors – then the referent pulse shape is adjusted to the measured pulses. The referent pulse itself is obtained by averaging the large number of measured and then normalized pulses, therefore it does not depend on assuming any analytical shape. Rather, it is given as pointwise and optimally matches the pulse shapes being analysed. The referent pulse shape is adjusted to the measured pulses applying the least-squares fitting procedure. From the fitted shape the amplitude of the pulse – made insensitive to the local signal fluctuations – may easily be read out. The amplitude of the pulse – which is for the fixed pulse shape perfectly proportional to the area under the pulse – is then used to determine the energy deposited in the detectors. From the adjusted pulse shape the arrival time of the pulse is also easily obtainable, by employing the constant fraction procedure, i.e. by finding the moment of the adjusted pulse crossing the fixed portion of the amplitude (e.g. 30%). This time information is used to assign the time of flight

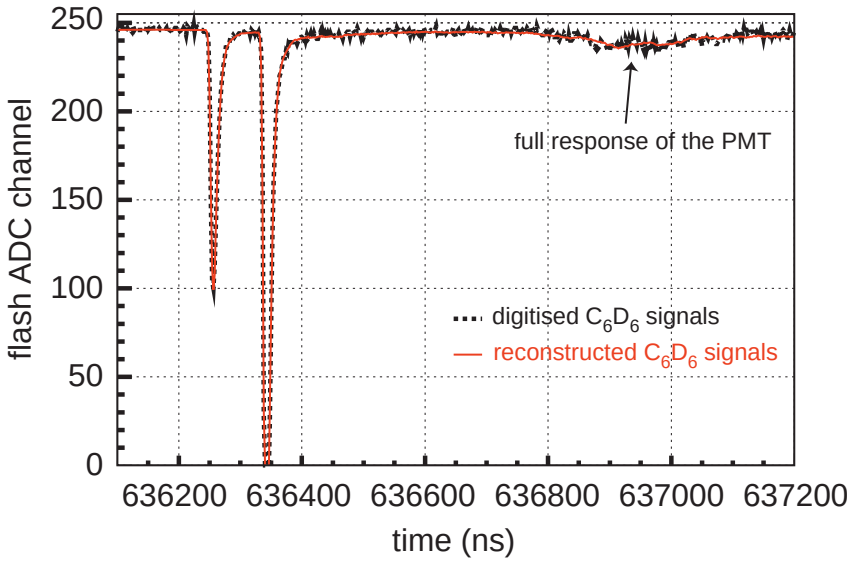

Figure 2.10 — Digitized signal from C_6D_6 detector. The results of the pulse shape adjustment are also shown (adopted from Ref. [63]).

to the detected counts. Figure 2.10 also shows the examples of pulse shapes adjusted to the measured pulses. For the detectors of variable pulse shapes the independent procedures for determining the amplitude, area under the pulse and the time of arrival are used. These are generally direct methods such as the pulse top fitting, pulse integration and the threshold crossing search for every pulse separately.

3

^{58}Ni neutron capture cross section

3.1 Experimental campaign

The experimental campaign on ^{58}Ni(n,γ) cross section lasted from 16. August to 18. September 2011. Alongside ^{58}Ni, three other samples were irradiated for various purposes: ^{197}Au, ^{nat}C and ^{nat}Pb sample. Table 3.1 lists the basic properties of these samples. The isotopic enrichment of ^{58}Ni sample amounts to 99.5%, with only 0.48% of ^{60}Ni, 0.01% of ^{61}Ni and 0.005% of both ^{62}Ni and ^{64}Ni.

Table 3.1 — Basic characteristics of the samples irradiated by the neutron beam.

	^{58}Ni	^{197}Au	^{nat}C	^{nat}Pb
Mass	2.069 g	0.596 g	7.13 g	0.313 g
Diameter	19.91 mm	19.94 mm	19.98 mm	19.90 mm
Thickness	0.72 mm	0.1 mm	10.0 mm	0.1 mm

The total proton delivery upon the spallation target amounts to 2×10^{18} protons. The distribution of protons between all samples irradiated by the neutron beam is presented in Table 3.2, reconstructed from the data files that were not discarded due to any kind of corruption or redundancy in a course of data analysis. The measurements with in-beam filters exhibiting strong neutron absorption resonances serve for background determination. During measurements the neutron flux arriving at the experimental area was monitored using a silicon-based neutron beam monitor SiMon [52], relying on ^{6}Li$(n,t)\alpha$ reaction, while minimally interfering with the incident neutron beam. In the ^{58}Ni campaign the two C_6D_6 detectors were mounted 8.2 cm upstream of the sample, at a distance of 6.8 cm from the centerline axis of the neutron beamline, thus reducing the effect of scattered in-beam γ-rays, while providing the reasonable geometric efficiency for detecting the capture γ-rays.

The aim of the following data analysis is to calculate a neutron energy dependent capture yield of ^{58}Ni$(n,\gamma)^{59}$Ni reaction. From the capture yield the pointwise capture cross section and the resonance parameters may then be extracted.

Table 3.2 — Protons delivery between different samples, pertaining to the data files kept for the analysis procedure.

Sample	^{58}Ni	^{197}Au	^{nat}C	^{nat}Pb	Empty
Without filters	1.05×10^{18}	1.73×10^{17}	9.83×10^{16}	5.38×10^{16}	1.56×10^{17}
With filters	1.85×10^{17}	5.36×10^{16}	7.66×10^{16}	7.75×10^{16}	/
Total protons			1.92×10^{18}		

3.2 Energy calibration

As a starting point in data analysis, a response stability of C_6D_6 detectors was inspected. For this purpose detectors were exposed to the standard ^{137}Cs, ^{88}Y and Am/Be calibration sources several times during a month long campaign. From Fig. 3.1 a perfect overlap of their respective γ-spectra may be observed, affirming the prolonged consistency of the detector response. Being fully compatible, all the calibration data for a given source were summed together for further energy-channel calibration.

As a first step in energy calibration, the falling edges of spectral peaks from Fig. 3.1 were identified as Compton edges for the source γ-rays. To precisely identify the channel x_{CE} corresponding to the Compton edge energy, the spectral edge was fitted to the Gaussian form $\exp[(x-\mu)^2/(2\sigma^2)]$, with x_{CE} being assigned the value at half the peak maximum:

$$x_{CE} = \mu + \sigma\sqrt{2\ln 2} \tag{3.1}$$

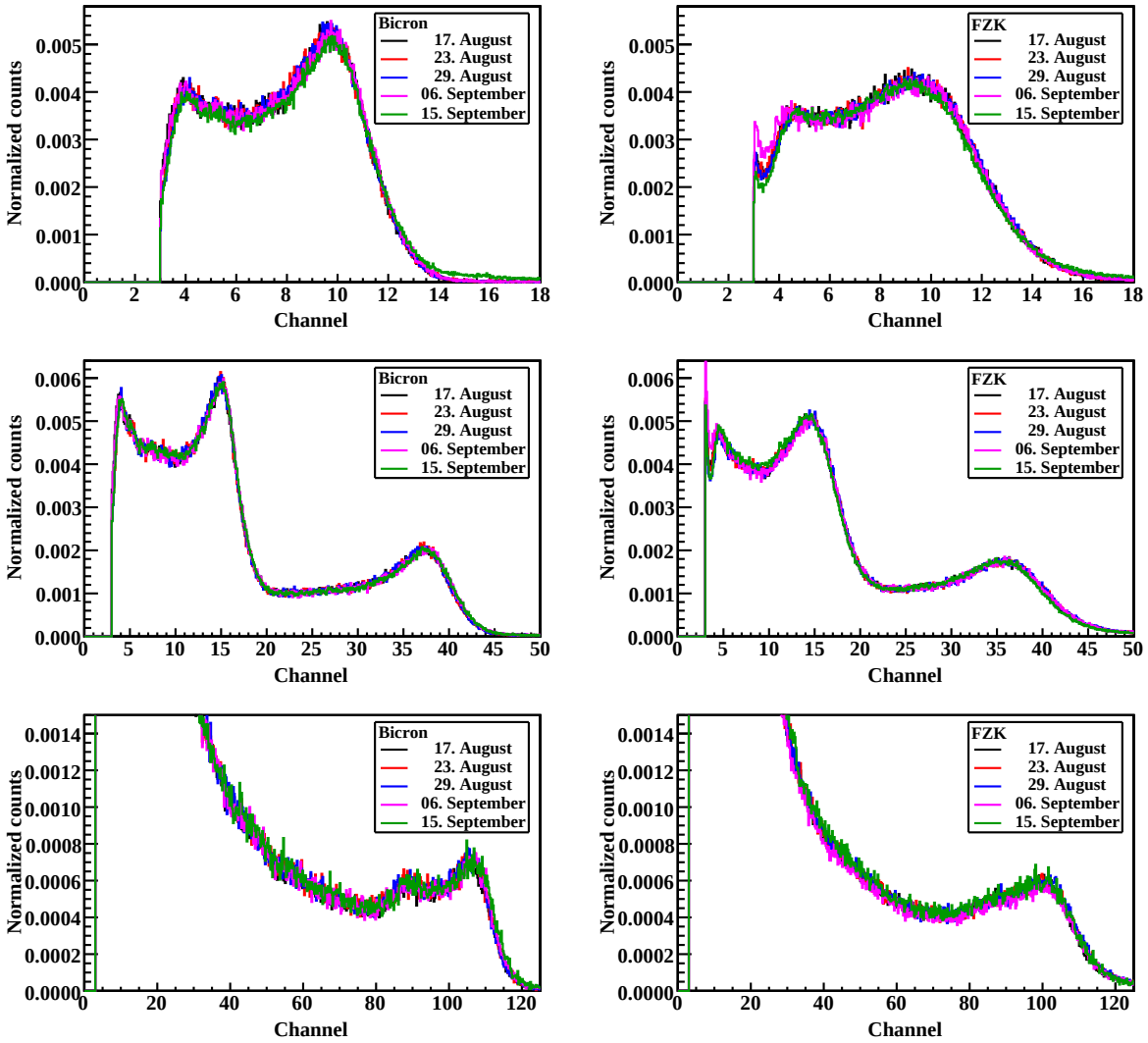

Figure 3.1 — Inspection of a response stability of two C_6D_6 detectors, performed – as indicated – on five separate occasions. From top to bottom, the spectra are overlapped for ^{137}Cs, ^{88}Y and Am/Be calibration sources, respectively.

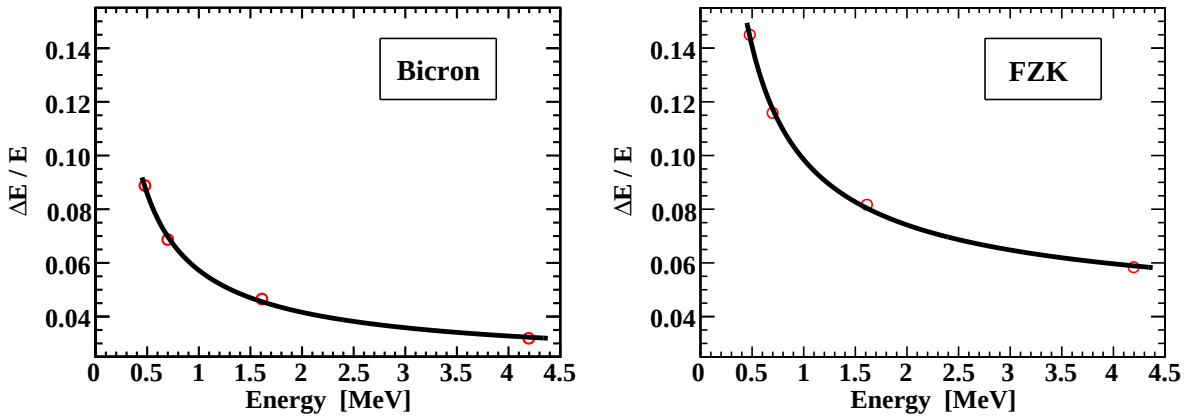

Figure 3.2 — Relative energy resolution for two C_6D_6 detectors, obtained by smearing a resolution-free simulated spectra by a Gaussian convolution until the satisfying overlaps with experimental widths were achieved.

In order to assign the γ-ray energies E_γ to the measured spectra of used sources – 662 keV for ^{137}Cs; 898 keV and 1836 keV for ^{88}Y; 4438 keV for Am/Be – the Compton edge energies E_{CE} were calculated as:

$$E_{CE} = \frac{2E_\gamma^2}{m_e c^2 + 2E_\gamma} \tag{3.2}$$

allowing to perform the initial $E_{CE}(x_{CE})$ calibration. More importantly, peak widths σ – initially fitted in terms of channel units – could now be expressed in terms of deposited energy.

As a next step a GEANT4 [65, 66] simulation of a detailed experimental setup was employed to obtain a monochromatic spectrum at four separate, calibration relevant values of E_γ. Unaffected by an inherent resolution of experimental apparatus, the simulated spectra could be artificially smeared until a satisfying overlap with measured spectra was achieved. Thus the detector resolution at four different values of E_{CE} was determined. Fitting these points to a predetermined form:

$$\frac{\Delta E}{E} = A + \frac{B}{E} + \frac{C}{\sqrt{E}} \tag{3.3}$$

a relative energy dependent detector resolution $\Delta E/E$ was extracted for the overall energy scale. The separate fit results for two C_6D_6 detectors are shown in Fig. 3.2, with extracted parameter values listed in Table 3.3.

Table 3.3 — Parameter values extracted fitting the energy resolution function (3.3). Large uncertainties for resolution parameters are due to only 4 points being subjected to a 3-parameter fit.

	Bicron	**FZK**
A	0.019 ± 0.007	0.034 ± 0.009
***B* [keV]**	22 ± 9	26 ± 11
***C* [keV$^{1/2}$]**	0.5 ± 0.5	1.2 ± 0.7

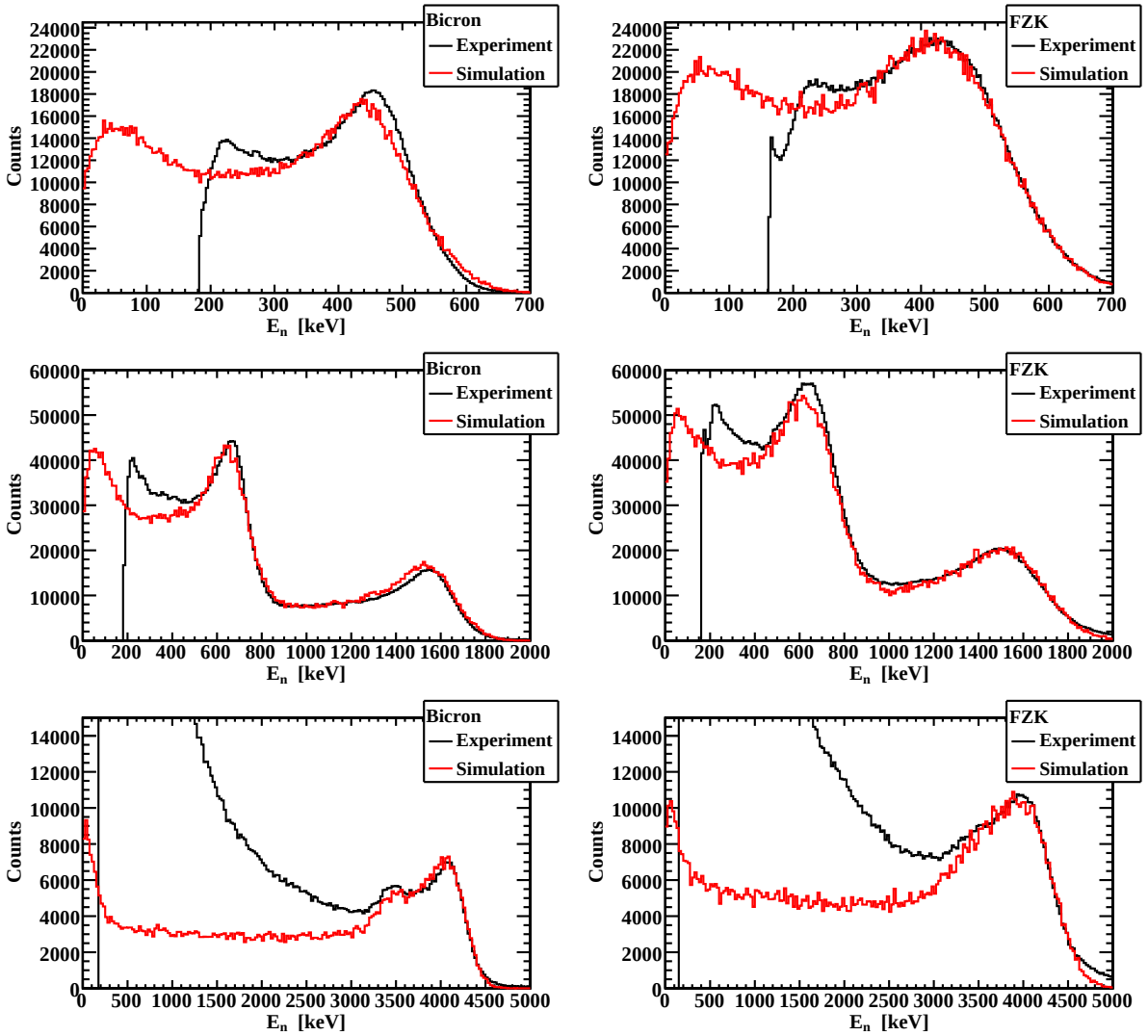

Figure 3.3 — Overlaps between experimental and resolution-smeared simulated spectra. From top to bottom the calibration sources are: ^{137}Cs, ^{88}Y and Am/Be. Due to consistency between measurements taken on separate occasions (Fig. 3.1), all the experimental data for a given source and detector were summed together.

Finally, a more subtle energy-channel calibration could be performed, compared to initial procedure relying upon calculated Compton edge energies. In order to achieve this, the simulated spectra – originally free of a detector resolution – were convoluted by a Gaussian resolution function $\exp\{E^2/[2(\Delta E)^2]\}$ with width ΔE energy dependent in a manner suggested by (3.3). Within Fig. 3.3 the resulting spectra are compared against those experimentally obtained. Repeating the procedure of identifying the Compton edge as energy value at half the maximum of a given peak – fitting the falling edge of a convoluted spectrum, followed by applying the relation analogue to (3.1) – experimental Compton edge channels x_{CE} could now be directly related to simulated values E'_{CE} of Compton edge energies. Final calibration was performed assuming slightly quadratic dependence:

$$E'_{\mathrm{CE}} = ax^2_{\mathrm{CE}} + bx_{\mathrm{CE}} + c \tag{3.4}$$

Figure 3.4 shows the results of such calibration for two detectors. Table 3.4 lists the parameter values obtained by a linear fitting procedure.

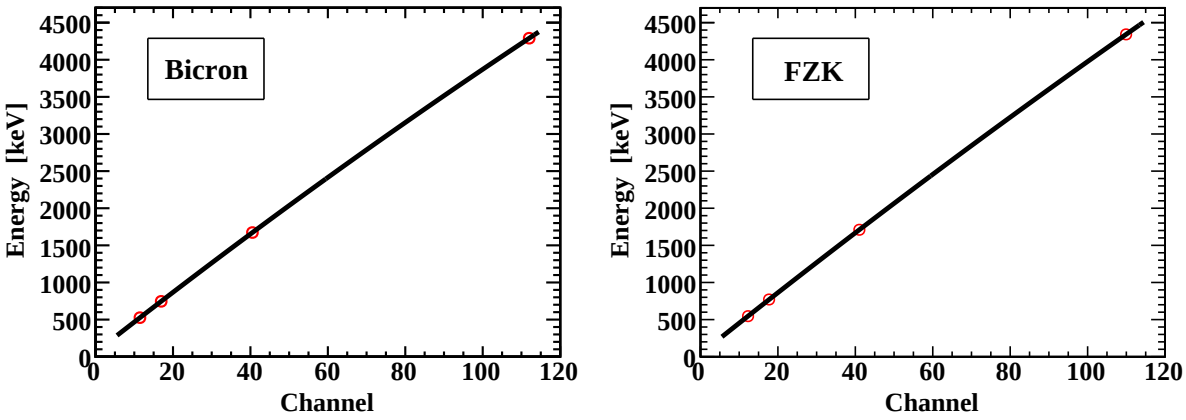

Figure 3.4 — Slightly quadratic energy-channel calibration for two C_6D_6 detectors, obtained by matching the falling edges of experimental and resolution-smeared simulated spectra, that were identified as Compton edges for characteristic γ-rays from calibration sources.

Table 3.4 — Parameter values extracted fitting the calibration function (3.4).

	Bicron	**FZK**
***a* [keV]**	-0.0284 ± 0.0003	-0.0232 ± 0.0009
***b* [keV]**	40.95 ± 0.03	41.70 ± 0.12
***c* [keV]**	60.2 ± 0.6	38.0 ± 2.2

3.3 Weighting function

The next step in the analysis was the calculation of the weighting function, a central component of the Pulse Height Weighting Technique (PHWT) originally proposed by Maier-Leibnitz [43]. The requirement for such a construct stems from a necessity for having a detector efficiency for detecting capture γ-rays known and well under control.

Following the neutron capture, a compound nucleus is left in a highly excited state, above the neutron separation energy. As illustrated in Fig. 3.5, it deexcites toward the ground state through a series of intermediate states, emitting a cascade of γ-rays in the process. Since the detection efficiency is dependent on the energy of a given γ-ray, an efficiency for detecting any of them can not be easily determined. Moreover, the average efficiency depends on the cascade details, in particular the transition probabilities between all the allowed states. The goal of the PHWT is to artificially modify the detection efficiency so as to make it independent of both the cascade path and the energy of a particular γ-ray being detected. This can be achieved if the detectors are characterized by a sufficiently low efficiency for detecting any of the γ-rays from any of the possible cascade paths. For a cascade path C, let $\varepsilon_i^{(C)}$ be the efficiency for detecting the i-th γ-ray of energy $E_i^{(C)}$. Then the total efficiency ε_C for detecting any of the γ-rays may be expressed as:

$$\varepsilon_C = 1 - \prod_i \left[1 - \varepsilon_i^{(C)}\right] \tag{3.5}$$

If all the terms $\varepsilon_i^{(C)}$ are sufficiently small, the previous expression may be approximated as:

$$\varepsilon_C \approx \sum_i \varepsilon_i^{(C)} \tag{3.6}$$

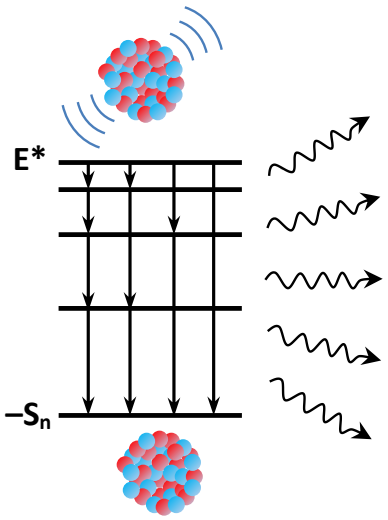

Figure 3.5 — Illustration of the γ-cascades. The nucleus excited by the neutron capture de-excites toward the ground state through the intermediate nuclear states, emitting a series of γ-rays in a process.

If the detection efficiencies were artificially modified so that they became proportional to the energy of a detected γ-ray:

$$\varepsilon_i^{(\mathrm{C})} = \alpha E_i^{(\mathrm{C})} \tag{3.7}$$

with α as an arbitrary proportionality factor, then for the total detection efficiency we would have:

$$\varepsilon_{\mathrm{C}} \approx \alpha \sum_i E_i^{(\mathrm{C})} = \alpha E_{\mathrm{x}} \tag{3.8}$$

where E_{x} is the total excitation energy of the compound nucleus, given by the sum of its neutron separation energy S_n and the total kinetic energy E^* available in the neutron-nucleus center of mass frame prior to the capture reaction:

$$E_{\mathrm{x}} = S_n + E^* \tag{3.9}$$

Therefore, the detection efficiency has been made independent of the cascade path and equal to the known excitation energy of the compound nucleus.

The proportionality from (3.7) can be achieved by applying the weighting function $W(E)$ to the experimental capture data. The weighting function itself is to be found by minimizing the following expression:

$$\sum_j \left[\int W(E')R(j;E')\mathrm{d}E' - \alpha E_\gamma(j) \right]^2 = \min. \tag{3.10}$$

with $R(j;E)$ as the j-th monochromatic spectrum, i.e. the detector response to a γ-ray of energy $E_\gamma(j)$. Since $R(j,E)$ may not be treated as continuous – due to the measured or simulated data being of a finite statistics – a binned version of a previous expression is required:

$$\sum_j \left[\sum_i W_i R_i(j) - \alpha E_\gamma(j) \right]^2 = \min. \tag{3.11}$$

to approach the histogrammed data. Evidently, for a successful and reliable calculation of a weighting function, it is a paramount prerequisite to have the genuinely monochromatic spectra $R(j;E)$ at one's disposal. Procuring them experimentally being a daunting, if not an impossible task, a detailed GEANT4 simulation was employed as an alternative deemed most reliable. In the simulations γ-rays were generated in the sample of accurately reproduced dimensions, according to a realistic depth profile. The profile may be uniform – as is generally the case for the combination of a thin sample and a moderate neutron capture cross section – or localized at the sample surface in a case of saturated resonances. In this case, the difference in depth profiles was found to be of a negligible effect on the weighting function. With an experimental setup of and surrounding the two C_6D_6 detectors programmed to the minor detail, not only are the intrinsic and geometric efficiency for detecting γ-rays taken into account, but also the finer effects such as the detection of stray photons scattered by the nearby components. Being fully automated to handle multiple spectra $R(j;E)$, i.e. instances of $E_\gamma(j)$ separately, a single run of GEANT4 simulation suffices to generate all the input data required by expression (3.11). Before calculating the separate weighting functions for two detectors, the simulated spectra were convoluted with the detector resolution function (3.3). The weighting functions are generally assumed to be polynomials of a

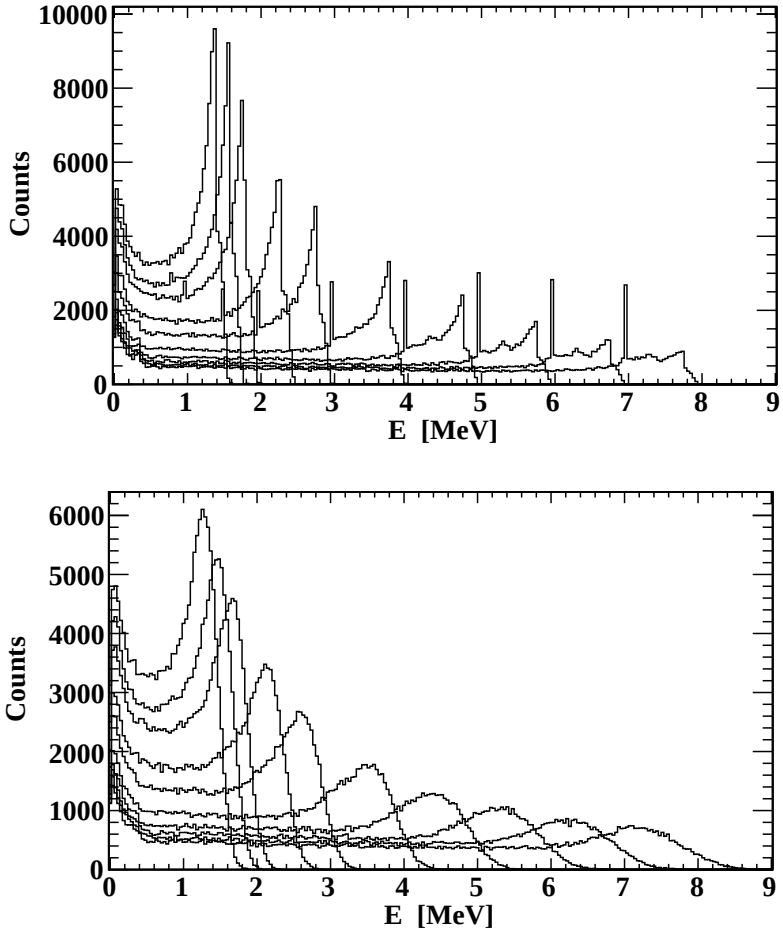

Figure 3.6 — Monochromatic spectra for several γ-ray energies E_γ from 1.6 MeV to 8 MeV for one of C_6D_6 detectors. Top panel shows detector response distributions as simulated by GEANT4 code, while bottom one those with detector resolution function having been applied. When submitted to the weighting function extrapolation algorithm, the resolution-smeared spectra are additionally voided below the experimentally set threshold of 0.2 MeV.

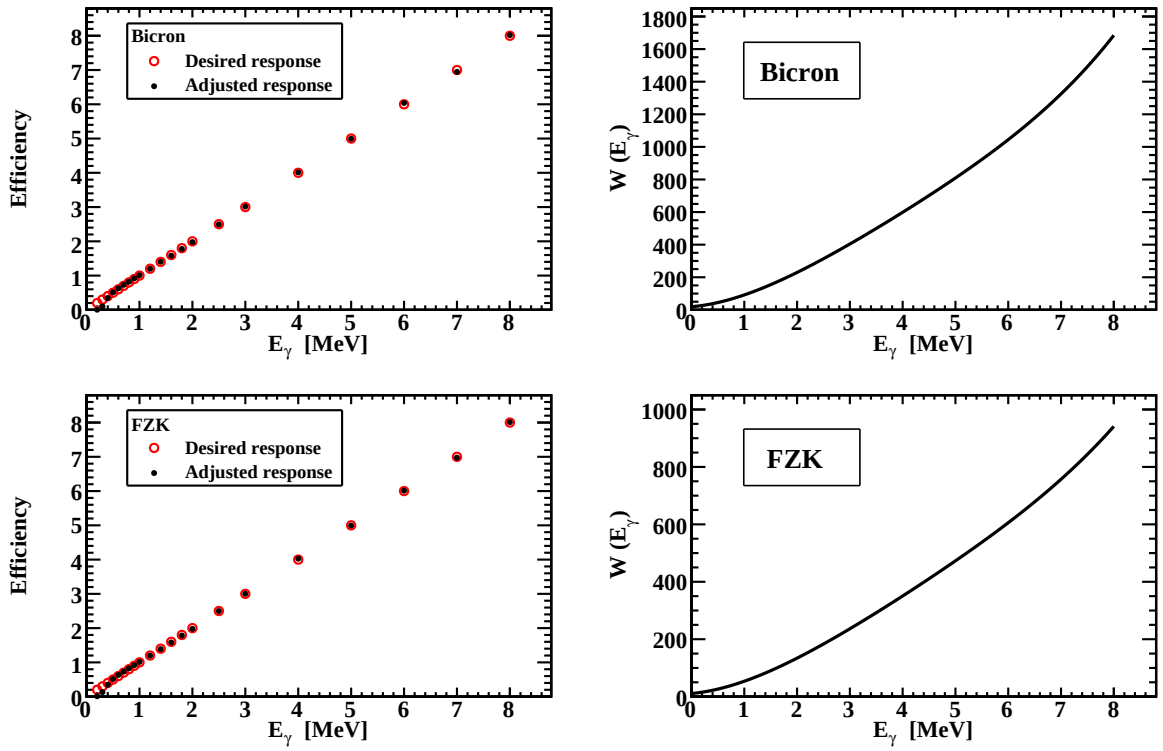

Figure 3.7 — Weighting functions for two C_6D_6 detectors (right panels), together with comparison between detection efficiency aimed to be $\varepsilon_\gamma = E_\gamma$ and efficiency remaining upon completion of the weighting function extrapolation (left panels). The discrepancy at low energies (below 0.5 MeV) is due to submitted monochromatic spectra being cut below the comparable threshold of 0.2 MeV. The widely differing scales of weighting functions are to be noted, being a direct consequence of different detection efficiencies between separate detectors.

degree N which is to be selected by user:

$$W(E) = \sum_{k=0}^{N} a_k E^k \tag{3.12}$$

Under such assumption, when arranged as vector components:

$$\begin{aligned} \vec{a} &\equiv [a_0, a_1, \ldots, a_N]^{\mathrm{T}} \\ \vec{E}_\gamma &\equiv [E_\gamma(1), E_\gamma(2), \ldots]^{\mathrm{T}} \end{aligned} \tag{3.13}$$

the set of coefficients $\{a_k\}$ may be obtained by a matrix algebra:

$$\vec{a} = \alpha \left(\mathrm{M}^{\mathrm{T}}\mathrm{M}\right)^{-1} \mathrm{M}^{\mathrm{T}}\, \vec{E}_\gamma \tag{3.14}$$

The elements of a matrix M are defined as:

$$\mathrm{M}_{jk} \equiv \sum_i R_i(j) E_i^k \tag{3.15}$$

with a summation index corresponding to the histogram bins. The details on the origin of the expression (3.14) are elaborated within Appendix A. Further description of the PHWT adopted at n_TOF may be found in Ref. [67].

For the polynomial degree of weighting functions we have adopted $N = 4$, with the value of an arbitrary proportionality factor selected as $\alpha = 1\ \mathrm{MeV}^{-1}$. Since experimentally obtained spectra are to be handled by the weighting function during subsequent data analysis, simulated monochromatic spectra – prior to being submitted to the weighting function calculation algorithm – must be subjected to a detector resolution smearing by means of a Gaussian convolution employing the energy dependent width (3.3). Examples of the monochromatic spectra for several γ-ray energies are presented in Fig. 3.6, both unaffected by a detector resolution and with the resolution function having been applied. To account for the threshold on data acquisition during the experimental campaign, the modified monochromatic spectra must also be submitted with data removed from below the same threshold value, set to $E_0 = 0.2$ MeV. Figure 3.7 shows the resulting weighting functions for two C_6D_6 detectors.

3.4 Neutron flight path

In order to access the neutron capture data, interpret and analyze them correctly, the neutron flight path must be precisely determined. For every proton pulse impinging upon Pb spallation target and producing the neutrons, an intense γ-flash is induced. Just as neutrons traverse through approximately 185 m long beamline (Fig. 3.8), γ-flash propagates to the experimental area, triggering the detectors – even blinding them for a period of time. The signal induced by a prompt γ-flash indicates the starting moment t_γ used for the determination of the neutron time of flight. Following the capture of a neutron, a sample nucleus promptly deexcites emitting the cascade of γ-rays which is subsequently detected by C_6D_6 scintillators, inducing a stop signal indicating the moment t_n of a neutron arrival. From these values a neutron time of flight Δt may be determined:

$$\Delta t = t_n - t_\gamma + L/c \tag{3.16}$$

having to be corrected for the delay L/c corresponding to the propagation of a γ-flash along the beamline of length L. From the time of flight, a captured neutron kinetic energy E_n is calculated using the relativistic expression:

$$E_n = m_n c^2 \left(\frac{1}{\sqrt{1 - \left(\frac{L}{c\Delta t}\right)^2}} - 1 \right) \tag{3.17}$$

with m_n as a mass of a neutron and c as a speed of light in vacuum.

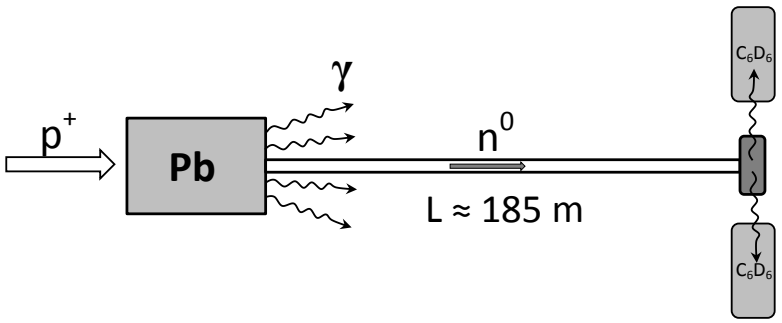

Figure 3.8 — Illustration of a sequence of events following every proton pulse impinging upon the Pb block. First, the intense γ-flash is induced, generating a start signal for measuring the neutron time of flight. Following the neutron capture, a sample nucleus undergoes a prompt γ-decay. Detecting a γ-ray by one of the C_6D_6 scintillators generates a stop signal.

However, the value of the neutron flight path L – central to the translation of a time of flight into neutron energy – is not easily determined by geometric means. For this purpose, the method of aligning the reconstructed resonances of a thin ^{197}Au sample with the well-established reference is employed, according to the description from Ref. [68]. The value of L is manually varied until the globally optimal overlap is achieved for a wide range of ^{197}Au resonances. Thus an optimum of $L = 184.00 \pm 0.05$ m was established, with an uncertainty of 5 cm estimated by a mere visual inspection. Several representative resonant peaks are presented in Fig. 3.9, showing the misalignment of the reconstructed data for the slight shifts in L.

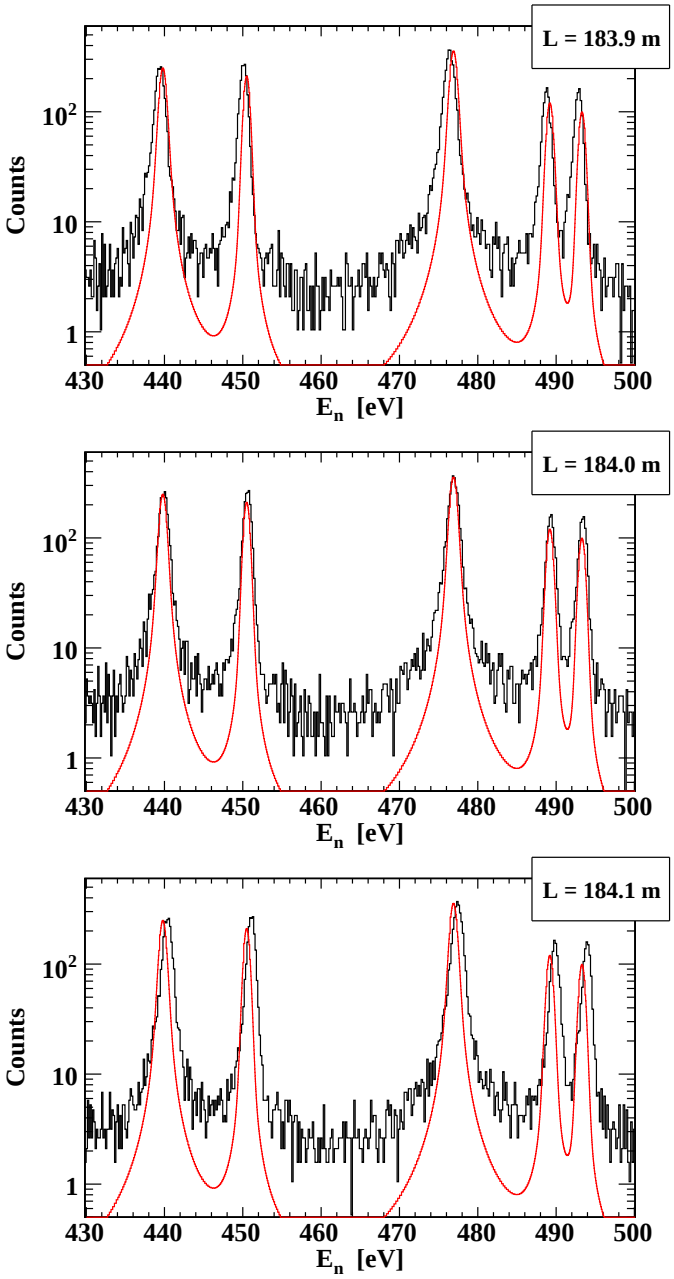

Figure 3.9 — Matching the alignment of reconstructed ^{197}Au resonances (black line) with reference data (red line) by varying the neutron flight path L. The optimal overlap (middle panel) is achieved for $L = (184.00 \pm 0.05)$ m. The upper and lower panels show the misalignment for the value of L shifted by –10 cm and +10 cm, respectively.

3.5 Capture yield

From the measurements, the capture yield $Y(E_n)$ is to be calculated as:

$$Y(E_n) = \frac{C_w(E_n) - B_w(E_n)}{N E_x(E_n)\phi(E_n)} \tag{3.18}$$

where $C_w(E_n)$ and $B_w(E_n)$ are the total weighted sample-related and background counts, respectively. The compound nucleus excitation energy E_x serves to correct for the detection efficiency, by the virtue of the Pulse Height Weighting Technique. As in (3.9), it is given by the sum of the total kinetic energy available in the neutron-nucleus center of mass frame prior to the capture reaction, and the neutron separation energy of the compound nucleus – 8.99 MeV for ^{59}Ni or 6.51 MeV for ^{198}Au. $\phi(E_n)$ is the total neutron flux intercepted by the sample, while N is the final absolute yield normalization factor, taking into account finer experimental effects. It is described in more detail at the end of this Section.

Several sources of background are present during the experiment. One is caused by the scattered in-beam γ-rays. It was measured with the Pb sample and found to be completely negligible. Another – so called *empty-frame background* – is independent of the sample and caused by the neutron beam alone. It is easily measured by removing the sample and irradiating an empty sample frame consisting of a 1.5 μm thin Mylar backing glued to the carbon fiber support. Next component is the environmental background – also referred to as the *beam-off background* – caused by the environmental radioactivity, both natural and one induced by the neutron activation. It was also measured, by simply turning off the neutron beam. It must be taken into account, however, that the portion of the environmental background is already contained within the empty-frame background, so the proper normalization must be performed. In Appendix B the correct expression for the true, neutron energy dependent capture counts per neutron bunch (i.e. the proton pulse) is derived, taking on the form:

$$N_{\text{PER PULSE}} = P_{\text{NOMINAL}} \left[\frac{N_{\text{SAMPLE}}}{P_{\text{SAMPLE}}} - \frac{N_{\text{EMPTY}}}{P_{\text{EMPTY}}} - \left(\frac{E_{\text{SAMPLE}}}{P_{\text{SAMPLE}}} - \frac{E_{\text{EMPTY}}}{P_{\text{EMPTY}}} \right) \frac{N_{\text{OFF}}}{E_{\text{OFF}}} \right] \tag{3.19}$$

Indices SAMPLE, EMPTY and OFF refer to the sample-related, empty-frame and beam-off measurements, respectively. N denotes the measured number of counts. P stands for the total number of protons delivered on the spallation target during the measurement, with $P_{\text{NOMINAL}} = 7 \times 10^{12}$ as the nominal number of protons per single proton pulse (see Section 2.2). E is the total number of events, corresponding to the total number of proton pulses in case of the sample-related and empty-frame measurements, or emulated number of proton pulses in case of the beam-off measurements. Expression (3.19) also hold for the weighted counts, i.e. after the PHWT has been applied. The *neutron background*, as the final background component, is caused by the neutrons scattered off the sample itself. It was determined by means of detailed, high-precision GEANT4 simulations, which are extensively described in Chapter 4.

Figure 3.10 shows the total ^{197}Au and ^{58}Ni capture measurements, together with the empty-frame and environmental background for the two detectors separately. Both the energy deposition spectra and the kinetic energy spectra reconstructed from the time

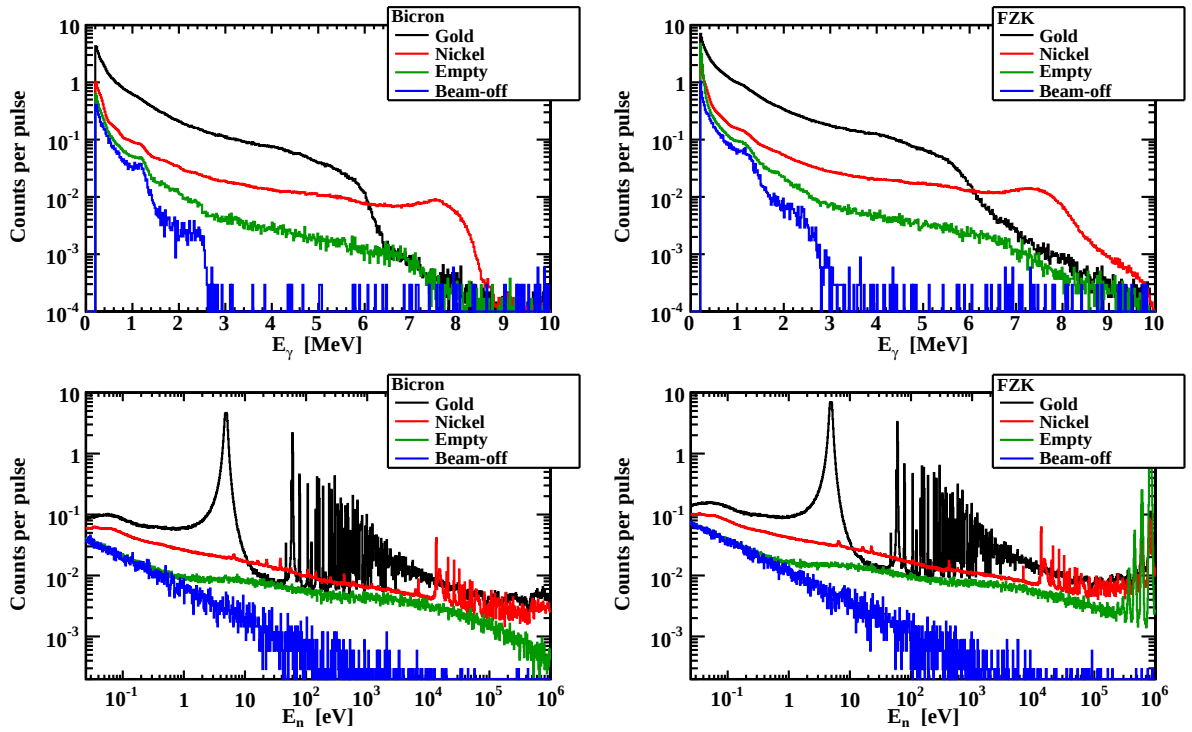

Figure 3.10 — Spectra of counts measured per single proton pulse. Spectra show the total ^{197}Au capture measurements, ^{58}Ni capture measurements, empty-frame backgound and environmental background (for which the proton pulses are emulated). The results for two detectors are shown separately. Upper panels show the energy deposited in C_6D_6 detectors, while lower panels show the energy reconstructed form the time of flight.

of flight are shown. All spectra are normalized to the number of proton pulses or emulated proton pulses in case of the environmental background. The difference in the absolute height between the two detectors may be noted, as a direct consequence of their different detection efficiencies. In the kinetic energy spectra, significant differences may be observed between the two detectors above 100 keV, related to a recovery problem of the photomultiplier after the initial γ-flash at a beginning of every neutron bunch. For Bicron detector the recovery is not fully successful. Therefore, only FZK data are used for the analysis above 100 keV. However, above 400 keV FZK exhibits the strong leftover signal oscillations from γ-flash, which limits the capture data analysis up to this particular energy.

An interesting feature of the environmental background spectrum, readily seen from Fig. 3.10, is its very well defined shape, due to the nature of the radioactive decay, independent of the characteristics of a specific experimental setup. Appendix C shows that, for histogram bins equally distributed over the logarithmic scale, the spectrum of environmental background counts follows a simple energy dependence:

$$p_{\log}(E_n) \propto \frac{1}{\sqrt{E_n}} \tag{3.20}$$

when the timestamps of the counts are translated into energy using the time-energy correlation for neutrons, in particular the non-relativistic version of (3.17). Though this simple dependence allows for the environmental background to be fitted and replaced by a smooth shape, we have selected to avoid this procedure during the background subtraction and use the pointwise spectrum of counts, as originally measured.

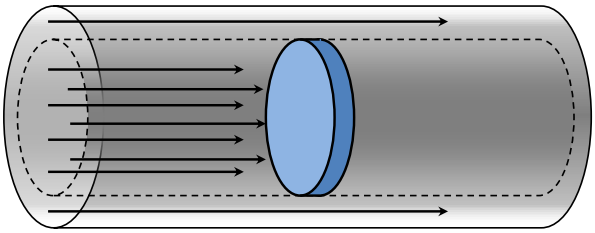

Figure 3.11 — Illustration of a neutron beam impinging upon a sample of a smaller diameter than that of the beam itself, giving rise to a beam interception factor. The beam intensity declines from the centerline axis, showing a radial profile of a Gaussian form in the capture collimation mode.

The neutron flux $\phi(E_n)$ intercepted by the sample differs from the evaluated neutron flux $\Phi(E_n)$ shown in Fig. 2.6, due to the sample dimensions being smaller than the spatial beam profile. The issue is illustrated in Fig. 3.11. Since the experimentally determined beam profile in the capture collimation mode shows approximately Gaussian shape covering approximately 3.5 cm in diameter [50], the samples of 2 cm diameter can not take advantage of the full incident neutron flux. This gives rise to the beam interception factor (BIF) – an energy dependent fraction of the total neutron flux intercepted by the sample. The energy dependence of BIF is a result of the beam profile being dependent on the neutron energy, since the very high energy neutrons are subjected to a lesser transversal spread. The beam profile and the resulting BIF have been evaluated by means of dedicated FLUKA [58–60] simulations for the full energy range of the n_TOF neutron beam. For samples of 2 cm diameter the energy dependece of BIF is shown in Fig. 3.12. The intercepted neutron flux per neutron bunch is, therefore, obtained by multiplying the experimentally evaluated flux with the beam interception factor found from simulations:

$$\phi_{\text{per bunch}}(E_n) = \Phi(E_n)\text{BIF}(E_n) \tag{3.21}$$

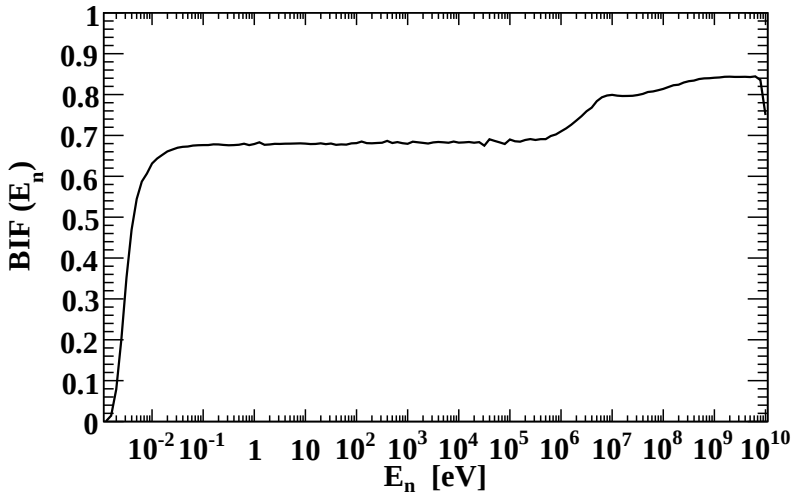

Figure 3.12 — Energy dependence of the beam interception factor for samples of 2 cm diameter and neutron beam in the capture collimation mode, as obtained by dedicated FLUKA simulations.

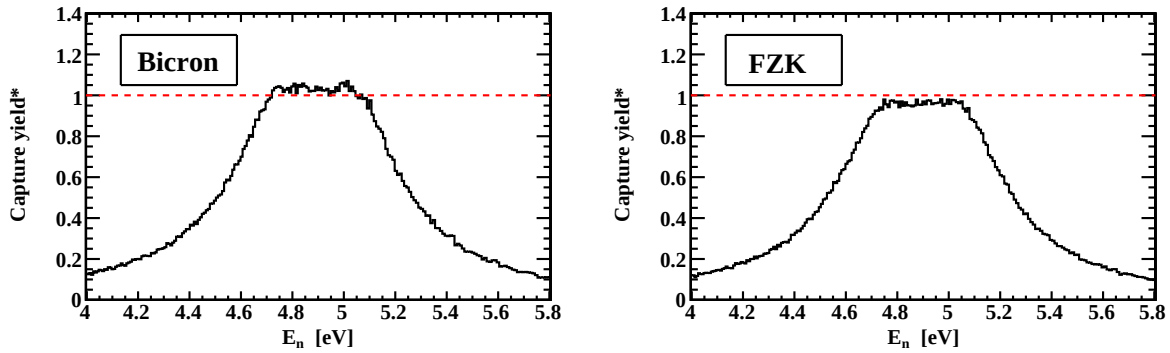

Figure 3.13 — Saturated capture resonance of ^{197}Au, for two detectors. Spectra show the capture yield, prior to correcting for the absolute normalization factor N.

When extracting any kind of physical spectra from histogrammed data, the correction for the binning, i.e. the arbitrarily selected bin widths must be performed. Additional complexities arise when the histogramming is performed with the bins equally distributed over the logarithmic scale, which is a common case with capture measurements due to the data extending over multiple orders of magnitude in energy. Appendix D addresses this issue, showing that the data histogrammed over the logarithmic scale must be scaled by the factor:

$$\frac{\mathrm{BINS}\cdot\log_{10} e}{\log_{10}\left(E_{\max}/E_{\min}\right)} \approx \frac{0.4343\cdot\mathrm{BINS}}{\mathrm{DECADES}} \tag{3.22}$$

where BINS stands for the total number bins within the histogram range extending from $E_{\min}$ to $E_{\max}$, covering the total of DECADES $= \log_{10}(E_{\max}/E_{\min})$ decades in energy. As a direct consequence of histogramming the data over the logarithmic scale, even after this correction the spectra of (weighted) counts remain artificially amplified by the local value of the argument (in this case the neutron energy E_n), due to the varying bins widths. However, since the evaluated neutron flux $\Phi(E_n)$ is histogrammed in the same manner, exhibiting the same kind of multiplicative amplification by E_n, this effect is implicitly canceled during the calculation of the capture yield.

The final, absolute yield normalization factor N from (3.18) has been obtained applying the saturated resonance technique to 4.9 eV capture resonance of ^{197}Au [69]. Within the energy region of a resonance exhibiting a huge capture cross section, one may expect the saturation of the capture probability, expressed through the capture yield. If we assume that subtle experimental effects might have been unaccounted for, or that slight inaccuracies were introduced by the weighting procedure, then the saturated capture yield would not have been properly normalized to unity. The normalization factor N serves to account for these second order corrections. Figure 3.13 shows the saturated resonance of ^{197}Au for two detectors, prior to extracting the absolute normalization factor N, which is given exactly by the height of the flat top of the saturated yield.

Figure 3.14 shows the total (background inclusive) experimental yield calculated for ^{197}Au and ^{58}Ni sample. The experimental empty-frame and environmental background and the simulated neutron background yield are also shown. For the most part, the environmental background yield is already included within the empty-frame yield. During the background subtraction, it was properly scaled in accordance with (3.19).

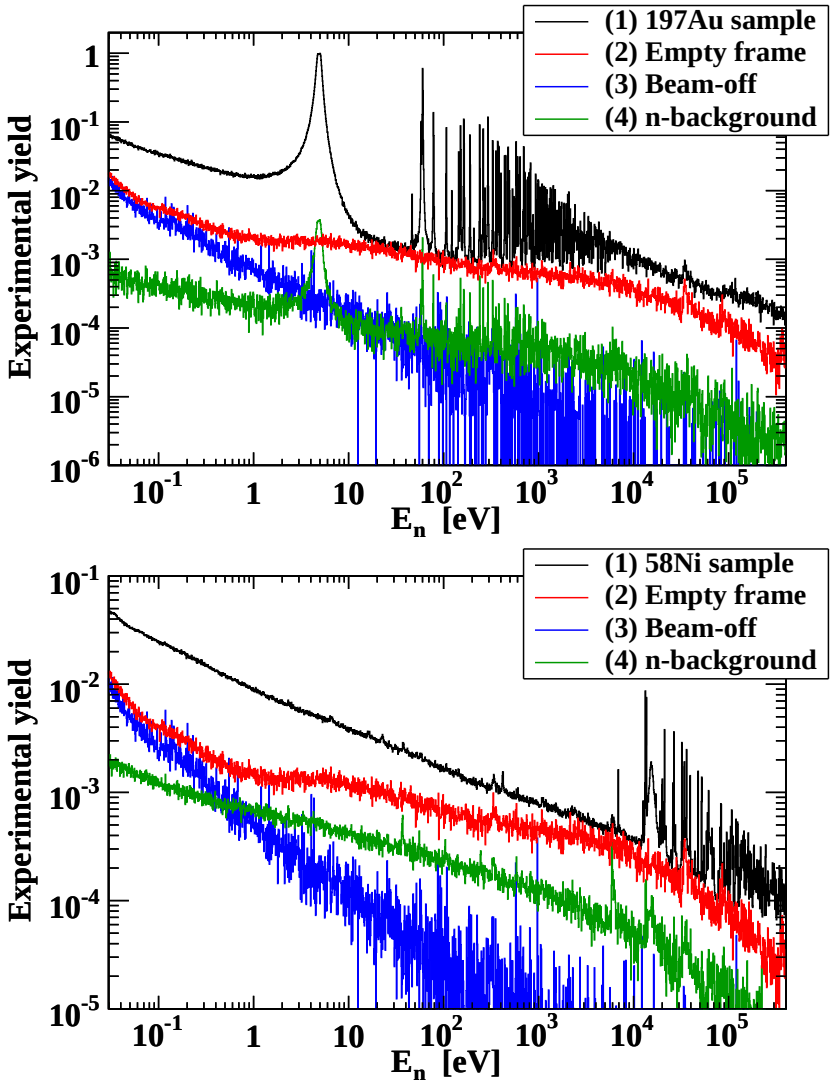

Figure 3.14 — Total experimental yield of ^{197}Au (top panel) and ^{58}Ni (bottom panel), together with the empty-frame and environmental background yield. The neutron background yield was obtained by means of dedicated GEANT4 simulations.

3.6 Neutron capture cross section

3.6.1 General notes

From a capture yield, a reliable parametrization of a capture cross section may only be obtained by a nontrivial mathematical treatment, since the capture yield is heavily affected by various experimental effects. Among these are the resolution function of a neutron beam, Doppler broadening of capture resonances, multiple scattering and self-shielding effects. Their impact on the measured capture resonances is well described in Ref. [50]. A multilevel *R*-matrix code SAMMY [22] – used in the subsequent analysis of the capture yield – is able to properly account for all these effects. In the following sections the capture yield at thermal energies, resolved resonance region and unresolved resonance region will be treated separately, due to the different challenges present therein.

3.6.2 Thermal capture cross section

The neutron capture cross section at low energies – more precisely, before the first capture resonance – exhibits $1/v$ dependence, where v is the speed of the incident neutron. Though this result is fully founded in quantum mechanical calculations, it may be understood intuitively, since the probability for the neutron capture depends on the time the neutron spends inside the nucleus, which is inversely proportional to its speed. This $1/v$ tail at low energies may be reproduced in SAMMY by adopting the resonances at negative neutron energies, i.e. those located below the neutron separation energy. The tails of the resonant curves then emulate the $1/v$ dependence in the immediate vicinity of the neutron separation energy. In order to fit ^{58}Ni capture yield up to 10 keV, two negative resonances were adopted, as suggested by the latest versions of the evaluated libraries, as well as by the latest compilation from Mughabghab [70]. Out of five resonant parameters per single resonance – energy E_R, orbital angular momentum ℓ, spin J, neutron width Γ_n and radiative capture width Γ_γ – only the capture width was left free during the fitting procedure, while the values of the remaining four were adopted from ENDF/B-VII.1 parameters database – accessed via JANIS interface [71] – and fixed. Fitting the data yields the following parameters of the negative resonances:

$$(E_R^{(1)}, \ell^{(1)}, J^{(1)}, \Gamma_\gamma^{(1)}, \Gamma_n^{(1)}) = (-78318\,\text{eV},\ 0,\ 1/2,\ 25\,\text{eV},\ 40685\,\text{eV})$$
$$(E_R^{(2)}, \ell^{(2)}, J^{(2)}, \Gamma_\gamma^{(2)}, \Gamma_n^{(2)}) = (-11674\,\text{eV},\ 0,\ 1/2,\ 1.6\,\text{eV},\ 4262.7\,\text{eV})$$

The portion of n_TOF capture data exhibiting $1/v$ dependence is shown in Fig. 3.15, together with the SAMMY fit. It is clear that the fit reproduces the global shape of the experimental spectrum very well. However, it may also be observed that it slightly overestimates the data at low energies, in the vicinity of the thermal point at 25.3 meV. Therefore, an independent $1/v$ fit was applied to the low energy region between 27 meV and 50 meV, in order to extrapolate the thermal value σ(25.3 meV) of the capture cross section. For this procedure, of course, the capture yield first had to be translated into the cross section. (One may observe that the data from Fig. 3.15 have already been presented as the cross section, rather than the yield.) This was done on the basis

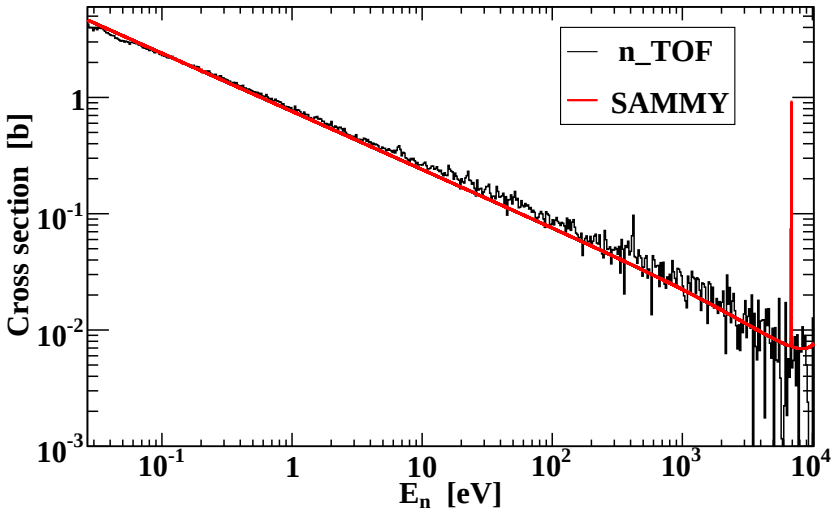

Figure 3.15 — Measured ^{58}Ni capture cross section between 27 meV and 10 keV. The SAMMY fit was obtained by adopting two negative-energy resonances.

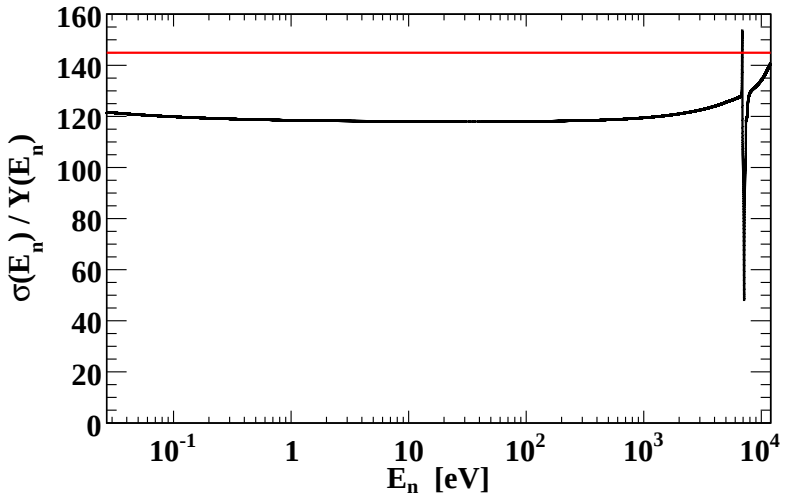

Figure 3.16 — Pointwise ratio of the capture cross section and the capture yield (black curve), obtained from SAMMY and used for the conversion of the measured yield into the measured cross section. The positioning of $1/n$ factor (n being the areal density), given by the red line, shows that the thin-target approximation is not appropriate due to the strong multiple scattering effects.

of SAMMY output. Once the resonance parameters (for negative energy resonances) have been established fitting the capture yield, from these parameters SAMMY may calculate both the pointwise capture yield $Y_{\mathrm{SAMMY}}(E_n)$ and the pointwise cross section $\sigma_{\mathrm{SAMMY}}(E_n)$ unaffected by experimental effects. Taking the pointwise ratio of their energy dependent values, one obtains the pointwise conversion factor which may be applied to the experimental yield $Y_{\mathrm{exp}}(E_n)$ in order to calculate the experimental cross section $\sigma_{\mathrm{exp}}(E_n)$:

$$\sigma_{\mathrm{exp}}(E_n) = \frac{\sigma_{\mathrm{SAMMY}}(E_n)}{Y_{\mathrm{SAMMY}}(E_n)} Y_{\mathrm{exp}}(E_n) \tag{3.23}$$

The conversion factor is shown in Fig. 3.16. However, this type of conversion may only be trusted outside the resonant region. Since the resolution function of the neutron beam and the Doppler broadening of capture resonances not only deform the resonances – in terms of yield – but also shift their maximums, relative to the resonances in the cross section [50]. They do not appear at exactly the same energies within the two spectra, causing the resonant structure in the conversion factor spectrum. An example may clearly be observed in Fig. 3.16, where the effect is shown for the first ^{58}Ni capture resonance at 6.9 keV.

In Fig. 3.16 an additional comparison is shown. It is common, during the calculation of the capture yield, to make the approximate calculation of the cross section employing the simple scaling by the constant factor. In the absence of the multiple scattering corrections, the exact relation between the capture yield $Y(E_n)$ and the capture cross section $\sigma_\gamma(E_n)$ takes on the form:

$$Y(E_n) = \left(1 - e^{-n\sigma_{\mathrm{tot}}(E_n)}\right) \frac{\sigma_\gamma(E_n)}{\sigma_{\mathrm{tot}}(E_n)} \tag{3.24}$$

with $\sigma_{\mathrm{tot}}(E_n)$ as the total cross section and n as the areal density (in number of atoms per unit area) of the sample. Assuming a thin target, such that $n\sigma_{\mathrm{tot}}(E_n) \ll 1$ holds,

Table 3.5 — Thermal cross section from n_TOF compared against previously reported experimental results from EXFOR [11], ENDF/B evaluations [13, 18] and the recommended value from Mughabghab [70]. The data denoted by MX are reported as Maxwellian averages.

Source	**σ(25.3 meV)**
n_TOF	$4385 \pm 22_{\text{stat}} \pm 137_{\text{sys}}$ mb
Pomerance$^{\text{MX}}$ (1952)	4200 ± 336 mb
Ishaq$^{\text{MX}}$ (1977)	4500 mb
Carbonari (1988)	4520 ± 100 mb
Weselka$^{\text{MX}}$ (1991)	4600 ± 300 mb
Venturini$^{\text{MX}}$ (1997)	4400 ± 200 mb
Raman$^{\text{MX}}$ (2004)	4130 ± 50 mb
ENDF/B-VII.0	4621 mb
ENDF/B-VII.1	4227 mb
Mughabghab	4370 mb

an exponential expansion $e^{-n\sigma_{\text{tot}}(E_n)} \approx 1 - n\sigma_{\text{tot}}(E_n)$ may be performed, leaving an approximate expression:

$$Y(E_n) \approx n\sigma_\gamma(E_n) \tag{3.25}$$

free of the total cross section dependence. Alongside the exact $\sigma_\gamma(E_n)/Y(E_n)$ ratio obtained by SAMMY, Fig. 3.16 shows the approximate $1/n$ conversion factor, clearly revealing that for the used ^{58}Ni sample this kind of approximation is inappropriate. This was noticed very early during the capture data analysis. The reason is, of course, a non-negligible multiple scattering, violating $n\sigma_{\text{tot}}(E_n) \ll 1$ assumption.

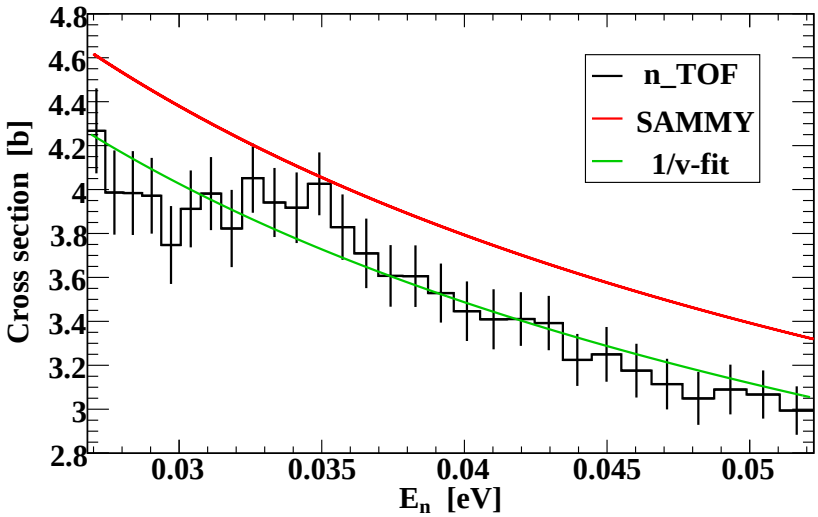

Figure 3.17 — Global SAMMY fit compared against an independent $1/v$ fit to the experimental data between 27 meV and 50 meV. Thermal value of the cross section was obtained extrapolating $1/v$ fit at 25.3 meV.

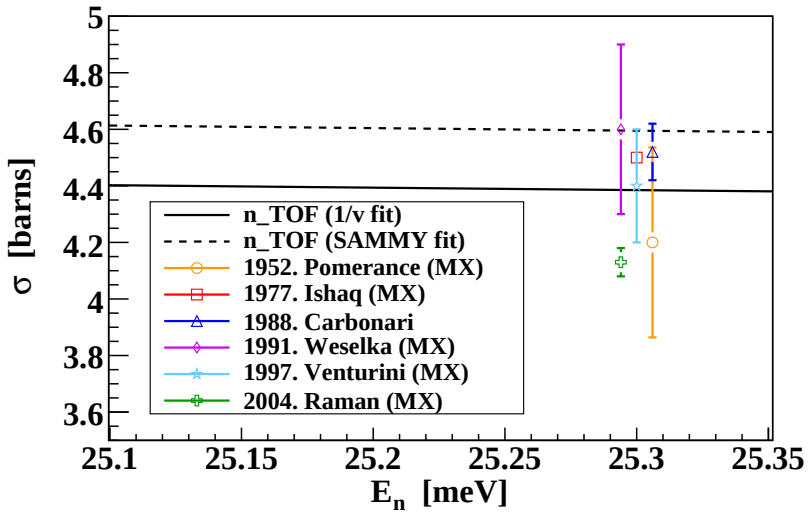

Figure 3.18 — Comparison between the n_TOF cross section extrapolated at thermal energies and the previous experimental data reported in EXFOR [11] and listed in Table 3.5. The points – all reported at 25.3 meV – are horizontally displaced in order to avoid the visual overlap.

Once the conversion from yield to the cross section has been performed using the pointwise conversion factor from SAMMY, an independent $1/v$ fit was applied to the data up to 50 meV, as shown in Fig. 3.17 together with the locally overestimating global fit from SAMMY. Extrapolating the thermal cross section at 25.3 meV, a value of $4385 \pm 22_{\text{stat}} \pm 137_{\text{sys}}$ mb was obtained. While the statistical uncertainty was adopted from the uncertainty in $1/v$ fit, the systematic uncertainty is determined by the uncertainty on the Pulse Height Weighting Technique (2%), evaluated neutron flux (2% at thermal energies) and the local value of the beam interception factor (1.3%). Table 3.5 compares the result from n_TOF with the evaluations from ENDF/B-VII.0 [13], ENDF/B-VII.1 [18], value recommended by Mughabghab [70] and the experimental data available from EXFOR [11]. Most of the results from EXFOR – shown also in Fig. 3.18 – are reported as Maxwellian averages at 25.3 meV. It is to be noted that, assuming

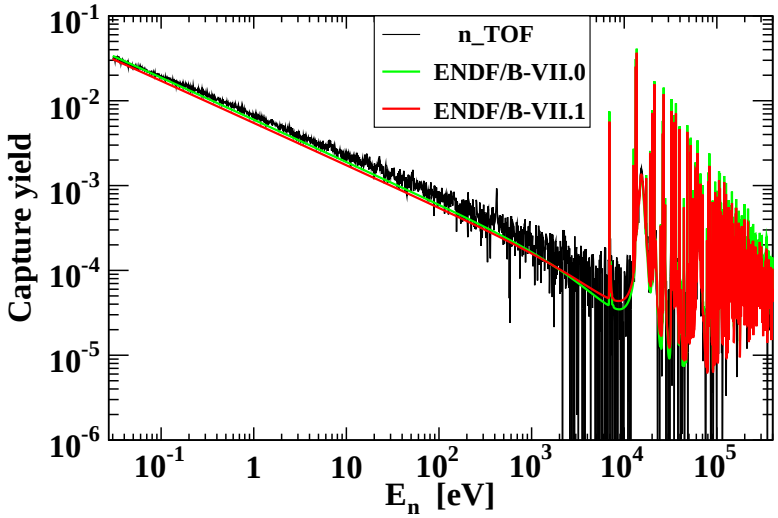

Figure 3.19 — Comparison between ^{58}Ni capture yield – corrected for the environmental, empty-frame and neutron background – and yields calculated by SAMMY, using ENDF/B-VII.0 and ENDF/B-VII.1 resonance parameters.

the pure $1/v$ dependence of the cross section: $\sigma(E_n) = \sigma(kT)\sqrt{kT/E_n}$, the Maxwelian average $\langle\sigma\rangle_{kT}$ at thermal energy kT perfectly corresponds to the local value $\sigma(kT)$:

$$\langle\sigma\rangle_{kT} = \frac{2}{\sqrt{\pi}}\frac{1}{(kT)^2}\int_0^\infty \sigma(kT)\sqrt{\frac{kT}{E_n}} \times E_n e^{-E_n/kT} \mathrm{d}E_n = \sigma(kT) \tag{3.26}$$

i.e. to the thermal cross section itself. Keeping that in mind, the thermal value from n_TOF is in a close agreement with the one reported by Raman et al. [17]. Furthermore, the agreement within 0.4% is obtained relative to the recommended value of 4370 mb from Mughabghab [70]. As for the ENDF evaluations, ENDF/B-VII.0 is a representative of the most recent versions of the other major libraries such as JENDL-4.0, JEFF-3.1.2, CENDL-3.1 and ROSFOND-2010 [72]. Figure 3.19 compares the capture yield calculated from ENDF/B-VII.0 and ENDF/B-VII.1 resonance parameters with the one measured at n_TOF. Relative to ENDF/B-VII.0, the low energy part of ENDF/B-VII.1 is mostly affected by the experimental work from Raman et al. [17], who reported a lower cross section than previously adopted throughout evaluation libraries. In this aspect, the n_TOF findings clearly favor the latest ENDF/B-VII.1 release.

3.6.3 Resolved resonance region

The resolved resonance region was considered up to 122 keV, where 51 resonances were identified and analyzed using SAMMY. Figure 3.20 shows the full resolved resonance region, together with the SAMMY fit extending over the full range of resolved resonances, while Fig. 3.21 presents some of the resonances shown in closer detail. The most important numbers obtainable from capture measurements alone (i.e. not combined with transmission measurements) are the capture kernels characteristic of single resonances. The kernels themselves are related to the integral cross section of a corresponding resonance as:

$$K = \frac{2}{\lambda^2}\int_{-\infty}^{\infty}\sigma(E_n)\mathrm{d}E_n = g_s\frac{\Gamma_n\Gamma_\gamma}{\Gamma_n+\Gamma_\gamma} \tag{3.27}$$

Here λ is the de Broglie wavelength of an incident neutron, approximately considered constant over the width of the resonance. With Γ_n and Γ_γ as the neutron and radiative withs, respectively, g_s is a statistical spin factor determined by the neutron spin I_n, ^{58}Ni ground state spin $I_{^{58}\mathrm{Ni}}$ and the resonance spin J:

$$g_s = \frac{2J+1}{(2I_n+1)(2I_{^{58}\mathrm{Ni}}+1)} \qquad \Rightarrow \qquad g_s(^{58}\mathrm{Ni}) = \frac{2J+1}{2} \tag{3.28}$$

For $I_n = 1/2$ and $I_{^{58}\mathrm{Ni}} = 0$, g_s remains dependent only on the resonance spin J.

During the fitting procedure by SAMMY, every resonance must be assigned the orbital angular momentum ℓ and resonance spin J. These – together with the initial values for Γ_n and Γ_γ – were adopted from ENDF/B-VII.1 parameters database [18]. Since the transmission measurements are required alongside the capture data in order to perform a reliable simultaneous fit to both widths Γ_n and Γ_γ, it was advisable to keep only one of them as a free parameter. When one of the widths is much larger than the other one, the rightmost side from (3.27) is sensitive only to the smaller of the two. Therefore, in such cases the larger width was kept fixed. The only exceptions to this procedure were the resonances with comparable widths. In these cases both Γ_n and Γ_γ were left free.

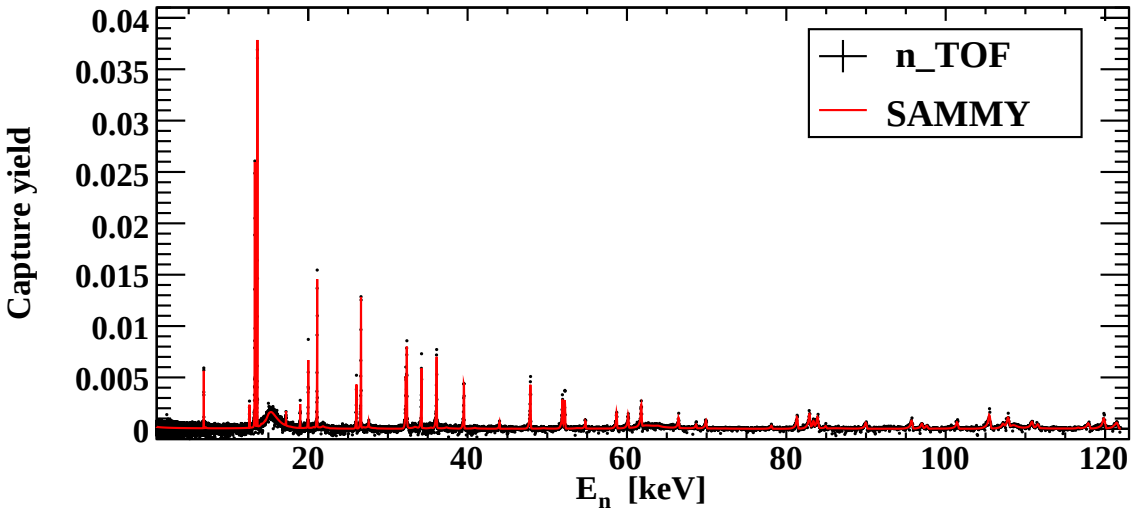

Figure 3.20 — Full resolved resonance region up to 122 keV, shown together with the global SAMMY fit.

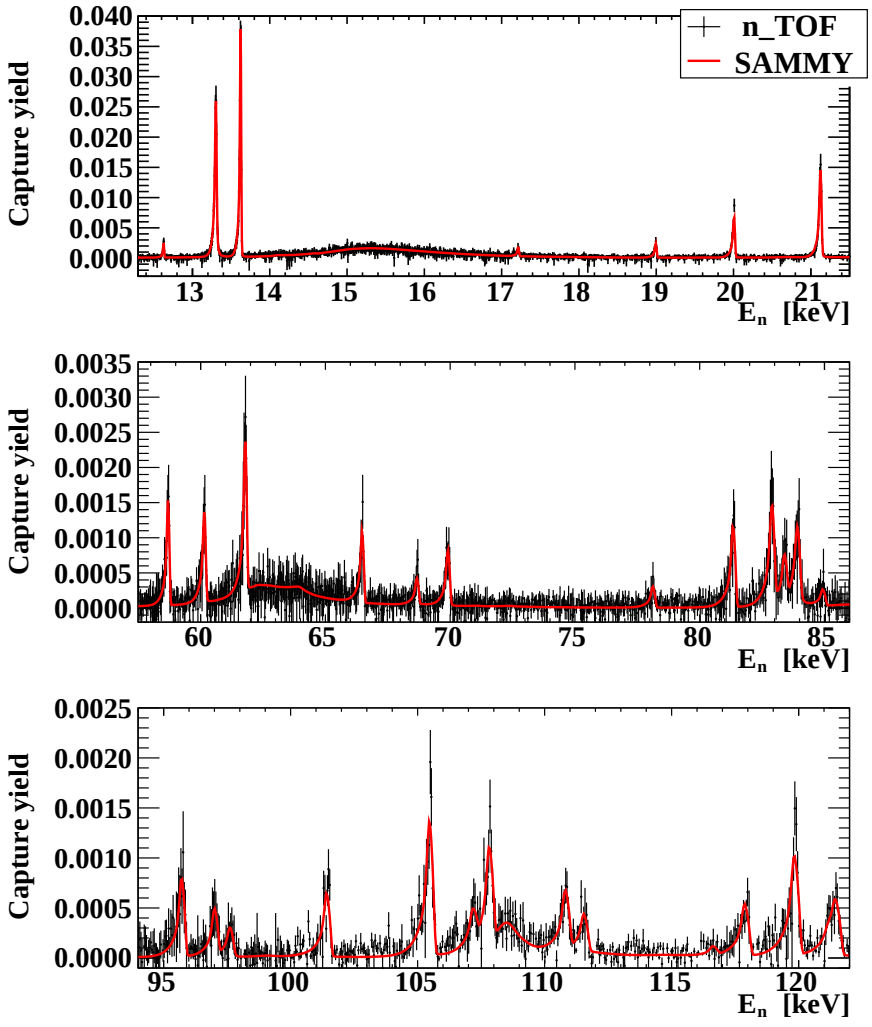

Figure 3.21 — Examples of the resolved resonances in the capture yield of ^{58}Ni. The global SAMMY fit is also shown.

Table 3.6 — Resonance parameters for 51 resolved capture resonances up to 122 keV. E_R is the resonance energy, ℓ is the orbital angular momentum and J is the resonance spin. From the statistical spin factor g_s, radiative width Γ_γ and neutron width Γ_n, capture kernels K were calculated.

E_R (keV)	ℓ	J	g_s	Γ_γ (meV)	Γ_n (meV)	K (meV)
6.8927(6)	1	1/2	1	500	21	$20 \pm 2_{\text{stat}} \pm 1_{\text{sys}}$
12.616(1)	1	1/2	1	500	27	$25 \pm 4 \pm 1$
13.2927(6)	1	1/2	1	653	7480	$601 \pm 21 \pm 33$
13.6114(3)	1	3/2	2	401	1118	$591 \pm 17 \pm 33$
15.350(7)	0	1/2	1	1281	1354062	$1279 \pm 41 \pm 71$
17.200(2)	1	1/2	1	500	41	$38 \pm 9 \pm 2$
18.976(2)	2	5/2	3	500	25	$71 \pm 10 \pm 4$
19.987(1)	1	1/2	1	315	1370	$256 \pm 18 \pm 14$
21.1051(8)	1	3/2	2	394	2097	$663 \pm 27 \pm 37$
26.024(2)	1	3/2	2	1971	141	$263 \pm 25 \pm 15$
26.596(1)	1	3/2	2	614	1457	$864 \pm 40 \pm 48$
27.573(4)	1	1/2	1	501	35	$33 \pm 14 \pm 2$
32.207(3)	2	5/2	3	1091	146	$388 \pm 39 \pm 21$
32.337(3)	1	1/2	1	1198	17148	$1120 \pm 74 \pm 62$
34.178(3)	1	3/2	2	535	969	$689 \pm 67 \pm 38$
36.073(3)	0	1/2	1	1085	17093	$1020 \pm 90 \pm 56$
39.492(3)	2	3/2	2	741	698	$719 \pm 62 \pm 40$
43.952(4)	2	5/2	3	932	43	$123 \pm 26 \pm 7$
47.822(3)	1	3/2	2	640	4760	$1128 \pm 87 \pm 62$
51.839(5)	2	5/2	3	3116	284	$780 \pm 87 \pm 43$
52.142(4)	2	3/2	2	945	741	$830 \pm 80 \pm 46$
54.711(3)	2	3/2	2	481	155	$235 \pm 44 \pm 13$
58.617(4)	1	3/2	2	355	1442	$570 \pm 62 \pm 32$
60.067(7)	1	3/2	2	309	15761	$606 \pm 79 \pm 34$
61.706(7)	1	1/2	1	1182	19751	$1115 \pm 123 \pm 62$
62.7(2)	0	1/2	1	2623	3752519	$2621 \pm 248 \pm 145$
66.379(6)	1	3/2	2	888	415	$565 \pm 78 \pm 31$
68.5706(8)	2	3/2	2	410	137	$205 \pm 53 \pm 11$
69.813(9)	1	1/2	1	570	7417	$529 \pm 76 \pm 29$
78.006(6)	1	1/2	1	462	490	$238 \pm 57 \pm 13$
81.217(1)	2	3/2	2	1689	732	$1021 \pm 146 \pm 48$
82.77(1)	1	3/2	2	781	41325	$1532 \pm 193 \pm 71$
83.268(8)	0	1/2	1	690	3308	$571 \pm 133 \pm 27$
83.79(1)	1	1/2	1	1323	37292	$1278 \pm 169 \pm 59$
84.803(4)	2	3/2	2	276	203	$234 \pm 77 \pm 11$
89.832(9)	1	3/2	2	377	5394	$705 \pm 128 \pm 33$
95.5580(5)	2	5/2	3	2528	395	$1025 \pm 175 \pm 48$
96.850(6)	2	5/2	3	581	309	$606 \pm 137 \pm 28$
97.46(2)	1	1/2	1	445	18712	$434 \pm 93 \pm 20$
101.255(7)	2	5/2	3	371	3681	$1011 \pm 98 \pm 47$
105.294(7)	2	3/2	2	1305	10458	$2320 \pm 144 \pm 108$
106.993(7)	1	1/2	1	844	1262	$506 \pm 105 \pm 23$

Continued on the next page.

Table 3.6: (Continued.)

E_R (keV)	ℓ	J	g_s	Γ_γ (meV)	Γ_n (meV)	K (meV)
107.640(8)	2	3/2	2	932	4598	$1549 \pm 156 \pm 72$
108.45(8)	0	1/2	1	2261	1073094	$2256 \pm 232 \pm 105$
110.627(7)	1	3/2	2	562	4276	$993 \pm 113 \pm 46$
111.3547(2)	2	5/2	3	450	480	$697 \pm 31 \pm 32$
116.420(4)	1	1/2	1	434	307	$180 \pm 58 \pm 8$
117.67(1)	1	3/2	2	641	7846	$1185 \pm 116 \pm 55$
119.624(8)	2	5/2	3	1052	3005	$2338 \pm 211 \pm 108$
120.958(8)	1	1/2	1	479	1086	$332 \pm 118 \pm 15$
121.25(1)	2	3/2	2	757	7562	$1377 \pm 163 \pm 64$

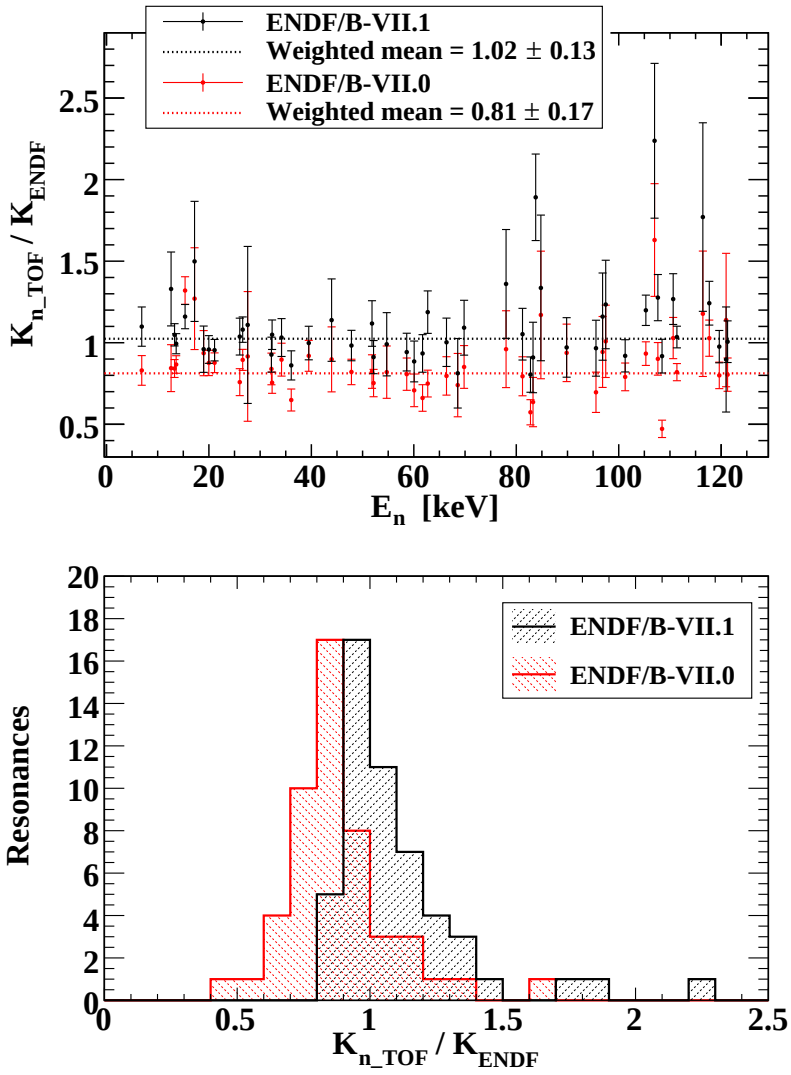

Figure 3.22 — Ratios between the n_TOF capture kernels and those calculated from ENDF/B-VII.0 and ENDF/B-VII.1 resonance parameters. Top panel: ratios for all 51 resolved resonances. Bottom panel: distribution of kernel ratios.

Within the n_TOF data up to 122 keV, 5 of the resonances from ENDF/B-VII.1 – characterized by very small capture kernels – could not be resolved from the baseline fluctuations. Those are the resonances at 24.77 keV, 35.06 keV, 48.47 keV, 83.97 keV and 92.73 keV. No new resonances were identified within this energy range. For all 51 resolved resonances, Table 3.6 lists the resonance parameters obtained by fitting, together with values adopted as the fixed input. The systematic uncertainties on the reported kernels come from the neutron flux (2% within 27 meV – 200 eV, 3% within 200 eV – 8 keV, 5% within 8 keV – 80 keV, 4% within 80 keV – 1 MeV), weighting function (2%) and the beam interception factor (1.3%). Figure 3.22 plots the ratios and the distribution of ratios between n_TOF kernels and those calculated from ENDF/B-VII.0 and ENDF/B-VII.1 resonance parameters. With a weighted mean of 0.81 ± 0.17 relative to ENDF/B-VII.0 and 1.02 ± 0.13 relative to ENDF/B-VII.1, the n_TOF data once again justify the changes introduced in the latest ENDF/B-VII.1 release. Together with the parameters for the resolved resonances above the neutron separation energy, the global SAMMY fit was complemented with the two negative-energy resonances – previously discussed – in order to parameterize the full neutron capture cross section up to 122 keV.

3.6.4 Unresolved resonance region

Though the resonant structure is still prominent in the capture yield above 122 keV – as clearly shown in Fig. 3.23 – due to the worsening of the energy resolution, this range was treated as the unresolved resonance region. A specialized code SESH [73] was used to simulate the smoothed capture yield between 122 keV and 400 keV. It is to be noted that in this energy region only the data from the FZK detector were used, as explained in Section 3.5. We remind that the upper bound of 400 keV is limited by the detector recovery from the γ-flash preceding every neutron bunch. The parameters required for the simulation of the capture yield by SESH were adjusted until the perfect agreement was achieved between the integrated experimental and simulated yield within the range from 122 keV to 400 keV. Thus optimized set of parameters was used

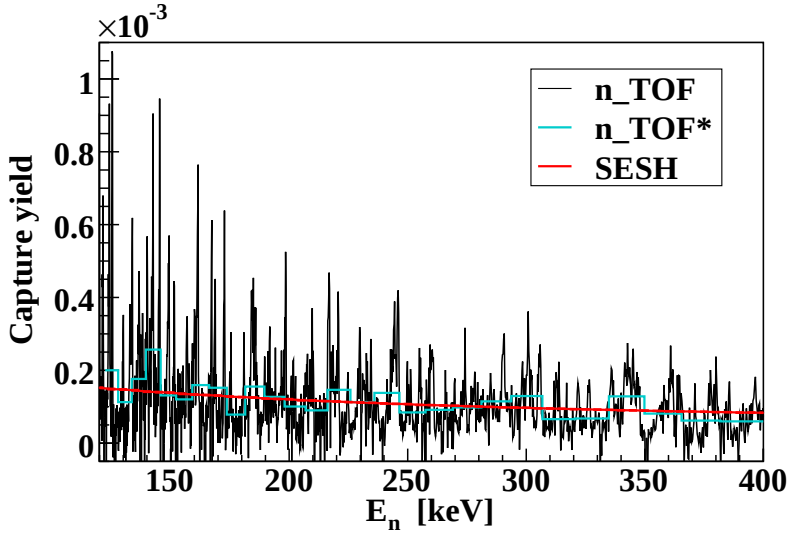

Figure 3.23 — Capture yield in the unresolved resonance region between 122 keV and 400 keV. The same experimental data are shown in fine and 50 times coarser binning. The smoothed capture yield simulated by SESH is also shown.

to extend the calculation of the smoothed capture cross section up to 1 MeV. Together with the still resonant experimental capture yield, Fig. 3.23 shows the smoothed reproduction of the yield calculated by SESH. In addition, the experimental data are also shown in 50 times coarser binning in order to facilitate the visual comparison with the final SESH results.

3.6.5 Maxwellian averaged cross sections

From the capture cross section parametrized by SAMMY up to 122 keV and by SESH up to 1 MeV, Maxwellian averaged cross sections (MACS):

$$\langle\sigma\rangle_{kT} = \frac{2}{\sqrt{\pi}}\frac{1}{(kT)^2}\int_0^\infty \sigma(E_n)E_n e^{-E_n/kT}\mathrm{d}E_n \tag{3.29}$$

were calculated over the full range of the astrophysically relevant temperatures, corresponding to the thermal energies of $kT = 5 - 100$ keV. Figure 3.24 shows the newly obtained MACS from n_TOF, comparing them with the those calculated from the capture cross sections from ENDF/B-VII.0 and ENDF/B-VII.1 libraries. The data available from KADoNIS v0.3 [74] compilation are also shown. The plotted MACS are listed in Table 3.7 for all thermal values found in KADoNIS v0.3 database. The sources of systematic uncertainties are the same as those reported for the capture kernels in Section 3.6.3. From Fig. 3.24 and Table 3.7 it is evident that below 10 keV n_TOF results are in better agreement with the values from ENDF/B-VII.0, while in the 15 keV – 50 keV range with those from ENDF/B-VII.1. Since other major evaluation libraries such as JENDL-4.0, JEFF-3.1.2, CENDL-3.1 and ROSFOND-2010 [72] are represented by ENDF/B-VII.0, an extensive reevaluation of ^{58}Ni capture data is strongly encouraged by the latest n_TOF results.

The latest MACS from n_TOF strongly support the theoretical results from Ref. [75], obtained using the relativistic quasiparticle random phase approximation (RQRPA) formulated within the framework of the relativistic Hartree-Bogoliubov (RHB) model [76]. Figure 3.25 shows the results of this model, together with the experimental results

Table 3.7 — Compilation of relevant MACS values from n_TOF, KADoNIS v0.3 and those calculated from ENDF/B-VII.0 and ENDF/B-VII.1 evaluation libraries.

kT (keV)	MACS (mb)			
	n_TOF	ENDF/B-VII.0	ENDF/B-VII.1	KADoNIS v0.3
5	$41.3 \pm 0.6_{\mathrm{stat}} \pm 2.3_{\mathrm{sys}}$	39.8	38.2	38.3
10	$50.1 \pm 0.7 \pm 2.8$	52.0	48.1	50.1
15	$45.9 \pm 0.7 \pm 2.5$	49.9	44.9	48.1
20	$41.0 \pm 0.6 \pm 2.2$	46.2	40.6	44.5
25	$37.2 \pm 0.6 \pm 2.0$	42.9	37.0	41.3
30	$34.2 \pm 0.6 \pm 1.8$	40.2	34.1	38.7
40	$30.3 \pm 0.5 \pm 1.5$	36.3	30.0	35.0
50	$27.7 \pm 0.4 \pm 1.4$	33.5	27.1	32.3
60	$25.8 \pm 0.3 \pm 1.3$	31.4	25.0	30.1
80	$23.2 \pm 0.3 \pm 1.1$	28.0	21.9	27.0
100	$21.3 \pm 0.2 \pm 1.0$	25.4	19.7	24.4

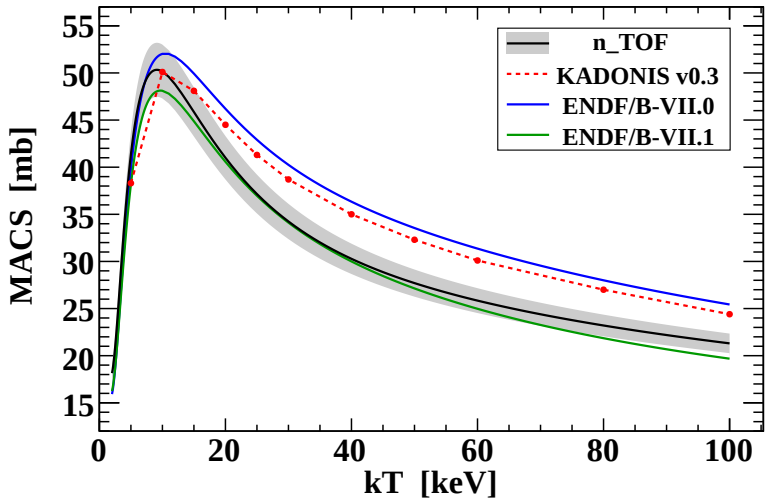

Figure 3.24 — MACS within the temperature range of astrophysical importance. The shaded area shows the standard uncertainty range for the experimental n_TOF data.

from several earlier works [12, 77–79]. In addition, Fig. 3.26 shows the ratio between these MACS and n_TOF values, clearly revealing the level of data novelty, brought forth by the most recent experiments. The global decrease in the capture cross section – as reported by Guber et al. – is clearly confirmed, particularly within the temperature domain around $kT = 30$ keV, which holds a special significance for the stellar nucleosynthesis. The theoretical results from Ref. [75], calculated using the fully self-consistent relativistic mean-field model (equivalent to the density functional theory), are also in a good agreement with this finding, falling inside the uncertainty rage of n_TOF results within the wide temperature range of kT = 20 – 80 keV. Above 70 keV theoretical results clearly converge towards the values reported by Guber et al. Below 20 keV, however, theoretical findings severely deviate from the experimental trend reported by all measurements, which is due to the statistical Hauser-Feshbach model for the nuclear level densities – employed in the calculations – not being reliable at low

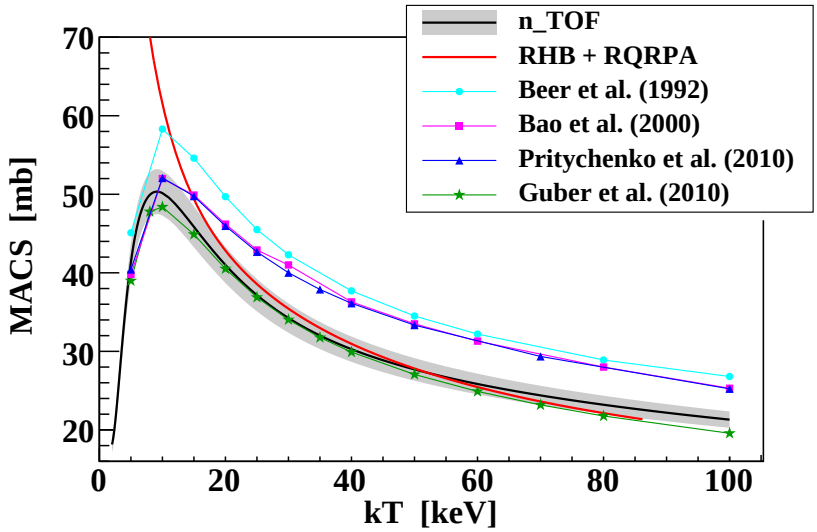

Figure 3.25 — MACS from n_TOF and compared to the ones from several earlier sources [12, 77–79] and to the theoretical results from Ref. [75].

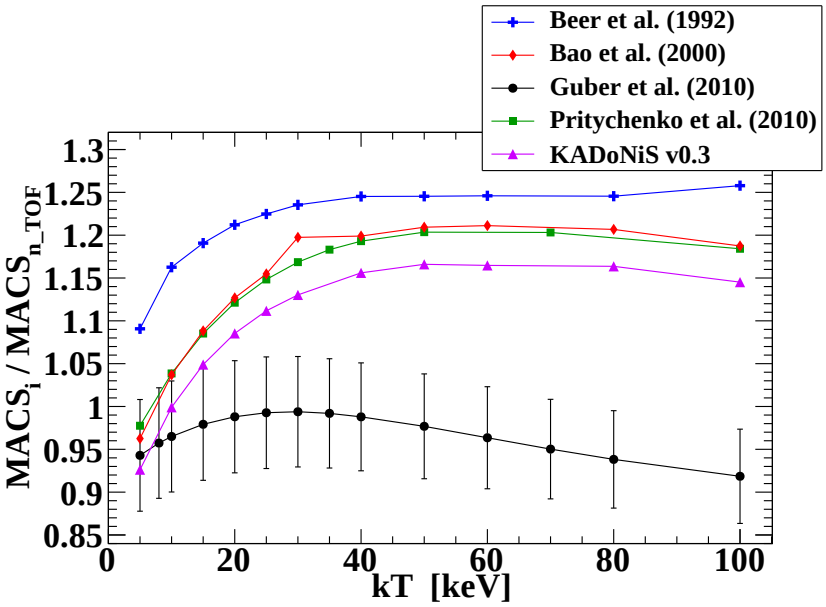

Figure 3.26 — MACS from several sources relative to the latest n_TOF results.

level densities [80]. As may be recalled from ^{58}Ni data – in particular, from Fig. 3.19 and Table 3.6 – the first capture resonance (corresponding to the first discrete level above the neutron separation energy) is located at 6.9 keV. Therefore, the absence of levels below this energy affects the experimental MACS all the way up to 20 keV due to the Maxwellian distribution still appreciably stretching over the energies in the vicinity and below the first resonance at 6.9 keV.

Several components contribute to the overall capture cross section and, hence, the MACS – the resonant capture (RC), direct capture (DC) and direct-semidirect (DSD) capture [81]. Earlier theoretical calculations reported by Guber et al. [12] reveal that DC and DSD components significantly affect the neutron capture by ^{58}Ni at lower energies – in particular the capture of s-wave neutrons – accounting for the part of $1/v$ dependence of the cross section, while contributing more than 30% to its thermal value. A negligible contribution from p-wave neutrons is expected at higher energies. In fact, the theoretical model from Ref. [82] predicts less than 1% contribution from p-wave neutrons to MACS at all temperatures. Concerning the n_TOF data, all the capture components – resonant, direct and direct-semidirect – were accounted for by the SAMMY fit assuming the negative-energy resonances. Therefore, DC and DSD components needed not to be considered separately.

The impact of the newly found n_TOF MACS on the s-process nucleosynthesis was investigated by means of the post-processing NuGrid code MPPNP [83], assuming a full 25M$_\odot$ model with an initial metal content of $Z = 0.02$ [84]. It was found that 12% reduction in MACS at 30 keV – relative to the recent KADoNIS v0.3 compilation (see Table 3.7) – causes a 60% increase in the final (leftover) ^{58}Ni content in massive stars. The cause of this outcome is a less efficient destruction of ^{58}Ni by neutron captures, due to the lower average cross section. However, apart for the ^{58}Ni content itself, the abundance distribution of the remaining stellar material remains basically unaffected, since ^{58}Ni abundance is much smaller (4.3% [7]) than that of the dominant s-process seed ^{56}Fe, and at the end of the s-process ^{58}Ni is efficiently depleted by the neutron captures, assuming either the old or the new MACS value.

4 Neutron background simulations

4.1 Motivation

Precise and reliable measurements of the neutron capture reactions – such as those performed at n_TOF – require detectors as insensitive to neutrons as possible. The foremost requirement for achieving any kind of neutron insensitivity is building hydrogen-free detectors. This course of action has been followed for more than 40 years, ever since Macklin and Gibbons [43] used a C_6F_6 scintillators for detecting γ-rays from the prompt (n,γ) reaction. However, in the following years these detectors were shown to exhibit large systematic uncertainties [44], besides providing a rather low γ-ray detection efficiency. This challenge was met by replacing them with C_6D_6 scintillators, alleviating some of the shortcomings of C_6F_6 counterparts. The use of C_6D_6 has continued to the present day.

At n_TOF a pair of C_6D_6 detectors has been employed for a decade. Since the beginning, they have been studied in great detail and optimized in such a manner as to ensure the lowest neutron sensitivity possible [61]. The optimization was performed investigating the efficiency ε_n for detecting a γ-ray produced in the neutron capture by any component of C_6D_6 detectors. Its relation to the maximal γ-ray detection efficiency $\varepsilon_\gamma^{\max}$ was used to define the neutron sensitivity $\varepsilon_n/\varepsilon_\gamma^{\max}$ of two detectors. However, in the real experiment the contribution to the total neutron induced background comes not only from the neutrons directly scattered towards and then captured by the C_6D_6 detectors themselves, but also from the neutrons scattered off or captured by the surrounding components inside the experimental hall. A major portion of this background is caused by the components closest to the neutron beam, i.e. those in the immediate vicinity of the irradiated sample.

The effect of neutrons scattered off the sample – giving rise to the *neutron background* – cannot be measured. Rather, it has to be estimated indirectly. Precisely identifying the neutron background would require separating the neutron capture properties from the neutron scattering properties of the sample. Since this is not an easy task, the dedicated simulations remain the only reliable, if not available option applicable to such a task. Clearly, the neutron background is the most notable for samples characterized by the neutron scattering cross section significantly higher than that for the neutron capture. The neutron sensitivity of the used detectors may serve as a figure of merit for estimating the level of the neutron background and the need of subtracting it. If – within the energy range of the available neutron flux – the capture-to-scattering ratio of a given sample becomes comparable to the neutron sensitivity, the neutron background may present a significant contribution to the experimentally obtained counts,

i.e. to the yield reconstructed during the offline analysis of the capture data. This circumstance has been recognized in case of ^{58}Ni.

Figure 4.1 compares the cross sections for the radiative capture and the elastic scattering of neutrons by ^{58}Ni, as evaluated in the ENDF/B-VII.1 database [18]. For completeness and the later use, the comparison is also shown for ^{197}Au and ^{nat}C, which have been crucial for validating the neutron background simulations. From ^{58}Ni spectra it is clear that in the first inter-resonance valley around 7 keV the elastic scattering exceeds the radiative capture by three to four orders of magnitude – the ratio uncomfortably close to the intrinsic neutron sensitivity of the order $10^{-5} - 10^{-4}$, as evaluated

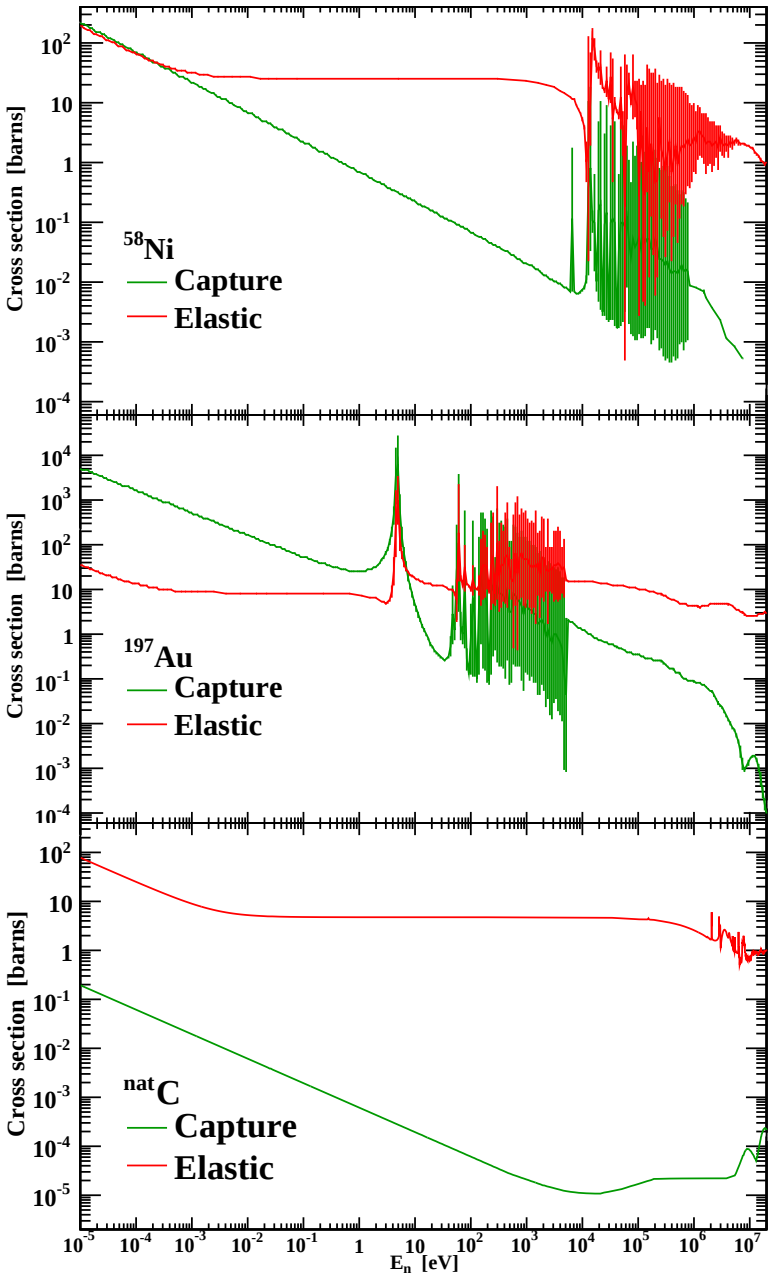

Figure 4.1 — Comparison between the neutron capture and elastic scattering cross sections of ^{58}Ni, ^{197}Au and ^{nat}C, as evaluated in the ENDF/B-VII.1 database [18].

in the past [61] for the two C_6D_6 detectors. Combined with the recent advances in the neutron physics section of GEANT4 simulation toolkit [65, 66], the ^{58}Ni case presented the perfect opportunity to use the improved neutron transport capabilities of GEANT4 in order to meet the high precision standards of the sophisticated analytical procedures applied to the high quality n_TOF capture data.

4.2 Overview of GEANT4 simulations

The simulations have been performed with GEANT4 version 9.6.p01. For the neutron-induced reactions up to 20 MeV it relies largely on the tabulated cross section data from ENDF/B-VII [13, 18].

4.2.1 Geometry

The geometry of the n_TOF experimental hall, as implemented within the simulation code, is shown in Fig. 4.2. Care has been taken to accurately reproduce the layout of the hall, which is not rectangular, but rather tilted in space. For the experiments involving intense neutron beams, the surrounding concrete walls must be considered, since they are – due to the rich hydrogen content – prime candidates for the neutron scattering and neutron capture via ^{1}H$(n,\gamma)^2$H reaction, producing 2.2 MeV γ-rays. The geometric description of the two C_6D_6 detectors has been completely transferred from a dedicated GEANT4 simulation used for obtaining the monochromatic spectra required for calculating the weighting function (Section 3.3). Adopting exactly the same geometric setup as used for obtaining the weighting functions ensures that the identical detection efficiencies are assumed by both simulations. Thus the output data – consisting of the detailed information on the detected counts – are perfectly consistent between the two simulations, making the same weighting functions that are applied to the experimental data, directly applicable to the output data of the simulation of the neutron background. As may be readily observed from Fig. 4.2, the adopted geometry also includes the full length of the aluminum beamline inside the experimental hall, beamline supports, false aluminum floor, sample exchanger and its supports, together with the crude description of the Total Absorption Calorimeter (TAC) and the corresponding supporting structure made of aluminum.

4.2.2 Physics list

Setting up the physics framework for the simulation consists in constructing the necessary particles and physical processes. The list of active particles was built calling upon the prearranged packages:

- G4BaryonConstructor
- G4LeptonConstructor
- G4BosonConstructor
- G4IonConstructor
- G4MesonConstructor
- G4ShortLivedConstructor

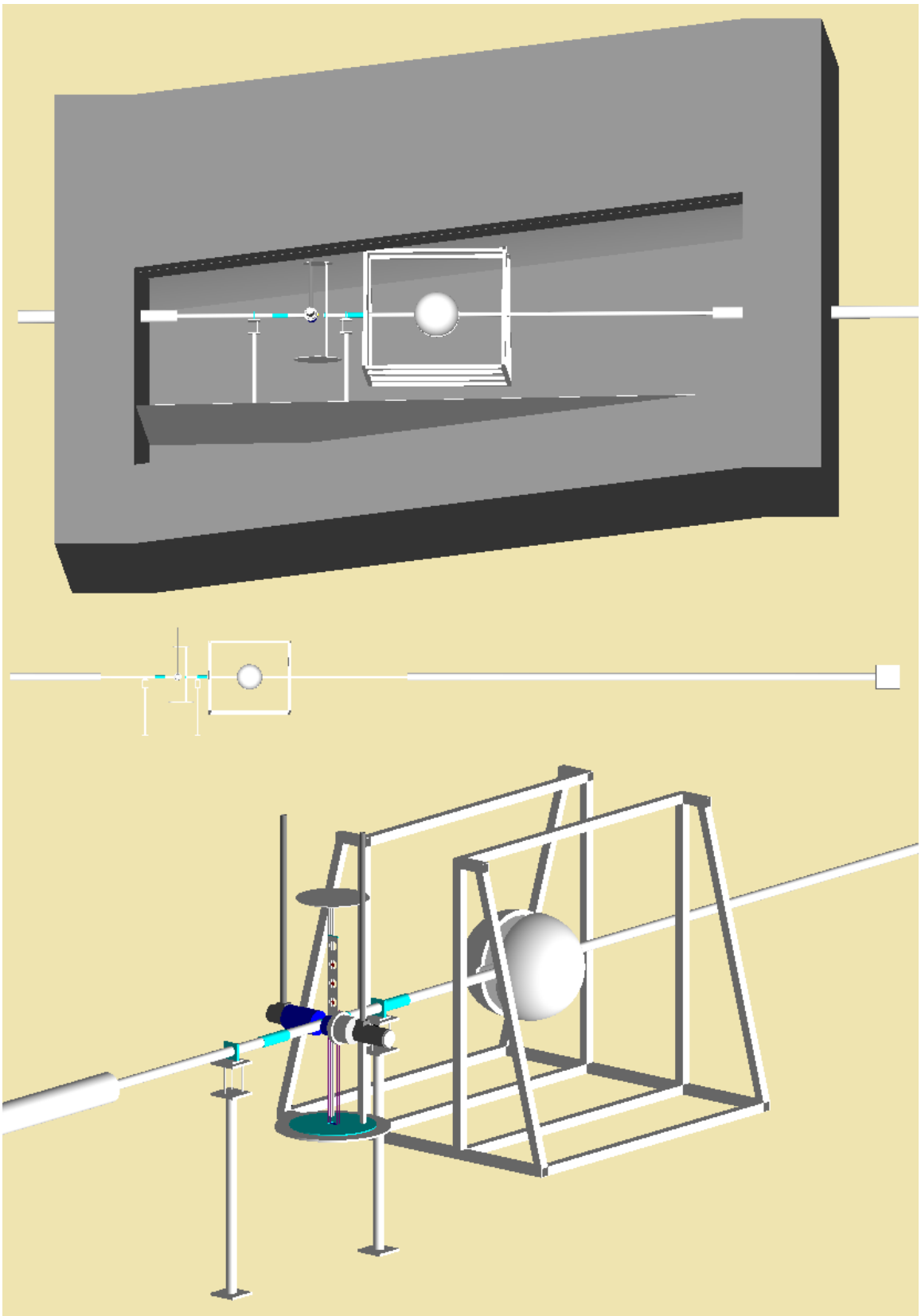

Figure 4.2 — Geometry of the n_TOF experimental hall and the experimental setup, adopted for GEANT4 simulations of the neutron background. The upper section shows the experimental setup surrounded by concrete walls; the middle section shows the adopted length of the beamline, ending in a beam dump; the lower section zooms in at the central setup.

The list of general physical processes – pertaining to all particles other than neutrons – was also set up from prearranged constructors:

- G4EmStandardPhysics
- G4DecayPhysics
- G4RadioactiveDecayPhysics
- G4IonPhysics
- G4EmExtraPhysics
- G4StoppingPhysics
- G4HadronElasticPhysics
- G4HadronInelasticQBBC

Neutron physics was given a special attention. First, all the processes assigned to the neutron through any of the previous packages were decoupled from the list. The physics framework for the neutron transport was then built manually, selecting the process and cross section packages one by one, based on their precision and availability within a given energy range. Elastic and inelastic scattering of neutrons, neutron capture and neutron induced fission have all been invoked. For certain, limited set of materials the neutron induced scintillations are also available through G4Scintillation class, which may be invoked via general G4OpticalPhysics constructor. However, its inclusion was not deemed necessary. The physical models selected for a given process are categorized in Table 4.1, together with the selected cross section datasets. All models have been assigned their respective energy range according to the model declarations or general recommendations. The energy range for the cross section datasets is determined by the internal GEANT4 procedures, since not all the datasets contain the data for all known nuclides.

Since GEANT4 offers a multitude of models for handling the given physical process within the given energy range, one must make an informed decision on what to select. Alongside the main selections, in Table 4.1 only the most seriously considered substitutes are listed. Up to 20 MeV, G4NeutronHP package offers separate high-precision models for elastic scattering, inelastic scattering, neutron capture and neutron induced fission. All are based on a direct sampling of the pointwise cross sections coming mostly from ENDF/B-VII [13, 18]. As may be readily observed from Table 4.1, for the inelastic scattering the G4NeutronHPInelastic model was entirely avoided. Though this decision is not necessarily the general recommendation of this work, it was made so that the experimental data for the carbon sample might be accurately reproduced. Therefore, the combination of the two GEANT4 native intra-nuclear cascades – G4BinaryCascade and G4CascadeInterface (so-called Bertini cascade) – has been selected below 10 GeV. Considering the fission process, G4ParaFissionModel was selected in place of G4NeutronHPFission because the latter does not produce the fission fragments. However, it is worth noting that the G4ParaFissionModel does not produce as much of the delayed neutrons as the G4NeutronHPFission model.

Table 4.1 — Neutron transport models and cross sections datasets used for the GEANT4 simulations of the neutron background.

Process	Cross section data	Model	
		Name	Range
Elastic scattering	G4NeutronHPThermalScatteringData[a]	G4NeutronHPThermalScattering	<4 eV
	G4NeutronHPElasticData[b]	G4NeutronHPElastic	4 eV – 20 MeV
	G4NeutronHPJENDLHEElasticData[c]	G4HadronElastic	>20 MeV
	G4BGGNucleonElasticXS[de]		
Inelastic scattering	G4NeutronHPThermalScatteringData[a]	G4BinaryCascade[g]	<30 MeV
	G4NeutronHPInelasticData[b]	G4CascadeInterface[g]	30 MeV – 10 GeV
	G4NeutronHPJENDLHEInelasticData[c]	G4TheoFSGenerator[h]	>10 GeV
	G4BGGNucleonInelasticXS[df]		
Capture	G4NeutronHPCaptureData[b]	G4NeutronHPCapture	<20 MeV
	G4HadronCaptureDataSet[d]	G4NeutronRadCapture	>20 MeV
Fission	G4NeutronHPFissionData[b]	G4ParaFissionModel[i]	<60 MeV
	G4HadronFissionDataSet[d]	G4LFission	>60 MeV

[a] Declared range: < 4 eV
[b] Declared range: < 20 MeV
[c] Declared range: $\lesssim 3$ GeV
[d] Declared range: < 100 TeV
[e] Substitute: G4HadronElasticDataSet
[f] Closest substitute: G4NeutronInelasticCrossSection
Additional substitute: G4HadronInelasticDataSet
[g] Substitute: G4NeutronHPInelastic (<20 MeV) and G4NeutronHPThermalScattering (<4 eV)
[h] Using: G4StringChipsParticleLevelInterface, G4QGSMFragmentation and G4QGSModel
Substitute: G4GeneratorPrecompoundInterface, G4LundStringFragmentation and G4FTFModel
[i] Substitute: G4NeutronHPFission (<20 MeV)

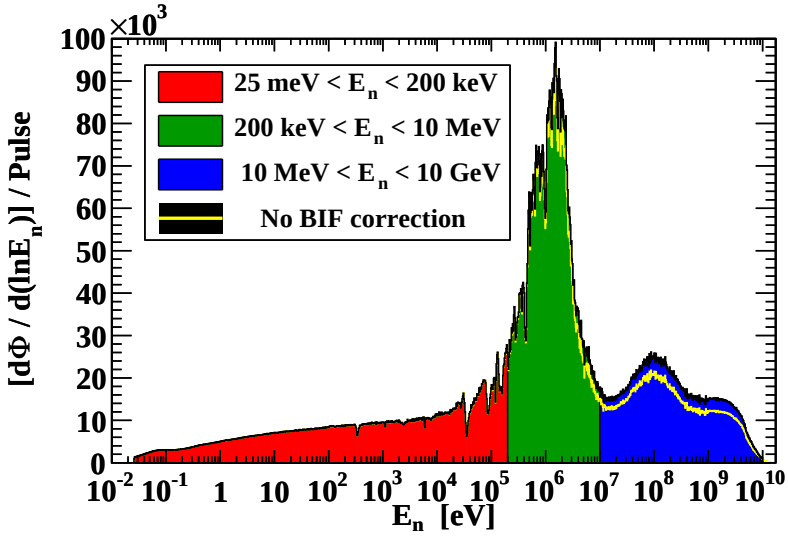

Figure 4.3 — Sample-incident neutron flux adopted for the GEANT4 simulations of the neutron background. Yellow line shows the shape of the evaluated flux not corrected for the energy dependence of the beam interception factor. For differently colored energy intervals separate simulation runs were performed, optimizing the CPU processing time.

In Table 4.1 the cross section datasets are also listed, according to the increasing energy range. Since recently, the Barashenkov-Glauber-Gribov parameterization of inelastic cross sections from G4BGGNucleonInelasticXS has been preferred to Laidlaw-Wellisch parameterization from G4NeutronInelasticCrossSection. For this reason the former was selected.

4.2.3 Neutron spectrum sampling

In the simulations the neutron energy is sampled from the energy distribution of the neutron beam impinging on the sample. This spectrum is obtained by multiplying the evaluated flux from Fig. 2.6 by the energy dependent beam interception factor from Fig. 3.12. The resulting neutron spectrum – incident on samples of 2 cm diameter – is shown in Fig 4.3. For comparison, the shape of the flux not corrected for the variations in BIF is also shown. The sampling of the flux has been achieved by adopting the algorithm for sampling an arbitrary distribution, starting from the uniform random number generator. The algorithm is described in Appendix E. In order to optimize the management of CPU processing time, separate simulations were run for the primary neutron energies between 25 meV – 200 keV, 200 keV – 10 MeV, and 10 MeV – 10 GeV, as indicated in Fig. 4.3. The relative portions of the flux within these intervals amount to 29.9%, 45.0% and 25.1%, respectively. The Gaussian profile was adopted for the neutron beam, with experimentally determined horizontal and vertical widths of $\sigma_x = \sigma_y = 7.5$ mm.

Since the used GEANT4 version 9.6.p01 is not parallel-processing oriented (by default), multiple instances of the simulation were also run for the same parts of the neutron spectrum in order to accumulate as much statistics as possible. However, it must be kept in mind that the default random number generators available in GEANT4 produce the same sequence of numbers from the start of every run. Therefore, this sequence was further randomized on the basis of the local starting time of a given run.

Thus, every run could yield the unique stream of the output data. The simple randomization procedure is described in Appendix F.

4.2.4 Internal procedures

The main aim of the simulation is to estimate the neutron background, caused by neutrons scattered off the sample. Having this goal in sight, all primary neutrons are required to pass through the sample with a non-negligible interaction. Otherwise, the neutron may be scattered off the beamline either before reaching the sample or after passing through the sample without being affected by it. However, this kind of contribution to the total neutron induced background is already contained within an empty-frame background, i.e. it has already been determined experimentally by irradiating the experimental setup without the sample in place. In order not to subtract these counts from the experimental data twice, the neutrons unaffected by the sample are dismissed at once. The reactions such as the neutron capture are immediately recognized as significant, since the outgoing particle is no longer the primary neutron. In case of the elastic scattering the outgoing particle is identical to the incoming one (as treated by GEANT4 transport code). Therefore, the condition for considering the elastic scattering as non-negligible had to be set manually. The condition was imposed on the cumulative scattering angle of the primary neutron at the exit surface of the sample, which needed to be greater than 0.2°.

4.2.5 Output data structure

The output data consist of the total number of neutrons emitted towards the sample, followed by the detailed list of information for every count detected in either of the two C_6D_6 detectors. The data for a single count have the following structure:

- *Neutron energy* – the primary neutron energy, sampled from the sample-incident neutron flux distribution (Fig. 4.3). This information can not be attained directly during the experiment, only reconstructed from the time of flight of the neutron. However, if the time-energy correlation is lost due to neutron scattering, the energy is reconstructed erroneously. From the simulation this information is easily extracted, allowing for the clear separation of the prompt and the delayed contribution to the neutron background.
- *Deposited energy* – the total energy deposited inside the C_6D_6 liquid scintillator, corresponding to the energy detected during the experiment. These data serve as the input for the Pulse Height Weighting Technique applied during the calculation of the yield.
- *Time of flight* – the time interval between the neutron emission and the earliest energy deposition (via secondary particle) inside the given C_6D_6 volume. These data are also being recorded during the experiment, ideally corresponding to the neutron time of flight from which the neutron kinetic energy is to be reconstructed.
- *Number of activated detectors* – the total number of detectors activated following the interaction of a single neutron. In case of the multiple detectors being activated, based on these data the counts from separate detectors may be assigned to the single neutron induced event.
- *Detector* – the designation of the activated detector.

- *Detected particle* – the designation of the particle being detected, e.g. a photon from a capture reaction.
- *Energy depositing particle* – the charged particle depositing energy inside the detector, e.g. an electron released by the Compton scattering of the photon from the neutron capture reaction.
- *Origin* – the designation of the physical volume in which the detected particle was generated. In case of the prompt capture the volume is necessarily the sample itself, otherwise the count is recognized as contributing to the neutron background.
- *Scatterer* – the designation of the last physical volume where the detected particle has undergone a non-negligible scattering. For example, the photon originating from the sample may be scattered by the component of the experimental setup before being detected inside the C_6D_6 liquid. The offset of the particle trajectory by at least 5° has been selected as the condition for considering the scattering as non-negligible.
- *Reactor* – the designation of the physical volume where the energy depositing particle has been released. For example, an electron may be ejected from the C_6D_6 housing, being subsequently detected in the scintillating liquid.
- *Creator process* – the physical process creating the detected particle, e.g. the neutron capture in case of the γ-ray, the elastic or inelastic scattering in case of the neutron, etc.
- *Interaction process* – the physical process releasing the energy depositing particle, e.g. the Compton scattering.

It is worth noting that – in the simulations – the neutrons are generated at the entrance of the experimental area, at a distance of 182 m from a spallation target. Therefore, in order to reconstruct the experimental analogue $\mathrm{ToF_{exp}}$ of the neutron time of flight, the $\mathrm{ToF_{sim}}$ extracted from the simulations had to be complemented by the neutron time of flight along the path from the spallation target to the entrance of the experimental area. This was achieved simply by adding the $\mathrm{ToF_0}(E_n)$ needed for the primary neutron of energy E_n to propagate along the flight path of 182 m:

$$\mathrm{ToF_{exp}} = \mathrm{ToF_{sim}} + \mathrm{ToF_0}(E_n) \tag{4.1}$$

4.3 Introductory considerations

4.3.1 Control case

Prior to studying the neutron transport within the complex experimental hall of n_TOF, the control case was investigated. A decade ago a simple geometric setup was adopted in Ref. [85] in order to examine the consistency – and thus the reliability – of two commonly used neutron transport codes: GEANT3 and MCNP-4B. The setup consists of a single rectangular slab of material (iron or concrete) which is irradiated by monoenergetic neutrons isotropically emitted from a point-like source. As the high degree of consistency was found between the reported results from the two simulation packages, this work was taken as a benchmark for a basic assessment of compatibility with the results from GEANT4. The attenuation and the moderation of the neutron beam passing

through both iron and concrete slab were examined. The GEANT4 output was found to be highly consistent with GEANT3 and MCNP-4B results. The most representative result is shown in Fig. 4.4. It shows the energy distribution of a neutron flux emerging from 30 cm thick iron slab, for initially monoenergetic neutron beams of 1 keV and 1 MeV. The spectra are in excellent agreement with those from Ref. [85], showing the same fine structure details, such as the dips at certain energies. Though these very basic checks are far from exhaustive investigations, they did allow building the more complex instances of GEANT4 code with fair confidence in the accuracy of the results.

4.3.2 The γ-ray cascades

The generation of γ-cascades within GEANT4 is a commonly pointed out issue. Two questions stand apart: are the cascades generated according to any tabulated data (as opposed to being sampled from an artificial continuous distribution)? If so, are the correlations between γ-rays properly simulated? A detailed investigation was performed in order to answer these questions. A separate GEANT4 simulation was constructed for the neutron irradiation of the materials consisting of a single isotopic component. Several prominent isotopes were selected: ^{23}Na, ^{28}Si, ^{56}Fe, ^{58}Ni... As soon as the γ-rays from the neutron capture were emitted, their energies were recoded, avoiding their interaction with the surrounding material. Figure 4.5 compares the accumulated spectra for ^{28}Si and ^{58}Ni with the tabulated thermal neutron capture data from Ref. [86]. Due to the relatively low number of known capture γ-rays, ^{28}Si is well suited for the visual examination of the spectra. Additionally, ^{58}Ni is shown for its central importance to this work. After a close inspection, the narrow peaks in the simulated spectra invariably lead to the conclusion that γ-cascades are indeed generated following the tabulated data. However, according to Ref. [87], the artificial continuous distribution is, in fact, resorted to if the data for a given isotope are not available. The continuous spectra outside the sharp peaks from Fig. 4.5 and the fact that the peak heights, i.e. γ-ray intensities are not accurately reproduced, present a clear evidence of the absence of correlations. It may be concluded that γ-cascades are simulated independently of

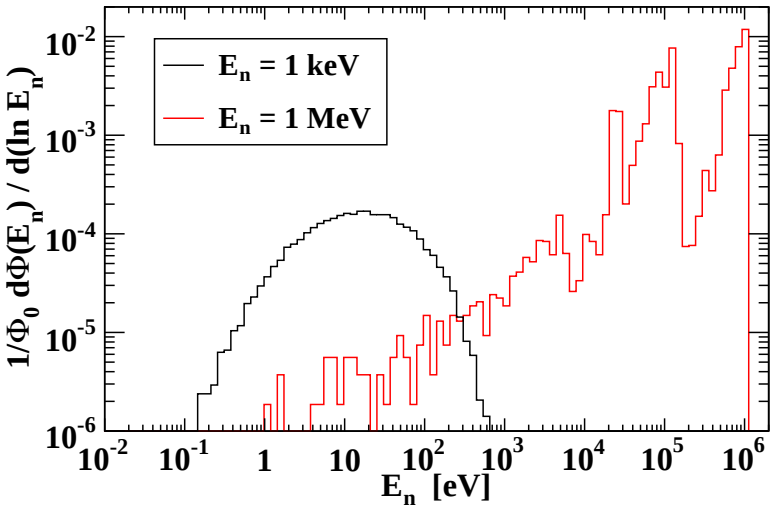

Figure 4.4 — Energy distributions of the neutrons emerging from 30 cm thick iron slab, initially irradiated by monoenergetic beams of 1 keV and 1 MeV. The spectra are to be compared with the highly consistent counterparts reported in Ref. [85].

the actual cascade paths allowed by structure of the nuclear states. Furthermore, in order to exactly reproduce the excitation energy of the compound nucleus, the final emitted γ-ray is subjected to the energy conservation requirement. This is the exact cause for the presence of counts in the simulated spectra between the peaks coinciding with the accurately tabulated data. Though the user may freely select to deactivate the production of the last, artificial γ-ray constrained by the energy conservation, it is of crucial importance for this work that this option is kept active. Such requirement is introduced by the Pulse Height Weighting Technique, which relies on the assumption that the sum of energies of all γ-rays from a single cascade corresponds to the excitation energy of a compound nucleus.

The lack of proper correlations between γ-rays sizably affects the simulated spectra of counts, relative to the experimental counterparts. To demonstrate this effect, the simulation for determining the neutron background was run for the ^{197}Au sample. The role of ^{197}Au sample in determining the absolute yield normalization factor has already been been discussed in Section 3.5. ^{197}Au is especially well suited as reference

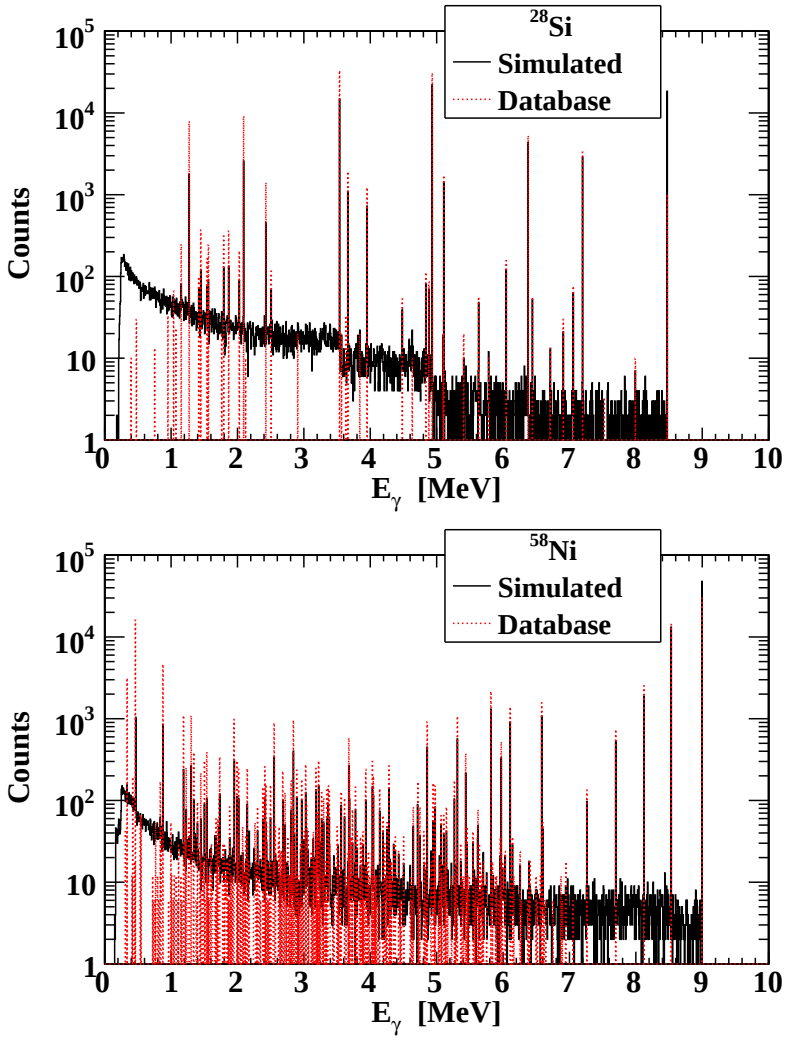

Figure 4.5 — Simulated spectra of γ-rays from the cascades induced by the thermal neutron capture on ^{28}Si (top panel) and ^{58}Ni (bottom panel). The simulated results are compared to the known γ-ray energies and intensities tabulated in Ref. [86].

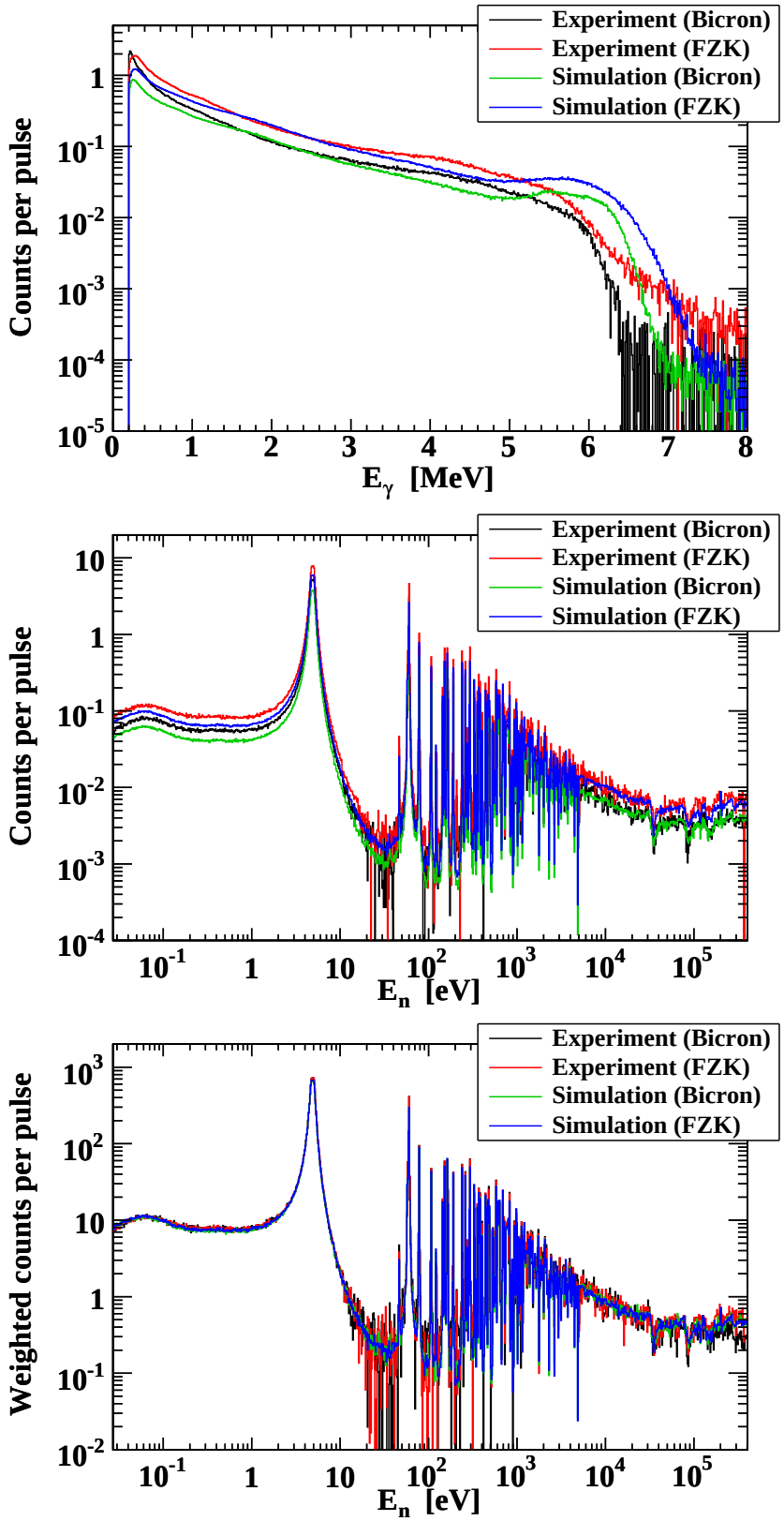

Figure 4.6 — Comparison between the experimental and simulated results for the radiative neutron capture on ^{197}Au. The spectra are shown in parallel for two C_6D_6 detectors. Top panel: γ-rays (energy deposition) spectra. Middle panel: capture counts in terms of the neutron energy calculated from the time of flight. Bottom panel: weighted capture counts (PHWT applied).

point for comparing the γ-rays spectra because it is characterized – below the huge resonance at 4.9 eV – by a radiative capture cross section much larger than for elastic scattering (Fig. 4.1). For this reason, both the simulated and experimental spectra will consist almost entirely of the γ-rays produced by ^{197}Au(n,γ) reaction. The top panel of Fig. 4.6 shows the difference between the experimental and simulated γ-rays spectra, as acquired by two C_6D_6 detectors. The middle panel shows the spectra of counts in terms of the incident neutron energy reconstructed from the neutron time of flight. The considerable difference between the experimental and simulated results may be observed. While the difference in shape of the γ-rays spectra is obvious, the difference in magnitude (due to the energy dependent detection efficiency) may not be as simple to infer visually from a logarithmic scale. Since all of the spectra from the top panel perfectly correlate to those from the middle panel – sharing the total number of counts – from the middle panel the difference in magnitude may be easily confirmed, particularly from the section below the saturated resonance at 4.9 eV. However, after applying the Pulse Height Weighting Technique to both the experimental and simulated results – following spectra being shown by the bottom panel of Fig. 4.6 – all spectra coincide. This outcome is guaranteed by the basic principles behind the PHWT, which consist in the artificial manipulation of the detector response so as to make the detection efficiencies of the used detectors independent of the actual cascade path.

We have demonstrated that the neutron transport capabilities of GEANT4 have become highly reliable and fully able to accurately reproduce the experimental data once the weighting functions have been taken into account. In addition, we have once again confirmed the key importance of PHWT itself, yielding the same weighted results after it has been applied to the genuinely different γ-cascades spectra. Therefore, we continue with high confidence the analysis of the simulated capture yield, calculated from the simulated capture counts in exactly the same manner as the experimental yield is calculated from the measured counts.

4.4 Neutron sensitivity

Prior to presenting the results on the true neutron background, we investigate the neutron sensitivity of the used detectors as defined in Ref. [61], since this approach has already been adopted at n_TOF in the past. The adopted definition of the neutron sensitivity is based on the ratio $\varepsilon_n/\varepsilon_\gamma^{max}$, with ε_n as the efficiency for detecting a neutron (via secondary particles produced by the neutron-induced reactions) and ε_γ^{max} as the maximal γ-ray detection efficiency of a given detector. The results reported here extend upon the ones from Ref. [61] in the following ways:

- While in the past the neutron sensitivity was considered for the neutron energies between 1 keV and 1 MeV, we extended this range by additional 5 orders of magnitude, covering the full energy range relevant for the capture measurements at n_TOF – from thermal to 1 MeV.

- Geometric configurations adopted in the past consist of the isolated detectors, irradiated by neutrons. We refer to this neutron sensitivity as the *intrinsic neutron sensitivity* of the detectors. We have also introduced the neutron sensitivity in the presence of the entire n_TOF experimental hall, which we refer to as the *overall neutron sensitivity*.

In order to determine the neutron sensitivity, the same simulations as described in Section 4.2 were used. The only difference regards the production of primary particles. Instead of being emitted at the entrance of the experimental area as a collimated beam, both γ-rays and neutrons – required for the determination of ε_γ^{max} and ε_n terms – were emitted isotropically from a point source at the sample position. As explained in Ref. [61], below the neutron energy of 1 MeV the only relevant contribution to the neutron detection comes from detecting the γ-rays from neutron induced capture reactions. Though neutrons may also produce the detectable signal through deuteron recoils within the C_6D_6 liquid, the scintillation light produced by such a heavy charged particle is significantly quenched, limiting the signals to be well below 200 keVee (electron equivalent) for neutron energies below 1 MeV. Since these signals are – both during the experiment and simulations – discarded by applying an appropriate threshold, only γ-rays have a non-negligible efficiency.

In the simulations the detectors were irradiated several times by monoenergetic γ-rays, each time assuming a different γ-ray energy. In determining the detection efficiency ε_γ as the ratio between the number of detected and emitted photons, a lower threshold of 200 keV on the deposited energy was taken into account, just as it has been done during the analysis of the experimental data. The resulting efficiencies for detecting γ-rays with energy between 300 keV and 10 MeV are shown in Fig. 4.7. No attempt has been made to decouple the intrinsic from the geometric efficiency on a basis of the solid angle covered by the detectors. Therefore, ε_γ remains the total detection efficiency. Due to the 200 keV threshold considerably affecting ε_γ at lower energies, the maximal efficiency ε_γ^{max} is shifted toward 900 keV, amounting to 1.81% for Bicron and 2.97% for FZK detector.

To obtain a measure of the neutron detection efficiency ε_n, the detectors were irradiated by the stream of neutrons emitted isotropically from a point source at the sample position, following the isolethargic $(1/E_n)$ energy distribution. The deposited energy threshold of 200 keV was again kept as a condition for considering the neutrons as detected. As previously stated, two detector configurations were irradiated. The first configuration – giving rise to the intrinsic neutron sensitivity – consists of an isolated

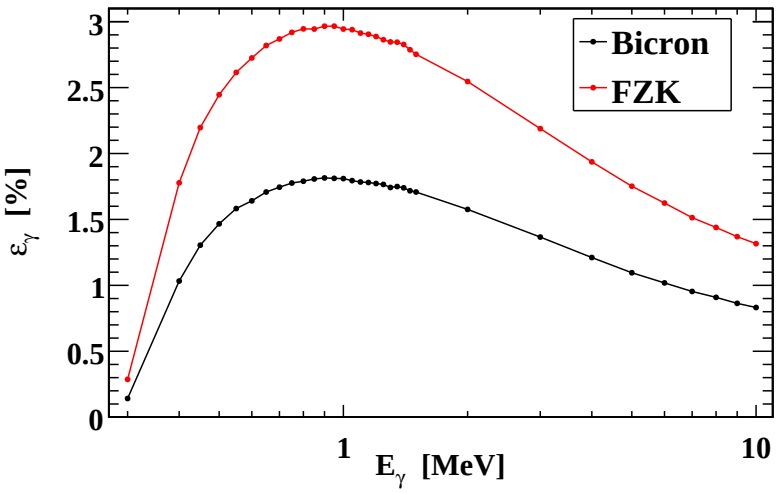

Figure 4.7 — Efficiency for detecting the monoenergetic γ-rays isotropically emitted from a point source at the sample position. Total (intrinsic $\times$ geometric) efficiency is shown for both C_6D_6 detectors, obtained with 200 keV energy deposition threshold.

detector, without the presence of a second detector and the surrounding experimental hall. This configuration has already been adopted in the past and the results reported in Ref. [61]. The second configuration – resulting in the overall neutron sensitivity – includes the entire geometric setup employed for the neutron background simulations – both detectors simultaneously, together with the overall experimental hall. Following the same procedure as for evaluating ε_γ, no solid angle corrections were performed in calculating ε_n. Thus the neutron sensitivity $\varepsilon_n/\varepsilon_\gamma^{\max}$ is implicitly corrected for the geometric contribution to both ε_n and $\varepsilon_\gamma^{\max}$. Figure 4.8 shows the neutron sensitivity of detectors in both configurations. From the results for the isolated detectors it is clear that the FZK detector – which was custom built with a specific purpose of minimizing the neutron sensitivity – has a clear advantage of a reduced intrinsic sensitivity over the Bicron one. This is due to the carbon fiber housing used for containing the C_6D_6 liquid in the case of FZK detector, as opposed to the aluminum housing used for the Bicron one. Aluminum is also the cause for the prominent resonant structure appearing mostly above 1 keV in the Bicron data. Relative to Bicron, the sensitivity of FZK is further reduced by the higher γ-ray detection efficiency $\varepsilon_\gamma^{\max}$ – consequence of the increased C_6D_6 content of 1027 ml, as opposed to 618 ml for Bicron. In the case of the second configuration the overall neutron sensitivity of both detectors is significantly higher, showing almost the same flat behavior above 10 eV. After averaging the data between 10 eV and 1 MeV we report the approximate magnitude of 2.0×10^{-3} for the overall neutron sensitivity of both detectors. It must be kept in mind that, by the adopted definition, the neutron sensitivity is the detector response to the neutrons *of* certain energy, not *at* the given energy (reconstructed from the time of flight). However, the true neutron background, discussed in depth in the following section, is heavily affected by the properties of the sample – acting as the primary neutron scatterer – and by the energy dependence of the available neutron flux. On the other hand, once the characteristics of the neutron beam irradiating the experimental setup are agreed upon, the adopted definition of the neutron sensitivity becomes genuinely independent of the sample – inherent to the detectors themselves and carrying the signature of the surrounding experimental apparatus. As such, the neutron sensitivity lends itself easily to general considerations when estimating the impact on the cross section measurements of the neutron induced reactions.

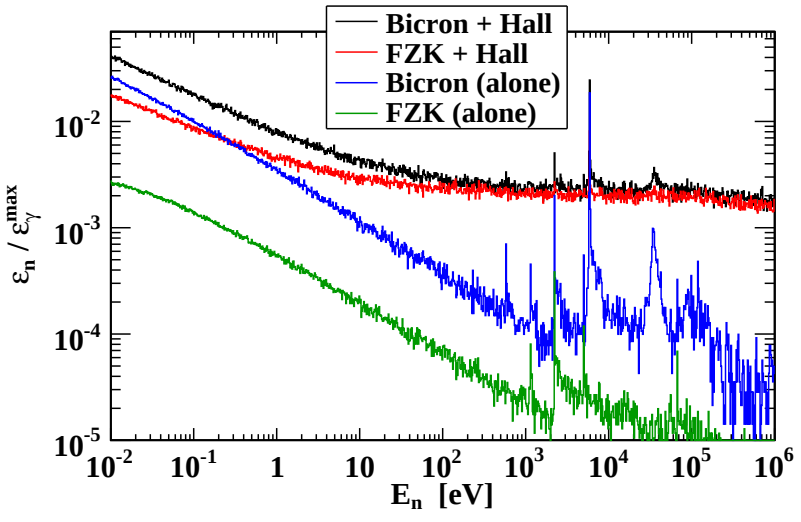

Figure 4.8 — Intrinsic and overall neutron sensitivity of two used C_6D_6 detectors (see the main text for the clarification of terms and the details of neutron emission).

4.5 Neutron background

4.5.1 ^{nat}C results

In principle, the approximate magnitude of the neutron background may be estimated experimentally by irradiating a sample of material exhibiting a very low capture-to-scattering ratio. Since natural carbon conforms to this requirement (see Fig. 4.1), the control ^{nat}C sample of 1 cm thickness and 2 cm diameter has been measured during the ^{58}Ni campaign. The declared high purity of the sample (99.95%) was confirmed by the chemical analysis at Paul Scherrer Institute, excluding the possibility of any notable contamination by high capture cross section isotopes. The experimental yield for carbon – calculated following exactly the same procedure as for calculating the ^{58}Ni yield – was taken as a benchmark for evaluating the quality of simulated neutron background. The comparison between the total experimental and simulated yield is shown in Fig. 4.9. It is clear that the simulations successfully reconstruct the experimental data throughout the entire energy range relevant for the capture measurements at n_TOF – from thermal up to hundreds of keV.

It may be observed from Fig. 4.9 that ^{nat}C yield is not composed solely of the neutron background. Contrary to initial expectations, irradiating ^{nat}C sample by the neutron beam from n_TOF leads to a significant production of β-radioactive isotopes, which are experimentally observed through the detection of outgoing β-rays. The ^{12}C$(n, p)^{12}$B inelastic reaction, which opens at the incident neutron energy of approximately 14 MeV, is by far the most important one for this outcome. The produced ^{12}B isotope is β^--radioactive with the mean electron energy of $\langle E_\beta \rangle$ = 6.35 MeV and a half-life of $T_{1/2}$ = 20.2 ms. Very high energy of emitted β-rays allows them to reach either of the two C_6D_6 detectors and deposit within the scintillation liquid a large fraction of their initial energy. Furthermore, a half-life of 20.2 ms causes almost the entire expo-

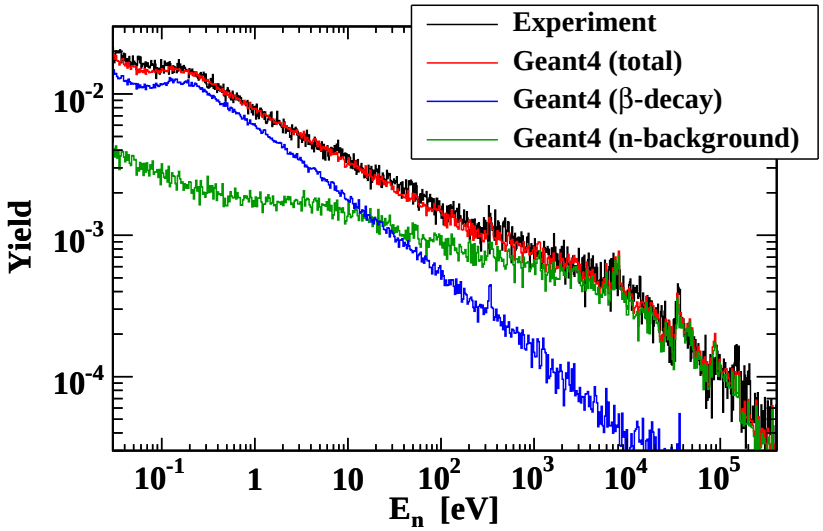

Figure 4.9 — Yield obtained with ^{nat}C sample of 1 cm thickness and 2 cm diameter. An excellent agreement is achieved between the experimental and total simulated yield. In case of the simulated results, the true neutron background was easily decoupled from the detection of β-rays, coming mostly from the decay of ^{12}B produced by ^{12}C$(n, p)^{12}$B reaction.

nential decay distribution to (in)conveniently fall within a 96 ms time-window used by the n_TOF data acquisition system for a digital recording of the electronic signals (see Section 2.5). As explained in Section 3.4, during the data analysis the energy is assigned to the primary neutron on a basis of a time-stamp of the signal. In case of a prompt neutron capture event, this time-stamp corresponds to the neutron time of flight. However, the time-stamp for β-rays is random in nature, given by the decay of the unstable nucleus. Thus the time-energy correlation for the primary neutron is lost, while the energies from above 14 MeV – the threshold for a ^{12}C$(n,p)^{12}$B reaction – are reconstructed within the thermal and epithermal range, as shown by the separate plot within Fig. 4.9. Alongside the contribution from the β-radioactive residuals created by the inelastic reactions in the ^{nat}C sample, the true neutron background is also shown separately. In case of the samples relevant for their radiative capture – such as ^{58}Ni and ^{197}Au – we consider the neutron background to consist of all the counts not caused by the detection of γ-rays produced by the neutron capture within the sample itself. Similarly, in case of the carbon sample, the neutron background is considered to consist of all the counts apart from those pertaining to the β-rays (detected directly or via secondary γ-rays) produced by the inelastic reactions within the sample. By definition, β-rays created by inelastic reactions outside the sample also contribute to the neutron background.

Starting from thermal energies, ^{12}B production by far dominates the inelastic contribution to the yield. Though ^{8}Li production via ^{12}C$(n,p+\alpha)^{8}$Li reaction is comparable in intensity – ^{8}Li also being β^--radioactive with $\langle E_\beta \rangle$ = 6.20 MeV – due to the rather long half-life of $T_{1/2}$ = 840.3 ms, most of the β-rays fall outside the 96 ms recording window. Further β^--radioactive residuals contributing rather insignificantly to the yield include ^{13}B, ^{9}Li and ^{6}He. Created via ^{13}C$(n,p)^{13}$B reaction, ^{13}B is a consequence of ^{13}C content in the natural carbon. Several β^+-radioactive residuals such as ^{11}C, ^{10}C and ^{9}C have also been observed in the output of the simulations, contributing to the yield mostly through the detection of γ-rays from the positron annihilation. Table 4.2 lists the aforementioned residuals, together with their basic β-decay properties and examples of reactions creating them. While some of the isotopes are created exclusively by a given reaction, some are produced through multiple reaction channels. Such is the case of ^{6}He, for which at least 8 different reactions were observed in GEANT4. They are also listed in Table 4.2 in order to illustrate the versatility of GEANT4 code. For very high incident neutron energies the products of $n+^{A}$X reaction may be considered to come from the immediate dissociation of ^{A}X nucleus. At lower energies they may also be interpreted as the particle decay products of an excited $^{A+1}$X* state, with the decay being processed by the intra-nuclear cascade codes themselves. For illustrative purposes we also mention the observed ^{12}C$(n, n+2p+\pi^+)^{9}$Li reaction, showing that even the production of (exotic) mesons is taken into account by GEANT4 models.

Figure 4.9 is central to understanding the neutron background measured with ^{nat}C sample. From the observation that below 1 keV the neutron background yield departs from the total yield, we conclude that the experimental data for ^{nat}C may be used for evaluating the neutron background only above this energy threshold. Furthermore, the threshold for ^{12}C$(n,p)^{12}$B reaction at 14 MeV implies that all neutron production facilities with the neutron flux extending above this particular energy may expect to encounter the same β-decay contribution when measuring the neutron background with ^{nat}C.

Table 4.2 — Neutron induced reactions on ^{nat}C – as identified from GEAN4 simulations – producing β-radioactive isotopes which may be detected via primary β-rays or secondary γ-rays. The ones listed herein are not necessarily the only ones leading to the production of a given isotope. As an example, an extended list of observed reactions is shown for ^{6}He. Production of ^{12}B is by far the most contributing to the n_TOF measurements.

	Isotope	Reaction	$\langle E_\beta \rangle$	$T_{1/2}$
β^-	^{12}B	^{12}C$(n,p)^{12}$B	6.35 MeV	20.2 ms
	^{13}B	^{13}C$(n,p)^{13}$B	6.35 MeV	17.3 ms
	^{8}Li	^{12}C$(n,p+\alpha)^{8}$Li	6.20 MeV	840.3 ms
	^{9}Li	^{12}C$(n,n+3p)^{9}$Li	5.70 MeV	178.3 ms
	^{6}He[a]	^{12}C$(n,p+d+\alpha)^{6}$He	1.57 MeV	806.7 ms
β^+	^{11}C	^{12}C$(n,2n)^{11}$C	0.38 MeV	20.3 min
	^{10}C	^{12}C$(n,3n)^{10}$C	0.81 MeV	19.3 s
	^{9}C	^{12}C$(n,4n)^{9}$C	6.43 MeV	126.5 ms

[a] Extended examples:
^{12}C$(n,n+3p+t)^{6}$He
^{12}C$(n,n+2p+\alpha)^{6}$He
^{12}C$(n,2p+d+t)^{6}$He
^{12}C$(n,p+d+\alpha)^{6}$He
^{12}C$(n,^{3}$He$+\alpha)^{6}$He
^{12}C$(n,^{7}$Be$)^{6}$He
^{13}C$(n,2n+2p)^{6}$He
^{13}C$(n,n+p+d+\alpha)^{6}$He

In the following section the neutron background for ^{nat}C will be analyzed. The purpose of analysis is to indicate the qualitative properties that are expected to be true for the neutron background caused by the other materials. However, while the general characteristics have been confirmed to hold in case of ^{58}Ni and ^{197}Au, the quantitative properties necessarily depend on their respective cross sections, primarily those for the elastic scattering of neutrons. This fact necessitates running the dedicated simulations for every single sample, within the full energy range of the available neutron flux.

One important aspect that could be investigated with the simulations is the contribution of the delayed neutron background component. Since the ^{58}Ni capture data were analyzed up to 400 keV, we will consider the energy range below 400 keV as the most relevant for the analysis. Therefore, we define the *delayed neutron background* as the contribution to the yield from the primary neutrons above 400 keV, contrary to the contribution from the primary neutrons below 400 keV, here referred to as the *prompt neutron background*. The aim of such distinction is to strongly emphasize the impact of the high energy part of the neutron flux on the neutron background. Both components – prompt and delayed – are clearly separated in Fig. 4.10. It may be observed that the delayed component constitutes the significant portion of the total neutron background, particularly at higher energies where it dominates the yield. During the calculation of the yield, the data at the given energy – reconstructed from the time of flight – are corrected for the local value of the neutron flux. Since this procedure does not account for the correlations with the primary neutron energy, it is of paramount importance to simulate the full available neutron flux (Fig. 4.3) following the exact energy distribution, as opposed to resorting to artificial (e.g. uniform) distributions.

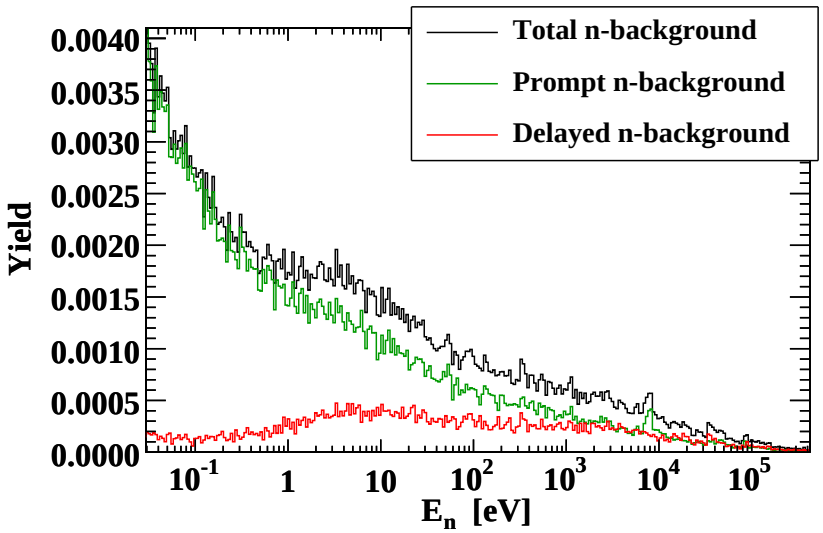

Figure 4.10 — Neutron background yield for ^{nat}C sample. The delayed component, reconstructed below 400 keV, is caused by the primary neutrons of energy higher than 400 keV. The prompt component is considered to originate from primary neutrons below 400 keV, even though the time-energy correlation may still be lost for a portion of counts.

The time structure of the neutron background counts is shown in Fig. 4.11 for the Bicron detector. The top plot shows the E_0–E_{ToF} correlations, with E_0 as the primary neutron energy and E_{ToF} as the energy reconstructed from the time-stamps, i.e. the time of flight of the detected counts. We remind that – while the line $E_{\mathrm{ToF}} = E_0$ is the true prompt component – we refer to all the counts with $E_0 < 400$ keV as the prompt neutron background. For the counts from the top plot, the bottom panel shows the projections on both axes. The condition $E_{\mathrm{ToF}} < 1$ MeV has been imposed on the shown counts. The significant loss of the time-energy correlations due to the neutron scattering inside the experimental hall or the delayed emission of secondary particles is clearly evident from the difference between the two spectra. While the spectrum of energies reconstructed from the time of flight is experimentally accessible, the spectrum of the primary neutron energies may only be inferred from the dedicated simulations. It is to be noted that in the $E_0 < 10$ MeV range the spectrum of primary neutron energies for the detected counts closely resembles the sampled neutron flux from Fig. 4.3. The final observation to be made from the top panel of Fig. 4.11 is the presence of several counts in the region defined by $E_0 < E_{\mathrm{ToF}}$. This does not imply the violation of causality. The appearance of these counts is to be understood from the procedure for determining the time-stamp of the signal, i.e. the corresponding time of flight. Due to the pulsed nature of the n_TOF neutron beam – with a repetition rate in multiples of 1.2 s and the mean period of 2.5 s between the pulses – the excessively delayed events (such as radioactive decays) may be detected in one of the successive neutron bunches. Since the start-signal for calculating the effective time of flight has been redefined by the arrival of the new neutron bunch, the causality may appear to be lost, while it is not truly the case. This pulsing effect has been faithfully reproduced for the analysis of the simulated data (see Appendix G). Having this in mind, it is sufficient to establish that the counts from the $E_0 < E_{\mathrm{ToF}}$ range are caused by the decay of the ^{28}Al (with a half-life of 2.2 min), activated by the near-thermal neutron capture on the aluminum (^{27}Al) components in the vicinity of C_6D_6 detectors.

As Fig. 4.11 shows the time structure of the neutron background, Fig. 4.12 does the same for the β-rays from the neutron induced inelastic reactions on ^{nat}C. Since the relevant inelastic channels open around 14 MeV, the time-energy correlations for the counts detected below 1 MeV are completely lost. Apart from the neutron flux itself, the shape of the primary neutron energies spectrum from bottom panel is mostly determined by the cross section for the dominant ^{12}C$(n, p)^{12}$B reaction. The distinct shape of the spectrum of energies reconstructed from the time of flight – here dominated by the β-decay of ^{12}B with the half-life of 20.2 ms – is addressed in Appendix H.

We bring our attention to the contribution of separate experimental components to the total neutron background yield. Figure 4.13 shows the stacked portions of the

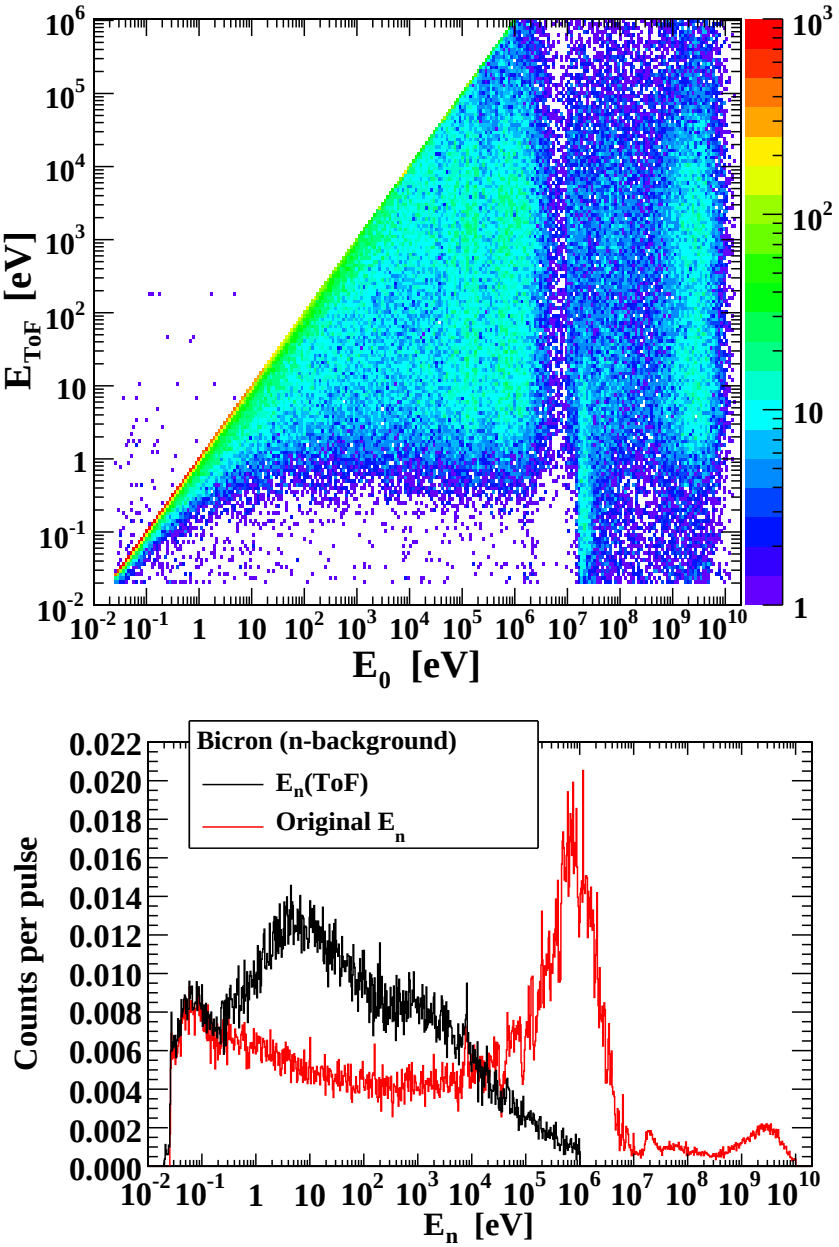

Figure 4.11 — Neutron background counts: the time structure for ^{nat}C sample and Bicron detector. Top panel: $E_0 - E_{\mathrm{ToF}}$ correlations, with E_0 as the primary neutron energies and E_{ToF} as those calculated from the time of flight. Bottom panel: projections on E_0- and E_{ToF}-axis. Only E_{ToF}-spectrum is obtainable from the experiment.

yield caused by the most representative sets of components – walls of the experimental hall, beamline tubes, detector parts of both detectors and the total remainder of components outside these sets. Several observations are to be made. As the plots for both C_6D_6 detectors show – the top plot for Bicron and the bottom plot for FZK – the walls of the experimental hall are the significant source of the neutron background, especially above 1 keV, where they completely dominate the yield. This fact is closely related to the increased relative contribution of the delayed neutron background from Fig. 4.10, since the walls are the prime candidates for the prolonged neutron scattering. Furthermore, the reason the beamline tubes notably contribute to the neutron background is their aluminum composition, in combination with the close proximity to both detectors. Finally, due to the aluminum housing of Bicron detector – as opposed to carbon fiber housing of FZK – the Bicron is characterized by the much higher neutron sensi-

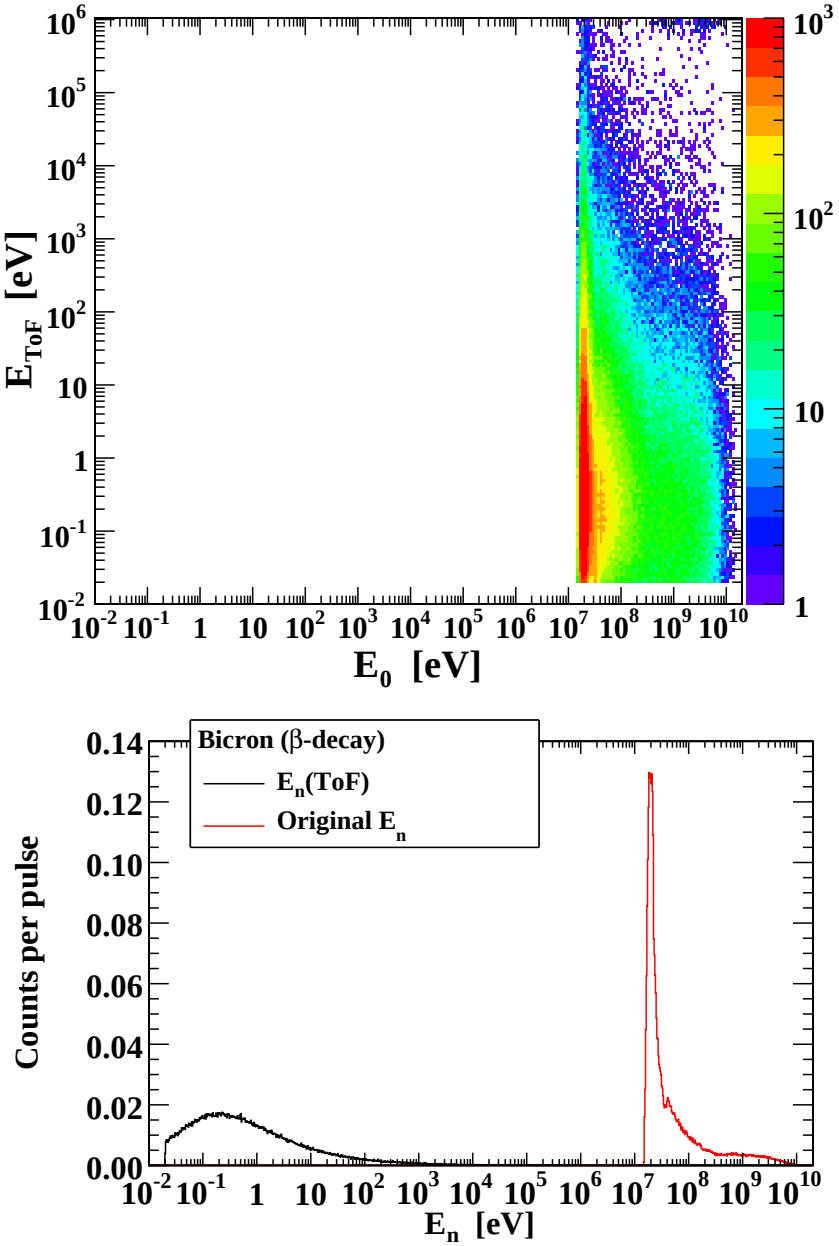

Figure 4.12 — Analogue to Fig. 4.11: detection of β-rays from the radioactive residuals produced in inelastic reactions by the high energy section of the neutron beam. The spectra are heavily affected by the dominant $^{12}C(n, p)^{12}B$ reaction.

tivity than FZK. As a consequence, its contribution to the neutron background of FZK is comparable to the contribution from the FZK itself.

Another observation that may be inferred from simulations regards the spatial origin of the particles depositing the energy inside the active C_6D_6 volumes. For example, the γ-ray created by the neutron capture in the material surrounding the sample may undergo the Compton scattering inside the C_6D_6 liquid itself, releasing an electron. This electron then deposits the energy required for the scintillations. However, the electron may be released outside the active volume, e.g. in the detector housing, subsequently reaching the scintillation liquid. Figure 4.14 shows the total contribution of these events, all properly accounted for by the weighting functions calculated from the simulations assuming the identical geometric setup.

Lastly, the contribution of the physical processes creating the neutron background was investigated. Figure 4.15 shows that for neutrons scattered by the ^{nat}C sample the

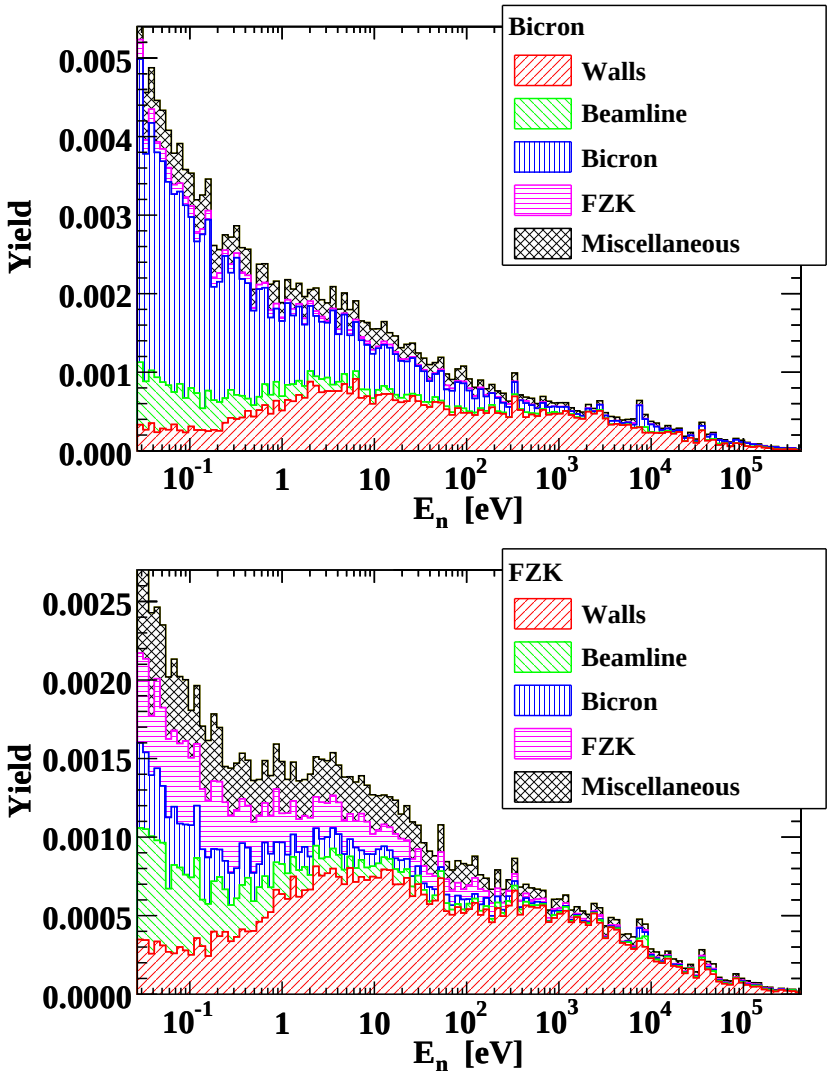

Figure 4.13 — Neutron background yield for Bicorn (top panel) and FZK (bottom panel) detector. The contributions from the different sets of experimental components are clearly separated and stacked together. The difference by a factor of 2 in absolute scales for two detectors is to be noted.

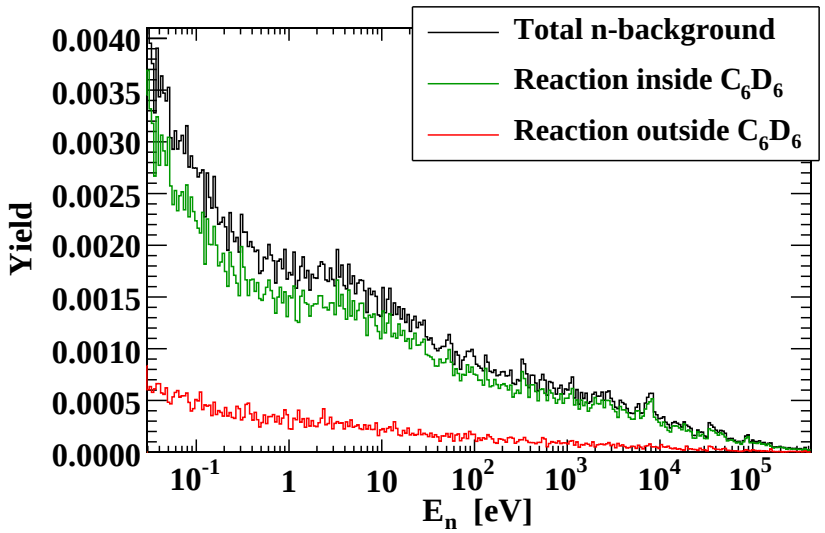

Figure 4.14 — Contribution to the neutron background yield of ^{nat}C from the energy depositing particles released inside or outside the C_6D_6 scintillation liquid.

neutron capture is by far the dominant reaction, producing the γ-rays which are then detected by either of the two C_6D_6 detectors. However, this is not necessarily the case for the capture samples, which will be discussed for ^{197}Au. The rest of the ^{nat}C neutron background is caused by the activation of the surrounding experimental components, either through the neutron capture or the neutron inelastic reactions. However, the process creating the detected β- or γ-rays is then the radioactive decay. Multi-step processes starting from the neutron capture have also been observed. For example, the γ-ray from the capture reaction may convert into the electron-positron pair, with the positron annihilating and the annihilation γ-ray being detected. Another example is the bremsstrahlung from the electron released by the interaction of the capture γ-ray with the material inside the experimental hall, with the bremsstrahlung photon being detected. In these cases, the annihilation and the bremsstrahlung are considered as the processes causing the neutron background.

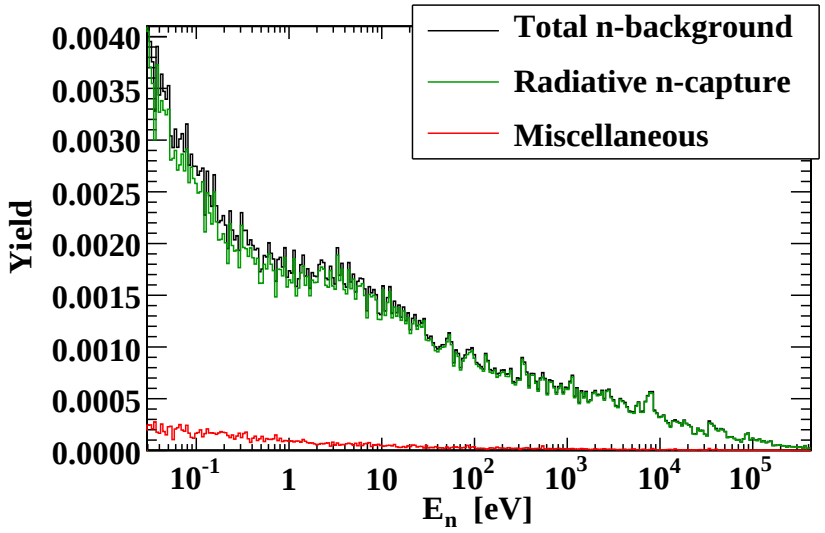

Figure 4.15 — Contribution to the neutron background yield of ^{nat}C from the radiative neutron capture by the experimental components, as opposed to all the other reactions (radioactive decay, annihilation, bremsstrahlung).

4.5.2 ^{197}Au results

Taking into account the available experimental data from ^{58}Ni campaign – consisting of measurements for ^{nat}C, ^{58}Ni and ^{197}Au – ^{nat}C may be considered as the extreme case for the neutron scattering, while ^{197}Au as the extreme case for the neutron capture. The successful reconstruction of the experimental carbon data by means of GEANT4 simulations has already been established. The successful reconstruction has also been confirmed for ^{197}Au. The weighted capture counts for this sample are shown in the bottom panel of Fig. 4.6. For completeness, Fig. 4.16 compares the total measured and simulated yield of ^{197}Au, also showing the contribution from the neutron background.

One aspect of the neutron background for ^{197}Au deserves a special attention. It is presented in Fig. 4.17 in a manner analogous to Fig. 4.15, with a single exception of focusing only on the prompt neutron background (caused by the primary neutrons of energy below 400 keV). It shows the portion of the prompt neutron background caused by the detection of particles produced by the neutron capture, as opposed to any other reaction. It may be observed that the relative contribution from the neutron capture is much lower than in a ^{nat}C case. This difference may be backtracked to the definition of a true capture event, which requires for a detected particle to be:

- a photon
- produced by the neutron capture
- created inside the irradiated sample

It is to be noted that the prompt neutron background yield caused by reactions other than neutron capture (Fig. 4.17) follows the shape of the true neutron capture yield of ^{197}Au from Fig. 4.16. Therefore, we may conclude that this contribution to the prompt neutron background comes from the true neutron capture, creating the γ-rays which have interacted with the surrounding material, releasing the electrons or positrons which have, in turn, undergone the bremsstrahlung or annihilation. Thus the secondary γ-rays are produced and detected by either of the two C_6D_6 detectors.

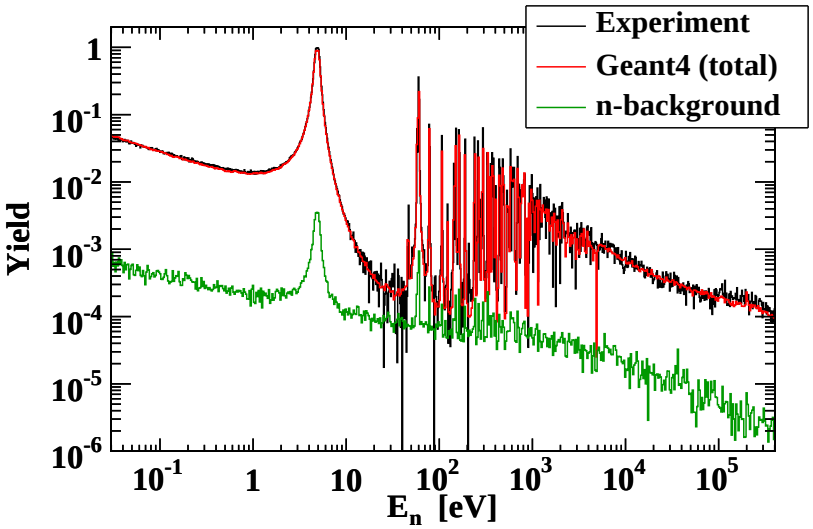

Figure 4.16 — Total and the neutron background yield of ^{197}Au. The results from GEANT4 simulations are compared to the experimental data.

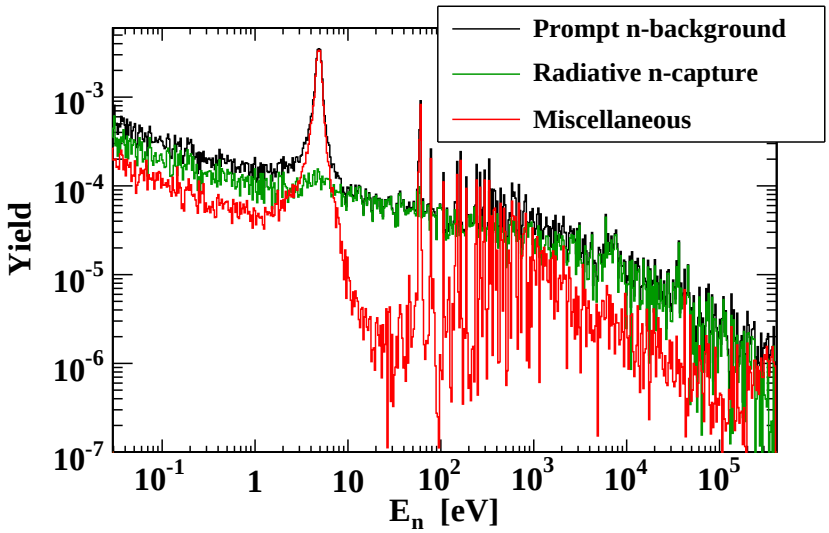

Figure 4.17 — Contribution to the prompt neutron background yield of ^{197}Au from the radiative neutron capture by the experimental components, as opposed to all the other reactions (annihilation, bremsstrahlung).

This contribution to the neutron background is equivalent to less than 0.4% of the true capture yield.

4.5.3 ^{58}Ni results

Having confirmed the reliability of GEANT4 neutron transport simulations for nominally extreme cases of ^{nat}C and ^{197}Au, the results for ^{58}Ni follow almost trivially. Together with the contribution from the neutron background for ^{58}Ni, Fig. 4.18 also shows the total experimental yield – corrected for the empty-frame and environmental background – compared to the simulated one. Expectedly, they are in excellent agreement. However, we stress that it was not the goal of these simulations to accurately

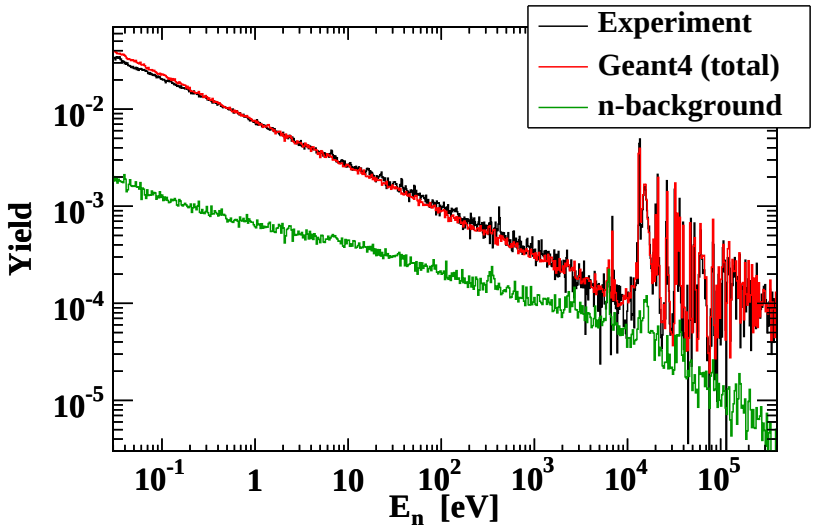

Figure 4.18 — Total and the neutron background yield of ^{58}Ni. The results from GEANT4 simulations are compared to the experimental data.

reproduce the total capture yield of ^{58}Ni, since the purpose of the experiment was to acquire an independent measurement, rather than to confirm the past results. Therefore, the high level of consistency between the total experimental and simulated results for ^{58}Ni is to be considered only as the fortunate by-product of the high-precision simulations.

By now, the reliability of the results from the neutron physics section of GEANT4 has been firmly established from the detailed analyses and comparisons with the multitude of measurements from n_TOF. For this reason, the simulated neutron background for ^{58}Ni was used for the first time at n_TOF, with a purpose of completing the analysis of ^{58}Ni experimental capture data, as reported in Section 3.5.

5
Conclusion

The cross section for ^{58}Ni(n,γ) reaction has been measured at the neutron time of flight facility n_TOF at CERN. The radiative neutron capture by ^{58}Ni plays a role in the *s*-process nucleosynthesis. Hence, the ^{58}Ni(n,γ) cross section is an important input to the nuclear astrophysics models. Moreover, ^{58}Ni is found among structural materials widely used in nuclear technologies, thus presenting a long-term radiation hazard through the production of a long-lived ^{59}Ni, characterized by the half-life of 7.5×10^4 years. Relative to the past experimental results and adopted evaluations, considerably lower ^{58}Ni(n,γ) cross section was reported from recent measurements, thus calling for a repeated and independent experimental evaluation, which was performed at n_TOF.

At n_TOF the neutrons are produced by irradiating the massive Pb spallation target by 20 GeV pulsed proton beam from CERN Proton Synchrotron. Initially fast flux of 2×10^{15} neutrons per pulse is moderated by the Pb block itself, together with the 1 cm layer of water from the cooling system and additional 4 cm layer of borated water. Final outgoing neutron flux reaching the experimental hall at approximately 185 m from the spallation target, spans 12 orders of magnitude in energy – from $\sim$10 meV to $\sim$10 GeV. Charged particles are removed from the neutron beam by a 1.5 T sweeping magnet and shaped by the two collimators, all placed along the evacuated beamline connecting the spallation target with the experimental area.

The radiative capture measurements were performed by detecting the γ-rays from the deexcitation γ-cascades, using the set of two optimized C_6D_6 (deuterated benzene) detectors. On the basis of a time-stamp of a detected event – relative to time-stamp of a start signal marked by an intense γ-flash originating at the spallation target – an energy is assigned to the captured neutrons through the time-of-flight–energy correlation. Independent measurements were performed in order to determine the energy calibration and the energy resolution of the detectors, the neutron flight path and the final normalization of the capture yield. The detection efficiency was accounted for through the Pulse Height Weighting Technique, relying on the high-precision simulations of the detectors' response to the γ-rays of varying energy. The energy dependence of the sample-incident neutron flux – indispensable for the calculation of the capture yield – was provided by the measurements and dedicated simulations only descriptively covered by this work. A special consideration regards the different types and sources of the background, including the background of scattered in-beam γ-rays, the background produced by the beam crossing the experimental area (empty-frame background), the environmental background (beam-off background) and the background of neutrons scattered off the sample itself (neutron background). All types of background have been reliably measured, except for the neutron background which was

determined by means of the dedicated GEANT4 simulations.

The capture data were analyzed for neutron energies between 27 meV and 400 keV. Within the resolved resonance region up to 122 keV a multilevel *R*-matrix code SAMMY was used for the analysis. Herein 51 resolved resonances were identified and analyzed. Additionally, two resonances at negative energies (below the neutron separation energy) were adopted in order to parameterize the capture yield extending from the thermal energies to the first resolved resonance at 6.9 keV. The energy region between 122 keV and 400 keV was considered as the unresolved resonance region, and treated with a specialized code SESH designed for simulating the smoothed capture yield, thus reconstructing the underlaying cross section parameters. The results of SESH fit were then used to evaluate the capture cross section up to 1 MeV. From a combined set of cross section parameters from SAMMY and SESH the Maxwellian averaged cross sections (MACS) were calculated for thermal energies kT = 5 – 100 keV characteristic of stellar environment. The impact of newly obtained MACS upon the stellar nucleosynthesis was investigated, finding that in massive stars the reduction of only 12% in MACS at 30 keV – relative to previously adopted value – leads to 60% increase in the final ^{58}Ni abundance, with only a marginal effect on heavier nuclides.

The GEANT4 simulations of the neutron background – as the new feature from n_TOF – and the in-depth analysis of the simulated data have been described in detail. Special attention was paid to building the faithful software replica of the n_TOF experimental hall. The most appropriate physics list was selected for handling the neutron interactions, consisting of models and cross section datasets for the elastic and inelastic scattering, neutron capture and the neutron induced fission. The neutron irradiation of the samples was accurately reproduced, following the experimental conditions as closely as possible. The lack of simulated correlations between the γ-rays from the capture-induced cascades was investigated in detail. It was confirmed that the Pulse Height Weighting Technique plays a central role in compensating for the effect of correlations – or the lack thereof – upon the calculated capture yield, bringing the simulated and experimental data into a close agreement. The neutron sensitivity of the two C_6D_6 detectors was simulated, following the procedure adopted in the past, while improving upon the past results. Finally, the neutron background was simulated for three different samples from ^{58}Ni experimental campaign – ^{58}Ni, ^{197}Au and ^{nat}C. The simulated capture data were then analyzed in exactly the same manner as the experimental data. For all samples an excellent agreement was found between the total simulated and experimental yields. In particular, the agreement between ^{nat}C data above 1 keV – where the yield consists almost purely of the neutron background – confirms the reliability of the latest neutron transport capabilities from GEANT4, justifying its use in determining the neutron background within the capture measurements. Below 1 keV an additional component in ^{nat}C yield was identified, caused by the detection of highly energetic β-rays coming mostly from the β-decay of ^{12}B produced by ^{12}C$(n, p)^{12}$B inelastic reaction opening at the neutron energy of approximately 14 MeV. As such, ^{nat}C experimental data from n_TOF may be considered as an integral measurement of the cross section for ^{12}C$(n, p)^{12}$B reaction, from the reaction threshold up to the neutron energy of 10 GeV.

Appendix

A Linear optimization

Assuming the weighting function to be a polynomial of a degree N, a nonlinear fitting procedure may be entirely avoided due to polynomial parameters optimization being fully linear in nature. Since several summation indices are going to appear in a course of further calculations, it is important to keep in mind their designation:

$$\begin{aligned} i &\rightarrow \text{HISTOGRAM BINS} \\ j &\rightarrow \text{MONOCHROMATIC SPECTRA} \\ k, l &\rightarrow \text{POLYNOMIAL TERM DEGREE} \end{aligned}$$

As a starting point, a basic requirement on the weighting function W is considered:

$$S \equiv \sum_j \left[\sum_i W_i R_i(j) - \alpha E_\gamma(j) \right]^2 = \min. \tag{A.1}$$

Being applied to the j-th monochromatic spectrum $R(j)$ associated with a γ-ray of energy $E_\gamma(j)$, the weighting function task is to compel the area below j-th modified spectrum to be proportional to the γ-ray energy $E_\gamma(j)$ for any j. Due to this area being directly related to the detection efficiency, the procedure is equivalent to the artificial manipulation of a detector response. The weighting function itself is applied one histogram bin at the time, with discrete values:

$$\begin{aligned} W_i &\equiv W(E_i) \\ R_i(j) &\equiv R(j; E_i) \end{aligned} \tag{A.2}$$

being evaluated at detection energy E_i corresponding to the i-th bin. Assuming a polynomial of a degree N for a weighting function:

$$W(E) = \sum_{k=0}^{N} a_k E^k \tag{A.3}$$

the minimization of (A.1) requires the condition:

$$\frac{\partial}{\partial a_l} \sum_j \left[\sum_{k=0}^{N} a_k \sum_i R_i(j) E_i^k - \alpha E_\gamma(j) \right]^2 = 0 \tag{A.4}$$

to be satisfied for every $a_l; l = 0, \ldots, N$. Differentiating (A.4), the following remains:

$$2 \sum_j \left[\sum_{k=0}^{N} a_k \sum_i R_i(j) E_i^k - \alpha E_\gamma(j) \right] \cdot \sum_{i'} R_{i'}(j) E_{i'}^l = 0 \tag{A.5}$$

which may rewritten as:

$$\sum_{k=0}^{N} a_k \sum_j \left[\sum_i R_i(j) E_i^k \cdot \sum_{i'} R_{i'}(j) E_{i'}^l \right] = \alpha \sum_j E_\gamma(j) \sum_{i'} R_{i'}(j) E_{i'}^l \tag{A.6}$$

From a previous expression a linear nature of finding the coefficients a_k is evident. Defining the following matrix term:

$$\mathrm{M}_{jk} \equiv \sum_i R_i(j) E_i^k \tag{A.7}$$

(A.6) is translated into:

$$\sum_j \sum_{k=0}^{N} \mathrm{M}_{jl} \mathrm{M}_{jk} a_k = \alpha \sum_j \mathrm{M}_{jl} E_\gamma(j) \tag{A.8}$$

Arranging the a_k and $E_\gamma(j)$ components into a vector form:

$$\begin{aligned} \vec{a} &\equiv [a_0, a_1, \ldots, a_N]^{\mathrm{T}} \\ \vec{E}_\gamma &\equiv [E_\gamma(1), E_\gamma(2), \ldots]^{\mathrm{T}} \end{aligned} \tag{A.9}$$

(A.8) may be expressed in a compact matrix form:

$$\mathrm{M}^{\mathrm{T}}\mathrm{M}\,\vec{a} = \alpha \mathrm{M}^{\mathrm{T}}\,\vec{E}_\gamma \tag{A.10}$$

with $(\cdot)^{\mathrm{T}}$ denoting the matrix transposition. The formal solution for (A.10) is given by:

$$\vec{a} = \alpha \left(\mathrm{M}^{\mathrm{T}}\mathrm{M}\right)^{-1} \mathrm{M}^{\mathrm{T}}\,\vec{E}_\gamma \tag{A.11}$$

requiring only matrix manipulation, entirely avoiding the nonlinear optimization. Evaluating the S from (A.1) for an extracted set of parameters $\{a_k\}$, the estimate on parameter uncertainties is further obtained by:

$$(\Delta a_k)^2 = \frac{S}{\dim(\vec{E}_\gamma) - \dim(\vec{a})} \left[\left(\mathrm{M}^{\mathrm{T}}\mathrm{M}\right)^{-1}\right]_{kk} \tag{A.12}$$

where $\dim(\cdot)$ stands for a vector dimension, i.e number of their components. It is already known that: $\dim(\vec{a}) = N + 1$.

B Experimental background subtraction

The sample-related background is affected both by the empty-frame background and the environmental (beam-off) background. However, the portion of the environmental background is already contained within the empty-frame measurements. Therefore, a proper normalization of background components must be performed. Let us denote by N the total number of measured counts, either with sample in place (SAMPLE), empty frame (EMPTY) or those related only to the environmental background (OFF). Then, let us denote by P the total number of protons incident on the spallation target, proportional to the total number of the neutrons irradiating the experimental setup in case of measurements with sample in place or with the empty frame. Finally, let us denote by E the total number of events, i.e. the proton pulses or – in case of the environmental background measurements – the equivalent proton pulses, proportional

to the duration of measurements. First, we correct separately the sample-related and empty-frame counts for the environmental background:

$$\begin{aligned} N_{\mathrm{SAMPLE-OFF}} &= N_{\mathrm{SAMPLE}} - \frac{E_{\mathrm{SAMPLE}}}{E_{\mathrm{OFF}}} N_{\mathrm{OFF}} \\ N_{\mathrm{EMPTY-OFF}} &= N_{\mathrm{EMPTY}} - \frac{E_{\mathrm{EMPTY}}}{E_{\mathrm{OFF}}} N_{\mathrm{OFF}} \end{aligned} \tag{B.1}$$

and then we perform the correction for the pure empty-frame background:

$$N_{\mathrm{SAMPLE-EMPTY-OFF}} = N_{\mathrm{SAMPLE-OFF}} - \frac{P_{\mathrm{SAMPLE}}}{P_{\mathrm{EMPTY}}} N_{\mathrm{EMPTY-OFF}} \tag{B.2}$$

Finally, in order to reconstruct the total number of pure sample-related counts per proton pulse, we need to scale the totality of measurements to the nominal number of protons per pulse ($P_{\mathrm{NOMINAL}} = 7 \times 10^{12}$):

$$N_{\mathrm{PER\,PULSE}} = \frac{P_{\mathrm{NOMINAL}}}{P_{\mathrm{SAMPLE}}} N_{\mathrm{SAMPLE-EMPTY-OFF}} \tag{B.3}$$

Combining all the previous expressions, we are left with a unique background subtraction formula:

$$N_{\mathrm{PER\,PULSE}} = P_{\mathrm{NOMINAL}} \left[\frac{N_{\mathrm{SAMPLE}}}{P_{\mathrm{SAMPLE}}} - \frac{N_{\mathrm{EMPTY}}}{P_{\mathrm{EMPTY}}} - \left(\frac{E_{\mathrm{SAMPLE}}}{P_{\mathrm{SAMPLE}}} - \frac{E_{\mathrm{EMPTY}}}{P_{\mathrm{EMPTY}}} \right) \frac{N_{\mathrm{OFF}}}{E_{\mathrm{OFF}}} \right] \tag{B.4}$$

C Environmental background counts

The source of the environmental background is the environmental radioactivity, both natural and the one induced by the neutron irradiation of the experimental hall. Therefore, the density $p(t)$ of detected γ-rays per unit time interval at the time t after the start-signal is given by all the radioactive decay rates:

$$p(t) = \sum_i \frac{\varepsilon_i N_i}{\tau_i} e^{-t/\tau_i} \tag{C.1}$$

where sum goes over all distinct radioactive sources. Here ε_i is the average efficiency for detecting γ-rays from an i-th source, τ_i is the lifetime of the same source and N_i is the total number of its atoms at the moment of the start-signal ($t = 0$). Since N_i may change over time due to the periodic renewal of the start signal, it is to be interpreted as the mean value over the duration of measurement. When attempting to express the distribution (C.1) as a function of a neutron kinetic energy E reconstructed from a time of flight, a probability conservation must be satisfied:

$$p(t)|\mathrm{d}t| = p(E)|\mathrm{d}E| \tag{C.2}$$

which yields the most general procedure for the distribution transformation between the complementary variables:

$$p(E) = p(t) \left| \frac{\mathrm{d}t}{\mathrm{d}E} \right| \tag{C.3}$$

Let us now consider that only the radioactive sources with lifetimes much longer than the duration of the data acquisition window (96 ms; following every start-signal) contribute to the environmental background. Otherwise, if any components of the induced radioactivity were prompt, they would be measured purely as a part of the empty-frame background. Therefore, within the duration of the data acquisition window, all the relevant exponential terms from (C.1) may be approximated as $e^{-t/\tau_i} \approx 1$, leaving:

$$p(t) = \sum_i \frac{\varepsilon_i N_i}{\tau_i} \equiv C \tag{C.4}$$

Here we have introduced the constant C in order to absorb all the time independent terms and simplify the expression for further calculation. Now we observe the non-relativistic expression for calculating the neutron kinetic energy from its time of flight t:

$$E = \frac{mL^2}{2t^2} \tag{C.5}$$

which is, alongside true neutron-induced counts, also applied to the environmental background counts. Here m is the mass of the neutron and L is the path length of 184 m between the spallation target and the sample position inside the experimental hall. Using this relation to find the derivative from (C.3), we are left with:

$$\left|\frac{\mathrm{d}t}{\mathrm{d}E}\right| = \sqrt{\frac{mL^2}{8E^3}} \tag{C.6}$$

Entering (C.4) and (C.6) into (C.3), we have:

$$p_{\mathrm{lin}}(E) = CL\sqrt{\frac{m}{8}}\frac{1}{\sqrt{E^3}} \tag{C.7}$$

where index 'lin' denotes the result that would be obtained filling the histogram with bins equally distributed over the linear scale. However, it is shown in Appendix D that when filling the bins equally distributed over the logarithmic scale, the histogram content is locally amplified as:

$$p_{\mathrm{log}}(E) = E \cdot p_{\mathrm{lin}}(E) \tag{C.8}$$

creating the distribution of counts:

$$p_{\mathrm{log}}(E) = CL\sqrt{\frac{m}{8}}\frac{1}{\sqrt{E}} \tag{C.9}$$

that may clearly be confirmed from the n_TOF measurements. Fig. C.1 shows for the case of the environmental background measured with FZK detector that the distribution of counts does, indeed, perfectly follow $1/\sqrt{E}$ trend.

In the end, we may even find the more general from of equation (C.9). Starting from the fully relativistic time-energy correlation:

$$E = mc^2\left(\frac{1}{\sqrt{1-\frac{L^2}{c^2t^2}}} - 1\right) \qquad \Rightarrow \qquad t = \frac{L}{c}\frac{1+E/mc^2}{\sqrt{(E/mc^2)^2+2E/mc^2}} \tag{C.10}$$

and calculating the corresponding derivative:

$$\left|\frac{\mathrm{d}t}{\mathrm{d}E}\right| = \frac{L\sqrt{m}}{\sqrt{[E(2+E/mc^2)]^3}} \tag{C.11}$$

we are left with:

$$p_{\log}(E) = \frac{CL\sqrt{m}}{\sqrt{E\,(2+E/mc^2)^3}} \tag{C.12}$$

However, below 1 MeV, where the capture data from n_TOF are analysed, the difference between (C.9) and (C.12) is perfectly negligible.

D Logarithmic histogramming

Let us assume we need to create a histogram with bins equally distributed over logarithmically scaled x-axis. For a histogram covering the range from $x_{\min}$ to $x_{\max}$, a bin width Δ is then equal:

$$\Delta = \frac{\log_a x_{\max} - \log_a x_{\min}}{\mathrm{BINS}} = \frac{\log_a \left(\frac{x_{\max}}{x_{\min}}\right)}{\mathrm{BINS}} \tag{D.1}$$

with BINS denoting the total number of bins, while allowing for an arbitrary basis a of a logarithmic scale. The bin boundaries $\{x_i\ ;\ i = 0, \ldots, \mathrm{BINS}\}$ are to be calculated as:

$$\log_a x_i = \log_a x_{\min} + i\Delta \tag{D.2}$$

For the moment, let us observe the general definition for a mean value $F_{[A,B]}$ of a function $f(x)$ averaged over interval $x \in [A, B]$:

$$F_{[A,B]} = \frac{1}{B-A}\int_A^B f(x)\mathrm{d}x \tag{D.3}$$

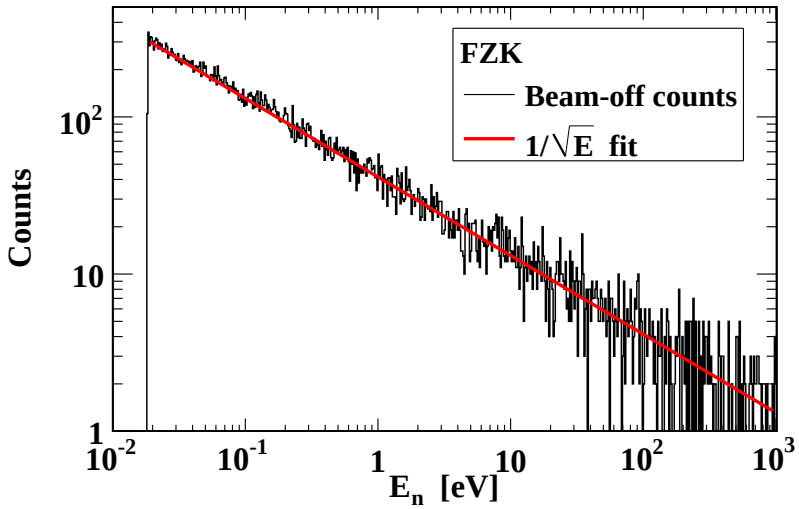

Figure C.1 — Environmental background measured with FZK detector. The histogram bins are equally distributed over the logarithmic scale.

Filling the histogram with discrete entries distributed according to the $f(x)$, one would expect – within the range of a single bin – to reconstruct an integral term from the right side of (D.3), as an area below $f(x)$. Therefore, the content of an i-th bin extending from x_{i-i} to x_i, i.e. its height $H_{[x_{i-1},x_i]}$ should equal:

$$H_{[x_{i-1},x_i]} = (x_i - x_{i-1})F_{[x_{i-1},x_i]} \tag{D.4}$$

For bins, i.e. averaging intervals uniformly distributed over logarithmic scale, from (D.2) follows:

$$\begin{aligned} x_{i-1} &= x_{\min}a^{(i-1)\Delta} = x_{\min}\left(\tfrac{x_{\max}}{x_{\min}}\right)^{\frac{i-1}{\mathrm{BINS}}} \\ x_i &= x_{\min}a^{i\Delta} = x_{\min}\left(\tfrac{x_{\max}}{x_{\min}}\right)^{\frac{i}{\mathrm{BINS}}} \end{aligned} \tag{D.5}$$

If we choose to parameterize the terms from (D.5) by an i-th bin central value X_i, which is within logarithmic scale naturally obtained as a geometric mean:

$$X_i \equiv \sqrt{x_{i-1}x_i} = x_{\min}a^{(i-1/2)\Delta} \tag{D.6}$$

then both more symmetric notation:

$$\begin{aligned} x_{i-1} &= X_i a^{-\Delta/2} \\ x_i &= X_i a^{\Delta/2} \end{aligned} \tag{D.7}$$

and more convenient parameterizations $F_\Delta(X_i)$ and $H_\Delta(X_i)$ of an aforementioned average and bin height:

$$\begin{aligned} F_\Delta(X_i) &\equiv F_{[x_{i-1},x_i]} \\ H_\Delta(X_i) &\equiv H_{[x_{i-1},x_i]} \end{aligned} \tag{D.8}$$

may be achieved. Entering (D.7) into (D.8) – or, equivalently, (D.4) – yields:

$$H_\Delta(X_i) = X_i\left(a^{\Delta/2} - a^{-\Delta/2}\right)F_\Delta(X_i) \tag{D.9}$$

For a large number of bins, i.e. sufficiently small Δ, exponential terms may be expanded as:

$$a^{\pm\Delta/2} = e^{\pm \ln a\cdot\Delta/2} \approx 1 \pm \ln a \cdot \tfrac{\Delta}{2} \tag{D.10}$$

leaving:

$$H_\Delta(X_i) = (X_i\Delta\ln a)\cdot F_\Delta(X_i) \tag{D.11}$$

As for the term $\Delta\ln a$, with few simple manipulations its invariance with respect to the basis a is shown:

$$\Delta\ln a = \frac{\log_a\left(\frac{x_{\max}}{x_{\min}}\right)}{\mathrm{BINS}\cdot\log_a e} = \frac{\ln\left(\frac{x_{\max}}{x_{\min}}\right)}{\mathrm{BINS}} \tag{D.12}$$

Rewriting (D.11):

$$H_\Delta(X_i) = \frac{X_i\ln(\frac{x_{\max}}{x_{\min}})}{\mathrm{BINS}}F_\Delta(X_i) \tag{D.13}$$

two separate observations may be made. First, normalizing the entire histogram content, i.e. all the bins by an equal factor is to be performed as:

$$X_i \cdot F_\Delta(X_i) = \frac{\text{BINS}}{\ln(\frac{x_{\max}}{x_{\min}})} H_\Delta(X_i) \tag{D.14}$$

However, it may be noted that instead of the genuine mean $F_\Delta(X_i)$, on the left side of (D.14) remains the value locally amplified by X_i. Therefore, in order to obtain the true average $F_\Delta(X_i)$ indicating at the source distribution $f(x)$, additional correction for the local value of an i-th bin position X_i should be performed.

To justify a previous claim, a sample histogram was built, as shown in Fig. D.1. All the bins were made of equal width within the logarithmic scale, in a manner prescribed by (D.2). As a next step the histogram was filled with 10^6 randomly generated entries following the uniform distribution $f(x) = 1$. As is clearly evident from Fig. D.1, the suspected increase in height for wider bins was confirmed. Finally, the histogram content was manually scaled by the varying factor $1/X_i$, recovering the original distribution $f(x) = 1$.

Returning to the integral from (D.3), it may be shown that the amplification by the factor X_i in (D.14) should not at all be surprising. If we consider that filling the logarithmically scaled histogram corresponds to integrating $f(x)$ over logarithmic scale, inverting the logarithmic derivative:

$$\frac{\mathrm{d}(\log_a x)}{\mathrm{d}x} = \frac{1}{x \ln a} \quad \Rightarrow \quad \mathrm{d}x = x \ln a \cdot \mathrm{d}(\log_a x) \tag{D.15}$$

directly indicates at the origin of the multiplicative X_i term:

$$\int_A^B f(x)\mathrm{d}x = \ln a \int_{\log_a A}^{\log_a B} x f(x) \cdot \mathrm{d}(\log_a x) \tag{D.16}$$

Evidently, it is a consequence of an integration kernel itself being made $xf(x)$ within logarithmically transformed scale.

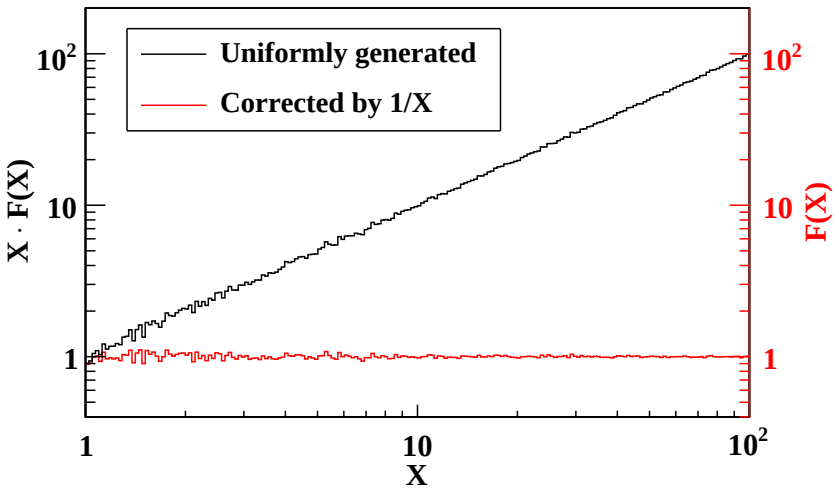

Figure D.1 — Artificially created histogram with bins equally distributed over the logarithmic scale, increasing in absolute width toward higher values of X. The histogram was filled with 10^6 uniformly generated entries, yielding a linearly increasing form. After scaling each bin content by a local value of $1/X$, original uniform distribution $f(x) = 1$ was recovered.

E Random sampling

We will describe a method for sampling an arbitrary distribution, as adopted for sampling the neutron flux within GEANT4 simulations. Let us consider a histogrammed distribution with the total number of bins N. The content of each bin is ϕ_n ($n = 1, ..., N$). There are $N + 1$ bin bounds E_m ($m = 0, ..., N$) to this histogram. If we fill the histogram single count at the time without correcting for the bin widths, then the content of a given bin is proportional to the true probability for having a count. Therefore, it is our goal to construct a cumulative distribution $F(E)$ such that its parts F_n – each defined over the n-th bin – satisfy the following conditions:

$$\begin{aligned} F_1(E_0) &= 0 \\ F_n(E_n) &= F_{n+1}(E_n) \\ F_N(E_N) &= 1 \end{aligned} \tag{E.1}$$

The values of the cumulative distribution at the (upper) bin bounds are simply constructed as:

$$F_n(E_n) = \frac{\sum_{i=1}^{n} \phi_i}{\sum_{i=1}^{N} \phi_i} \tag{E.2}$$

Along the span of the given bin we apply a linear approximation to $F_n(E)$:

$$F_n(E) = a_n E + b_n \tag{E.3}$$

Leading coefficients a_n are easy to find:

$$a_n = \frac{F_n(E_n) - F_n(E_{n-1})}{E_n - E_{n-1}} = \frac{1}{\sum_{i=1}^{N} \phi_i} \cdot \frac{\phi_n}{E_n - E_{n-1}} \tag{E.4}$$

from where the free coefficients b_n also follow:

$$b_n = F_n(E_n) - a_n E_n = \frac{1}{\sum_{i=1}^{N} \phi_i} \left(\sum_{i=1}^{n} \phi_i - \frac{E_n}{E_n - E_{n-1}} \phi_n \right) \tag{E.5}$$

Finally, $F(E)$ is defined by parts as:

$$F(E) = \begin{cases} F_1(E) & ; \; E \in [E_0, E_1] \\ \vdots & \\ F_n(E) & ; \; E \in [E_{n-1}, E_n] \\ \vdots & \\ F_N(E) & ; \; E \in [E_{N-1}, E_N] \end{cases} \tag{E.6}$$

If the values of the cumulative distribution $F(E)$ are generated uniformly, as the random variable x:

$$F(E) = x \in [0, 1] \tag{E.7}$$

then the argument E is generated following the distribution $F(E)$. In order to obtain these randomly generated arguments, one only needs to calculate the inverse:

$$E = F^{-1}(x) \tag{E.8}$$

F Randomization

The following is the description of the procedure used for a construction of a new sequence of random numbers starting from an original sequence generated by GEANT4, which is the same for every simulation run. First, the integer number T is determined from the starting time of the simulation. Then the seed S is constructed as the remainder (modulo operation) after division by the preselected integer number N:

$$S = T \bmod N \tag{F.1}$$

Then the uniform random numbers R from the interval $[0, 1\rangle$ are generated by GEANT4. The sequence of these numbers is same for every run. From R the new random number X is constructed by keeping only the fractional part of the product SR:

$$X = SR - \lfloor SR \rfloor \tag{F.2}$$

Here $\lfloor \cdot \rfloor$ denotes the so called *floor* function – the largest integer not greater than the argument. Newly randomized numbers X also follow the uniform distribution and, by construction, are limited to the interval $[0, 1\rangle$. Care must be taken in selecting the number N. Since numbers T increase periodically (every second), N must be large enough to provide the sufficiently long time interval for reseting the seed S. Evidently, S will reset every N seconds. On the other hand, due to the finite numerical precision of the numerical types from C++ – e.g. 16 decimal places in case of *double* – the fractional part of the product SR will be severely truncated for excessively large N. Therefore, the value $N = 10^6$ was selected, providing the period of 11.6 days for reseting the seed S, while retaining the precision of 10 decimal places.

G Pulsing emulation

In order to emulate the pulsing effect of the n_TOF neutron beam, the Poisson distribution $P_\lambda(x)$ of the "quantized" time intervals $t_n = (1.2\,\mathrm{s})x_n$ between the two consecutive pulses was assumed. The Poisson occurrence x_n of pulses is then simulated:

$$t_N = (1.2\,\mathrm{s}) \cdot \sum_{n=1}^{N} x_n \tag{G.1}$$

until the total sum t_N of accumulated time intervals exceeds the true time of flight ToF_0 of a given event. The next-to-last value of the sum – therefore, the greatest value t_N still less than ToF_0:

$$T = t_N \quad \text{for maximal } N \text{ such that} \quad t_N \leq \mathrm{ToF}_0 \tag{G.2}$$

is taken as the total time interval T truncated by the arrival of the latest neutron bunch, preceding the detection event. Subtracting this sum from ToF_0:

$$\mathrm{ToF} = \mathrm{ToF}_0 - T \tag{G.3}$$

yields the corresponding time of flight ToF as it would have been measured during the experiment. A special consideration regards the value λ adopted for parameterizing the Poisson distribution. Recalling that the mean interval between the pulses is 2.5 s,

at first we might be tempted to identify it with $\lambda = 2.5\,\mathrm{s}/1.2\,\mathrm{s} \approx 2.1$, since for a pure Poisson distribution λ exactly corresponds to its mean value. However, for our purposes the term $x = 0$ does not hold a physical meaning, since it implies the two separate pulses coming simultaneously. Therefore, the Poisson distribution $P_\lambda(x)$ we are concerned with is the truncated one:

$$P_\lambda(x) = \begin{cases} 0 & ;\ x = 0 \\ \dfrac{\lambda^x e^{-\lambda}}{x!} & ;\ x > 0 \end{cases} \tag{G.4}$$

giving rise to the following mean value $\langle x \rangle$:

$$\langle x \rangle = \frac{\sum_{x=0}^{\infty} x P_\lambda(x)}{\sum_{x=0}^{\infty} P_\lambda(x)} = \frac{\lambda}{1 - e^{-\lambda}} \tag{G.5}$$

From here follows the value for λ:

$$\langle x \rangle = 2.5\,\mathrm{s}/1.2\,\mathrm{s} \approx 2.1 \qquad \Rightarrow \qquad \lambda \approx 1.7 \tag{G.6}$$

which was used for emulating the neutron beam pulses.

H Radioactive decay counts

We will show how the radioactive decay spectrum looks when plotted in terms of energy calculated from a time of flight, since this procedure is applied to all such counts if they are found among the capture measurements. Let us consider a normalized radioactive decay distribution:

$$p(t) = \frac{1}{\tau} e^{-t/\tau} \tag{H.1}$$

Just as in (C.3) (Appendix C), the probability invariance dictates:

$$p(E) = p(t) \left| \frac{\mathrm{d}t}{\mathrm{d}E} \right| \tag{H.2}$$

Following the procedure analogous to the one yielding the result from (C.9), we obtain in this case:

$$p_{\log}(E) = \frac{\varepsilon}{2} \cdot \frac{e^{-\varepsilon/\sqrt{E}}}{\sqrt{E}} \tag{H.3}$$

where we have introduced:

$$\varepsilon \equiv \frac{L}{\tau} \sqrt{\frac{m}{2}} \tag{H.4}$$

Figure H.1 shows an example of β-decay counts from $^{12}\mathrm{C}(n, p)^{12}\mathrm{B}$ reaction, measured with FZK detector. All the background components – empty-frame, environmental and neutron background – have been subtracted. The fit to a distribution (H.3) is also shown.

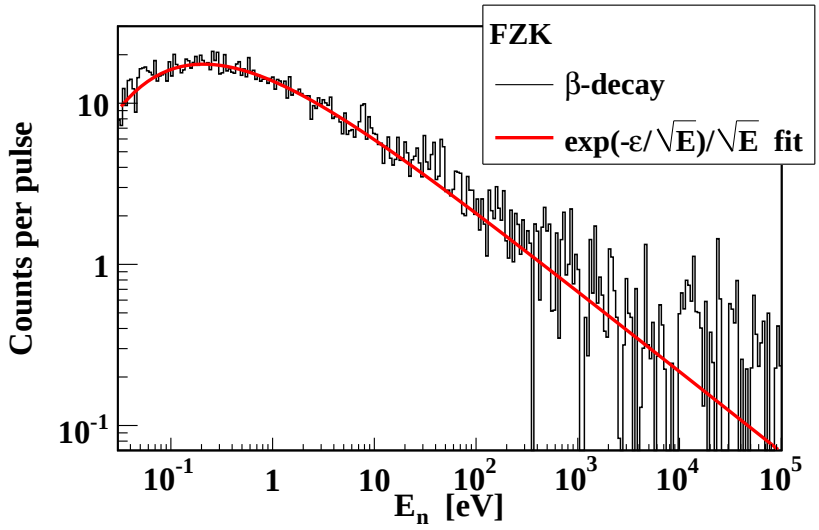

Figure H.1 — β-decay spectrum of ^{12}B, as measured with FZK detector, corrected for all the background components.

6 Prošireni sažetak

6.1 Uvod

6.1.1 Motivacija za mjerenje udarnoga presjeka za uhvat neutrona na izotopu ^{58}Ni

Precizno poznavanje udarnog presjeka za radijativni uhvat neutrona na izotopu ^{58}Ni nalazi primjenu u okvirima nuklearne astrofizike i nuklearnih tehnologija. Kao bitna sastavnica građevnih materijala naširoko korištenih u nuklearnim reaktorima, po ozračivanju neutronima ^{58}Ni doprinosi opasnosti od dugotrajnog zračenja stvaranjem dugo-živućeg izotopa ^{59}Ni s vremenom poluživota od 7.5×10^4 godina. Uz to, niz reakcija $^{58}\mathrm{Ni}(n,\gamma)^{59}\mathrm{Ni}(n,\alpha)^{56}\mathrm{Fe}$ kojim se stvara helij u nehrđajućim čelicima, doprinosi i oštećenju građevnih materijala [1, 2].

Detaljni podaci o uhvatu neutrona nezaobilazni su u modeliranju zvjezdane nukleosinteze elemenata težih od željeza. Dok su elementi do željeza stvoreni reakcijama nabijenih čestica – neki od njih primordijalnom nukleosintezom nakon Velikog Praska, neki kasnijom zvjezdanom nukleosintezom nakon stvaranja prvih zvijezda – za stvaranje elemenata u masenom području iznad željeza izravno ili posredno su odgovorne reakcije izazvane neutronima, posebice uhvati neutrona koji su glavni pokretački mehanizam procesa sporog uhvata neutrona (s-procesa) kojim je stvorena približno polovica ukupne količine elemenata težih od željeza [3]. Druga polovica ponajvećim dijelom je stvorena procesom brzog uhvata neutrona (r-procesom), svojstvenim zvjezdanim okruženjima krajnje visokog toka neutrona, poput (super)nova ili sudara neutronskih zvijezda. Stoga težnja za temeljnim razumijevanjem ovih procesa nije ništa manje od težnje za razotkrivanjem porijekla tvari u svemiru. I dok ovaj poduhvat zaokuplja maštu čovječanstva od njegova nastanka, razotkrivanje ove kozmičke tajne omogućeno je tek u 20. stoljeću razvojem nuklearne fizike. Napretkom modela s- i r-procesa – koji su tijekom vremena dovedeni u sve bolje slaganje s eksperimentalnim opažanjima, postupno gradeći dosljednu i sveobuhvatnu sliku zvjezdane evolucije – uočeno je da detaljni podaci o uhvatu neutrona na širokom rasponu izotopa imaju ključan utjecaj na konačne rezultate modela i njihovu pouzdanost. I dok su eksperimentalni podaci o uhvatu neutrona svakako poželjni za sve izotope stvorene u prirodi – imajući, u najmanju ruku, temeljnu znanstvenu vrijednost – podaci za neke od njih od iznimne su važnosti. Među tim probranim izotopima nalaze se tzv. točke grananja s-procesa – β-nestabilni nuklidi vremena života usporedivog sa srednjim vremenom između uzastopnih uhvata neutrona u zvjezdanom mediju. Slika 6.1.1 ilustrira put s-procesa duž karte nuklida počevši od primarnog sjemena ^{56}Fe, pokazujući da s-proces napreduje uhvatima neutrona i β-raspadima. Međutim, tijek s-procesa

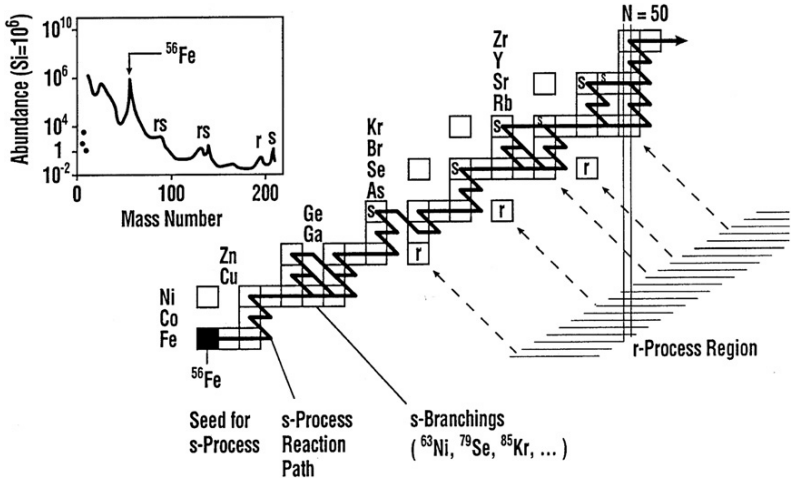

Slika 6.1.1 — Put *s*-procesa duž karte nuklida, s početkom u primarnom sjemenu ^{56}Fe (preuzeto iz Reference [4]).

posebno je osjetljiv na točke grananja u kojima se usporedive vjerojatnosti ovih dvaju ishoda natječu i potpomažu različite puteve nukeosinteze, određujući njene daljnje korake. Jedna od takvih točka grananja, iz grupe nikla, je ^{63}Ni, čiji je udarni presjek za uhvat neutrona po prvi put mjeren [5, 6] na n_TOF postrojenju *neutronskog vremena proleta* u CERN-u.

U okviru nuklearne astrofizike ^{58}Ni bitna je sastavnica *s*-procesa u kojem sudjeluje kao sekundarno sjeme mnogo niže zastupljenosti (4.3% [7]) od one primarnog sjemena ^{56}Fe. U sklopu zvjezdane evolucije *s*-proces odvija se tijekom gorenja helija i ugljika, na temperaturama između 0.1 i 1 GK (kT = 8 do 90 keV) [4]. Dvije su osnovne komponente koje doprinose ukupnoj zastupljenosti elemenata između željeza i aktinida u Sunčevom sustavu – *glavna* i *slaba* komponenta – potpomognute dodatnim doprinosom *snažne* komponente koja se veže uz porijeklo Pb i Bi. Glavna komponenta *s*-procesa odvija se u zvijezdama manje mase (1-5 $M_\odot$) iz asimptotske grane divova (tzv. AGB-zvijezde) te proizvodi gotovo sav *s*-procesom nastao materijal iznad $A = 90$. Ovaj zaključak može se izvesti temeljem usporedbe eksperimentalnih opažanja i rezultata glavne komponente *s*-procesa za izotope proizvedene isključivo *s*-procesom. S obzirom da AGB-zvijezde manje mase ne mogu pokrenuti gorenje inertne C/O sredice, *s*-proces odvija se u gorućoj He-ljusci. Zbog miješanja materijala koje prati termalne pulseve tijekom zvijezdane evolucije, ^{13}C izotop proizvodi se se $^{12}C(p,\gamma)^{13}N(\beta^+\nu)^{13}C$ reakcijom, snabdjevajući gorivom $^{13}C(\alpha,n)^{16}O$ reakciju koja igra ulogu osnovnog izvora neutrona. U kasnijoj fazi glavnog *s*-procesa javlja se marginalni doprinos $^{22}Ne(\alpha,n)^{25}Mg$ reakcije proizvodnji neutrona. Slabu komponentu *s*-procesa, koja se odvija u masivnim ($>8M_\odot$) zvijezdama i tijekom gorenja helija i tijekom gorenja ugljika – neutronima ponajviše opskrbljuje upravo $^{22}Ne(\alpha,n)^{25}Mg$ reakcija. Sam izotop ^{22}Na proizveden je $^{14}N(\alpha,n)^{18}F(\beta^+\nu)^{18}O(\alpha,n)^{22}Ne$ reakcijom koja kreće od ^{14}N sjemena preostalog iz ranijeg CNO ciklusa aktivnog tijekom izgaranja vodika. Zajednička predviđanja modela glavne i slabe komponente *s*-procesa uspješno reproduciraju opažene zatupljenosti elemenata u Sunčevom sustavu, i ispod i iznad $A = 90$. Izotop ^{58}Ni – koji čini 68% prirodnog nikla – sekundarno je sjeme za nukleosintezu *s*-procesom. Poznato je da nikal u Sunčevom sustavu potječe i od supernova s urušenjem sredice [8] i od termonuklearnih supernova tipa Ia [9]. Pri tome spektroskopska opažanja ukazuju da je približno 30% njegova udjela proizvedeno urušenjem sredice masivnih zvijezda, dok je 70% proizvedeno termonuklearnim supernovama [10].

Za izračun brzine odvijanja astrofizičkih procesa potrebno je poznavati energijsku ovisnost udarnog presjeka za uhvat neutrona sve do energije neutrona od nekoliko stotina keV. Nekoliko je eksperimentalnih skupova podataka za ^{58}Ni(n,γ) reakciju dostupno u EXFOR bazi podataka (tzv. Bazi eksperimentalnih nuklearnih podataka) [11], no svega nekoliko ih pokriva pun raspon energija od astrofizičkog značaja. Guberova grupa s ORELA postrojenja (elektronski linearni akcelerator u Oak Ridgeu) nedavno je provela mjerenje ^{58}Ni(n,γ) reakcije [12] te analizom došla do globalno manje vrijednosti udarnoga presjeka nego što je bilo prihvaćeno u ranijim bazama izvrjednjenih podataka koje uključuju i ENDF/B-VII.0 [13]. Među mjerenjima koja su utjecala na ENDF/B-VII.0 bazu je ono koju je provela Pereyjeva grupa [14] koristeći C_6F_6 detektore, čija je neutronska osjetljivost viša od osjetljivosti C_6D_6 detektora koje je koristila Guberova grupa. Nedavno mjerenje Rugelove grupe [15] također ukazuje na globalno smanjenje udarnoga presjeka za uhvat neutrona na izotopu ^{58}Ni, s obzirom na ranije prihvaćene vrijednosti. Uzevši u obzir ove rezultate – zajedno s transmisijskim mjerenjem visoke rezolucije koje je provela Bruseganova grupa [16] i novom termalnom vrijednošću koju je odredila Ramanova grupa [17] – udarni presjek ^{58}Ni(n,γ) reakcije preinačen je u ENDF/B-VII.1 verziji baze podataka [18]. Cilj novog mjerenja visoke rezolucije s n_TOF postrojenja [19] je razjasniti razlike između ranijih eksperimentalnih podataka i usmjeriti buduća izvrjednjenja udranog presjeka za uhvat neutrona na izotopu ^{58}Ni.

6.1.2 Neutronska međudjelovanja

Iako je uhvat neutrona reakcija od središnje važnosti u uvome radu, za uspješan razvoj i izvedbu neutronskih eksperimenata visoke preciznosti nužno je biti dobro upoznat sa svim vrstama neutronskih međudjelovanja. Ovo je, naravno, uvjetovano činjenicom da konstrukcija detektora i izbor ispravnih eksperimentalnih postupaka moraju biti podređeni zahtjevima i izazovima fizikalnih procesa aktivnih u temeljima i pozadini eksperimenta. Pored uhvata neutrona, u ovome radu značajnima će se pokazati i elastično i neelastično raspršenje neutrona kao izvor velikog dijela neutronima izazvanih pozadinskih događaja koje ćemo detaljno proučiti. Štoviše, izdvojena neelastična (n,p) reakcija pokazat će se ključnom u mjerenjima s uzorkom prirodnog ugljika ($^{\text{nat}}$C). Stoga u sljedećem dijelu nudimo kratak pregled osnovnih svojstava neutronima izazvanih reakcija.

U principu, neutroni su podložni svim četirima temeljnim međudjelovanjima – snažnom i slabom nuklearnom, elektromagnetskom i gravitacijskom. Snažna nuklearna međudjelovanja su najšire korištena u praktičnim primjena ovog relativno dugoživućeg hadrona bez električnog naboja. Po samoj svojoj prirodi, neutroni su također podložni slabom nuklearnom međudjelovanju. Najbolji primjer je raspad neutrona – bilo raspad slobodnog neutrona s poluživotom od približno 10 minuta, bilo β-raspad neutrona vezanih unutar atomskih jezgara. Iako su neutroni u cjelini električki neutralni, imaju magnetski moment, a također pokazuju i prostornu raspodjelu naboja zahvaljujući svojoj složenoj kvarkovskoj strukturi. Prema tome, elektromagnetska međudjelovanja su u potpunosti unutar domene neutronske fizike. Konačno, gravitacijska međudjelovanja su neizbježna za čestice konačne mase. Pri tome neutronske zvijezde predstavljaju najpoznatiji primjer gravitacijskih efekata vezanih uz neutrone.

Neutronska međudjelovanja s tvari mogu se podijeliti u četiri osnovne skupine:

- *Elastično raspršenje neutrona.* Tijekom elastičnog raspršenja reakcijski partner – poput atomske jezgre – nije pobuđen u više kvantno stanje prolaskom neutrona. No prijenos energije svakako je prisutan jer je nužan za kinematički odboj svih čestica iz reakcije. Jedna od osnovnih primjena elastičnog raspršenja je neutronska difrakcija – metoda proučavanja atomske i magnetske strukture materijala korištenjem niskoenergijskih (termalnih ili hladnih) neutrona. Drugi primjer je neutronska moderacija, s obzirom da je elastično raspršenje najvažniji mehanizam gubitka energije za neutrone čija je energija reda veličine MeV-a.
- *Neelastično raspršenje neutrona.* Tijekom neelastičnog raspršenja reakcijski partner ostaje pobuđen i/ili mijenja svoju čestičnu strukturu. Prema tome, reakcije tipa (n,p), (n,d), (n,t), (n,α) (...) pa čak i produkciju visokoenergijskih hadronskih pljuskova svrstavamo u ovu kategoriju. U praktičnim primjenama neelastično raspršenje također nalazi mjesto u neutronskoj moderaciji i istraživanjima svojstava čvrstih tvari.
- *Radijativni uhvat neutrona.* Tijekom (n,γ) reakcije jezgra apsorbira upadni neutron te ostaje u visokopobuđenom stanju iznad energije odvajanja neutrona. Deekscitacija se odvija praktički trenutno emisijom niza (kaskade) γ-zraka, koji je određen strukturom nuklearnih stanja. Podaci o uhvatima neutrona su neophodni za nuklearnu astrofiziku te također nalaze primjenu u izgradnji i razvoju nuklearnih reaktora i akceleratorskih postrojenja. Naime, dostupni podaci utječu na izbor strukturnih materijala, s ciljem poboljšanja zaštite od zračenja u takvim postrojenjima. Nadalje, u nuklearnim reaktorima nužno je osigurati da se u reaktorsku jezgru ne unesu nepoznati neutronski otrovi koji bi mogli usporiti ili čak zaustaviti nuklearnu lančanu reakciju kojom se proizvodi korisna energija.
- *Neutronima izazvana fisija.* Upadni neutron destabilizira tešku jezgru, izazivajući njenu fisiju – cijepanje na lakše fragmente koji često uključuju i sekundarne neutrone. Neutronima izazvana fisija zauzima značajno mjesto u modernoj proizvodnji energije.

Sve navedene reakcije obilježene su pripadnim, energijski ovisnim udarnim presjecima: $\sigma_{\text{elastično}}$, $\sigma_{\text{neelastično}}$, σ_{uhvat}, σ_{fisija}. Ukupni udarni presjek σ_{ukupno}, koji mjeri vjerojatnost da dođe bilo do koje reakcije u danome materijalu, dan je zbrojem pojedinih komponenata:

$$\sigma_{\text{ukupno}} = \sigma_{\text{elastično}} + \sigma_{\text{neelastično}} + \sigma_{\text{uhvat}} + \sigma_{\text{fisija}} \tag{6.1.1}$$

6.1.3 Postrojenja za proizvodnju neutrona

Nekoliko je većih postrojenja za proizvodnju neutrona u radu diljem svijeta. Takva postrojenja posebno su prilagođena mjerenjima reakcija izazvanih neutronima koje su od ključne važnosti u raznim područjima temeljnih znanstvenih istraživanja, kao i u primjenjenim znanostima [24, 25]. U temeljnim znanostima detaljni podaci o neutronskim reakcijama bitni su za nuklearnu astrofiziku, odnosno za modeliranje zvjezdane nukleosinteze [4, 26]. Nadalje, nazamjenjivi su u proučavanju neutronima izazvanog slamanja simetrije [27, 28], u proučavanju energija odvajanja neutrona, pobuđenih stanja iznad energije odvajanja neutrona, gustoće nuklearnih stanja [29–31] itd. U primjenjenim znanostima ovi podaci igraju značajnu ulogu u zaštiti od zračenja, dozimetriji, nuklearnoj medicini te, povrh svega, u proizvodnji energije. Trenutno,

proizvodnja nuklearne energije oslanja se na nuklearnu fisiju te je podložna problemima niske učinkovitosti, postupnog iscrpljivanja zaliha urana i proizvodnje radioaktivnog nuklearnog otpada. Zbog toga se istražuju zamjenske tehnologije, među kojima najznačajnije mjesto zauzimaju akceleratorima tjerani sustavi i brzi nuklearni reaktori IV. generacije [25]. U sklopu akceleratorima tjeranih sustava nuklearne reakcije održavaju su neutronskim ozračivanjem nuklearnog goriva u potkritičnim uvjetima. Sigurnosne prednosti ovakvog sustava su očite. Štoviše, mogu se izabrati goriva za kojima nakon trošenja ostaje nuklearni otpad mnogo kraćeg vremena života (stotine godina) od onog koji se trenutno proizvodi (milijuni godina za uranov otpad). Nuklearni reaktori IV. generacije, pak, temelje se na učinkovitijem izgaranju transuranijskih aktinida, čime proizvode više energije i manje nuklearnog otpada. Za razvoj akceleratorima tjeranih sustava i/ili reaktora IV. generacije potrebni su novi visokoprecizni podaci o neutronskim reakcijama – posebice o uhvatu, fisiji i neelastičnim reakcijama na aktinidima.

Pored n_TOF postrojenja neutronskog vremena proleta s CERN-a, opisanog u Poglavlju 6.2, veća postrojenja za proizvodnju neutrona koja djeluju u svijetu uključuju:

- GELINA – Elektronski Linearni Akcelerator u Geelu (Geel, Belgija) [32]
- ORELA – Elektronski Linearni Akcelerator u Oak Ridgeu (Oak Ridge, Tennessee) [33]
- SNS – Spalacijski Izvor Neutrona u Oak Ridgeu (Oak Ridge, Tennessee) [34]
- LANSCE – Znanstveni Centar za Neutronska Istraživanja u Los Alamosu (Los Alamos, New Mexico) [35]
- J-PARC – Japanski Istraživački Centar s Protonskim Akceleratorom (Tokai, Japan) [36]
- Gaerttnerov LINAC – Gaerttnerov Laboratorij s Linearnim Akceleratorom (Troy, New York) [37]
- IPNS – Intenzivni Pulsni Izvor Neutrona u Lemontu (Lemont, Illinois) [38]

Sva navedena postrojenja pulsni su izvori bijelih snopova neutrona. GELINA, ORELA i Gaerttnerov LINAC koriste elektronski akcelerator kako bi proizveli neutrone (γ, n) reakcijom, dok preostala postrojenja koriste protonski akcelerator, oslanjajući se na protonima izazvanu spalaciju. Visoke energije primarnog snopa čestica – koje se protežu od desetaka MeV za elektrone do 20 GeV za protone – čine ova postrojenja visoko učinkovitima u proizvodnji neutona. Nakon moderacije spektri neutrona pokrivaju nekoliko redova veličine u energiji – od termalnih energija do najmanje nekoliko desetaka MeV. Zbog intenzivnog γ-bljeska oslobođenog ozračivanjem mete za stvaranje neutrona mjerenja se moraju provoditi nakon podužeg puta proleta, kako bi detektori imali vremena oporaviti se od početnog pulsa izazvanog γ-bljeskom. Stoga se putevi proleta u uvim postrojenjima kreću od približno 10 m (npr. na LANSCE postrojenju) do 400 m (na GELINA postrojenju). Na manjim akceleratorskim postrojenjima neutroni se mogu proizvesti nuklearnim reakcijama poput ^{7}Li$(p, n)^7$Be. Iako se intenzitet ovakvih izvora ne može mjeriti s onim velikih postrojenja, manji postavi nude nižu razinu pozadinskih događaja te omogućuju korištenje kraćih puteva proleta. Ovakvi eksperimentalni uvjeti posebno pogoduju aktivacijskim mjerenjima, koja nalaze moge praktične primjene [4]. Međutim, jedino postrojenja neutronskog vremena proleta omogućuju određivanje detaljnih parametara koji opisuju neutronima izazvane reakcije unutar širokog energijskog područja.

6.1.4 Eksperimentalne metode

Kalorimetri Potpune Apsorpcije čine jedan tip detektora korištenih za mjerenje neutronskih uhvata. Uobičajeno su sastavljeni od zasebnih BaF_2 kristala postavljeih u 4π prostornu konfiguraciju. Njihovo najzapaženije svojstvo je učinkovitost od gotovo 100% za detekciju reakcije uhvata. Sami BaF_2 kristali koriste se zbog visoke energijske rezolucije, niske razine pozadinskih događaja i vrlo brzog odaziva koji nudi izvrsnu vremensku rezoluciju pri obradi signala. Jedan takav postav sastavljen od BaF_2 kristala koristi se na n_TOF postrojenju [39]. Drugi primjer je detektor DANCE s LANSCE postrojenja [40], sastavljen od 160 kristala. Ovako visoka podjela omogućuje učinkovito odbacivanje pozadinskih događaja – temeljem multipliciteta aktiviranih kristala – i smanjenje toka podataka po pojedinom kristalu. Općenito, visoka detekcijska učinkovitost 4π detektora i sposobnost odbacivanja pozadinskih događaja omogućuju mjerenja na vrlo malenim i/ili radioaktivnim uzorcima koji izazivaju visoku razinu razinu pozadinskih događaja koje je potrebno potisnuti.

Unatoč mogućnosti potisnuća pozadinskih događaja izazvanih detekcijom nekoreliranih γ-zraka, Kalorimetri Potpune Apsorpcije osjetljivi su na pozadinu uzrokovanu raspršenim neutronima, što postaje problem kod mjerenja na uzorcima udarnog presjeka za raspršenje neutrona mnogo većeg od onog za njihov uhvat. Ovakvi pozadinski događaji donekle se mogu potisnuti okruživanjem uzorka štitom za apsorpciju neutrona, obogaćenim ^{7}Li [40, 41] ili ^{10}B [39] materijalom. Međutim, za nuklide čiji omjer udarnih presjeka za raspršenje i uhvat neutrona nadmašuje nekoliko redova veličine – poput nuklida s čarobnim brojem neutrona, tj. zatvorenom neutronskom ljuskom – veliki detektori više nisu najbolji izbor u mjerenju uhvata neutrona. Kao odgovor na ovaj izazov razvijeni su Moxon-Rae detektori niske osjetljivosti na raspršene neutrone i niske učinkovitosti za detekciju γ-zraka [42]. Nužan preduvjet za korištenje ovakvih detektora je osigurati da je detekcijska učinkovitost proporcionalna ukupnoj energiji oslobođenoj emitiranom kaskadom γ-zraka. Da bi se ostvario ovaj uvjet, potrebno je preinačiti odaziv detektora – npr., tijekom kasnije obrade podataka – na pojedine γ-zrake. Nadalje, zbog zahtjeva za niskom osjetljivošću na neutrone materijal Moxon-Rae detektora sastoji se od lakih izotopa niskog udarnog presjeka za uhvat neutrona (^{2}H, ^{12,13}C, ^{19}F) koji su, kao materijali za detekciju γ-zraka, podložni zanemarivom fotoelektričnom efektu. Stoga spektri deponiranih energija mjereni ovakvim detektorima ne pokazuju foto-vrhove, čime su dodatno otežani rekonstrukcija energije γ-zrake i njeno dovođenje u vezu s ukupnom energijom kaskade. Kao odgovor na ove izazove razvijena je metoda primjene težinske funkcije [43] kojom se tijekom obrade podataka manipulira detektiranim signalima primjenom odgovarajućih težinskih faktora. Na ovaj način detekcijska učinkovitost postaje proporcionalna ukupnoj energiji kaskade i neovisna o detaljima same kaskade. Metoda primjene težinske funkcije opisana je u Poglavlju 6.3.3.

Metoda primjene težinske funkcije u početku je ispitivana na podacima mjerenim C_6F_6 detektorima [43], za koje se ubrzo pokazalo da su podložni znatnim sistematskim nepouzdanostima [44]. Stoga su zamijenjeni C_6D_6 (deuterirani benzen) detektorima koji ostaju u upotrebi do današnjeg dana.

Izotop ^{58}Ni pripada skupini izotopa vrlo niskog omjera udarnih presjeka za uhvat i raspršenje neutrona. Stoga su za mjerenje njegova uhvata neutrona korištena dva C_6D_6 detektora, u skladu s iznesenim razmatranjima. Potrebno je naglasiti da raspršenje neutrona na ^{58}Ni stvara toliku razinu pozadinskih događaja da nije bilo dovoljno samo koristiti detektore najniže izvedive neutronske osjetljivosti, već je bilo potrebno provesti posebne simulacije neutronske pozadine kako bi se identificirao doprinos takvih događaja i odstranio iz ukupnosti mjerenja. Rezultati simulacija – praćeni mjerenim doprinosima pozadinskim događajima – predstavljaju prvu potpunu identifikaciju pozadinskih događaja u mjerenjima neutronskih uhvata s n_TOF postrojenja [45].

Poglavlje 6.2 ovoga rada opisuje opće značajke n_TOF postrojenja s CERN-a. Poglavlje 6.3 predstavlja analizu eksperimentalnih podataka za uhvat neutrona na izotopu ^{58}Ni i istražuje njihove rezultate. Poglavlje 6.4 detaljno opisuje GEANT4 simulacije neutronske pozadine, čiji su rezultati korišteni u analizi eksperimentalnih podataka. Konačno, Poglavlje 6.5 sažima najvažnije zaključke ovoga rada.

6.2 n_TOF postrojenje

6.2.1 CERN postrojenje

Postrojenje *neutronskog vremena proleta* n_TOF u CERN-u (Europska organizacija za nuklearna istraživanja [46]) djeluje od 2001. godine [47]. U osnovi, n_TOF je pulsni izvor neutrona na koji se nastavlja 200 m dugačak put proleta. Postrojenje je namijenjeno istraživanju neutronima izazvanih reakcija u rasponu energija od nekoliko meV do nekoliko GeV. Shema n_TOF postrojenja prikazana je Slikom 6.2.1.

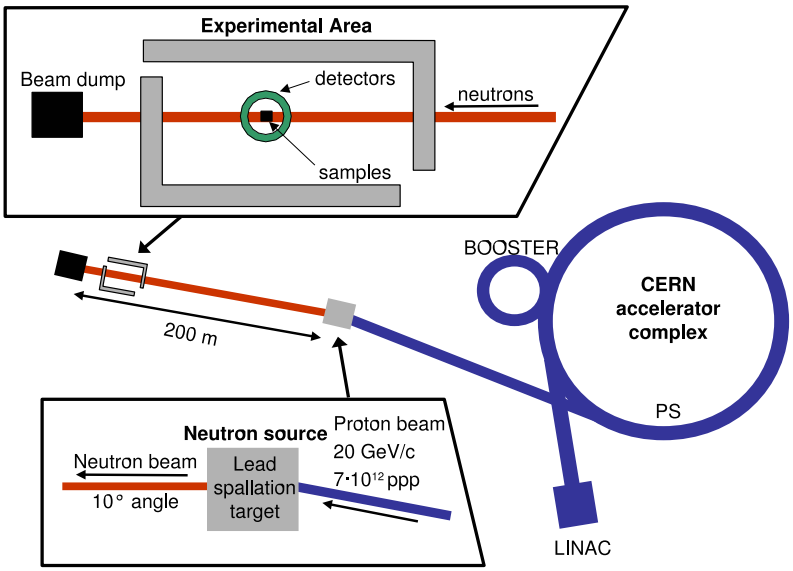

Slika 6.2.1 — Shema n_TOF postrojenja u sklopu CERN-a (preuzeto iz Reference [50]).

6.2.2 Proizvodnja neutrona

Na n_TOF postrojenju neutroni se proizode izlaganjem masivne olovne spalacijske mete – duljine 40 cm, promjera 60 cm – intenzivnom protonskom snopu iz Protonskog Sinkrotrona s CERN-a. Snop dovodi protone energije 20 GeV, radeći u pulsnome modu s peridom ponavljanja u višekratnicima od 1.2 s te širinom pulsa od 7 ns. Vrlo niska prosječna učestalost dovođenja pulseva od 0.4 Hz uklanja problem vremenskog preklapanja uzastopnih neutronskih pulseva te omogućuje učinkovito odvođenje topline, tj. hlađenje spalacijske mete. Raspodjela broja protona po pulsu (ppp) jasno pokazuje dvije komponente – zastupljeniju s prosječnim brojem protona od 8×10^{12} ppp te manje zastupljenu s prosječnim brojem od 3×10^{12} ppp. Nominalan broj dovedenih protona čini cjelokupan prosjek od 7×10^{12} ppp. Tijekom spalacije u olovnome bloku oslobađa se prosječno 300 neutrona po upadnome protonu, dajući prosječno 2×10^{15} neutrona po pulsu. Osim samog olovnog bloka, ispočetka brze neutrone usporavaju i 1 cm širok sloj vode iz rashladnog sustava te dodatan 4 cm širok sloj borirane vode. Konačni spektar neutrona pokriva 12 redova veličine u energiji, protežući se od termalnih energija (nekoliko meV) sve do nekoliko GeV-a. Korištenje borirane vode (H_2O + 1.28% H_3BO_3; maseni udjeli) kao neutronskog moderatora karakteristika je druge faze rada n_TOF postrojenja (n_TOF-Phase2) koja je započela 2008. godine, nakon nadogradnje spalacijske mete. Prva faza rada postrojenja (n_TOF-Phase1) trajala je od 2001. do 2004. godine, kada je umjesto borirane vode korištena demineralizirana voda, rezultirajući znatno višim tokom termalnih neutrona. Zahvaljujući $^{10}B(n, \alpha)$ reakciji visokog udarnog presjeka za apsorpciju neutrona, borirana voda potiskuje pretjeranu emisiju 2.2 MeV γ-zraka iz uhvata neutrona na vodiku, no još uvijek osiguravajući dovoljno intenzivnu termalnu komponentu. Odvraćanjem neutrona od $^1H(n, \gamma)$ reakcije, uhvat na izotopu ^{10}B pomaže u smanjenju intenziteta početnog γ-bljeska koji dopire do eksperimentalne prostorije i privremeno zasljepljuje C_6D_6 detektore prije dolaska svakog neutronskog snopa.

Evakuirani cjevovod nastavlja se na spalacijsku metu, vodeći prema eksperimentalnoj prostoriji odaljenoj približno 185 m. Čestice nastale spalacijom (neutroni, nabijene čestice, γ-zrake) koje nisu odaslane izravno u cjevovod zaustavljaju se masivnim betonskim zidovima te 3.5 m širokim željeznim štitom. Neutronski snop pročišćuje se od nabijenih čestica snažnim magnetom indukcije 1.5 T, udaljenim 145 m od spalacijske mete. Neutronski snop oblikuje se sustavom dvaju kolimatora – jednog na udaljenosti od 137 m, drugog na udaljenosti od 178 m. Otvor drugog kolimatora može se podesiti na 19 mm ili 80 mm, što dogovara tzv. *modu uhvata* ili *modu fisije*, respektivno. Uz boriranu vodu kao moderator, ukupan integrirani tok neutrona (do 1 GeV) na ulazu u eksperimentalnu prostoriju iznosi 5.5×10^5 neutrona po pulsu u modu uhvata, odnosno 1.2×10^7 neutrona po pulsu u u modu fisije. Mjerenje uhvata na ^{58}Ni provedeno je s drugim kolimatorom u modu uhvata. Cjevovod završava izvan eksperimentalne prostorije, gdje se neutronski snop učinkovito zaustavlja te se minimizira učinak unatrag raspršenih neutrona. Dodatni detalji o n_TOF postrojenju mogu se pronaći u Referencama [47, 50].

Tablica 6.1 — Popis detektora za mjerenje toka neutrona na n_TOF postrojenju. Navedene su reakcije koje pojedini detektori koriste, zajedno s njihovim energijskim rasponima koji su korišteni za određivanje jedinstvenog spektra neutronskog toka.

Detektor	Reakcija	Energijski raspon
SiMon	$^{6}\mathrm{Li}(n,t)$	30 meV – 100 keV
MGAS	$^{10}\mathrm{B}(n,\alpha)$	30 meV – 100 keV
	$^{235}\mathrm{U}(n,f)$	100 keV – 1 MeV
PTB	$^{235}\mathrm{U}(n,f)$	30 meV – 10 MeV
PPAC	$^{235}\mathrm{U}(n,f)$	10 MeV – 1 GeV

6.2.3 Mjerenje toka neutrona

Tok neutrona na n_TOF postrojenju mjeri se četirima različitim detektorima koji koriste različite neutronima izazvane reakcije:

- SiMon – monitor neutronskog snopa temeljen na siliciju [52]
- MGAS – Micromegas plinski detektor [53, 54]
- PTB – baždarena fisijska komora s Physikalisch Technische Bundesanstalt [55]
- PPAC – skup lavinskih brojača s paralelnim pločama [56]

Korištene reakcije uključuju $^{6}\mathrm{Li}(n,t)$, $^{10}\mathrm{B}(n,\alpha)$ i $^{235}\mathrm{U}(n,f)$. Svaka od njih predstavlja prihvaćen standard udarnog presjeka u ograničenom energijskom području. Stoga su mjerenja različitih detektora preklopljena u svrhu određivanja jedinstvenog spektra neutronskoga toka koji pokriva energijski raspon od termalnih energija sve do 1 GeV. Tablica 6.1 navodi reakcije koje koriste pojedini detektori i njihove energijske raspone koji su prihvaćeni za pouzdano određivanje neutronskoga toka. Dodatni detalji o mjerenju toka neutrona na n_TOF postrojenju mogu se pronaći u Referencama [50, 57].

Dok su mjerenja neutronskog toka dostupna do 1 GeV, posebne FLUKA [58–60] simulacije korištene su kako bi se spektar toka proširio do 17 GeV, zahvaljujući izvrsnom slaganju eksperimentalnih i simuliranih rezultata ispod 1 GeV (vidjeti

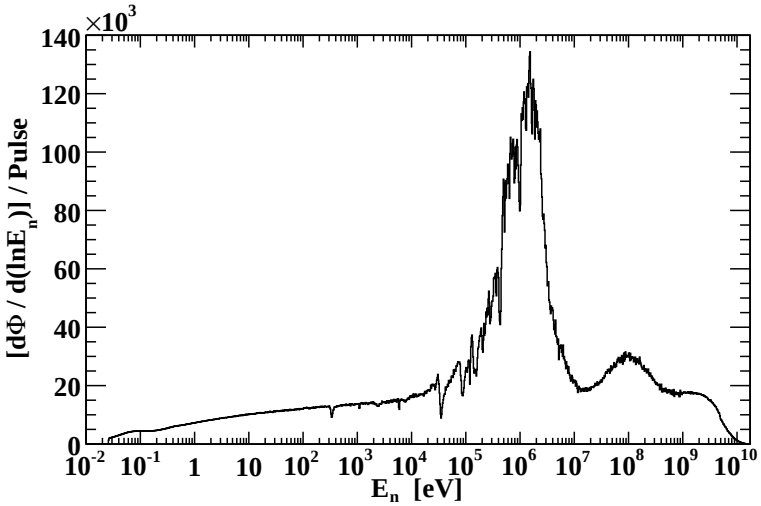

Slika 6.2.2 — Energijska ovisnost toka neutrona s n_TOF postrojenja. Eksperimentalni podaci dostupni su do 1 GeV, dok su iznad 1 GeV podaci preuzeti iz posebnih FLUKA simulacija.

Referencu [57]). Iako je ovo proširenje daleko od nužnog za analizu eksperimentalnih podataka za uhvat neutrona na ^{58}Ni, prošireni spektar neutronskog toka korišten je za simulacije neutronske pozadine, opisane u Poglavlju 6.4. Cjelokupan tok neutrona od termalnih energija do 17 GeV prikazan je Slikom 6.2.2.

6.2.4 Detektori

Za mjerenje neutronskih uhvata na n_TOF postrojenju – koje se provodi detekcijom γ-zraka trenutno emitiranih nakon reakcije uhvata – korištena su dva C_6D_6 (deuterirani benzen) tekuća scintilacijska detektora. Jedan je preinačena verzija Bicron detektora dostupnog u prodaji, dok je drugi – nazvan FZK detektor – izgrađen po narudžbi u Forschungszentrum Karlsruhe [61]. Volumen scintilacijskih tekućina bio je 618 ml za Bicron i 1027 ml za FZK detektor. Oni moraju biti dovoljno niski da osiguraju toliko nisku detekcijsku učinkovitost da se može detektirati najviše jedna γ-zraka iz svake γ-kaskade. Ovaj zahtjev nametnut je metodom primjene težinske funkcije, korištenom tijekom analize eksperimentalih podataka (vidjeti Poglavlje 6.3.3).

C_6D_6 detektori posebno su optimizirani kako bi im se čim više umanjila neutronska osjetljivost, što je potrebno za smanjenje stvaranja i detekcije pozadinskih događaja izazvanih raspršenjem neutrona. Ovakav doprinos mjerenoj pozadini razrađen je u Poglavlju 6.4. Kao što je prikazano Slikom 6.2.3, dva detektora postavljena su jedan nasuprot drugome, okomito na cjevovod za vođenje neutronskog snopa te nekoliko centimetara ispred mjerenog uzorka. Potpornji za detektore i uzorak izrađeni su od ugljičnih vlakana kako bi se dodatno smanjila neutronska osjetljivost eksperimentalnog postava. Općenito govoreći, za potrebe minimizacije neutronskih uhvata izazvanih raspršenim neutronima, ugljik je poželjan materijal zbog svoje kemijske stabilnosti, dostupnosti i, iznad svega, vrlo niskoga udarnog presjeka za uhvat neutrona.

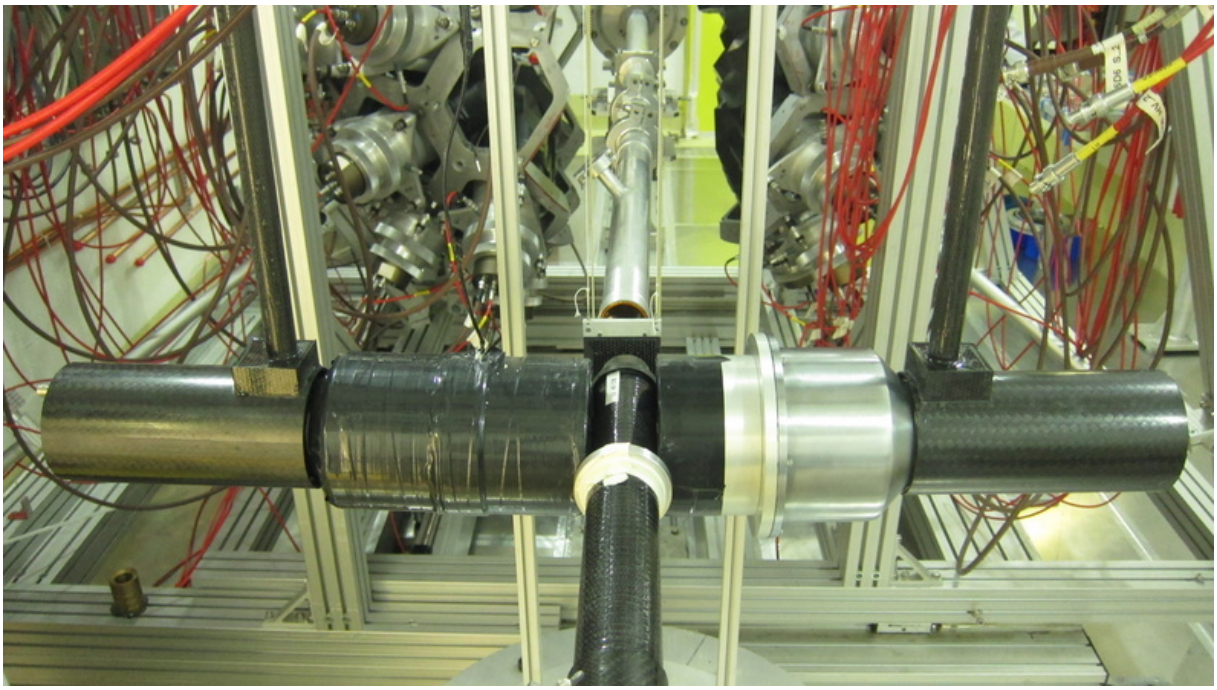

Slika 6.2.3 — C_6D_6 tekući scintilacijski detektori poduprti oklopom od ugljičnih vlakana. Lijevi je FZK, dok je desni Bicron detektor.

6.2.5 Sustav za prikupljanje podataka

Digitalni sustav za prikupljanje podataka – visoke brzine i preciznosti – korišten je za bilježenje elektroničkih signala dvaju detektora. Sustav se sastoji od 8-bitnih Acqirisovih [62] FADC-jedinica (*eng.* flash analog-to-digital converters) radne frekvencije od 500 MHz. Ove jedinice, poznate kao *digitalizatori signala*, omogućuju pohranjivanje čitavih mjerenih signala zapisivanjem njegovih naponskih vrijednosti u vremenu, točku po točku. Ovako pohranjenim signalima može se pristupiti u bilo kojem kasnijem trenutku te ih se može, po potrebi opetovano, obrađivati. Veličina memorijskog spremnika je 48 MB, što omogućuje zapisivanje signala duljine 96 ms te dosezanje energije neutrona od 20 meV metodom vremena proleta. No donja granica za analizu eksperimentlanih podataka određena je donjom granicom mjerenog toka neutrona od 27 meV. Jednom digitalizirani i pohranjeni, elektronički signali kasnije se mogu obrađivati posebno razvijenim i optimiziranim algoritmima. Dodatni detalji o sustavu za prikupljanje podataka i algoritmima za njihovu analizu mogu se pronaći u Referenci [63].

Iz zapisanih signala potrebno je izračunati fizikalne veličine poput vremena proleta neutrona i energije deponirane γ-zrakama (i/ili drugim česticama), što se postiže primjenom posebih algoritama za analizu podataka. Prvo je potrebno unutar cjelokupnog signala identificirati prisutnost i položaje naponskih pulseva, uzrokovanih scintilacijama iz aktivnog dijela detektora u kojem γ-zrake i druge prolazne čestice deponiraju energiju. Primjer izoliranih pulseva iz C_6D_6 detektora prikazan je Slikom 6.2.4. Nakon prepoznavanja pulseva slijedi izračun naponske baze signala – prosječne naponske vrijednosti oko koje signal fluktuira u odsutstvu pulseva. Pri tome je dostupno nekoliko algoritama, čija primjena ovisi o lokalnoj stabilnosti naponske baze. Iz pulseva od kojih je odračunata naponska baza ekstrahiraju se fizikalne veličine kojima je definiran detektirani događaj. Ako je oblik pulsa iz danoga detektora jasno definiran – kao što je slučaj s C_6D_6 detektorima – primjenjuje se metoda prilagodbe mjerenih pulseva na predodređeni oblik. Sam predodređeni oblik pulsa određuje se usrednjavanjem velikog

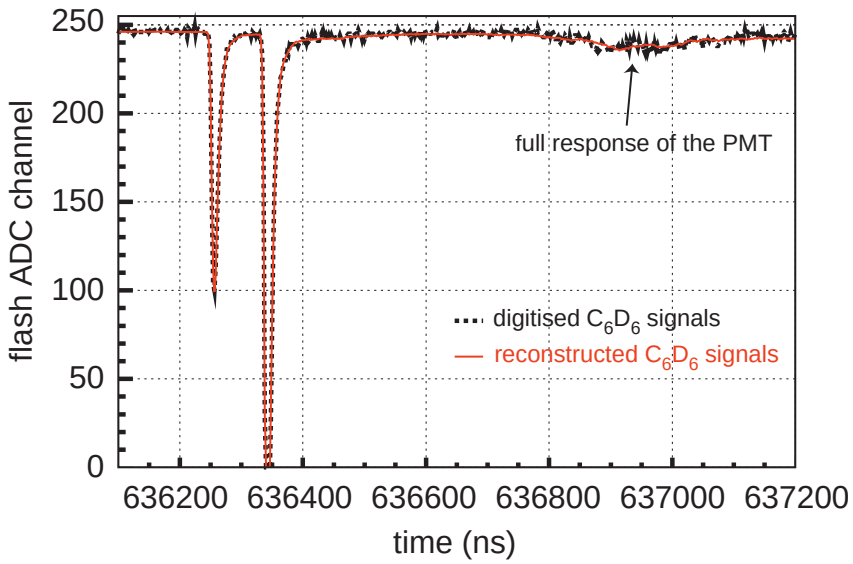

Slika 6.2.4 — Digitalizirani signal iz C_6D_6 detektora. Rezultati prilagodbe pulseva na predodređeni oblik su također prikazani (preuzeto iz Reference [63]).

broja mjerenih i prikladno normaliziranih pulseva. Prema tome, konačan oblik je optimalno prilagođen odazivu danog detektora. Nakon prilagodbe pojedinih mjerenih pulseva, energija deponirana u detektoru pripisuje im se na temelju amplitude predodređenog pulsa (koja je po konstrukciji proporcionalna površini pod njme). Iz prilagođenog pulsa također se određuje i trenutak njegove pojave primjenom metode prelaska konstantnog dijela amplitude, koja se sastoji u nalaženja trenutka u kojem naponska vrijednost signala prelazi unaprijed određeni dio (npr. 30%) naponske vrijednosti amplitude pulsa. Na temelju trenutaka pojave pulsevima se pripisuje vrijeme proleta neutrona. Za detektore čiji oblik pulsa nije jasno definiran primjenjuju se nezavisne, uglavnom izravne metode određivanja amplitude pulsa (npr. prilagodbom njegova vrha), površine pod njime (integracijom) i njegova trenutka pojave (nalaženjem trenutka prelaska naponskog praga za svaki puls zasebno).

6.3 Udarni presjek za uhvat neutrona na izotopu ^{58}Ni

6.3.1 Eksperiment

Mjerenje udarnog presjeka ^{58}Ni(n,γ) reakcije trajalo je od 16. kolovoza do 18. rujna 2011. Za potrebe obrade podataka, uz ^{58}Ni tri dodatna uzorka ozračena su neutronima: ^{197}Au, ^{nat}C i ^{nat}Pb. Tablica 6.2 navodi osnovna svojstva ovih uzoraka. Izotopna čistoća ^{58}Ni uzorka iznosi 99.5%, s primjesom ^{60}Ni od samo 0.48%, primjesom ^{61}Ni od 0.01% te primjesama ^{62}Ni i ^{64}Ni od 0.005%.

Tablica 6.2 — Osnovna svojstva uzoraka ozračenih neutronskim snopom.

	^{58}Ni	^{197}Au	^{nat}C	^{nat}Pb
Masa	2.069 g	0.596 g	7.13 g	0.313 g
Promjer	19.91 mm	19.94 mm	19.98 mm	19.90 mm
Širina	0.72 mm	0.1 mm	10.0 mm	0.1 mm

Spalacijska meta ozračena je s ukupno 1.92×10^{18} protona, pri čemu je 1.05×10^{18} protona posvećeno središnjem mjerenju s ^{58}Ni uzorkom, dok je ostatak od 0.87×10^{18} protona posvećen kalibracijskim mjerenjima s ostalim uzorcima. Tijekom mjerenja tok neutrona u eksperimentalnoj prostoriji nadziran je SiMon detektorom [52] koji se temelji na ^{6}Li$(n,t)\alpha$ reakciji te neznatno utječe na neutronski snop. Tijekom ^{58}Ni eksperimenta dva C_6D_6 detektora postavljena su 8.2 cm ispred uzorka, na udaljenosti 6.8 cm od osi cjevovoda za propuštanje neutrona, čime je umanjen učinak raspršenih γ-zraka iz dolaznoga snopa, no još je uvijek osigurana dovoljna geometrijska učinkovitost za detekciju γ-zraka iz neutronskih uhvata.

Cilj sljedeće obrade podataka je izračunati vjerojatnost uhvata neutrona u ^{58}Ni(n,γ) reakciji, i to u ovisnosti o energiji upadnih neutrona. Iz vjerojatnosti uhvata tada se mogu odrediti energijski ovisan udarni presjek i pripadni parametri za opis rezonanci.

6.3.2 Energijsko baždarenje

Kao prvi korak u obradi podataka proučena je stabilnost odaziva C_6D_6 detektora. U tu svrhu detektori su izloženi uobičajenim baždarnim izvorima ^{137}Cs, ^{88}Y i Am/Be nekoliko puta tijekom mjesec dana dugog eksperimenta. Slika 6.3.1 prikazuje savršen preklop γ-spektara pojedinih izvora, čime je potvrđena stabilnost odaziva detektora tijekom čitavog eksperimenta. S obzirom na dosljednost između ponovljenih mjerenja, svi podaci za dani izvor zajedno su uzeti u obzir pri sljedećem energija-kanal baždarenju.

Energijsko baždarenje započinje poistovjećenjem rubova spektralnih vrhova sa Slike 6.3.1 s comptonskim rubovima odgovarajućih γ-zraka. Kanal x_{CR} koji odgovara polo-žaju comptonskog ruba precizno je određen prilagodbom spektralnoga ruba na gaussijanski oblik $\exp[(x-\mu)^2/(2\sigma^2)]$, pri čemu je kanalu x_{CR} pripisana vrijednost na

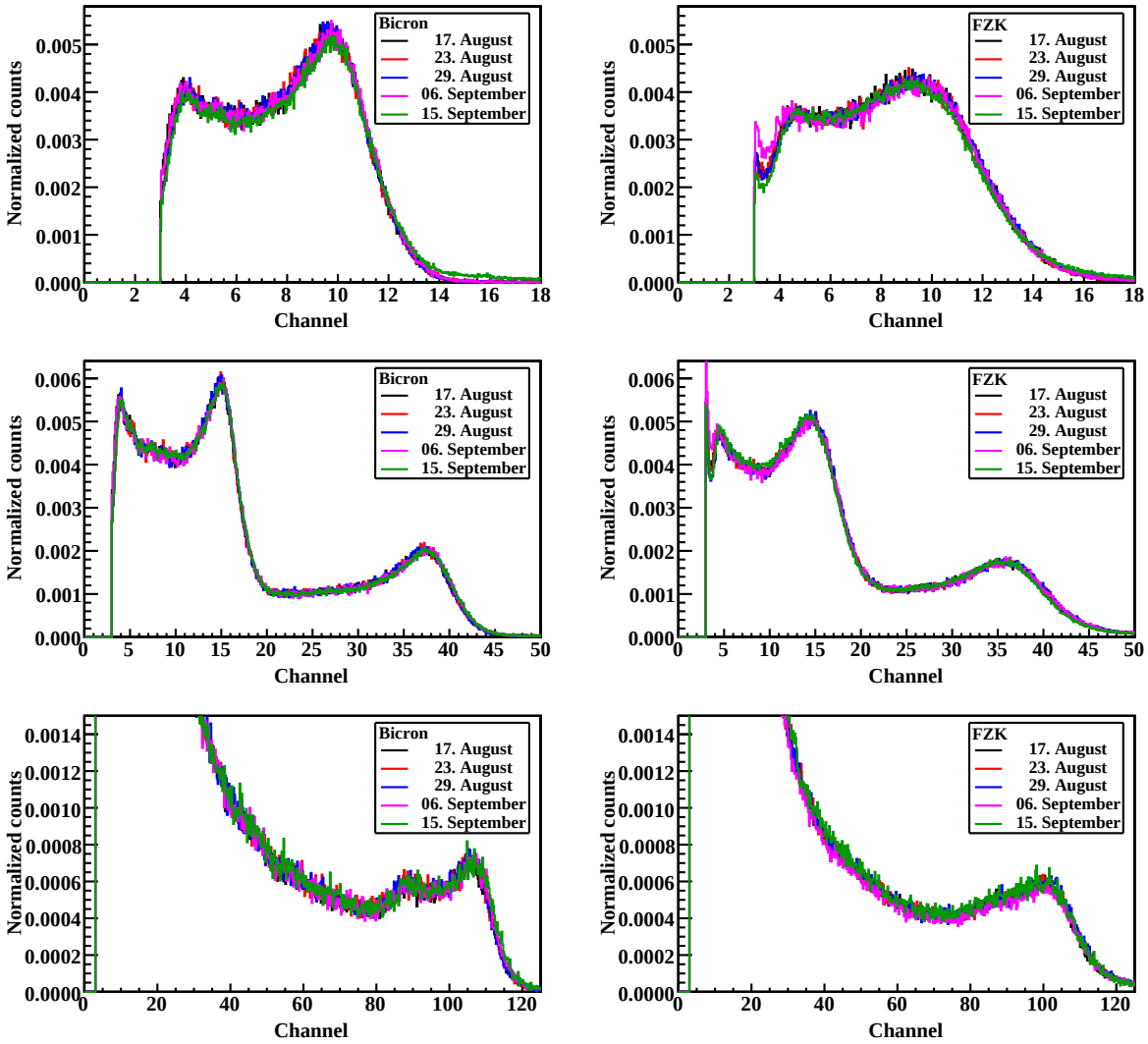

Slika 6.3.1 — Provjera stabilnosti odaziva dvaju C_6D_6 detektora, provedena pet puta tijekom ^{58}Ni eksperimenta. Od gornjih prema donjima, spektri se odnose na baždarne izvore ^{137}Cs, ^{88}Y i Am/Be, respektivno.

polovici visine spektralnoga vrha:

$$x_{\mathrm{CR}} = \mu + \sigma\sqrt{2\ln 2} \tag{6.3.1}$$

Pridruživši mjerenim spektrima energije E_γ γ-zraka pojedinih baždarnih izvora – 662 keV za ^{137}Cs, 898 keV i 1836 keV za ^{88}Y te 4438 keV za Am/Be – izračunate su energije E_{CR} comptonskih rubova:

$$E_{\mathrm{CR}} = \frac{2E_\gamma^2}{m_e c^2 + 2E_\gamma} \tag{6.3.2}$$

čime je omogućeno početno $E_{\mathrm{CR}}(x_{\mathrm{CR}})$ baždarenje. Također, širine vrhova σ – prvotno određene u jedinicama kanala – sad se mogu izraziti u jedinicama detektirane energije.

U sljedećem koraku korištene su detaljne GEANT4 [65, 66] simulacije eksperimentalnog postava u svrhu nalaženja monokromatskih spektara pripadnih četirima energijama E_γ γ-zraka korištenih za baždarenje. Neosjetljivi na rezoluciju svojstvenu cjelokupnom eksperimentalnom uređaju, ovi spektri umjetno su proširivani detekcijskom rezolucijom sve dok nije postignuto slaganje s mjerenim spektrima. Na ovaj način određena je je rezolucija detektora za četiri vrijednosti E_{CR}. Prilagodbom ovih točaka na unaprijed određen oblik:

$$\frac{\Delta E}{E} = A + \frac{B}{E} + \frac{C}{\sqrt{E}} \tag{6.3.3}$$

određena je relativna energijski ovisna rezolucija $\Delta E/E$.

U konačnici, provedeno je naprednije energija-kanal baždarenje (s obzirom na prvotni postupak koji se oslanja na izračunate energije comptonskih rubova). Pri tome su originalni simulirani spektri konvoluirani s gaussijanskom rezolucijskom funkcijom $\exp\{E^2/[2(\Delta E)^2]\}$, gdje je energijska ovisnost širine ΔE dana izrazom (6.3.3). Ponovnim nalaženjem comptonskog ruba E'_{CR} na polovici visine danoga spektralnog vrha (prilagodbom padajućeg ruba konvoluiranog spektra) eksperimentalni kanali x_{CR} sada se mogu dovesti u izravnu vezu sa simuliranim vrijednostima E'_{CR}. Konačno baždarenje provedeno je prilagodbom četiriju točaka na pretpostavljenu blago kvadratnu ovisnost:

$$E'_{\mathrm{CR}} = a x_{\mathrm{CR}}^2 + b x_{\mathrm{CR}} + c \tag{6.3.4}$$

6.3.3 Težinska funkcija

Sljedeći postupak u obradi podataka izračun je težinskih funkcija, koje su od središnje važnosti u tzv. metodi primjene težinske funkcije [43]. Potreba za ovakvim matematičkim objektom proizlazi iz nužnosti poznavanja učinkovitosti detekcije γ-zraka iz neutronskih uhvata. Primjenom težinske funkcije učinkovitost detekcije na umjetan način će se dovesti pod kontrolu.

Složena jezgra stvorena uhvatom neutrona ispočetka se nalazi u visoko-pobuđenom stanju iznad energije odvajanja neutrona. Kao što je ilustrirano Slikom 6.3.2, prema osnovnom stanju se deekscitira kroz niz među-stanja, emitirajući pri tome kaskadu γ-zraka. Kako je detekcijska učinkovitost ovisna o energiji pojedine γ-zrake, učinkovitost detekcije bilo koje od njih nije jednostavno odrediti. Štoviše, prosječna učinkovitost

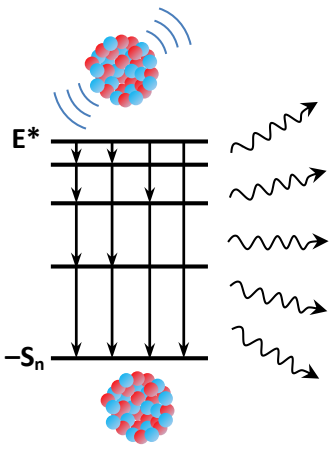

Slika 6.3.2 — Ilustracija γ-kaskada. Jezgra pobuđena uhvatom neutrona deekscitira se prema osnovnom stanju kroz niz među-stanja, emitirajući pri tome niz γ-zraka.

ovisna je o detaljima kaskade, posebno o vjerojatnostima prijelaza između dostupnih među-stanja. Cilj metode primjene težinske funkcije je na umjetan način utjecati na učinkovitost detekcije kaskade, tako da je se učini neovisnom i o načinu deekscitacije prema osnovnom stanju i o energiji pojedine detektirane γ-zrake. Ovo je moguće postići za detektore dovoljno niske učinkovitosti, kada se učinkovitost ε_{K} detekcije kaskade K može prikazati sumom učinkovitosti $\varepsilon_i^{(\mathrm{K})}$ za detekciju pojedinih γ-zraka iz dane kaskade:

$$\varepsilon_{\mathrm{K}} \approx \sum_i \varepsilon_i^{(\mathrm{K})} \tag{6.3.5}$$

Primjenom težinske funkcije, zasebene učinkovitosti $\varepsilon_i^{(\mathrm{K})}$ učinit će se proporcionalnima energiji $E_i^{(\mathrm{K})}$ detektirane γ-zrake:

$$\varepsilon_i^{(\mathrm{K})} = \alpha E_i^{(\mathrm{K})} \tag{6.3.6}$$

kako bi ukupna učikovitost:

$$\varepsilon_{\mathrm{K}} \approx \alpha \sum_i E_i^{(\mathrm{K})} = \alpha E_{\mathrm{x}} \tag{6.3.7}$$

postala ovisnom jedino o ukupnoj enegiji pobuđenja novonastale složene jezgre. Pri tome je energija pobuđenja E_{x} dana energijom odvajanja neutrona S_n i ukupnom kinetičkom energijom E^* u sustavu centra mase neutrona i jezgre prije reakcije uhvata:

$$E_{\mathrm{x}} = S_n + E^* \tag{6.3.8}$$

te je potpuno neovisna o detaljima kaskade.

Proporcionalnost iz (6.3.6) može se postići na način da se pojedinim eksperimentalnim podacima pridruže odgovarajući težinski faktori, određeni težinskom funkcijom $W(E)$. Sama težinska funkcija nalazi se minimizacijom izraza:

$$\sum_j \left[\int W(E') R(j;E') \mathrm{d}E' - \alpha E_\gamma(j) \right]^2 = \min. \tag{6.3.9}$$

pri čemu je $R(j;E)$ j-ti monokromatski spektar, tj. detekcijski odaziv na γ-zrake energije $E_\gamma(j)$. Sasvim je očito da su za uspješan i pouzdan izračun težinske funkcije

potrebni istinski monokromatski spektri, koje je eksperimentalno praktički nemoguće osigurati. Detaljne i visoko pouzdane GEANT4 simulacije su, stoga, izabrane kao alternativan način njihova nalaženja. Tijekom simulacije γ-zrake su emitirane duž uzorka precizno reproduciranih dimenzija, prateći unaprijed određenu dubinsku raspodjelu. Zahvaljujući visokoj preciznosti geometrijske rekonstrukcije eksperimentalnog postava unutar programskoga kôda, ne samo da su intrinzična i geometrijska učinkovitost za detekciju γ-zraka uzeti u obzir, već i fini efekti poput detekcije fotona raspršenih na komponentama mjernog uređaja. Dodatni detalji o metodi primjene težinske funkcije na n_TOF postrojenju mogu se pronaći u Referenci [67].

Pri minimizaciji izraza (6.3.9) težinska funkcija modelirana je polinomom četvrtoga stupnja:

$$W(E) = \sum_{k=0}^{4} a_k E^k \tag{6.3.10}$$

uz vrijednost proizvoljnog faktora proporcionalnosti α iz (6.3.6) izabranu kao $\alpha = 1\ \mathrm{MeV}^{-1}$. Budući da je svrha težinske funkcije primjeniti je na eksperimentalne spektre, simulirani monokromatski spektri prije izračuna težinske funkcije moraju biti

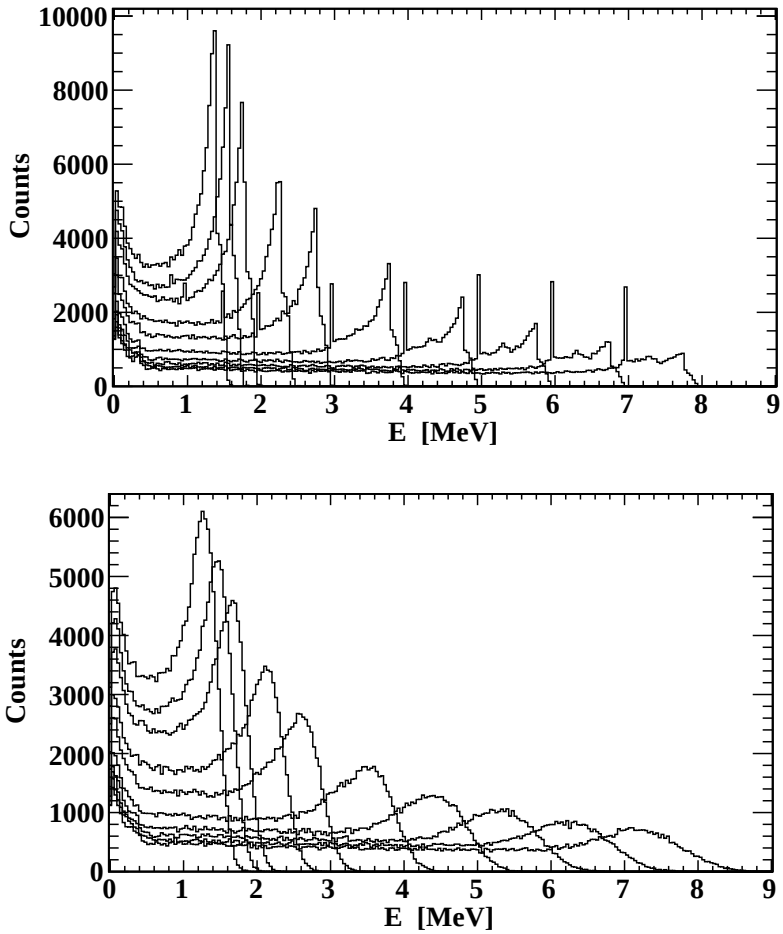

Slika 6.3.3 — Monokromatski spektri za nekoliko energija γ-zraka između 1.6 MeV i 8 MeV, za jedan od dvaju C_6D_6 detektora. Gornji graf prikazuje odaziv detektora izravno simuliran GEANT4 programskim paketom, dok je na donjem grafu dodatno primjenjena rezolucijska funkcija danog detektora. Pri izračunu težinske funkcije, na rezolucijom proširene spektre također je primjenjen i donji prag od 0.2 MeV, prisutan tijekom eksperimenta.

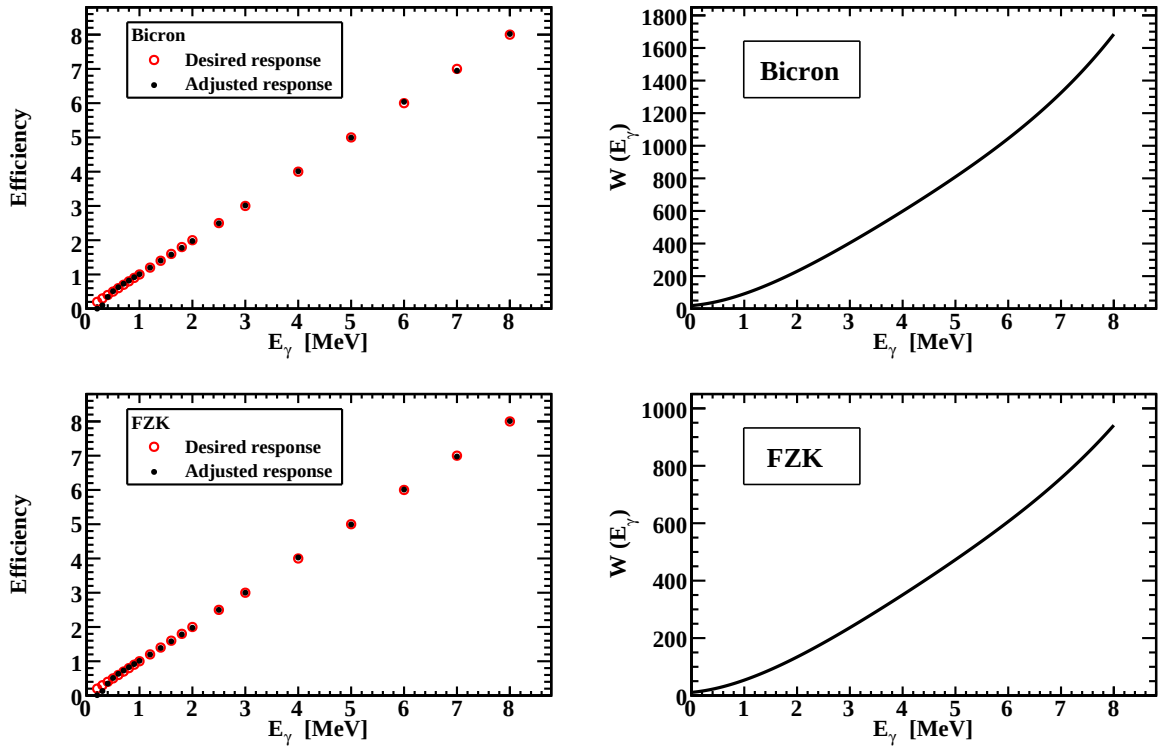

Slika 6.3.4 — Težinske funkcije za dva C_6D_6 detektora (desni okvir) te usporedba između željene detekcijske učinkovisti $\varepsilon_\gamma = E_\gamma$ i one preostale nakon primjene težinske funkcije (lijevi okvir). Uzrok neslaganja na najnižim energijama (ispod 0.5 MeV) je usporediv donji prag od 0.2 MeV, primjenjen na monokromatske spektre podnesene algoritmu za izračun težinskih funkcija. Valja primjetiti bitno različite skale dviju težinskih funkcija, što je izravna posljedica različitih detekcijskih učinkovitosti dvaju detektora.

proširen gaussijanskom konvolucijom s rezolucijskom funkcijom (6.3.3). Primjeri simiiranih monkromatskih spektara za nekoliko različitih energija γ-zraka prikazani su Slikom 6.3.3, prije i poslije proširenja rezolucijskom funkcijom. Donji prag od 0.2 MeV postavljen na spektre detektiranih energija tijekom mjerenja također je morao biti postavljen i na proširene monokromatske spektre prije izračuna težinske funkcije. Slika 6.3.4 prikazuje konačne težinske funkcije korištene za obradu podataka dvaju C_6D_6 detektora.

6.3.4 Put proleta neutrona

Put proleta neutrona mora biti precizno određen kako bi se iz njegova vremena proleta mogla rekonstruirati njegova početna energija. Udarom svakog protonskog pulsa o spalacijsku olovnu metu oslobađa se intenzivan γ-bljesak. Kao što neutroni prolaze put od približno 185 m kroz cjevovod do eksperimentalne prostorije, tako i γ-bljesak dolazi do prostorije (Slika 6.3.5), gdje se detektira tolikom žestinom da zasljepljuje detektore na određeno vrijeme. Signal izazvan γ-bljeskom označuje početni trenutak t_γ za mjerenje vremena proleta neutrona. Detekcija γ-zraka trenutno emitiranih po uhvatu neutrona, pak, označuje završni trenutak t_n. Na temelju ovih dviju vrijednosti vrijeme proleta neutrona Δt računa se kao:

$$\Delta t = t_n - t_\gamma + L/c \tag{6.3.11}$$

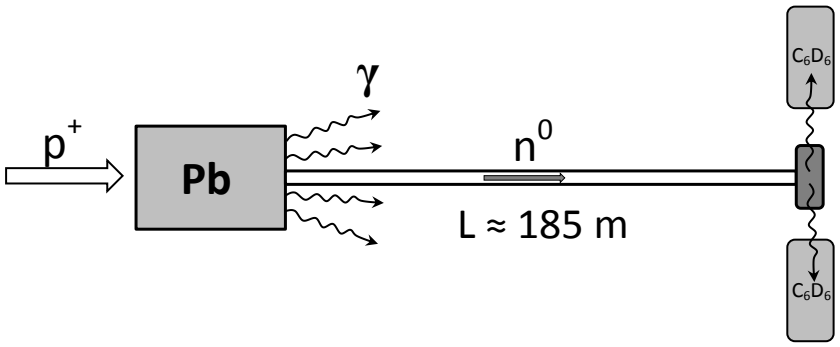

Slika 6.3.5 — Ilustracija slijeda događaja nakon svakog protonskog pulsa. Po udaru protona o spalacijski olovni blok oslobađa se intenzivan γ-bljesak, stvarajući početni signal za mjerenje vremena proleta neutrona. Nakon uhvata neutrona složena jezgra se (gotovo) trenutno deekscitira γ-raspadom. Detekcija γ-zraka C_6D_6 scintilatorom stvara završni signal.

pri čemu je potrebno korigirati rezultat za zakašnjenje L/c uzrokovano propagacijom γ-bljeska kroz cjevovod duljine L. Iz vremena proleta energiju E_n uhvaćenog neutrona računamo relativističkom relacijom:

$$E_n = m_n c^2 \left(\frac{1}{\sqrt{1 - \left(\frac{L}{c\Delta t}\right)^2}} - 1 \right) \tag{6.3.12}$$

uz m_n kao masu neutrona te c kao brzinu svjetlosti u vakuumu.

Put proleta neutrona – od središnje važnosti za uspostavu vrijeme-energija korelacije – nije jednostavno odrediti geometrijskim mjerenjima. Umjesto toga korištena je metoda podešavanja položaja mjerenih rezonanci tankog uzorka ^{197}Au s rezonancama iz dobro utvrđenog standarda, prateći postupak opisan u Referenci [68]. Pri tome se vrijednost puta proleta L manualno varira sve do postizanja optimalnog globalnog preklopa položaja rezonanci. Na ovaj način utvrđena je optimalna vrijednost od $L = 184.00 \pm 0.05$ m, uz nepouzdanost od 5 cm procjenjenu jednostavnom vizualnom provjerom odstupanja položaja pri daljnjem variranju parametra L.

6.3.5 Vjerojatnost uhvata neutrona

Iz mjerenih podataka vjerojatnost uhvata neutrona $Y(E_n)$ računa se prema:

$$Y(E_n) = \frac{C_w(E_n) - B_w(E_n)}{N E_x(E_n) \phi(E_n)} \tag{6.3.13}$$

pri čemu su $C_w(E_n)$ ukupni otežani događaji mjereni s uzorkom postavljenim u neutronski snop, dok su $B_w(E_n)$ ukupni otežani pozadinski događaji. Zahvaljujući konstrukciji težinske funkcije, energija pobuđenja E_x složene jezgre korigira podatke za detekcijsku učinkovitost. Prema (6.3.8) energija pobuđenja dana je zbrojem ukupne kinetičke energije neutrona i početne jezgre u sustavu centra mase te energije odvajanja neutrona novonastale jezgre – 8.99 MeV u slučaju ^{59}Ni, odnosno 6.51 MeV u slučaju ^{198}Au. $\phi(E_n)$ je ukupan tok neutrona propušten kroz uzorak, dok je N završni faktor normiranja, kojim su u obzir uzeti manji eksperimentalni efekti.

Nekoliko je izvora pozadinskih događaja prisutnih tijekom mjerenja. Jedna pozadinska komponenta uzrokovana je raspršenjem γ-zraka iz dolaznog neutronskog snopa. Ova komponenta mjerena je postavljanjem olovnoga uzorka u snop te je utvrđeno da je potpuno zanemariva. Sljedeća komponenta uzrokovana je prolaskom neutronskog snopa kroz eksperimentalnu prostoriju te se lako mjeri jednostavnim uklanjanjem uzorka iz neutronskog snopa. Nadalje, pozadina uzrokovana prirodnim i induciranim zračenjem iz eksperimentalnog okruženja mjerena je nakon gašenja neutronskog snopa. Uzeto je u obzir da su ovakvi pozadinski događaji dijelom već prisutni unutar mjerene pozadine s ozračenim eksperimentalanim postavom te je provedeno ispravno normiranje ovih dviju komponenti. Završna komponenta, tzv. *neutronska pozadina*, uzrokovana je raspršenjem neutrona na samome uzorku te je identificirana detaljnim GEANT4 simulacijama, opisanim u Poglavlju 6.4.

Slika 6.3.6 prikazuje ukupne događaje mjerene s ^{197}Au i ^{58}Ni uzorkom te pozadinske događaje uzrokovane prolaskom neutronskog snopa kroz eksperimentalnu prostoriju te one uzrokovane prirodnim i induciranim zračenjem. Za oba detektora prikazani su spektri energija oslobođenih u aktivnom volumenu te kinetičkih energija izračunatih iz vremena proleta. Svi spektri normirani brojem protonskih pulseva, odnosno emuliranih protonskih pulseva u slučaju pozadine uzrokovane prirodnim i induciranim zračenjem. Valja primjetiti razliku u apsolutnim skalama dvaju detektora, što je izravna posljedica razlike u njihovim detekcijskim učinkovitostima. U spektrima kinetičkih energija vidljiva je značajna razlika između dvaju detektora iznad 100 keV,

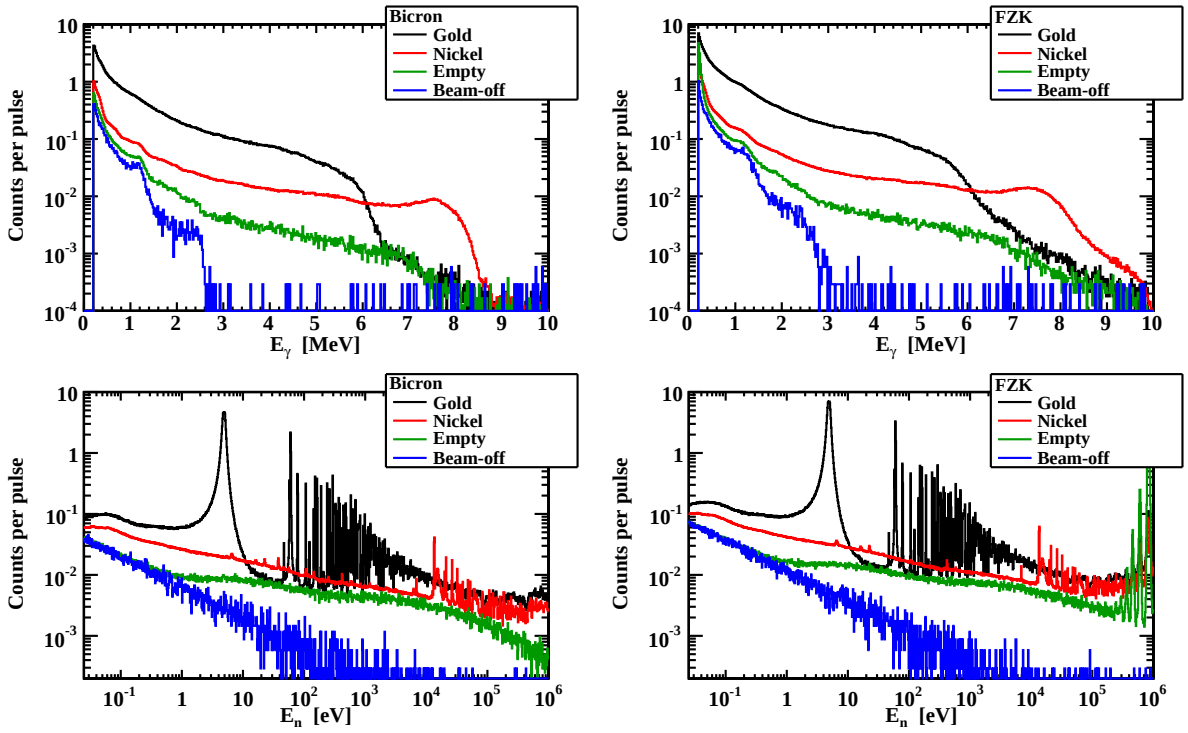

Slika 6.3.6 — Događaji mjereni po jednom protonskom pulsu. Spektri prikazuju ukupna mjerenja s ^{197}Au i ^{58}Ni uzorkom, pozadinu uzrokovanu prolaskom neutronskog snopa kroz eksperimentalnu prostoriju te pozadinu uzrokovanu prirodnim i induciranim zračenjem (za koju je broj protonskih pulseva emuliran). Rezultati dvaju detektora su prikazani odvojeno. Gornji okviri prikazuju energiju oslobođenu u C_6D_6 detektorima, a donji okviri raspodjelu energija izračunatih iz vremena proleta.

koja je vezana uz problem oporavka nakon početnog γ-bljeska izazvanog svakim protonskim pulsom. U slučaju Bicron detektora ovaj oporavak nije sasvim uspješan, stoga su za analizu iznad 100 keV korišteni samo podaci mjereni FZK detektorom. Iznad 400 keV FZK pokazuje snažne oscilacije zaostale za γ-bljeskom, koje ograničuju obradu podataka do ove vrijednosti u energiji.

Tok neutrona $\phi(E_n)$ koji prolazi površinom uzorka razlikuje se od ukupnog toka $\Phi(E_n)$ koji dolazi do eksperimentalne prostorije, a prikazan je Slikom 6.2.2. Ovome je uzrok promjer uzorka od 2 cm, koji je manji od raspona snopa od približno 3.5 cm. Energijski ovisan udio neutrona koji prolazi površinom uzorka opisan je tzv. faktorom presretanja snopa (*eng.* beam interception factor – BIF). Sama energijska ovisnost posljedica je ovisnosti raspona snopa o energiji neutrona, s obzirom da su visokoenergijski neutroni podložni manjem poprečnom rasapu. Raspon snopa i pripadni faktor presretanja određeni su posebnim FLUKA [58–60] simulacijama unutar čitavog energijskog raspona snopa s n_TOF postrojenja. Za uzorke promjera 2 cm energijska ovisnost faktora presretanja snopa prikazana je Slikom 6.3.7. Tok neutrona po jednom pulsu koji prolazi površinom uzorka, prema tome, dan je umnoškom ukupnog mjerenog toka neutrona i simuliranog faktora presretanja snopa:

$$\phi_{\text{po pulsu}}(E_n) = \Phi(E_n)\text{BIF}(E_n) \tag{6.3.14}$$

Pri izračunu bilo koje vrste fizikalnih parametara iz histogramiranih podataka, nužno je provesti korekciju za proizvoljno izabranu širinu podjeljka histograma. Zadatak dobiva na složenosti u slučaju da su podjeljci jednoliko raspodjeljeni unutar logaritamske skale, kao što je uobičajeno s mjerenjima uhvata zbog neutronskih energija koje se protežu preko nekoliko redova veličine. Može se pokazati da se tako histogramirani podaci moraju skalirati faktorom:

$$\frac{\text{PODJELJCI} \cdot \log_{10} e}{\log_{10}\left(E_{\max}/E_{\min}\right)} \approx \frac{0.4343 \cdot \text{PODJELJCI}}{\text{DEKADE}} \tag{6.3.15}$$

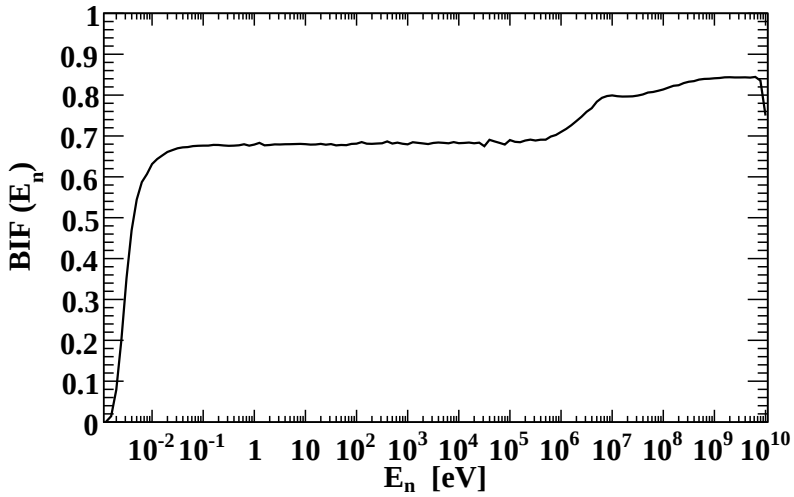

Slika 6.3.7 — Energijska ovisnost faktora presretanja snopa za uzorke promjera 2 cm i neutronski snop u kolimacijskome modu uhvata. Rezultati su određeni posebnim FLUKA simulacijama.

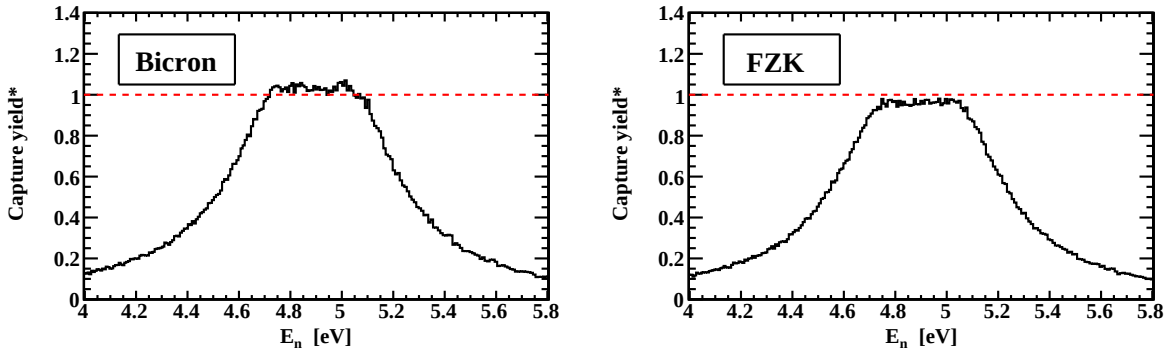

Slika 6.3.8 — Zasićena rezonanca u vjerojatnosti uhvata neutrona na uzorku ^{197}Au, prikazana odvojeno za dva detektora prije korekcije normalizacijskim faktorom N.

gdje je s PODJELJCI označen ukupan broj podjeljaka histograma unutar raspona energija od E_{min} do E_{max}, koje se protežu preko DEKADE $= \log_{10}(E_{\text{max}}/E_{\text{min}})$ dekada. Izravna posljedica histogramiranja podataka u logaritamskoj skali je da čak i nakon prethodnog skaliranja podaci ostaju umjetno pojačani lokalnom vrijednošću argumenta (energije neutrona E_n), i to zbog promjenjive širine podjeljaka. No kako je tok neutrona $\Phi(E_n)$ histogramiran na jednak način, ovaj efekt se implicitno poništava tijekom izračuna vjerojatnosti uhvata.

Završni faktor normiranja N iz 6.3.13 određen je metodom zasićene rezonance primjenjene na 4.9 eV rezonancu u vjerojatnosti uhvata za uzorak ^{197}Au [69]. Unutar energijskog raspona rezonance vrlo visokog udarnog presjeka može se očekivati zasićenje vjerojatnosti uhvata. Pretpostavimo li postojanje manjih eksperimentalnih efekata koji dosada nisu uzeti u obzir ili mogućnost manjih grešaka izazvanih primjenom težinske funkcije, zasićena vjerojatnost uhvata blago će odstupati od jedinice. Faktor normiranja N će, stoga, apsorbirati i ispraviti sve takve uzroke globalnog pomaka u skaliranju. Slika 6.3.8 prikazuje zasićenu rezonancu uzorka ^{197}Au mjerenu dvama detektrima, prije skaliranja faktorom normiranja N, koji je određen upravo visinom ravnog horizontalnog dijela vjerojatnosti uhvata.

Slika 6.3.9 prikazuje ukupnu vjerojatnost uhvata (koja uključuje i doprinose pozadinskih događaja) izračunatu za uzorke ^{197}Au i ^{58}Ni. Također je prikazana mjerena pozadina uzrokovana prolaskom neutronskog snopa kroz eksperimentalnu prostoriju i pozadina uzrokovana prirodnim i induciranim zračenjem te simulirana neutronska pozadina. Pozadina prirodnog i induciranog zračenja većim dijelom već je uključena u sklopu pozadine uzrokovane prolaskom snopa kroz eksperimentalnu prostoriju.

6.3.6 Udarni presjek za uhvat neutrona

Krećući od vjerojatnosti uhvata, pouzdana parametrizacija udarnog presjeka može se postići jedino netrivijalnim matematičkim pristupom, s obzirom da na samu vjerojatnost uhvata utječu razni eksperimentalni efekti. Među njima se nalaze rezolucijska funkcija neutronskog snopa, Dopplerovo širenje rezonanci, višestruko raspršenje neutrona te zasjenjenje snopa samim uzorkom. Utjecaj ovih efekata na mjerene rezonance u vjerojatnosti uhvata opisan je u Referenci [50]. Programski kod SAMMY [22] koji koristi formalizam R-matrice, a korišten je u matematičkoj obradi vjerojatnosti uhvata, na ispravan način uzima sve navedene efekte u obzir.

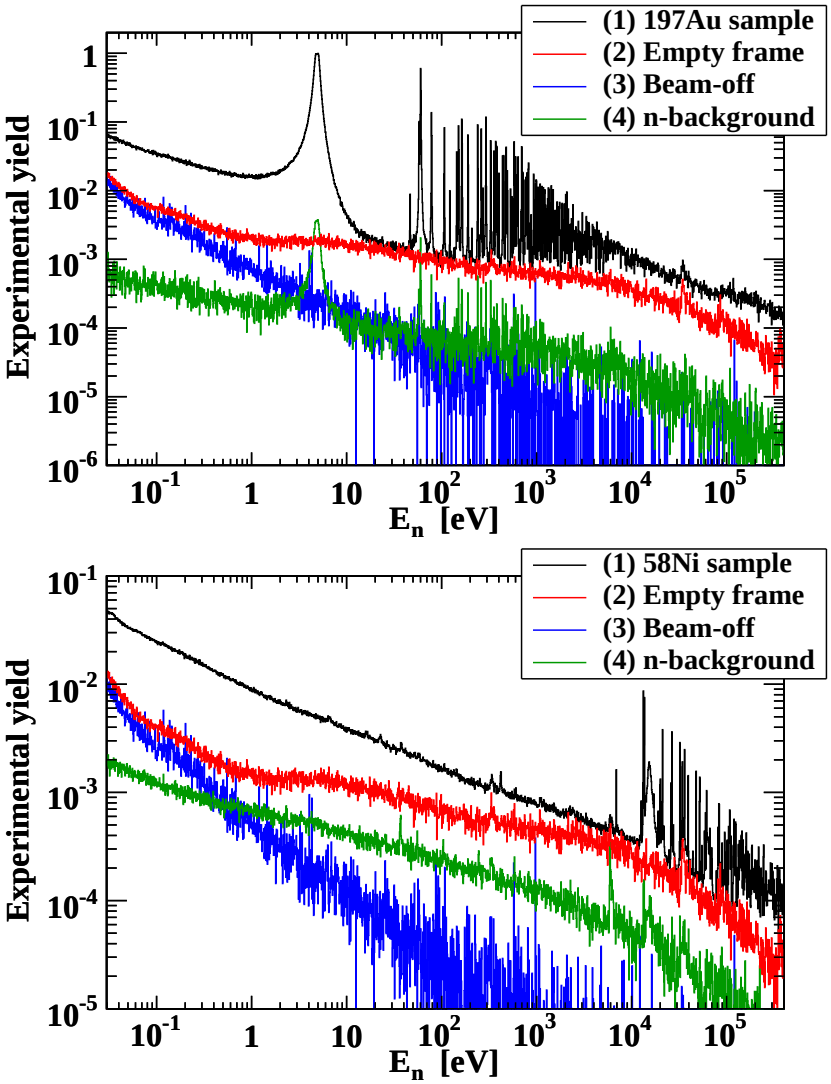

Slika 6.3.9 — Ukupna mjerena vjerojatnost uhvata za ^{197}Au (gornji okvir) i ^{58}Ni (donji okvir). Također je prikazana pozadina uzrokovana prolaskom neutronskog snopa kroz eksperimentalnu prostoriju te pozadina uzrokovana prirodnim i induciranim zračenjem. Neutronska pozadina identificirana je GEANT4 simulacijama.

Termalna vrijednost udarnog presjeka

Udarni presjek na niskim energijama – točnije, prije prve rezonance – pokazuje $1/v$ ovisnost, gdje je v brzina upadnog neutrona. Ovaj rezultat u potpunosti je utemeljen u kvantnomehaničkim računima, no može se razumjeti i na intuitivnoj razini jer je vjerojatnost uhvata proporcionalna vremenu koje neutron u letu provodi unutar jezgre, a koje je obrnuto proporcionalno njegovoj brzini. Ovaj $1/v$ rep na niskim energijama može se reproducirati tijekom analize programom SAMMY usvoji li se jedna ili više rezonanci na negativnim energijama, odnosno na energijama ispod energije odvajanja neutrona. Repovi rezonantnih krivulja u tom slučaju oponašaju $1/v$ ovisnost u neposrednoj blizini energije odvajanja neutrona. U svrhu prilagodbe ^{58}Ni podataka do 10 keV, usvojene su dvije negativne rezonance, po uzoru na posljednje baze izvrjednjenih udarnih presjeka te u skladu s posljednjom Mughabghabovom kompilacijom podataka [70]. Od pet rezonantnih parametara po pojedinoj rezonanci – energije E_R, orbitalnog angularnog momenta ℓ, ukupnog angularnog momenta J, neutronske širine

Γ_n i radijativne širine Γ_γ – samo je radijativna širina ostavljena slobodnom tijekom prilagodbe podataka, dok su vrijednosti preostalih četiriju usvojene iz ENDF/B-VII.1 liste parametara, dostupne preko JANIS sučelja [71]. Nakon prilagodbe podataka zadržane su sljedeće parametrizacije dviju negativnih rezonanci:

$$(E_R^{(1)}, \ell^{(1)}, J^{(1)}, \Gamma_\gamma^{(1)}, \Gamma_n^{(1)}) = (-78318\,\text{eV},\ 0,\ 1/2,\ 25\,\text{eV},\ 40685\,\text{eV})$$
$$(E_R^{(2)}, \ell^{(2)}, J^{(2)}, \Gamma_\gamma^{(2)}, \Gamma_n^{(2)}) = (-11674\,\text{eV},\ 0,\ 1/2,\ 1.6\,\text{eV},\ 4262.7\,\text{eV})$$

Dio mjerenih podataka koji pokazuje $1/v$ ovisnost prikazan je Slikom 6.3.10, zajedno s rezultatom prilagodbe podataka programom SAMMY. Jasno je vidljivo da rezultat prilagodbe vrlo dobro opisuje globalni oblik mjerenog spektra, no može se primjetiti da blago precjenjuje podatke na niskim energijama, u blizini termalne vrijednosti pri 25.3 meV. Stoga je provedena nezavisna prilagodba podataka na $1/v$ oblik u niskoenergijskom području između 27 meV i 50 meV kako bi se ekstrapolacijom odredila termalna vrijednost $\sigma(25.3\,\text{meV})$ udarnog presjeka. U tu svrhu, naravno, vjerojatnost uhvata prvo je bilo potrebno prevesti u udarni presjek, što je učinjeno temeljem omjera između vjerojatnosti uhvata i udarnog presjeka, izračunatih programom SAMMY nakon optimizacije parametara dviju negativnih rezonanci. (Valja primjetiti da su podaci sa Slike 6.3.10 već prikazani kao udarni presjek, umjesto vjerojatnost uhvata.) Konačni rezultat nezavisne prilagodbe podataka između 27 meV i 50 meV je termalna vrijednost udarnog presjeka od $4385 \pm 22_{\text{stat}} \pm 137_{\text{sys}}$ mb. Za statističku nepouzdanost preuzeta je nepouzdanost krajnjeg rezultata provedene prilagodbe podataka, dok je sistematska nepouzdanost određena nepouzdanošću težinske funkcije (2%), mjerenog toka neutrona (2% na termalnim energijama) te lokalne vrijednosti faktora presretanja snopa (1.3%). Tablica 6.3 uspoređuje rezultat s n_TOF postrojenja s vrijednostima iz ENDF/B-VII.0 [13] i ENDF/B-VII.1 [18] baze izvrjednjenih udarnih presjeka, s preporučenom vrijednošću iz Mughabghabove kompilacije [70] te se eksperimentalnim podacima iz EXFOR [11] baze podataka. Većina rezultata iz EXFOR baze navedeni su kao maxwellowski prosjeci pri 25.3 meV. Valja primjetiti

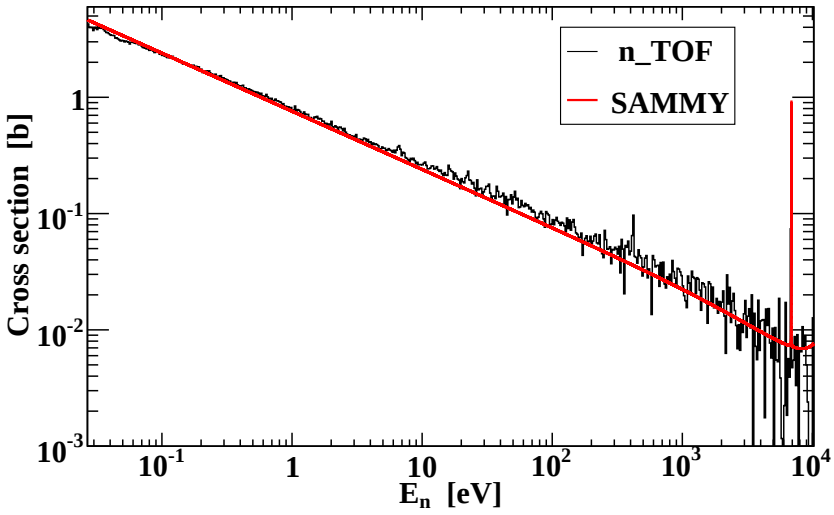

Slika 6.3.10 — Mjereni udarni presjek za uhvat neutrona na uzorku ^{58}Ni, između 27 meV i 10 keV. Prilagodba podataka programom SAMMY provedena je usvajanjem dviju rezonanci na negativnim energijama.

Tablica 6.3 — Usporedba termalne vrijednosti udarnog presjeka mjernog na n_TOF postrojenju s ranijim eksperimentalnim rezultatima iz EXFOR [11] baze podataka, s rezultatima iz ENDF/B baze izvrjednjenih udarnih presjeka [13, 18] te s preporučenom vrijednošću iz Mughabghabove kolekcije podataka [70]. Podaci označeni s MX navedeni su kao maxwellovski prosjeci.

Izvor	σ**(25.3 meV)**
n_TOF	$4385 \pm 22_{\text{stat}} \pm 137_{\text{sys}}$ mb
Pomerance$^{\text{MX}}$ (1952)	4200 ± 336 mb
Ishaq$^{\text{MX}}$ (1977)	4500 mb
Carbonari (1988)	4520 ± 100 mb
Weselka$^{\text{MX}}$ (1991)	4600 ± 300 mb
Venturini$^{\text{MX}}$ (1997)	4400 ± 200 mb
Raman$^{\text{MX}}$ (2004)	4130 ± 50 mb
ENDF/B-VII.0	4621 mb
ENDF/B-VII.1	4227 mb
Mughabghab	4370 mb

da uz pretpostavku čiste $1/v$ ovisnosti udarnog presjeka: $\sigma(E_n) = \sigma(kT)\sqrt{kT/E_n}$, maxwellowski prosjek $\langle\sigma\rangle_{kT}$ na termalnoj energiji kT odgovara upravo lokalnoj vrijednosti $\sigma(kT)$:

$$\langle\sigma\rangle_{kT} = \frac{2}{\sqrt{\pi}}\frac{1}{(kT)^2}\int_0^\infty \sigma(kT)\sqrt{\frac{kT}{E_n}} \times E_n e^{-E_n/kT}\mathrm{d}E_n = \sigma(kT) \tag{6.3.16}$$

tj. samoj termalnoj vrijednosti udarnog presjeka. Imajući ovo na umu, termalna vrijednost s n_TOF postrojenja bliska je Ramanovom rezultatu [17]. Nadalje, postignuto je slaganje unutar 04.% s preporučenom vrijednošću od 4370 mb iz Mughabghabove kompilacije [70]. Što se tiče ENDF baza izvrjednjenih udarnih presjeka, ENDF/B-VII.0 je predstavnica posljednjih verzija ostalih značajnih baza poput JENDL-4.0, JEFF-3.1.2, CENDL-3.1 i ROSFOND-2010 [72]. U usporedbi s ENDF/B-VII.0, promjene u niskoenergijskom dijelu ENDF/B-VII.1 baze potaknute su Ramanovim eksperimentalnim rezultatima [17]. Očito je da u ovom pogledu n_TOF rezultat opravdava promjenu termalnog dijela udarnog presjeka iz posljednje ENDF/B-VII.1 baze.

Područje raspoznatljivih rezonanci

Područje raspoznatljivih rezonanci analizirano je do 122 keV programom SAMMY. U ovom području pronađena je i parametrizirana 51 rezonanca u vjerojatnosti uhvata neutrona. Slika 6.3.11 prikazuje primjere izdvojenih rezonanci, zajedno s konačnim rezultatom prilagodbe podataka koju SAMMY provodi korištenjem formalizma R-matrice. Najvažniji parametri koji se mogu rekonstruirati iz mjerenja uhvata koja nisu popraćena transmisijskim mjerenjima, snage su pojedinih rezonanci. Snaga rezonance K u izravnoj je vezi s integralnim udarnim presjekom iste rezonance:

$$K = \frac{2}{\lambda^2}\int_{-\infty}^{\infty}\sigma(E_n)\mathrm{d}E_n = g_s\frac{\Gamma_n\Gamma_\gamma}{\Gamma_n+\Gamma_\gamma} \tag{6.3.17}$$

pri čemu je λ de Brogliejeva valna duljina upadnog neutrona, aproksimirana konstantom unutar raspona rezonance. Uz Γ_n i Γ_γ kao neutronsku i radijativnu širinu, respek-

tivno, g_s je statistički spinski faktor određen spinom neutrona I_n, ukupnim angularnim momentom $I_{^{58}\mathrm{Ni}}$ osnovnog stanja jezgre ^{58}Ni te ukupnim angularnim momentom J same rezonance:

$$g_s = \frac{2J+1}{(2I_n+1)(2I_{^{58}\mathrm{Ni}}+1)} \qquad \Rightarrow \qquad g_s(^{58}\mathrm{Ni}) = \frac{2J+1}{2} \tag{6.3.18}$$

Za $I_n = 1/2$ i $I_{^{58}\mathrm{Ni}} = 0$, faktor g_s ostaje ovisan jedino o angularnom momentu J rezonance.

Tijekom prilagodbe podataka programom SAMMY svakoj rezonanci potrebno je pripisati orbitalni angularni moment ℓ i ukupni angularni moment J. Ove vrijednosti – zajedno s početnim vrijednostima za Γ_n i Γ_γ – usvojene su iz ENDF/B-VII.1 baze parametara [18]. Budući da su mjerenja uhvata i transmisijska mjerenja potrebna za pouzdano određivanje obiju širina Γ_n i Γ_γ, bilo je uputno zadržati samo jednu od njih slobodnom. Kad je jedna od širina mnogo veća od druge, desna strana jednadžbe (6.3.17) osjetljiva je jedino na manju od njih. Stoga u takvim slučajevima veća širina nije varirana tijekom prilagodbe podataka. U slučaju rezonanci usporedivih širina, obje su ostavljene slobodnima.

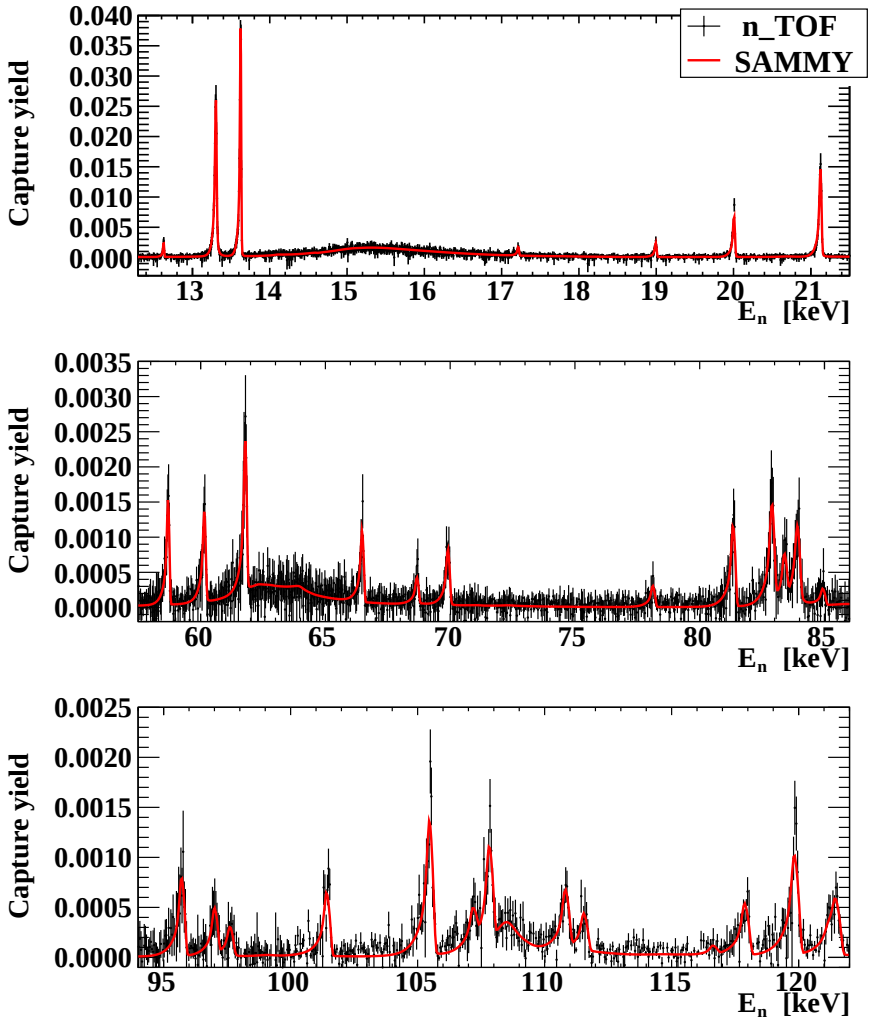

Slika 6.3.11 — Primjeri raspoznatljivih rezonanci u vjerojatnosti uhvata neutrona za uzorak ^{58}Ni. Također je prikazan rezultat globalne prilagodbe podataka programom SAMMY.

Tablica 6.4 — Rezonantni parametri za 51 rezonancu u udarnome presjeku za uhvat neutrona do 122 keV. E_R je energija rezonance, ℓ njen orbitalni angularni moment, a J ukupni angularni moment. Snaga K svake rezonance izračunata je uzimajući u obzir statistički spinski faktor g_s, radijativnu širinu Γ_γ te neutronsku širinu Γ_n.

E_R (keV)	ℓ	J	g_s	Γ_γ (meV)	Γ_n (meV)	K (meV)

(Vidjeti Tablicu 3.6.)

Unutar vjerojatnosti uhvata do 122 keV, 5 rezonanci iz ENDF/B-VII.1 baze – vrlo niskih snaga uhvata – nisu raspoznate od pozadinskih fluktuacija u podacima. Njih čine rezonance pri 24.77 keV, 35.06 keV, 48.47 keV, 83.97 keV i 92.73 keV. Nove rezonance nisu pronađene u ovom energijskom području. Tablica 6.4 navodi parametre rezonanci određene prilagodbom podataka, zajedno s usvojenim fiksnim vrijednostima. Sistematskoj nepouzdanosti doprinose nepouzdanost toka neutrona (2% između 27 meV – 200 eV, 3% između 200 eV – 8 keV, 5% između 8 keV – 80 keV, 4% između 80 keV – 1 MeV), težinske funkcije (2%) i faktora presretanja snopa (1.3%). Slika 6.3.12 prikazuje omjere između snaga rezonanci određenih iz podataka s n_TOF postrojenja i onih izračunatih iz ENDF/B-VII.0 i ENDF/B-VII.1 parametara. Uz otežani prosjek od 0.81 ± 0.17 s obzirom na ENDF/B-VII.0 i 1.02 ± 0.13 s obzirom na ENDF/B-VII.1, podaci s n_TOF postrojenja ponovno opravdavaju promjene u posljedjoj ENDF/B-VII.1 inačici baze podataka. Pored parametara raspoznatljivih rezonanci, globalna prilagodba podataka programom SAMMY upotpunjena je parametrima dviju negativnih rezonanci u svrhu parametrizacije cjelokupnog udarnog presjeka za uhvat neutrona do 122 keV.

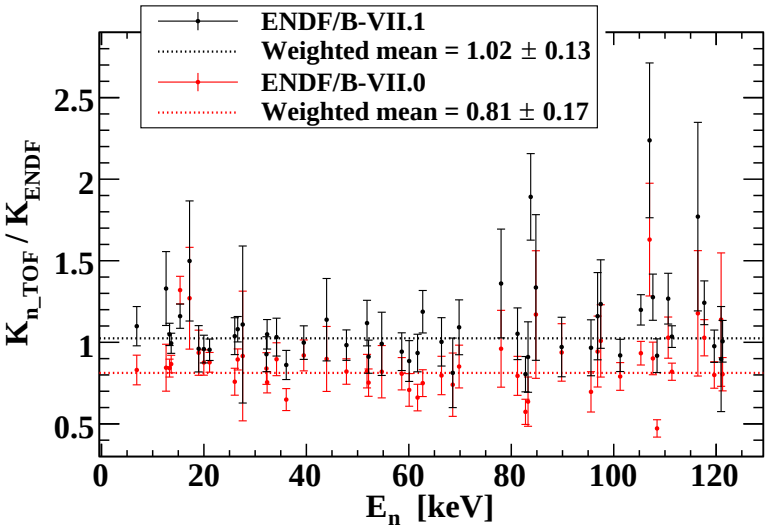

Slika 6.3.12 — Omjeri snaga rezonanci s n_TOF postrojenja i onih izračunatih iz ENDF/B-VII.0 i ENDF/B-VII.1 baza podataka.

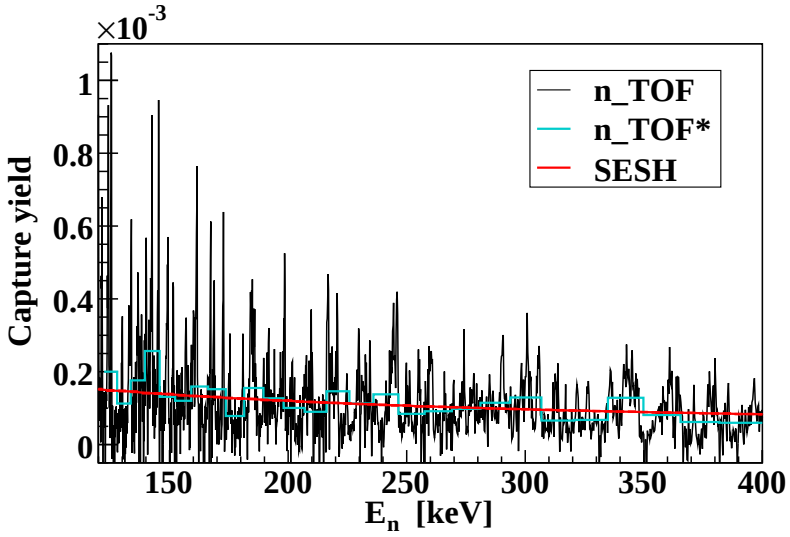

Slika 6.3.13 — Vjerojatnost uhvata u području neraspoznatljivih rezonanci između 122 keV i 400 keV. Isti eksperimentalni podaci histogramirani su nad velikim i 50 puta manjim brojem podjeljaka. Također je prikazana zaglađena vjerojatnost uhvata simulirana programom SESH.

Područje neraspoznatljivih rezonanci

Iako je razonantna struktura i dalje izražena u vjerojatnosti uhvata iznad 122 keV – što se jasno može vidjeti sa Slike 6.3.13 – zbog degradacije energijske rezolucije ovo područje analizirano je poput područja neraspoznatljivih rezonanci. Poseban programski kod SESH [73] korišten je u svrhu simulacije zaglađene vjerojatnosti uhvata između 122 keV i 400 keV. Valja primjetiti da su u ovom području korišteni samo podaci FZK detektora, kao što je objašnjeno u Poglavlju 6.3.5. Ponovno napominjemo da je gornja granica od 400 keV određena oporavkom detektora nakon γ-bljeska koji prethodi svakom neutronskom pulsu. Parametri potrebni za simulaciju vjerojatnosti uhvata programom SESH podešavani su sve do postizanja savršenog slaganja između integrala mjerene i simulirane vjerojatnosti uhvata u rasponu od 122 keV do 400 keV. Ovako optimiziran skup parametara iskorišten je za proširenje izračuna zaglađenog udarnog presjeka sve do 1 MeV. Zajedno s još uvijek rezonantnom vjerojatnošću uhvata, Slika 6.3.13 prikazuje zaglađenu vjerojatnost uhvata reproduciranu programom SESH. U svrhu olakšanja vizualne usporedbe s rezultatima programa SESH, eksperimentalni podaci također su prikazani unutar histograma 50 puta grublje podjele.

6.3.7 Maxwellovski usrednjeni udarni presjeci

Na temelju parametrizacije udarnog presjeka do 122 keV programom SAMMY te do 1 MeV programom SESH, maxwellovski usrednjeni udarni presjeci:

$$\langle\sigma\rangle_{kT} = \frac{2}{\sqrt{\pi}}\frac{1}{(kT)^2}\int_0^\infty \sigma(E_n)E_n e^{-E_n/kT}\mathrm{d}E_n \tag{6.3.19}$$

izračunati su unutar čitavog temperaturnog područja od astrofizičkog značaja, koje odgovara termalnim energijama u rasponu kT = 5 – 100 keV. Slika 6.3.14 prikazuje maxwellovske prosjeke s n_TOF postrojenja, uspoređujući ih s onima izračunatima iz ENDF/B-VII.0 i ENDF/B-VII.1 baze izvrjednjenih udarnih presjeka. Također su prikazani podaci iz KADoNIS v0.3 [74] kompilacije. Prikazani podaci navedeni su

Tablica 6.5 — Popis bitnih vrijednosti maxwellovski usrednjenih udarnih presjeka s n_TOF postrojenja, iz KADoNIS v0.3 baze podataka te vrijednosti izračunatih iz ENDF/B-VII.0 i ENDF/B-VII.1 podataka.

kT (keV)	MACS (mb)			
	n_TOF	ENDF/B-VII.0	ENDF/B-VII.1	KADoNIS v0.3
5	$41.3 \pm 0.6_{\text{stat}} \pm 2.3_{\text{sys}}$	39.8	38.2	38.3
10	$50.1 \pm 0.7 \pm 2.8$	52.0	48.1	50.1
15	$45.9 \pm 0.7 \pm 2.5$	49.9	44.9	48.1
20	$41.0 \pm 0.6 \pm 2.2$	46.2	40.6	44.5
25	$37.2 \pm 0.6 \pm 2.0$	42.9	37.0	41.3
30	$34.2 \pm 0.6 \pm 1.8$	40.2	34.1	38.7
40	$30.3 \pm 0.5 \pm 1.5$	36.3	30.0	35.0
50	$27.7 \pm 0.4 \pm 1.4$	33.5	27.1	32.3
60	$25.8 \pm 0.3 \pm 1.3$	31.4	25.0	30.1
80	$23.2 \pm 0.3 \pm 1.1$	28.0	21.9	27.0
100	$21.3 \pm 0.2 \pm 1.0$	25.4	19.7	24.4

u Tablici 6.5 za sve temperaturne vrijednosti dostupne u KADoNIS v0.3 bazi. Izvori sistematskih nepouzdanosti jednaki su onima navedenima za nepuzdanost snaga rezonanci iz Poglavlja 6.3.6. Sa Slike 6.3.14 i Tablice 6.5 jasno je da su ispod 10 keV rezultati s n_TOF postrojenja u boljem slaganju s vrijednostima iz ENDF/B-VII.0 baze, dok u rasponu 15 keV – 50 keV s onima iz ENDF/B-VII.1 baze. Budući je po pitanju podataka za uhvat neutrona na ^{58}Ni ENDF/B-VII.0 predstavnica ostalih značajnih baza podataka poput JENDL-4.0, JEFF-3.1.2, CENDL-3.1 i ROSFOND-2010 [72], podaci s n_TOF postrojenja snažno ukazuju na potrebu izmjene općeprihvaćenih podataka.

Najnoviji rezultati s n_TOF postrojenja podupiru teorijske rezultate iz Reference [75], dobivene korištenjem relativističke kvazičestične aproksimacije slučajnih faza (RQRPA – *eng.* relativistic quasiparticle random phase approximation) formulirane unutar okvira relativističkog Hartree-Bogoliubovljevog (RHB) modela [76]. Slika 6.3.15

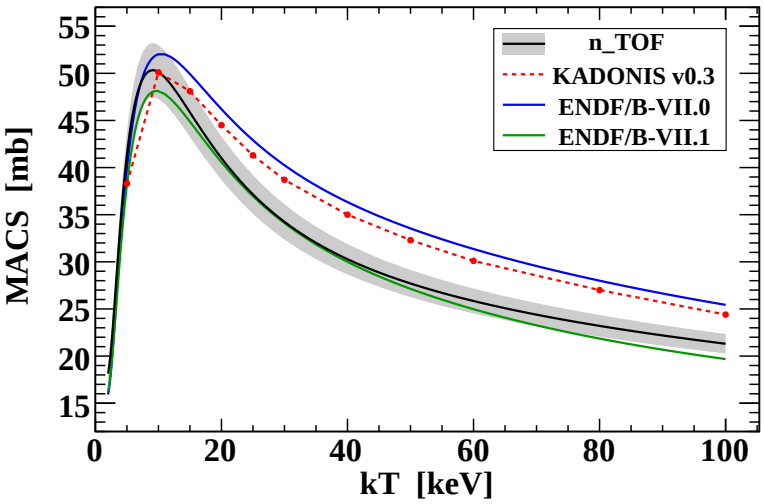

Slika 6.3.14 — Maxwellovski usrednjeni udarni presjeci unutar temperaturnog raspona of astrofizičkog značaja. Zasjenjeno područje prikazuje područje standardne nepouzdanosti eksperimentalnih podataka s n_TOF postrojenja.

prikazuje rezultate modela, zajedno s eksperimentlanim podacima iz nekolicine ranijih izvora [12, 77–79]. Globalno smanjenje udarnog presjeka – u skladu s Guberovim pronalaskom [12] – jasno je potvrđeno, posebice u temperaturnom području oko kT= 30 keV, koje je od posebnog značaja za zvjezdanu nukleosintezu. Teorijski rezultati iz Reference [75], izračunati korištenjem potpuno samosuglasnog relativističkog modela srednjeg polja (ekvivalentnog teoriji funkcionala gustoće), također su u dobrom slaganju s ovim opažanjem. Međutim, ispod 20 keV teorijska predviđanja značajno se razilaze s eksperimentalnim podacima, čemu je razlog neprimjenjivost korištenog statističkog Hauser-Feshbachovog modela za gustoću nuklearnih stanja unutar područja niske gustoće stanja. S obzirom da se prva rezonanca za uhvat neutrona na izotopu ^{58}Ni nalazi na 6.9 keV, nedostatak diskretnih nuklearnih stanja ispod ove energije utječe na eksperimentalne MACS vrijednosti sve do 20 keV zbog Maxwellove raspodjele koja se još uvijek značajno proteže preko energija u blizini i ispod prve rezonance na 6.9 keV.

Nekoliko procesa doprinosi ukupnome udarnom presjeku za uhvat neutrona i, prema tome, maxwelloski usrednjenim udarnim presjecima – rezonantni uhvat (RU), izravni uhvat (IU) te izravni-puluizravni (IPI) uhvat [81]. Raniji teorijski izračuni prikazani u Guberovom radu [12] pokazuju da IU i IPI procesi značajno doprinose udarnome presjeku za uhvat neutrona na ^{58}Ni pri niskim energijama. Ovo se posebno odnosi na uhvat neutrona orbitalnog angularnog momenta $\ell = 0$, koji je odgovoran za dio $1/v$ ovisnosti udranog presjeka, doprinoseći više od 30% njegovoj termalnoj vrijednosti. Na višim energijama očekivani doprinos uhvata neutrona orbitalnog angularnog momenta $\ell = 1$ je zanemariv. Štoviše, teorijski model iz Reference [82] predviđa da je doprinos takvih neutrona maxwellovskim prosjecima manji od 1% na svim temperaturama. Što se tiče podataka s n_TOF postrojenja, svi doprinosi uhvatu – rezonantni, izravni i izravni-poluizravni – uzeti su u obzir tijekom prilagodbe podataka programom SAMMY, i to usvajanjem dviju rezonanci na negativnim energijama. Stoga IU i IPI doprinose nije bilo potrebno posebno razmatrati.

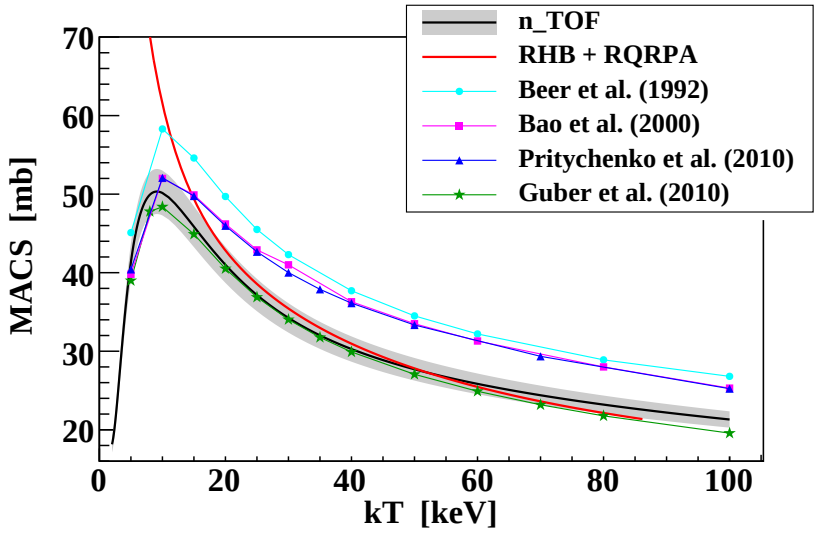

Slika 6.3.15 — Maxwellovski usrednjeni udarni presjeci s n_TOF postrojenja u usporebi s ranijim eksperimentalnim podacima [12, 77–79] i teorijskim rezulatima iz Reference [75].

Utjecaj upravo određenih vrijednosti maxwellovski usrednjenih udarnih presjeka na nukleosintezu *s*-procesom istražen je programskim NuGrid kodom MPPNP [83], uz pretpostavku punog $25M_{\odot}$ modela s početnim metalnim sadržajem od $Z = 0.02$ [84]. Utvrđeno je da smanjenje maxwellovskog prosjeka od 12% pri 30 keV – s obzirom na posljednju KADoNIS v0.3 kompilaciju (vidjeti Tablicu 6.5) – u masivnim zvijezdama vodi na porast od 60% u sadržaju ^{58}Ni zaostalom po završetku *s*-procesa. Uzrok ovakvog ishoda je manja učinkovitost trošenja ^{58}Ni zbog niže vrijednosti prosječnog udarnog presjeka. No uz iznimku sadržaja samog ^{58}Ni, raspodjela preostalog zvjezdanog materijala ostaje nepromijenjenom jer je zastupljenost ^{58}Ni mnogo manja (4.3% [7]) od zastupljenosti ^{56}Fe kao dominantnog sjemena *s*-procesa te je po završetku *s*-procesa ^{58}Ni temeljito iscrpljen neutronskim uhvatima, neovisno o pretpostavci ranije ili najnovije vrijednosti maxwellovskog prosjeka.

6.4 Simulacije neutronske pozadine

6.4.1 Motivacija

Na n_TOF postrojenju par C_6D_6 detektora koristi se već čitavo desetljeće u mjerenjima neutronskih uhvata. Od samog početka upotrebe detaljno su ispitani i optimizirani kako bi osigurali najnižu izvedivu neutronsku osjetljivost [61]. Optimizacija je provedena proučavanjem učinkovistosti ε_n za detekciju γ-zraka emitiranih po uhvatu neutrona na komponentama C_6D_6 detektora. Na osnovi njenog odnosa spram maksimalne učinkovitosti $\varepsilon_\gamma^{\max}$ za detekciju γ-zraka, definirana je neutronska osjetljivost $\varepsilon_n/\varepsilon_\gamma^{\max}$ dvaju detektora. No u stvarnom eksperimentu ukupnim pozadinskim događajima ne doprinose jedino reakcije na samim detektorima, već i reakcije bilo na kojoj komponenti unutar eksperimentalne prostorije. Značajan doprinos pozadini izazvanoj neutronima uzrokovan je njihovim raspršenjem na komponentama najbližim samim detektorima, tj. onima u neposrednoj blizini ozračenog uzorka.

Doprinos pozadinskim događajima uzrokovan raspršenjem neutrona na samome uzorku – tzv. *neutronska pozadina* – ne može se zasebno mjeriti, već ga je potrebno odrediti neizravim metodama. Precizna identifikacija neutronske pozadine zahtijeva fizikalno odvajanje neutronskih uhvata od neutronskih raspršenja na danome uzorku. S obzirom da ovo nije nimalo lak zadatak, detaljne simulacije ostaju jedini pouzdan i uopće moguć pristup problemu. Jasno je da će neutronska pozadina biti od najvećeg značaja za uzorke čiji je udarni presjek za raspršenje neutrona znatno viši od onoga za njihov uhvat. Neutronska osjetljivost korištenih detektora može poslužiti za procjenu nužnosti jasne identifikacije neutronske pozadine. Ako je unutar energijskog raspona dostupnog toka neutrona omjer između udarnog presjeka za uhvat i raspršenje neutrona na danome uzorku usporediv s neutronskom osjetljivošću, tada je za očekivati da će neutronska pozadina predstavljati značajan doprinos mjerenim podacima. Ova okolnost prepoznata je upravo u slučaju uzorka ^{58}Ni.

6.4.2 Pregled sadržaja GEANT4 simulacija

Za pokretanje simulacija korištena je inačica 9.6.p01 programskog paketa GEANT4, koja se za propagaciju neutrona energije do 20 MeV oslanja na popisane udarne presjeke iz ENDF/B-VII baze podataka [13, 18].

Geometrija

Geometrija eksperimentalne prostorije s n_TOF postrojenja detaljno je reproducirana unutar GEANT4 simulacije za određivanje neutronske pozadine. Posebna pažnja posvećena je preciznoj reprodukciji unutrašnjosti prostorije, koja nije pravokutna, već nakošena u prostoru. U slučaju eksperimenata koji koriste snažne neutronske snopove, betonski zidovi prostorije moraju se uzeti u obzir jer su zahvaljujući visokom sadržaju vodika vrlo bitne lokacije neutronskih uhvata kojima se oslobađaju γ-zrake energije 2.2 MeV. Geometrijski opis dvaju C_6D_6 detektora u potpunosti je prenesen iz simulacija za određivanje monokromatskih spektara potrebnih za izračun težinske funkcije (Poglavlje 6.3.3). Usvajanjem potpuno jednakog geometrijskog postava osigurane su jednake detekcijske učinkovitosti u objema simulacijama. Stoga su krajnji rezultati dviju simulacija potpuno konzistentni, čineći težinske funkcije izravno primjenjivima na rezultate posljednje simulacije za određivanje neutronske pozadine. Osim samih detektora, usvojena geometrija također uključuje cjevovod za provođenje neutronskog snopa, njegove potpornje, aluminijski pod, izmjenjivač uzoraka te Kalorimetar Potpune Apsorpcije (TAC – *eng.* Total Absorption Calorimeter) i njegovu nosivu strukturu.

Fizikalni procesi

Izgradnja fizikalnog okvira simulacije sastoji se od pozivanja odgovarajućih čestica i fizikalnih procesa. Popis aktivnih čestica uspostavljen je pozivom na unaprijed pripremljene programske pakete: G4BaryonConstructor, G4LeptonConstructor, G4BosonConstructor, G4IonConstructor, G4MesonConstructor i G4ShortLivedConstructor. Popis općenitih fizikalnih procesa – vezanih uz sve čestice osim neutrona – također je uspostavljen pozivom na unaprijed pripremljene procedure: G4EmStandardPhysics, G4DecayPhysics, G4RadioactiveDecayPhysics, G4IonPhysics, G4EmExtraPhysics, G4StoppingPhysics, G4HadronElasticPhysics i G4HadronInelasticQBBC. Posebna pažnja posvećena je neutronskim procesima, koji su pozivani jedan za drugim temeljem njihove preciznosti i primjenjivosti unutar danog energijskog područja. Od procesa su pozvani: elastično i neelastično raspršenje neutrona, neutronski uhvat i neutronima izazvana fisija. Fizikalni modeli izabrani za pojedini proces navedeni su u Tablici 6.6, zajedno s pripadnim udarnim presjecima. Svim modelima pripisan je energijski raspon u skladu s općim preporukama. Određivanje energijskog raspona pojedinih udarnih presjeka prepušteno je unutarnjim procedurama programskog paketa GEANT4, s obzirom da ne sadrže sve kolekcije udarih presjeka podatke za sve poznate nuklide.

Budući da GEANT4 nudi mnoštvo modela za provedbu fizikalnih procesa unutar danog energijskog područja, potrebno je odlučiti koje od njih izabrati. Pored završnih izbora, Tablica 6.6 navodi i najbliže zamjene koje su bile razmatrane. Do 20 MeV G4NeutronHP paket nudi zasebne modele visoke preciznosti koji se temelje na izravnom praćenju detaljnih udarnih presjeka iz ENDF/B-VII baze podataka [13, 18]. Iz Tablice 6.6 može se primjetiti da je G4NeutronHPInelastic model za neelastično raspršenje u potpunosti izbjegnut. Iako ovakav izbor nije nužno opća preporuka ovoga rada, proveden je u svrhu optimalne reprodukcije eksperimentalnih podataka za uzorak prirodnog ugljika. Prema tome, ispod 10 GeV korištena su dva modela svojstvena GEANT4 paketu – G4BinaryCascade i G4CascadeInterface (tzv. Bertinijeva kaskada).

Tablica 6.6 — Fizikalni modeli i udarni presjeci korišteni za transport neutrona u GEANT4 simulacijama neutronske pozadine.

Proces	Udarni presjek	Model	
		Naziv	**Raspon**
Elastic scattering	G4NeutronHPThermalScatteringData[a]	G4NeutronHPThermalScattering	<4 eV
	G4NeutronHPElasticData[b]	G4NeutronHPElastic	4 eV – 20 MeV
	G4NeutronHPJENDLHEElasticData[c]	G4HadronElastic	>20 MeV
	G4BGGNucleonElasticXS[de]		
Inelastic scattering	G4NeutronHPThermalScatteringData[a]	G4BinaryCascade[g]	<30 MeV
	G4NeutronHPInelasticData[b]	G4CascadeInterface[g]	30 MeV – 10 GeV
	G4NeutronHPJENDLHEInelasticData[c]	G4TheoFSGenerator[h]	>10 GeV
	G4BGGNucleonInelasticXS[df]		
Capture	G4NeutronHPCaptureData[b]	G4NeutronHPCapture	<20 MeV
	G4HadronCaptureDataSet[d]	G4NeutronRadCapture	>20 MeV
Fission	G4NeutronHPFissionData[b]	G4ParaFissionModel[i]	<60 MeV
	G4HadronFissionDataSet[d]	G4LFission	>60 MeV

[a] Navedeni raspon: < 4 eV
[b] Navedeni raspon: < 20 MeV
[c] Navedeni raspon: $\lesssim 3$ GeV
[d] Navedeni raspon: < 100 TeV
[e] Zamjena: G4HadronElasticDataSet
[f] Najbliža zamjena: G4NeutronInelasticCrossSection
Dodatna zamjena: G4HadronInelasticDataSet
[g] Zamjena: G4NeutronHPInelastic (<20 MeV) i G4NeutronHPThermalScattering (<4 eV)
[h] Nadopuna: G4StringChipsParticleLevelInterface, G4QGSMFragmentation i G4QGSModel
Zamjenska nadopuna: G4GeneratorPrecompoundInterface, G4LundStringFragmentation i G4FTFModel
[i] Zamjena: G4NeutronHPFission (<20 MeV)

Za fisiju je izabran G4ParaFissionModel umjesto G4NeutronHPFission modela jer drugi ne proizvodi fisijske fragmente. No valja uzeti u obzir da G4ParaFissionModel ne proizvodi toliko zakašnjelih neutrona koliko to čini G4NeutronHPFission model. Tablica 6.6 također navodi izabrane udarne presjeke prema porastu u energiji. Nedavno je Barashenkov-Glauber-Gribovljeva parametrizacija udarnih presjeka za neelastično raspršenje iz G4BGGNucleonInelasticXS paketa dobila prednost pred Laidlaw-Wellischevom iz G4NeutronInelasticCrossSection paketa, zbog čega je i korištena u ovom radu.

Simulacija toka neutrona

Tijekom simulacije izravno se prati spektar toka neutrona koji prolazi površinom uzorka, a dobiven je množenjem spektra neutrona sa Slike 6.2.2 i energijske ovisnosti faktora presretanja snopa sa Slike 6.3.7. Dobiveni spektar neutrona koji prolaze uzorkom promjera 2 cm prikazan je na Slici 6.4.1. Radi usporedbe prikazan je i oblik spektra prije množenja energijskom ovisnošću faktora presretanja snopa. Praćenje toka neutrona izvedeno je usvajanjem algoritma za praćenje proizvoljne raspodjele, čija je polazna točka generator jednoliko raspodjeljenih slučajnih brojeva. U svrhu optimizacije radnog vremena računala, zasebne simulacije provedene su za energije upadnih neutrona u rasponu između 25 meV – 200 keV, 200 keV – 10 MeV te 10 MeV –10 GeV, kao što je označeno na Slici 6.4.1. Relativni udjeli toka neutrona koji prolazi površinom uzorka unutar ovih energijskih intervala iznose 29.9%, 45.0% i 25.1%, respektivno. Profil neutronskog snopa opisan je dvodimenzionalnim gaussijanom, eksperimentalno određene horizontalne i vertikalne širine od $\sigma_x = \sigma_y = 7.5$ mm.

Budući da korištena inačica 9.6.p01 GEANT4 programskog paketa nije prilagođena istovremenom korištenju više računalnih jezgara, višestruke simulacije pokrenute su kako bi se prikupila čim bogatija statistika. Pri tome treba imati na umu da generatori slučajnih brojeva iz GEANT4 paketa proizvode jednak niz brojeva u svakom pokretanju. Na temelju trenutka pokretanja simulacije ovim nizovima pripisan je dodatan

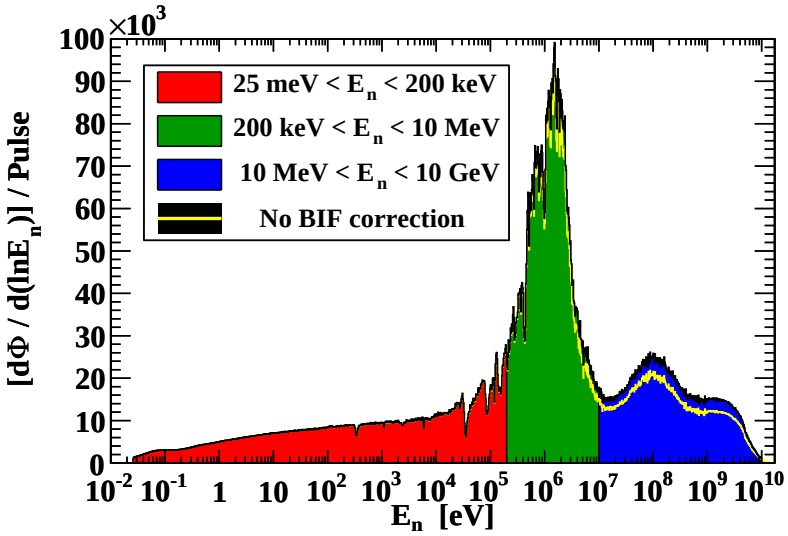

Slika 6.4.1 — Spektar neutrona koji prolazi površinom uzorka, usvojen za praćenje u GEANT4 simulacijama neutronske pozadine. Žuta linija prikazuje oblik spektra prije množenja energijskom ovisnošću faktora presretanja snopa. Za različito obojene energijske intervale provedene su zasebne simulacije u svrhu optimizacije radnog vremena računala.

slučajni faktor, zahvaljujući kojem svako pokretanje simulacije u konačnici rezultira jedinstvenim nizom slučajnih brojeva.

Unutarnje procedure

Osnovni cilj simulacije je odrediti neutronsku pozadinu uzrokovanu neutronima raspršenim na samome uzorku. Imajući to u vidu, svi upadni neutroni moraju proći kroz uzorak uz nezanemarivu interakciju. U suprotnome, neutron se može raspršiti na cjevovodu ispred uzorka ili može proći uzorkom bez raspršenja na njemu. Ovakav doprinos pozadinskim događajima već je sadržan unutar pozadine uzrokovane prolaskom snopa kroz eksperimentalnu prostoriju te je kao takav već izmjeren ozračivanjem čitavog postava s uklonjenim uzorkom. Kako se ovakvi događaji ne bi uzeli dva puta u obzir, svi neutroni koji ne međudjeluju s uzorkom odmah se odbacuju. Reakcije poput uhvata neutrona odmah se prepoznaju kao bitne jer dolazi do promjene čestice. No u slučaju elastičnog raspršenja izlazni neutron identičan je ulaznome, stoga je uvjet nezanemarivosti elastičnog raspršenja bilo potrebno manualno nametnuti. Ovaj uvjet postavljen je na kumulativni kut raspršenja na izlazu iz uzorka, koji je morao biti veći od 0.2°.

Struktura ispisanih podataka

Izlazni podaci sastoje se od ukupnog broja neutrona emitiranih u smjeru uzorka te detaljnog popisa podataka za svaki događaj detektiran C_6D_6 detektorima. Ovi podaci uključuju energiju upadnog neutrona, energiju deponiranu u aktivnom dijelu detektora, pripadno vrijeme proleta te podatke o vrsti, porijeklu i mehanizmu nastanka detektirane čestice. Valja naglasiti da su tijekom simulacije neutroni emitirani pri ulazu u eksperimentlanu prostoriju na udaljenosti od 182 m od spalacijske mete. Prema tome, da bi se rekonstruirao eksperimentalni analogon $\mathrm{ToF}_{\mathrm{exp}}$ vremena proleta neutrona, vrijeme proleta $\mathrm{ToF}_{\mathrm{sim}}$ dobiveno iz simulacije bilo je nužno uvećati za vremenski interval $\mathrm{ToF}_0(E_n)$ potreban početnome neutronu za propagaciju duž puta duljine 182 m:

$$\mathrm{ToF}_{\mathrm{exp}} = \mathrm{ToF}_{\mathrm{sim}} + \mathrm{ToF}_0(E_n) \tag{6.4.1}$$

6.4.3 Kaskade γ-zraka

Dva su bitna pitanja koja se uobičajeno vežu uz simulaciju γ-kaskada GEANT4 programskim paketom: prate li energije γ-zraka ikakve dostupne podatke (nasuprot umjetnim kontinuiranim raspodjelama) i jesu li korelacije između γ-zraka uzete u obzir? Kako bi se odgovorilo na ova pitanja, provedene su posebne GEANT4 simulacije u sklopu kojih su neutronima ozračeni materijali koji se sastoje od jedne jedine izotopne komponente: ^{23}Na, ^{28}Si, ^{56}Fe, ^{58}Ni, ... Odmah po emisiji γ-zraka iz neutronskog uhvata, njihove energije su zabilježene bez potrebe za njihovom interakcijom s okolnim materijalom. Slika 6.4.2 uspoređuje dobiveni spektar za ^{28}Si s energijama γ-zraka popisanima u Referenci [86]. ^{28}Si izabran je zbog relativno malenog broja γ-zraka, čime je olakšana vizualna usporedba. Detaljna provjera uskih spektralnih vrhova vodi do zaključka da su kaskade γ-zraka doista simulirane prateći dostupne eksperimentalne podatke. No valja naglasiti da se kontinuirane energijske raspodjele doista koriste u slučaju nedostatka takvih podataka [87]. Kontinuirani spektar van oštrih vrhova sa Slike 6.4.2 i činjenica da visine vrhova, odnosno intenziteti γ-zraka

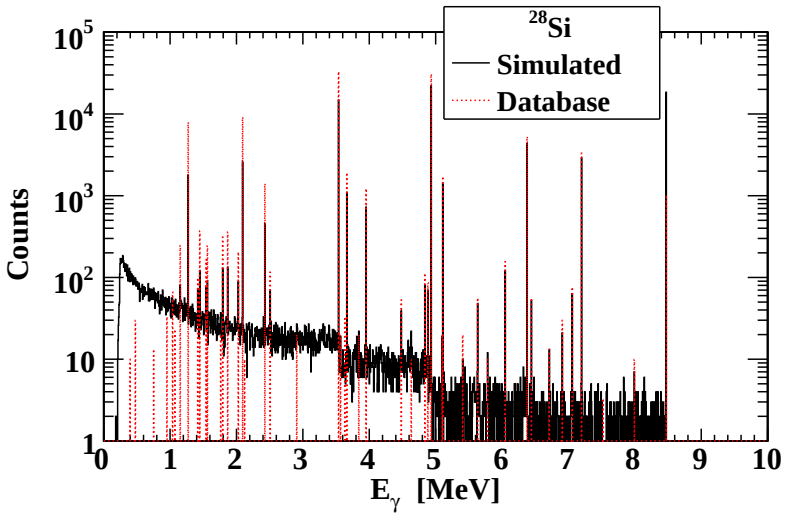

Slika 6.4.2 — Simulirani spektar γ-zraka emitiranih po uhvatu termalnih neutrona na izotopu ^{28}Si. Rezultati simulacije uspoređeni su s poznatim energijama i intenzitetima γ-zraka iz Reference [86].

nisu vjerno reproducirani jasan su potpis nedostatka korelacija. Krajnji zaključak analize je da su γ-zrake simulirane neovisno o redoslijedu kaskade dozvoljenom strukturom nuklearnih stanja. Nadalje, kako bi se reproducirala energija pobuđenja složene jezgre, energija posljednje emitirane γ-zrake određena je zahtjevom za očuvanjem energije. Upravo ovo je uzrok proširenja simuliranih spektara između vrhova koji se podudaraju s detaljno popisanim podacima. Iako korisnik može isključiti proizvodnju posljednje γ-zrake, njena produkcija od ključne je važnosti za ovaj rad. Naime, potreba za njome nametnuta je metodom primjene težinske funkcije koja se temelji na pretpostavci da je zbroj energija svih γ-zraka iz pojedine kaskade jednak energiji pobuđenja složene jezgre.

Nedostatak korelacija između γ-zraka značajno utječe na simulirane spektre detektiranih događaja. Kako bismo prikazali ovaj efekt, simulacije za određivanje neutronske pozadine provedene su za uzorak ^{197}Au, koji se koristi za nalaženje faktora normiranja pri izračunu vjerojatnosti uhvata (vidjeti Poglavlje 6.3.5). ^{197}Au posebno je prikladan kao referentna točka za usporedbu spektara γ-zraka zbog udarnog presjeka za uhvat neutrona koji je – prije vrlo velike rezonance na 4.9 eV – mnogo veći od onog za njihovo elastično raspršenje. Stoga će se i eksperimentalni i simulirani spektri sastojati gotovo u potpunosti od detekcije γ-zraka iz ^{197}Au(n,γ) reakcije. Gornji okvir sa Slike 6.4.3 prikazuje razliku između simuliranih i eksperimentalnih spektara energije deponirane γ-zrakama, i to za oba C_6D_6 detektora. Srednji okvir prikazuje spektre početnih energija neutrona izračunatih iz vremena proleta. Iz ovih spektara može se primjetiti jasna razlika između eksperimentalnih i simuliranih rezultata. Dok je razlika u obliku spektara deponiranih energija očita (zbog detekcijske učinkovitosti ovisne o energiji γ-zraka), razliku u njihovoj visini nije toliko jednostavno uočiti u logaritamskoj skali. Budući da svim spektrima iz gornjeg okvira savršeno odgovaraju oni iz srednjeg – imajući jednake brojeve događaja – razlika u visini spektara lako se može potvrditi sa srednjeg okvira, posebno s dijela ispred zasićene rezonance na 4.9 eV. Međutim, nakon primjene težinske funkcije i na eksperimentalne i na simulirane podatke – uz pripadne spektre prikazane donjim okvirom Slike 6.4.3 – svi spektri savršeno se slažu.

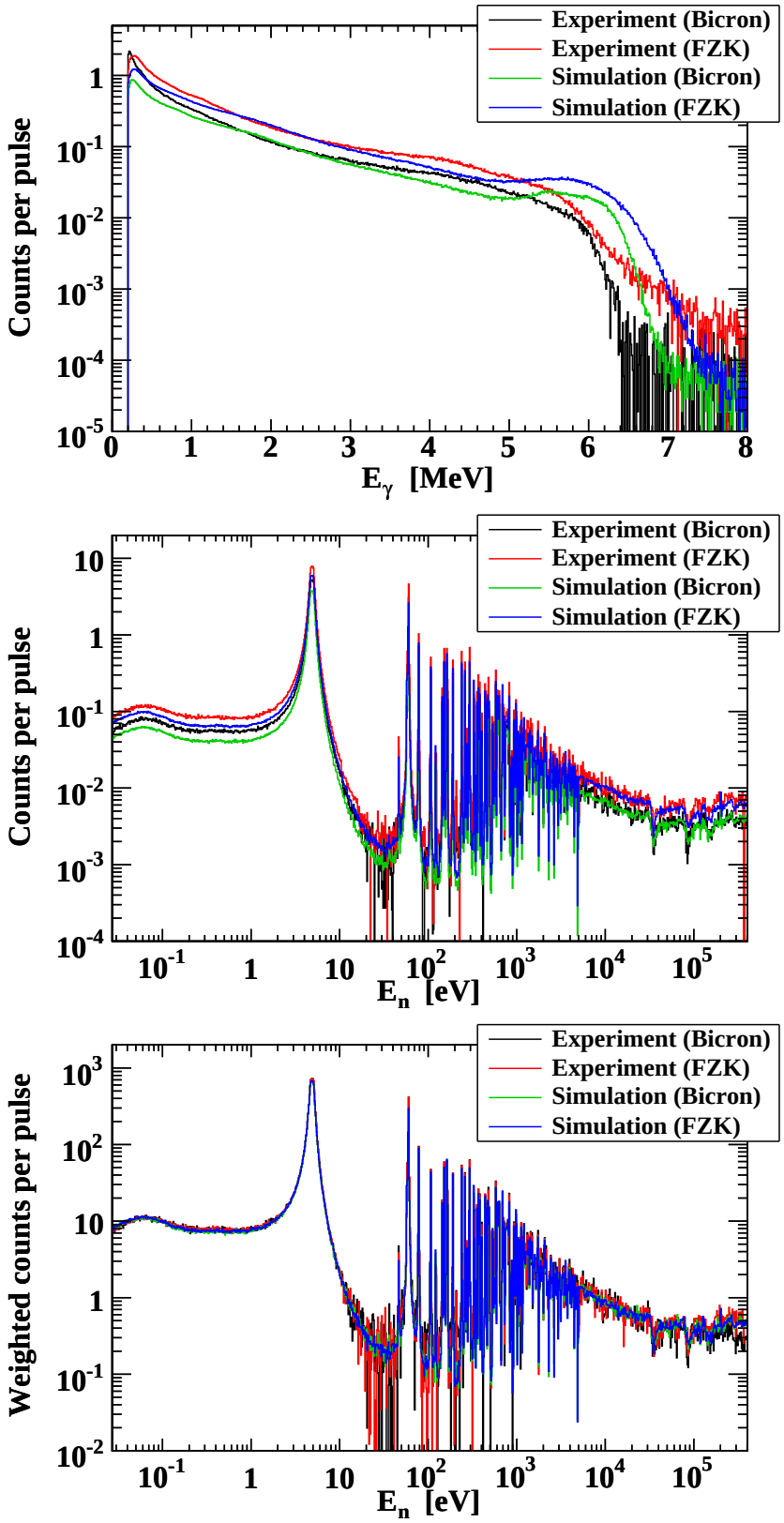

Slika 6.4.3 — Usporedba eksperimentalnih i simuliranih rezultata za uhvat neutrona na izotopu ^{197}Au. Spektri su prikazani za oba C_6D_6 detektora. Gornji okvir: energija deponirana γ-zrakama. Srednji okvir: spektar energija rekonstruiranih iz vremena proleta. Donji okvir: spektar energija rekonstruiranih iz vremena proleta, nakon primjene težinske funkcije.

Ovaj ishod zajamčen je osnovnim principima metode primjene težinske funkcije, koja umjetnom manipulacijom odaziva detektora čini njihovu detekcijsku učinkovitost neovisnom o redoslijedu emisije kaskade γ-zraka.

Pokazali smo da su simulacije transporta neutrona programskim paketom GEANT4 postale visoko pouzdane i u mogućnosti reproducirati eksperimentalne podatke, uz uvjet da su težinske funkcije uzete u obzir. Također, ponovno smo potvrdili ključnu ulogu same težinske funkcije, koja vodi do jednakih rezultata nakon primjene na spektre istinski različitih kaskada γ-zraka. Stoga nastavljamo s visokim pouzdanjem analizu simulirane vjerojatnosti uhvata, koju iz simuliranih podataka računamo na potpuno jednak način kao i eksperimentalnu vjerojatnost uhvata iz mjerenih podataka.

6.4.4 Neutronska osjetljivost

Prije predstavljanja razultata za neutronsku pozadinu, proučit ćemo neutronsku osjetljivost korištenih detektora. Pri tome pratimo pristup iz Reference [61] – ranije usvojen na n_TOF postrojenju – koji definira neutronsku osjetljivost kao omjer $\varepsilon_n/\varepsilon_\gamma^{\max}$ između učinkovitosti ε_n za detekciju neutrona (posredstvom sekundarnih čestica proizvedenih neutronskim reakcijama) i maksimalne učiknovitosti $\varepsilon_\gamma^{\max}$ za detekciju γ-zraka danim detektorom. Geometrijski postav ranije korišten u Referenci [61] sastoji se od izoliranih detektora ozračenih neutronima. Osjetljivost izračunatu po ovakvim uvjetima nazivamo *intrinzičnom neutronskom osjetljivošću*. Najnovije simulacije omogućile su uključiti i ostatak eksperimentalne prostorije, stoga osjetljivost izračunatu ozračivanjem detekotra u takvom okruženju nazivamo *sveukupnom neutronskom osjetljivošću*. U svrhu određivanja neutronske osjetljivosti korištene su simualcije opisane u Poglavlju 6.4.2. Jedina razlika odnosi se na emisiju primarnih čestica. Umjesto emisije kolimiranoga snopa na ulazu u eksperimentalnu prostoriju, i γ-zrake i neutroni – potrebni za određivanje $\varepsilon_\gamma^{\max}$ i ε_n – izotropno su emitirani iz točkastog izvora na mjestu uzorka.

Za određivanje maksimalne učinkovitosti $\varepsilon_\gamma^{\max}$ detektori su ozračeni nekoliko puta monoenergijskim γ-zrakama, svaki put različite energije. Tijekom izračuna detekcijske učinkovitosti ε_γ kao omjera između broja detektiranih i emitiranih fotona, u obzir je uzet donji prag od 200 keV postavljen na deponirane energije, po uzoru na eksperimentalnu proceduru. Pri tome intrinzična učinkovitost nije odvojena od geometrijske (na temelju prostornog kuta obuhvaćenog detektorima). Stoga ε_γ predstavlja ukupnu detekcijsku učinkovitost. Budući da donji prag od 200 keV značajno utječe na ε_γ na nižim energijama, maksimum $\varepsilon_\gamma^{\max}$ pomaknut je prema 900 keV te iznosi 1.81% za Bicron i 2.97% za FZK detektor.

U svrhu određivanja učinkovistosti ε_n za detekciju neutrona, detektori su ozračeni neutronima izotropno emitiranima iz točkastog izvora na mjestu uzorka, prateći izoletargičnu $(1/E_n)$ raspodjelu energija. Zadržan je donji prag na deponirane energije od 200 keV pri zadržavanju događaja kao detektiranih. Kao što je ranije naglašeno, ozračene su dvije konfiguracije detektora. Prva, koja se sastoji od pojedinog izoliranog detektora bez prisutnosti drugoga i ostatka eksperimentalne prostorije, vodi na intrinzičnu neutronsku osjetljivost. Druga, koja se sastoji od cjelokupnog eksperimentalnog postava usvojenog u simulacijama neutronske pozadine, vodi na sveukupnu neutronsku osjetljivost. U skladu s ε_γ, nisu provedene posebne geometrijske korek-

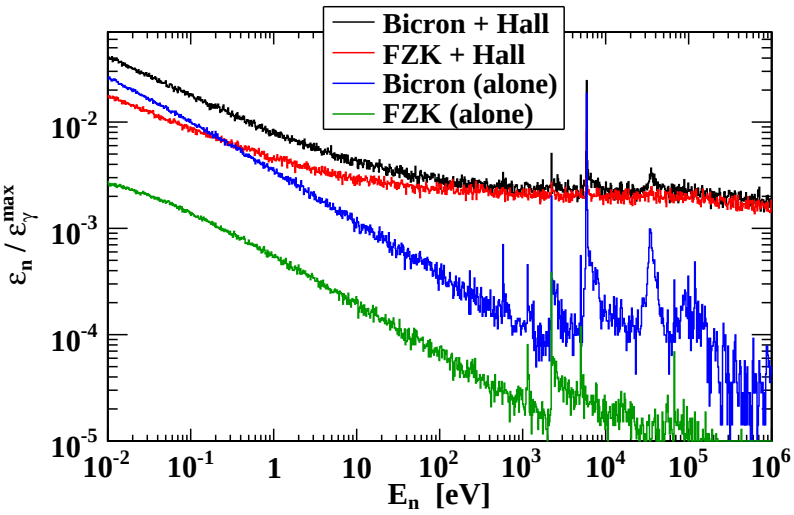

Slika 6.4.4 — Intrinzična i sveukupna neutronska osjetljivost dvaju korištenih C_6D_6 detektora (vidjeti glavni tekst za pojašnjenje pojmova i pojedinosti emisije neutrona).

cije pri izračunu ε_n. Stoga se unutar neutronske osjetljivosti $\varepsilon_n/\varepsilon_\gamma^{max}$ geometrijski doprinosi objema učinkovitostima implicitno poništavaju. Slika 6.4.4 prikazuje neutronsku osjetljivost detektora u objema konfiguracijama. Iz rezultata za izolirane detektore jasno je da po narudžbi izgrađen FZK detektor pokazuje znatno manju neutronsku osjetljivost od Bicron detektora. Uzrok ovome jest oklop od ugljičnih vlakana u slučaju FZK detektora, nasuprot aluminijskom oklopu Bicron detektora. Aluminij je također i uzrok istaknute rezonantne strukture koja se pojavljuje ponajviše iznad 1 keV u podacima Bicron detektora. U odnosu na njega, neutronska osjeljivost FZK detektora dodatno je umanjena višom učinkovitošću ε_γ^{max} za detekciju γ-zraka, koja je posljedica bogatijeg sadržaja C_6D_6 tekućine (1027 ml za FZK; 618 ml za Bicron). U drugoj konfiguraciji neutronske osjetljivosti obaju detektora značajno su više te pokazuju gotovo jednaku konstantnu vrijednost iznad 10 eV. Usrednjavanjem podataka između 10 eV i 1 MeV, određena je približna vrijednost sveukupne neutronske osjetljivosti obaju detektora od 2.0×10^{-3}. Valja imati na umu da, prema usvojenoj definiciji, neutronska osjetljivost je odaziv detektora na neutrone *dane energije*, umjesto *pri danoj energiji* (izračunatoj iz vremena proleta). Međutim, na istinsku neutronsku pozadinu, opisanu u sljedećem poglavlju, značajno utječu energijska ovisnost toka neutrona i svojstva samog uzorka na kojem se neutroni primarno raspršuju.

6.4.5 Neutronska pozadina

Rezultati za ^{nat}C uzorak

U principu, približna razina neutronske pozadine može se odrediti eksperimentalno ozračivanjem uzorka čiji je udarni presjek za uhvat neutrona mnogo niži od onoga za njihovo raspršenje. Budući da je prirodni ugljik upravo takav materijal, kontrolni ^{nat}C uzorak širine 1 cm te promjera 2 cm ozračen je neutronskim snopom tijekom ^{58}Ni eksperimenta. Visoka čistoća uzorka (99.95%) potvrđena je kemijskom analizom na Paul Scherrer Institutu, čime je isključena mogućnost onečišćenja izotopima visokog udarnog presjeka za uhvat neutrona. Analogon vjerojatnosti uhvata za ugljik nadalje ćemo nazivati *vjerojatnošću detekcije*. Mjerena vjerojatnost detekcije – izračunata potpuno jednakom procedurom kao i vjerojatnost uhvata za ^{58}Ni – usvojena je kao refer-

entna točka za ocjenu kvalitete simulirane neutronske pozadine. Usporedba između ukupnih eksperimentalnih i simuliranih rezultata prikazana je Slikom 6.4.5. Sasvim je jasno da simulacije uspješno rekonstruiraju mjerene podatke unutar čitavog energijskog područja bitnog za mjerenja uhvata na n_TOF postrojenju – od termalnih energija sve do nekoliko stotina keV.

Sa Slike 6.4.5 može se primjetiti da se vjerojatnost detekcije za ^{nat}C ne sastoji isključivo od neutronske pozadine. Suprotno početnim očekivanjima, ozračivanje ^{nat}C uzorka neutronskim snopom s n_TOF postrojenja uzrokuje značajno stvaranje β-radioaktivnih izotopa, koji se eksperimentalno opažaju detekcijom emitiranih β-zraka. Neelastična ^{12}C$(n,p)^{12}$B reakcija, čiji se kanal otvara na energiji od približno 14 MeV, daleko je najzaduženija za ovaj ishod. Stvoreni ^{12}B izotop je β^--radioaktivan sa srednjom energijom elektrona od $\langle E_\beta \rangle$ = 6.35 MeV i vremenom poluživota od $T_{1/2}$ = 20.2 ms. Vrlo visoka energija emitiranih β-zraka omogućuje im doseći bilo koji od C_6D_6 detektora i deponirati u njihovom aktivnom dijelu značajnu količinu energije nošene iz β-raspada. Nadalje, zbog vremena poluživota od 20.2 ms gotovo čitava eksponencijalna raspodjela raspada (ne)prikladno upada unutar vremenskog prozora od 96 ms, korištenog za prikupljanje podataka (vidjeti Poglavlje 6.2.5). Kao što je objašnjeno u Poglavlju 6.3.4, tijekom analize podataka energija je pripisana upadnom neutronu na temelju trenutka pojave elektroničkog pulsa. U slučaju pravog uhvata neutrona ovaj trenutak odgovara njegovom vremenu proleta. Međutim, trenutak pojave pulsa koji odgovara detekciji β-zrake po prirodi je slučajan, određen raspadom nestabilne jezgre. Stoga je korelacija između vremena detekcije i energije upadnog neutrona izgubljena, dok su energije neutrona iznad 14 MeV – što je prag ^{12}C$(n,p)^{12}$B reakcije – rekonstruirane unutar termalnog i epitermalnog područja, kao što je prikazano izdvojenim grafom sa Slike 6.4.5. Pored doprinosa β-radioaktivnih izotopa stvorenih neelastičnim reakcijama na ^{nat}C uzorku, prava neutronska pozadina također je posebno izdvojena. U slučaju uzoraka bitnih zbog uhvata neutrona – poput ^{58}Ni i ^{197}Au – neu-

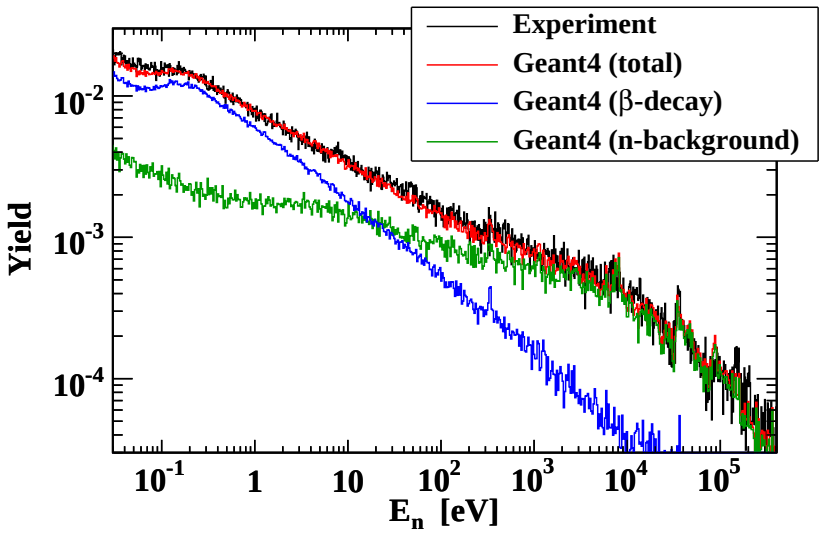

Slika 6.4.5 — Vjerojatnost detekcije za uzorak ^{nat}C promjera 2 cm. Izvrsno slaganje postignuto je između eksperimentalne i ukupne simulirane vjerojatnosti detekcije. U slučaju simuliranih rezultata, prava neutronska pozadina odvojena je od detekcije β-zraka, ponajviše emitiranih iz raspada ^{12}B izotopa stvorenih ^{12}C$(n,p)^{12}$B reakcijom.

tronsku pozadinu smatramo sastavljenom od svih događaja koji nisu uzrokovani detekcijom γ-zraka stvorenih uhvatom neutrona unutar samog uzorka. U slučaju ^{nat}C uzorka smatramo da neutronskoj pozadini doprinose svi događaji osim onih koji se odnose na detekciju β-zraka (detektiranih izravno ili posredstvom sekundarnih γ-zraka) stvorenih neelastičnim reakcijama unutar uzorka. Prema definiciji, β-zrake stvorene neelastičnim reakcijama van uzorka također doprinose neutronskoj pozadini.

Počevši od termalnih energija, stvaranje ^{12}B izotopa daleko dominira neelastičnim doprinosom vjerojatnosti detekcije. Iako je intenzitet stvaranja ^{8}Li reakcijom ^{12}C$(n, p + \alpha)^{8}$Li usporediv sa stvaranjem ^{12}B – pri čemu je ^{8}Li također β^--radioaktivan s $\langle E_\beta \rangle$ = 6.20 MeV – zbog duljeg vremena poluživota od $T_{1/2}$ = 840.3 ms većina β-zraka detektirana je izvan vremenskog prozora od 96 ms. Dodatni β^--radioaktivni izotopi koji zanemarivo doprinose vjerojatnosti detekcije uključuju ^{13}B, ^{9}Li i ^{6}He. Stvoren ^{13}C$(n, p)^{13}$B reakcijom, izotop ^{13}B je jasan potpis prisutstva izotopa ^{13}C u prirodnom ugljiku. Nekoliko β^+-radioaktivnih izotopa poput ^{11}C, ^{10}C i ^{9}C također su opaženi u rezultatima simulacije, doprinoseći vjerojatnosti detekcije ponajviše kroz detekciju γ-zraka iz anihilacije pozitrona. Neki od izotopa proizvedeni su različitim reakcijskim kanalima, poput ^{6}He za koji je opaženo barem 8 različitih reakcija. U ilustrativne svrhe navodimo i primjer opažene ^{12}C$(n, n + 2p + \pi^+)^{9}$Li reakcije koja ukazuje da je čak i stvaranje (egzotičnih) mezona uzeto u obzir u GEANT4 simulacijama.

Slika 6.4.5 od središnje je važnosti u razumijevanju neutronske pozadine mjerene s uzorkom ^{nat}C. Iz opažanja da se ispod 1 keV neutronska pozadina razilazi s ukupnom vjerojatnošću detekcije zaključujemo da se eksperimentalni podaci za ^{nat}C uzorak mogu koristiti za procjenu neutronske pozadine jedino iznad ovog energijskog praga. Nadalje, prag ^{12}C$(n, p)^{12}$B reakcije pri 14 MeV ukazuje da sva postrojenja na kojima se proizvode neutroni iznad ove energije mogu očekivati doprinos ovakvih β-raspada pri mjerenju neutronske pozadine s ^{nat}C uzorkom.

U sljedećem odjeljku analizirat ćemo neutronsku pozadinu ^{nat}C uzorka. Svrha ove analize je ukazati na kvalitativna svojstva od kojih je za očekivati da su zajednička neutronskim pozadinama preostalih uzoraka. Iako je potvrđeno da opće značajke neutronske pozadine doista vrijede i za uzorke ^{58}Ni i ^{197}Au, precizna kvantitativna svojstva nužno ovise o njihovim udarnim presjecima, posebice onima za elastično raspršenje neutrona. Zbog ovoga je potrebno provesti detaljne simulacije za svaki uzorak posebno, unutar čitavog energijskog raspona dostupnoga toka neutrona.

Vremenska struktura događaja koji doprinose neutronskoj pozadini prikazana je Slikom 6.4.6 za Bicron detektor. Gornji okvir prikazuje $E_0 - E_{\mathrm{ToF}}$ korelacije, uz E_0 kao energiju upadnih neutrona te E_{ToF} kao energiju izračunatu iz vremena pojave signala, tj. vremena proleta za detektirane događaje. Jedino su duž linije $E_{\mathrm{ToF}} = E_0$ korelacije očuvane te je rekonstrukcija energije upadnog neutrona metodom vremena proleta ispravna. Donji okvir prikazuje projekcije događaja s gornjeg okvira na obje koordinatne osi. Uvjet $E_{\mathrm{ToF}} < 1$ MeV postavljen je na prikazane događaje. Iz razlike između spektara jasno je vidljiv značajan gubitak korelacija između energije neutrona i vremena proleta, koji je uzrokovan dugotrajnim raspršenjem neutrona unutar eksperimentalne prostorije ili zakašnjelom emisijom sekundarnih čestica. Dok je spektar energija rekonstruiranih iz vremena proleta eksperimentalno dostupan, spektar početnih energija neutrona može se odrediti samo simulacijama. Vrijedi primjetiti da u području

$E_0 < 10$ MeV spektar početnih energija neutrona za detektirane događaje prati energijsku ovisnost toka neutrona sa Slike 6.4.1. No tijekom analize podataka lokalnom vrijednošću neutronskog toka korigiran je spektar energija izračunatih iz vremena proleta. S obzirom da ovaj postupak ne uzima u obzir korelacije s početnom energijom neutrona, od ključnog je značaja detaljno simulirati dostupan tok neutrona, umjesto pribjegavati umjetnim (npr. jednolikim) raspodjelama. U konačnici, sa Slike 6.4.6 valja primjetiti i pojavu nekolicine događaja u energijskom području definiranom s $E_0 < E_{\mathrm{ToF}}$. Ovo ne podrazumijeva narušenje kauzalnosti. Riječ je, naime, o toliko zakašnjelim događajima da su detektirani unutar nekog od sljedećih neutronskih pulseva (s obzirom na onaj kojim je dostavljen neutron koji je izazvao reakciju). Kako je u tom slučaju početni trenutak za određivanje vremena signala redefiniran novim

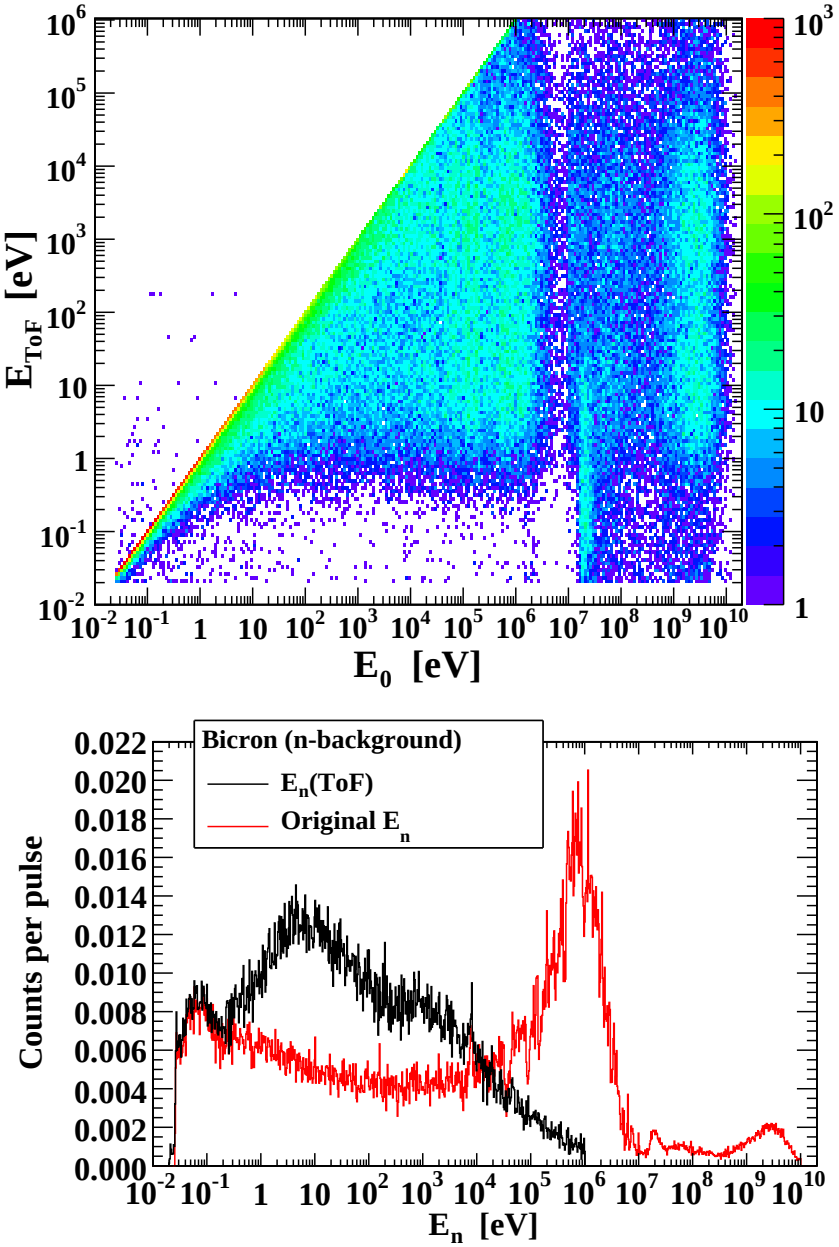

Slika 6.4.6 — Vremenska struktura pozadinskih događaja koji čine neutronsku pozadinu $^{\mathrm{nat}}$C uzorka, prikazana za Bicron detektor. Gornji okvir: $E_0 - E_{\mathrm{ToF}}$ korelacije, uz E_0 kao energiju primarnih neutrona te E_{ToF} kao energiju izračunatu iz vremena proleta. Donji okvir: projekcije na E_0- i E_{ToF}-os. Jedino je E_{ToF}-spektar moguće eksperimentalno odrediti.

γ-bljeskom, svaka korelacija između E_0 i E_{ToF} u potpunosti je izgubljena. Stoga je dovoljno ustvrditi da su takvi događaji uzrokovani raspadom ^{28}Al (vremena poluživota od 2.2 min) aktiviranog uhvatom termalnih neutrona na aluminijskim (^{27}Al) komponentama eksperimentalnog postava u blizini C_6D_6 detektora.

Kao što Slika 6.4.6 prikazuje vremensku strukturu neutronske pozadine, Slika 6.4.7 čini isto za detekciju β-zraka iz neutronima induciranih neelastičnih reakcija na $^{\mathrm{nat}}$C uzorku. Budući da se bitni neelastični kanali otvaraju oko 14 MeV, korelacije s događajima detektiranima ispod 1 MeV su potpuno izgubljene. Osim oblikom samog neutronskog toka, spektar početnih energija neutrona s donjeg okvira ponajviše je određen energijskom ovisnošću udarnog presjeka za dominantnu ^{12}C$(n,p)^{12}$B reakciju.

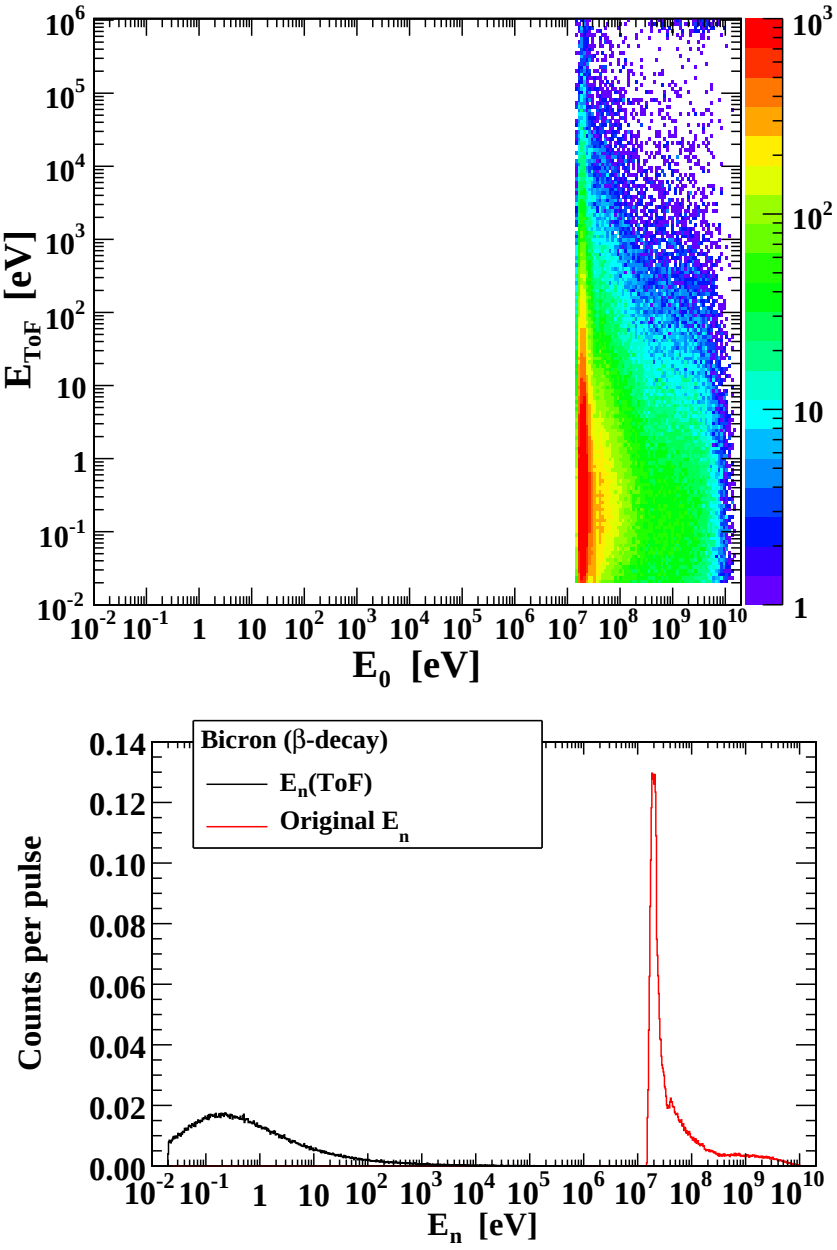

Slika 6.4.7 — Analogon Slike 6.4.6: detekcija β-zraka iz raspada radioaktivnih izotopa stvorenih neelastičnim reakcijama induciranima visokoenergijskim neutronima. Na spektre značajno utječe dominantna ^{12}C$(n,p)^{12}$B reakcija.

U mogućnosti smo proučiti i doprinose izdvojenih eksperimentalnih komponenti ukupnoj vjerojatnosti detekcije. Slika 6.4.8 prikazuje nagomilane udjele vjerojatnosti detekcije, uzrokovane reprezentativnim skupovima komponenata – zidovima eksperimentalne prostorije, cjevovodom, obama detektorima te ukupnim ostatkom do sada neobuhvaćenih komponenata. Kao što grafovi pokazuju za oba detektora – u gornjem okviru za Bicron, a u donjem za FZK detektor – zidovi eksperimentalne prostorije značajan su izvor neutronske pozadine, posebice iznad 1 keV gdje potpuno dominiraju vjerojatnošću detekcije. Cjevovod također primjetno doprinosi neutronskoj pozadini zbog aluminijskog sadržaja i blizine obama detektorima. Konačno, zbog aluminijskog oklopa Bicron detektora – nasuprot oklopu FZK detektora od ugljičnih vlakana – neutronska pozadina Bicron detektora mnogo je viša od one FZK detektora. Štoviše, doprinos Bicron detektora neutronskoj pozadini FZK detektora usporediv je s doprinosom samog FZK detektora vlastitoj pozadini.

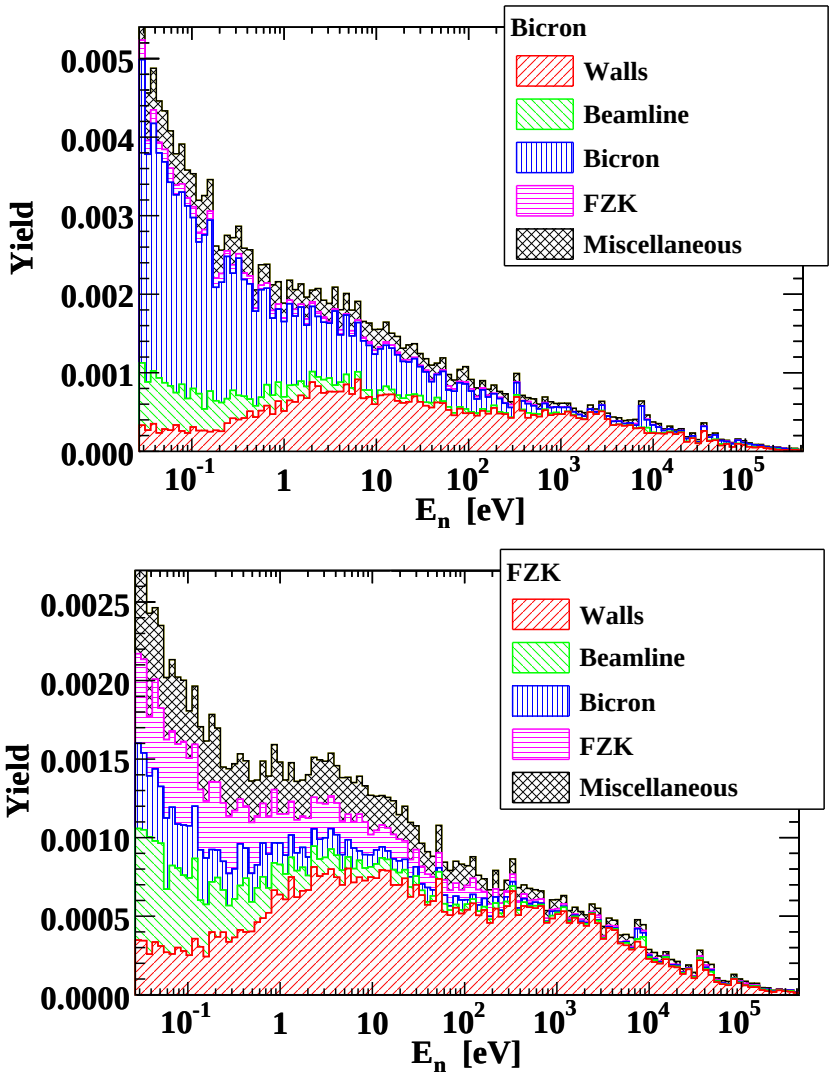

Slika 6.4.8 — Neutronska pozadina izražena vjerojatnošću detekcije za Bicron (gornji okvir) i FZK (donji okvir) detektor. Doprinosi različitih skupova eksperimentalnih komponenata su jasno izdvojeni i nagomilani jedan nad drugim. Valja primjetiti razliku za faktor 2 u apsolutnim skalama dvaju detektora.

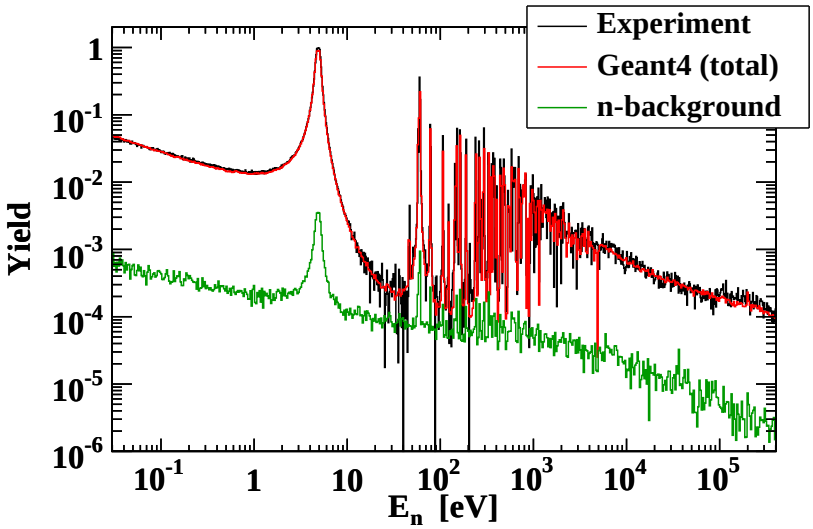

Slika 6.4.9 — Ukupna vjerojatnost uhvata i neutronska pozadina za ^{197}Au uzorak. Rezultati GEANT4 simulacija uspoređeni su s eksperimentalnim podacima.

Rezultati za ^{197}Au uzorak

Uzevši u obzir dostupne eksperimentalne podatke iz ^{58}Ni eksperimenta koji uključuju mjerenja s ^{nat}C, ^{58}Ni i ^{197}Au uzorcima, ^{nat}C uzorak možemo smatrati krajnjim slučajem neutronskih raspršnja, a ^{197}Au krajnjim slučajem neutronskih uhvata. Već smo potvdili uspješnu rekonstrukciju eksperimentalnih podataka za ^{nat}C uzorak GEANT4 simulacijama. Uspješna rekonstrukcija također je potvrđena za ^{197}Au uzorak, čemu svjedoči donji okvir sa Slike 6.4.3 koji prikazuje mjerene i simulirane događaje nakon primjene težinskih funkcija. Radi potpunosti, Slika 6.4.9 uspoređuje ukupnu mjerenu i simuliranu vjerojatnost uhvata za ^{197}Au uzorak, uspoređujući ih s neutronskom pozadinom.

Rezultati za ^{58}Ni uzorak

Nakon potvrde pouzdanosti GEANT4 simulacija primjenjenih na nominalno krajnje slučajeve ^{nat}C i ^{197}Au uzoraka, rezultati za ^{58}Ni uzorak slijede gotovo trivijalno. Pored doprinosa neutronske pozadine za ^{58}Ni, Slika 6.4.10 također uspoređuje ukupnu simuliranu s eksperimentalnom vjerojatnošću uhvata – korigiranom za pozadinu uzrokovanu prolaskom neutronskog snopa kroz eksperimentalnu prostoriju te pozadinu uzrokovanu prirodnim i induciranim zračenjem. U skladu s očekivanjima, vjerojatnosti uhvata u izvrsnom su slaganju. No valja naglasiti da cilj provedenih simulacija nije bio reproducirati vjerojatnost uhvata na ^{58}Ni uzorku, s obzirom da je svrha eksperimenta nije bila potvrditi prošle rezultate, već provesti nezavisno mjerenje. Stoga visoki stupanj slaganja između ukupnih eksperimentalnih i simuliranih rezultata treba smatrati jedino sretnom okolnošću omogućenom simulacijama visoke preciznosti.

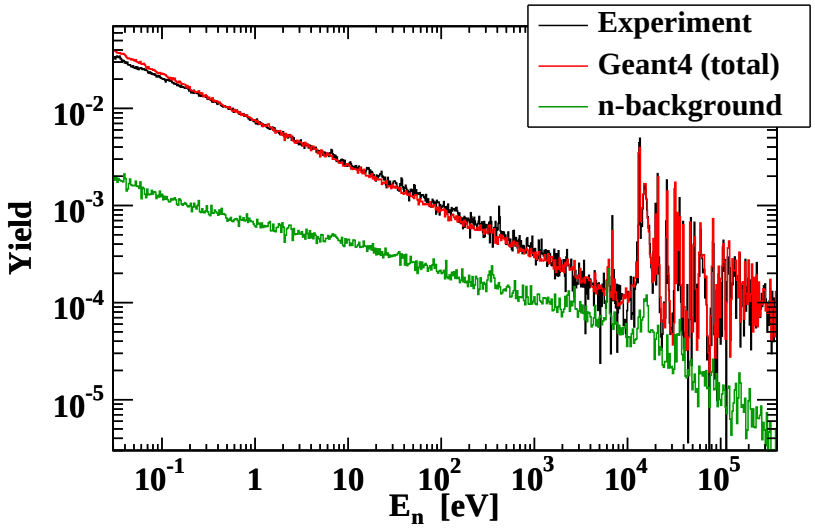

Slika 6.4.10 — Ukupna vjerojatnost uhvata i neutronska pozadina za ^{58}Ni uzorak. Rezultati GEANT4 simulacija uspoređeni su s eksperimentalnim podacima.

6.5 Zaključak

Udarni presjek za ^{58}Ni(n,γ) reakciju mjeren je na postrojenju neutronskog vremena proleta n_TOF na CERN-u. Radijativni uhvat neutrona na ^{58}Ni nalazi svoje mjesto u opisu *s*-procesa nukleosinteze. Stoga ^{58}Ni(n,γ) udarni presjek čini bitan doprinos nuklearnoj astrofizici. Nadalje, ^{58}Ni nalazi se među strukturnim materijalima naširoko korištenima u nuklearnim tehnologijama te kao takav mora biti uzet u obzir pri zaštiti od zračenja jer tijekom neutronskog ozračivanja predstavlja izvor dugoživućeg ^{59}Ni izotopa s vremenom poluživota od 7.5×10^4 godina. U usporedbi s ranijim eksperimentalnim rezultatima i prihvaćenim vrijednostima, nedavno provedena mjerenja ukazala su na znatno niži ^{58}Ni(n,γ) udarni presjek, zahtijevajući ponovljenu i nezavisnu eksperimentalnu provjeru, koja je provedena na n_TOF postrojenju.

Na n_TOF postrojenju neutroni se proizvode ozračivanjem masivne olovne spalacijske mete pulsnim snopom protona energije 20 GeV iz Protonskog Sinkrotrona s CERN-a. Prvotni spektar od 2×10^{15} brzih neutrona po pulsu moderira se se prolaskom snopa kroz sam olovni blok, kroz 1 cm širok sloj vode iz rashladnog sustava te dodatan 4 cm širok sloj borirane vode. Konačan spektar neutrona na ulazu u eksperimentalnu prostoriju na udaljenosti od približno 185 m od spalacijske mete, proteže se preko 12 redova veličine u energiji – od $\sim$10 meV do $\sim$ 10 GeV. Snop neutrona pročišćuje se od nabijenih čestica snažnim magnetom indukcije 1.5 T te se oblikuje dvama kolimatorima. I magnet i kolimatori postavljeni su duž evakuiranog cjevovoda koji spaja spalacijsku metu s eksperimentalnom prostorijom.

Mjerenja radijativnog uhvata provedena su detekcijom γ-zraka iz uhvatima izazvanih γ-kaskada. Pri tome su korištena dva optimizirana C_6D_6 (deuterirani benzen) detektora. Na temelju trenutka pojave detektiranog događaja – s obzirom na trenutak pojave početnog signala izazvanog intenzivnim γ-bljeskom oslobođenim iz spalacijske mete – uhvaćenome neutronu pripisuje se kinetička energija zahvaljujući korelaciji s njegovim vremenom proleta. Nezavisna mjerenja provedena su kako bi se odredile en-

ergijska kalibracija i rezolucija dvaju detektora, put proleta neutrona te završni faktor normiranja vjerojatnosti uhvata. Korekcija mjerenih podataka za detekcijsku učinkovitost provedena je metodom primjene težinske funkcije, koja se oslanja na simulacije odaziva detektora na prolazak γ-zraka različitih energija. Energijska ovisnost neutronskog toka koji prolazi površinom uzorka – nezaobilazna za izračun vjerojatnosti uhvata – dobivena je mjerenjima i simulacijama samo ukratko opisanima u ovome radu. Poseban osvrt posvećen je različitim izvorima pozadinskih događaja, koji uključuju pozadinu raspršenih γ-zraka iz dolaznoga neutronskog snopa, pozadinu uzrokovanu prolaskom snopa kroz eksperimentalnu prostoriju, pozadinu prirodnog i induciranog zračenja iz eksperimentalnog okruženja te pozadinu neutrona raspršenih na samome mjerenom uzorku. Sve vrste pozadinskih događaja osim posljednje – tzv. neutronske pozadine – pouzdano su mjerene. Iznimno, neutronska pozadina određena je posebnim GEANT4 simulacijama.

Mjereni podaci analizirani su u rasponu neutronskih energija od 27 meV do 400 keV. Za analizu područja raspoznatljivih rezonanci do 122 keV, korišten je programski kod SAMMY koji se oslanja na formalizam *R*-matrice. U ovome području identificirana je 51 rezonanca u udarnom presjeku za uhvat neutrona. Također, dvije rezonance negativnih energija (ispod energije odvajanja neutrona) uvedene su kako bi se parametrizirao udarni presjek u području od termalnih energija sve do prve raspoznatljive rezonance na 6.9 keV. Energijsko područje između 122 keV i 400 keV obrađivano je kao područje neraspoznatljivih rezonanci, pri čemu je korišten poseban programski kod SESH za simulaciju uprosječene vjerojatnosti uhvata. Na taj način rekonstruirani su parametri udarnog presjeka koji su potom iskorišteni za njegovo izvrjednjenje sve do 1 MeV. Iz združenog skupa parametara dobivenih programima SAMMY i SESH izračunati su maxwellovski usrednjeni udarni presjeci za termalne energije $kT = 5 – 100$ keV, karakteristične za unutrašnjost zvijezda. Proučen je utjecaj novodobivenih vrijednosti na zvjezdanu nukleosintezu, pri čemu je otkriveno da u masivnim zvijezdama umanjenje mawellowski usrednjenog udarnog presjeka za samo 12% pri 30 keV – s obzirom na ranije prihvaćenu vrijednost – vodi do povećanja zastupljenosti ^{58}Ni od čak 60%, gotovo ni uz kakav utjecaj na teže izotope.

GEANT4 simulacije neutronske pozadine – kao nova posebnost s n_TOF postrojenja – detaljno su opisane i popraćene temeljitom analizom simuliranih podataka. Posebna pažnja posvećena je vjernoj geometrijskoj reprodukciji eksperimentalne prostorije. Izabran je najprimjereniji fizikalni okvir za opis neutronskih međudjelovanja, koji se sastoji od modela i udarnih presjeka za elastično i neelastično raspršenje, radijativni uhvat te neutronima izazvanu fisiju. Ozračivanje uzoraka neutronskim snopom također je vjerno reproducirano, detaljno prateći eksperimentalne uvjete. Detaljno je proučen Nedostatak simuliranih korelacija između γ-zraka iz neutronima izazvanih γ-kaskada. Potvrđeno je da metoda primjene težinske funkcije igra središnju ulogu u poništenju učinaka korelacija – i njihovog izostanka – pri izračunu vjerojatnosti uhvata, u konačnici dovodeći eksperimentalne i simulirane podatke u izvrsno slaganje. Prateći postupak ranije usvojen na n_TOF postrojenju, simulirana je neutronska osjetljivost dvaju C_6D_6 detektora te su znatno unaprjeđeni raniji rezultati. U konačnici, simulirana je puna neutronska pozadina za tri različita uzorka – ^{58}Ni, ^{197}Au i ^{nat}C – korištena tijekom niza mjerenja sa središnjim ^{58}Ni uzorkom. Simulirani podaci analizirani su na identičan način kao i eksperimentalni. Za sve uzorke postignuto je izvrsno slaganje između eksperimentalnih i simuliranih rezultata. Posebno, slaganje između podataka

za ^{nat}C iznad 1 keV – gdje se prikupljeni podaci sastoje gotovo potpuno od neutronske pozadine – potvrđuje pouzdanost najnovije inačice GEANT4 paketa u simuliranju neutronskih međudjelovanja. Ispod 1 keV otkrivena je dodatna komponenta u podacima prikupljenim s ^{nat}C uzorkom, uzrokovana detekcijom visokoenergijskih β-zraka iz – u najvećoj mjeri – raspada ^{12}B izotopa proizvedenog neelastičnom ^{12}C$(n, p)^{12}$B reakcijom čiji se kanal otvara pri energiji neutrona od približno 14 MeV. Kao takvi, eksperimentalni podaci za ^{nat}C s n_TOF postrojenja mogu se smatrati integralnim mjerenjem udarnog presjeka ^{12}C$(n, p)^{12}$B reakcije, u energijskom rasponu od praga reakcije sve do 10 GeV.

Bibliography

[1] V. Gopalakrishnan, R.V. Nandedkar and S. Ganesan, J. Nucl. Materials 228, 207 (1996)

[2] C. Weiß, C. Guerrero, E. Griesmayer et al., Nucl. Data Sheets 120, 208 (2014)

[3] M. Pignatari, R. Gallino, M. Heil et al., Astrophys. J. 710, 1557 (2010)

[4] F. Käppeler, R. Gallino, S. Bisterzo and W. Aoki, Rev. Mod. Phys. 83, 157 (2011)

[5] C. Lederer, C.Massimi, S. Altstadt et al., Phys. Rev. Lett.110, 022501 (2013)

[6] C. Lederer, C. Massimi, E. Berthoumieux et al., Phys. Rev. C 89, 025810 (2014)

[7] K. Lodders, H. Palme and H.-P. Gail, Abundances of the Elements in the Solar System, Landolt-Börnstein, New Series, Vol. VI/4B (Springer, Berlin, 2009), Chap 4.4.

[8] S. E. Woosley, A. Heger and T. A. Weaver, Rev. Mod. Phys. 74, 1015 (2002)

[9] I. R. Seitenzahl, F. Ciaraldi-Schoolmann, F. K. Röpke et al., Mon. Not. R. Astron. Soc. 429, 1156 (2013)

[10] T. V. Mishenina, M. Pignatari, S. A. Korotin et al., Astron. Astrophys. 552, A128 (2013)

[11] Experimental Nuclear Reaction Data (EXFOR), database version of December 18, 2012, http://www-nds.iaea.org/exfor/

[12] K. H. Guber, H. Derrien, L. C. Leal et al., Phys. Rev. C 82, 057601 (2010)

[13] M. B. Chadwick, P. Obložinský, M. Herman et al., Nucl. Data Sheets 107, 2931 (2006)

[14] C. M. Perey, F. G. Perey, J. A. Harvey et al., Phys. Rev. C 47, 1143 (1993)

[15] G. Rugel, I. Dillmann, T. Faestermann et al., Nucl. Instrum. Methods B 259, 683 (2007)

[16] A. Brusegan, G. Rohr and R. Shelley et al., in Proceedings of the International Conference on Nuclear Data for Science and Technology, Gatlinburg, May 1994, Vol. 1 (unpublished), p. 224.

[17] S. Raman, X. Ouyang, M. A. Islam et al., Phys. Rev. C 70, 044318 (2004)

[18] M. B. Chadwick, M. Herman, P. Obložinský et al., Nucl. Data Sheets 112, 2887 (2011)

[19] P. Žugec, M. Barbagallo, N. Colonna et al., Phys. Rev. C 89, 014605 (2014)

[20] E. Wigner., Phys. Rev. 70, 606 (1946)

[21] E. Wigner and L. Eisenbud., Phys. Rev. 72, 29 (1947)

[22] N. M. Larson, Oak-Ridge National Laboratory Technical Report No. ORNL/TM-9179/R8, 2008 (unpublished)

[23] F. H. Fröhner, Evaluation and Analysis of Nuclear Resonance Data, JEFF Report 18, OECD NEA, Paris (2000)

[24] F. Gunsing, U. Abbondanno, G. Aerts et al., Nucl. Instrum. Methods B 261, 925 (2007)

[25] N. Colonna, S. Andriamonje, J. Andrzejewski et al., Nucl. Instrum. Methods B 269, 3251 (2011)

[26] G. Wallerstein et al., Rev. Mod. Phys. 69, 995 (1997)

[27] G. E. Mitchell, J. D. Bowman, H. A. Weidenmüller, Rev. Mod. Phys. 71, 445 (1999)

[28] Y. Masuda, J. D. Bowman, R. D. Carlini et al., Nucl. Phys. A 721, 485C (2003)

[29] T. von Egidy, D. Bucurescu, Phys. Rev. C 72, 044311 (2005)

[30] H. Nakamura, T. Fukahori, Phys. Rev. C 72, 064329 (2005)

[31] W.P. Abfalterer, R.W. Finlay, S.M. Grimes, Phys. Rev. C 72, 064312 (2000)

[32] A. Bensussan, Nucl. Instrum. Methods 155, 11 (1978)

[33] K. H. Guber, D. C. Larson, P. E. Koehler et al, Proceedings of the International Conference on Nuclear Data for Science and Technology, Italian Physical Society Conference Proceedings Vol. 59 (Italian Physical Society, Bologna, Italy, 1998), Part I, p. 559

[34] Spallation Neutron Source, Technical Report, Oak Ridge National Laboratory (2004); http://www.sns.gov/

[35] P. Lisowski, C. Bowman, G. Russell and S. Wender, Nucl. Sci. Eng. 106, 208 (1990)

[36] Japan Proton Accelerator Complex, Technical Report, JAERI and KEK (2004); http://j-parc.jp/

[37] E. R. Gaerttner, M. L. Yeater and R. R. Fullwood, Rensselaer Polytechnic Institute Linac Facility, Proceedings of Symposium on Neutron Physics, RPI, May, 1961; http://www.linac.rpi.edu/

[38] J. M. Carpenter, D. L. Price and N. J. Swanson, IPNS-A National Facility for Condensed Matter Research, Argonne National Laboratory ANL-78-88 (1978)

[39] C. Guerrero, U.Abbondanno, G.Aerts et al., Nucl. Instrum. Methods A 608, 424 (2009)

[40] R. Reifarth, T. A. Bredeweg, A. Alpizar-Vicente et al., Nucl. Instrum. Methods A 531, 530 (2004)

[41] M. Heil, R. Reifarth, M.M. Fowler, Nucl. Instrum. Methods A 459, 229 (2001)

[42] M. Moxon and E. Rae, Nucl. Instrum. Methods 24, 445 (1963)

[43] R. L. Macklin and J. H. Gibbons, Phys. Rev. 159, 1007 (1967)

[44] K. Wisshak, F. Käppeler, G. Reffo., F. Fabbri, Nucl. Sci. Eng. 86, 168 (1984)

[45] P. Žugec, N. Colonna, D. Bosnar et al., Nucl. Instrum. Methods A 760, 57 (2014)

[46] http://home.web.cern.ch/

[47] https://ntof-exp.web.cern.ch/ntof-exp/

[48] G. Battistoni, F. Broggi, M. Brugger et al., Nucl. Instrum. Methods B 269, 2850 (2011)

[49] The nTOF Collaboration, Study of the Background in the Measuring Station at the nTOF Facility at CERN: Sources and Solutions, CERN/SL/Note 2001-046, CERN/INTC 2001-038

[50] C. Guerrero, A. Tsinganis, E. Berthoumieux et al., Eur. Phys. J. A 49, 27 (2013)

[51] C. Borcea, P. Cennini, M. Dahlfors et al., Nucl. Instrum. Methods A 513, 524 (2003)

[52] S. Marrone, P. F. Mastinu, U. Abbondanno et al., Nucl. Instrum. Methods A 517, 389 (2004)

[53] Y. Giomataris, Ph. Rebourgeard, J.P. Robert and G.Charpak, Nucl. Instrum. Methods A 376, 29 (1996)

[54] S. Andriamonje, M. Calviani, Y. Kadi et al., J. Korean Phys. Soc. 59, 1597 (2011)

[55] D.B. Gayther, Metrologia 27, 221 (1990)

[56] C. Paradela, L. Tassan-Got, L. Audouin et al., Phys. Rev. C 82, 034601 (2010)

[57] M. Barbagallo, C. Guerrero, A. Tsinganis et al., Eur. Phys. J. A 49, 156 (2013)

[58] A. Ferrari, P. Sala, A. Fassò and J. Ranft, FLUKA: A Multi-Particle Transport Code, CERN-2005-10 (2005), INFN/TC_05/11, SLAC-R-773

[59] G. Battistoni, S. Muraro, P.R. Sala et al., The FLUKA code: description and benchmarking, in: M. Albrow, R. Raja (eds.), Proceedings of the Hadronic Shower Simulation Workshop 2006, Fermilab 6–8 September 2006, AIP Conference Proceeding, 896 (2007) pp. 31–49

[60] http://www.fluka.org/

[61] R. Plag, M. Heil, F. Käppeler et al., Nucl. Instrum. Methods A 496, 425 (2003)

[62] http://www.agilent.com/

[63] U. Abbondanno, G. Aerts, F. Álvarez et al., Nucl. Instrum. Methods A 538, 692 (2005)

[64] M. Morháč, Nucl. Instrum. Methods A 600, 478 (2009)

[65] S. Agostinelli, J. Allison, K. Amako et al., Nucl. Instrum. Methods A 506, 250 (2003)

[66] http://geant4.cern.ch/

[67] U. Abbondanno, G. Aerts, H. Alvarez et al., Nucl. Instrum. Methods A 521, 454 (2004)

[68] G. Lorusso, N. Colonna, S. Marrone et al., Nucl. Instrum. Methods A 532, 622 (2004)

[69] R.L. Macklin, J. Halperin and R.R.Winters, Nucl. Instrum. Methods A 164, 213 (1979)

[70] S. F. Mughabghab, Atlas of Neutron Resonances, Resonance Parameters and Thermal Cross Sections Z = 1–100 (Elsevier, Amsterdam, 2006)

[71] http://www.oecd-nea.org/janis/

[72] IAEA Nuclear Data Services, http://www-nds.iaea.org/

[73] F. Froehner, SESH code, Gulf General Atomic Report No. GA-8380, 1968 (unpublished)

[74] I. Dillmann, M. Heil, F. Käppeler et al., in Capture Gamma-Ray Spectroscopy and Related Topics: 12th International Symposium, Notre Dame, Indiana, 2005, edited by A. Woehr and A. Aprahamian, AIP Conf. Proc. No. 819 (AIP, New York, 2006), p. 123; KADoNiS v0.3, 2013, http://www.kadonis.org/

[75] N. Popara, Nuklearne reakcije u evoluciji supernove (diploma thesis); Department of Physics, Faculty of Science, University of Zagreb; Zagreb (2013)

[76] N. Paar, P. Ring, T. Nikšić and D. Vretenar, Phys. Rev. C 67, 034312 (2003)

[77] H. Beer, F. Voss and R. Winters, Astrophys. J. Suppl. Ser. 80, 403 (1992)

[78] Z. Y. Bao, H. Beer, F. Käppeler et al., At. Data Nucl. Data Tables 76, 70 (2000)

[79] B. Pritychenko, S. F.Mughaghab and A. A. Sonzogni, At. Data Nucl. Data Tables 96, 645 (2010)

[80] T. Rauscher, F.-K. Thielemann and K.-L. Kratz, Nucl. Phys. A 621, 331c (1997)

[81] W. E. Parker, M. B. Chadwick, F. S. Dietrich et al., Phys. Rev. C 52, 252 (1995)

[82] A. Mengoni, T. Otsuka and M. Ishihara, Phys. Rev. C 52, R2334 (1995)

[83] F. Herwig, M. E. Bennett, S. Diehl, C. L. Fryer et al., PoS (NIC X) 023 (2008)

[84] M. Pignatari, R. Hirschi, M. Wiescher et al., Astrophys. J. 762, 31 (2013)

[85] N. Collona and S. Altieri, Health Phys. 82, 840 (2002)

[86] http://www.nndc.bnl.gov/capgam/

[87] GEANT4 Physics Reference Manual; available from: http://geant4.cern.ch/

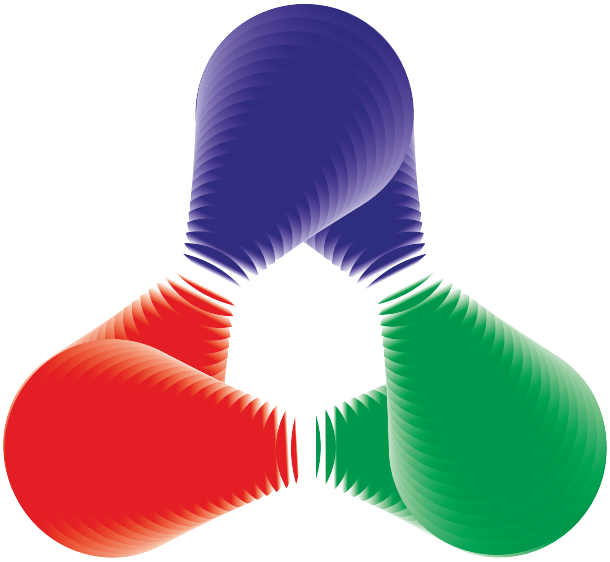

Životopis

Petar Žugec je rođen 19. veljače 1987. godine u Zagrebu. Do 2001. godine pohađa osnovnu školu Nikole Tesle u Zagrebu, a do 2005. godine V. gimnaziju u Zagrebu. Iste godine započinje dodiplomski i diplomski studij istraživačkog smjera fizike na Prirodoslovno-matematičkom fakultetu Sveučilišta u Zagrebu, koji završava obranom diplomskoga rada 2010. godine. Od 2011. godine zaposlen je kao znanstveni novak – asistent na Fizičkom odsjeku Prirodoslovno-matematičkog fakulteta u Zagrebu, kada upisuje poslijediplomski studij nuklearne fizike. Jednomjesečnu stipendiju Međunarodne agencije za atomsku energiju (IAEA) dobio je 2010. godine za znanstveno usavršavanje na Institutu za nuklearnu fiziku Johannes-Gutenberg sveučilišta u Mainzu (Njemačka), a 2014. godine za znanstveno usavršavanje u CERN-u (Švicarska). Od 2012. godine član je n_TOF kolaboracije iz CERN-a.

Popis objavljenih radova

1. **Žugec Petar**, Colonna N., Bosnar D., Mengoni A., Altstadt S., Andrzejewski J., Audouin L., Barbagallo M., Bécares V., Bečvář F., Belloni F., Berthoumieux E., Billowes J., Boccone V., Brugger M., Calviani M., Calviño F., Cano-Ott D., Carrapiço C., Cerutti F., Chiaveri E., Chin M., Cortés G., Cortés-Giraldo M. A., Cosentino L., Diakaki M., Domingo-Pardo C., Dressler R., Duran I., Eleftheriadis C., Ferrari A., Finocchiaro P., Fraval K., Ganesan S., García A. R., Giubrone G., Gómez-Hornillos M. B., Gonçalves I. F., González-Romero E., Griesmayer E., Guerrero C., Gunsing F., Gurusamy P., Heinitz S., Jenkins D. G., Jericha E., Käppeler F., Karadimos D., Kivel N., Kokkoris M., Krtička M., Kroll J., Langer C., Lederer C., Leeb H., Leong L. S., Lo Meo S., Losito R., Manousos A., Marganiec J., Martìnez T., Massimi C., Mastinu P. F., Mastromarco M., Mendoza E., Milazzo P. M., Mingrone F., Mirea M., Mondalaers W., Musumarra A., Paradela C., Pavlik A., Perkowski J., Plompen A., Praena J., Quesada J. M., Rauscher T., Reifarth R., Riego A., Roman F., Rubbia C., Sarmento R., Saxena A., Schillebeeckx P., Schmidt S., Schumann D., Tagliente G., Tain J. L., Tarrío D., Tassan-Got L., Tsinganis A., Valenta S., Vannini G., Variale V., Vaz P., Ventura A., Versaci R., Vermeulen M. J., Vlachoudis V., Vlastou R., Wallner A., Ware T., Weigand M., Weiß C., Wright T.; ***Measurement of the $^{12}C(n,p)^{12}B$ cross section at n_TOF at CERN by in-beam activation analysis***, Physical Review C 90, 021601(R) (2014)

2. Fraval K., Gunsing F., Altstadt S., Andrzejewski J., Audouin L., Barbagallo M., Bécares V., Bečvář F., Belloni F., Berthoumieux E., Billowes J., Boccone V., Bosnar D., Brugger M., Calviani M., Calviño F., Cano-Ott D., Carrapiço C., Cerutti F., Chiaveri E., Chin M., Colonna N., Cortés G., Cortés-Giraldo M. A., Diakaki M., Domingo-Pardo C., Duran I., Dressler R., Dzysiuk N., Eleftheriadis C., Ferrari A., Ganesan S., García A. R., Giubrone G., Gómez-Hornillos M. B., Gonçalves I. F., González-Romero E., Griesmayer E., Guerrero C., Gurusamy P., Hernández-Prieto

A., Jenkins D. G., Jericha E., Kadi Y., Käppeler F., Karadimos D., Kivel N., Koehler P., Kokkoris M., Krtička M., Kroll J., Lampoudis C., Langer C., Leal-Cidoncha E., Lederer C., Leeb H., Leong L. S., Losito R., Mallick A., Manousos A., Marganiec J., Martìnez T., Massimi C., Mastinu P. F., Mastromarco M., Meaze M., Mendoza E., Mengoni A., Milazzo P. M., Mingrone F., Mirea M., Mondalaers W., Paradela C., Pavlik A., Perkowski J., Plompen A., Praena J., Quesada J. M., Rauscher T., Reifarth R., Riego A., Robles M. S., Roman F., Rubbia C., Sabaté-Gilarte M., Sarmento R., Saxena A., Schillebeeckx P., Schmidt S., Schumann D., Tagliente G., Tain J. L., Tarrío D., Tassan-Got L., Tsinganis A., Valenta S., Vannini G., Variale V., Vaz P., Ventura A., Versaci R., Vermeulen M. J., Vlachoudis V., Vlastou R., Wallner A., Ware T., Weigand M., Weiß C., Wright T., **Žugec Petar**; ***Measurement and analysis of the $^{241}Am(n,\gamma)$ cross section with liquid scintillator detectors using time-of-flight spectroscopy at the n_TOF facility at CERN***, Physical Review C 89, 044609 (2014)

3. Lederer C., Massimi C., Berthoumieux E., Colonna N., Dressler R., Guerrero C., Gunsing F., Käppeler F., Kivel N., Pignatari M., Reifarth R., Schumann D., Wallner A., Altstadt S., Andriamonje S., Andrzejewski J., Audouin L., Barbagallo M., Bécares V., Bečvář F., Belloni F., Berthier B., Billowes J., Boccone V., Bosnar D., Brugger M., Calviani M., Calviño F., Cano-Ott D., Carrapiço C., Cerutti F., Chiaveri E., Chin M., Cortés G., Cortés-Giraldo M. A., Dillmann I., Domingo-Pardo C., Duran I., Dzysiuk N., Eleftheriadis C., Fernández-Ordóñez M., Ferrari A., Fraval K., Ganesan S., García A. R., Giubrone G., Gómez-Hornillos M. B., Gonçalves I. F., González-Romero E., Gramegna F., Griesmayer E., Gurusamy P., Harrisopulos S., Heil M., Ioannides K., Jenkins D. G., Jericha E., Kadi Y., Karadimos D., Korschinek G., Krtička M., Kroll J., Langer C., Lebbos E., Leeb H., Leong L. S., Losito R., Lozano M., Manousos A., Marganiec J., Marrone S., Martìnez T., Mastinu P. F., Mastromarco M., Meaze M., Mendoza E., Mengoni A., Milazzo P. M., Mingrone F., Mirea M., Mondalaers W., Paradela C., Pavlik A., Perkowski J., Plag R., Plompen A., Praena J., Quesada J. M., Rauscher T., Riego A., Roman F., Rubbia C., Sarmento R., Schillebeeckx P., Schmidt S., Tagliente G., Tain J. L., Tarrío D., Tassan-Got L., Tsinganis A., Tlustos L., Valenta S., Vannini G., Variale V., Vaz P., Ventura A., Vermeulen M. J., Versaci R., Vlachoudis V., Vlastou R., Ware T., Weigand M., Weiß C., Wright T. J., **Žugec Petar**; ***$^{62}Ni(n,\gamma)$ and $^{63}Ni(n,\gamma)$ cross sections measured at the n_TOF facility at CERN***, Physical Review C 89, 025810 (2014)

4. **Žugec Petar**, Barbagallo M., Colonna N., Bosnar D., Altstadt S., Andrzejewski J., Audouin L., Bécares V., Bečvář F., Belloni F., Berthoumieux E., Billowes J., Boccone V., Brugger M., Calviani M., Calviño F., Cano-Ott D., Carrapiço C., Cerutti F., Chiaveri E., Chin M., Cortés G., Cortés-Giraldo M. A., Diakaki M., Domingo-Pardo C., Duran I., Dzysiuk N., Eleftheriadis C., Ferrari A., Fraval K., Ganesan S., García A. R., Giubrone G., Gómez-Hornillos M. B., Gonçalves I. F., González-Romero E., Griesmayer E., Guerrero C., Gunsing F., Gurusamy P., Jenkins D. G., Jericha E., Kadi Y., Käppeler F., Karadimos D., Koehler P., Kokkoris M., Krtička M., Kroll J., Langer C., Lederer C., Leeb H., Leong L. S., Losito R., Manousos A., Marganiec J., Martìnez T., Massimi C., Mastinu P. F., Mastromarco M., Meaze M., Mendoza E., Mengoni A., Milazzo P. M., Mingrone F., Mirea M., Mondalaers W., Paradela C., Pavlik A., Perkowski J., Pignatari M., Plompen A., Praena J., Quesada J. M., Rauscher T., Reifarth R., Riego A., Roman F., Rubbia C., Sarmento R., Schillebeeckx P., Schmidt S., Tagliente G., Tain J. L., Tarrío D., Tassan-Got L., Tsinganis A.,

Valenta S., Vannini G., Variale V., Vaz P., Ventura A., Versaci R., Vermeulen M. J., Vlachoudis V., Vlastou R., Wallner A., Ware T., Weigand M., Weiß C., Wright T.; ***Experimental neutron capture data of ^{58}Ni from the CERN n_TOF facility***, Physical Review C 89, 014605 (2014)

5. **Žugec Petar**, Colonna N., Bosnar D., Altstadt S., Andrzejewski J., Audouin L., Barbagallo M., Bécares V., Bečvář F., Belloni F., Berthoumieux E., Billowes J., Boccone V., Brugger M., Calviani M., Calviño F., Cano-Ott D., Carrapiço C., Cerutti F., Chiaveri E., Chin M., Cortés G., Cortés-Giraldo M. A., Diakaki M., Domingo-Pardo C., Dressler R., Duran I., Dzysiuk N., Eleftheriadis C., Ferrari A., Fraval K., Ganesan S., García A. R., Giubrone G., Gómez-Hornillos M. B., Gonçalves I. F., González-Romero E., Griesmayer E., Guerrero C., Gunsing F., Gurusamy P., Heinitz S., Jenkins D. G., Jericha E., Kadi Y., Käppeler F., Karadimos D., Kivel N., Koehler P., Kokkoris M., Krtička M., Kroll J., Langer C., Lederer C., Leeb H., Leong L. S., Lo Meo S., Losito R., Manousos A., Marganiec J., Martìnez T., Massimi C., Mastinu P. F., Mastromarco M., Meaze M., Mendoza E., Mengoni A., Milazzo P. M., Mingrone F., Mirea M., Mondalaers W., Paradela C., Pavlik A., Perkowski J., Plompen A., Praena J., Quesada J. M., Rauscher T., Reifarth R., Riego A., Roman F., Rubbia C., Sarmento R., Saxena A., Schillebeeckx P., Schmidt S., Schumann D., Tagliente G., Tain J. L., Tarrío D., Tassan-Got L., Tsinganis A., Valenta S., Vannini G., Variale V., Vaz P., Ventura A., Versaci R., Vermeulen M. J., Vlachoudis V., Vlastou R., Wallner A., Ware T., Weigand M., Weiß C., Wright T.; ***GEANT4 simulation of the neutron background of the C_6D_6 set-up for capture studies at n_TOF***, Nuclear Instruments and Methods in Physics Research A 760, 57 (2014)

6. Tarrío D., Leong L. S., Audouin L., Duran I., Paradela C., Tassan-Got L., Le Naour C., Bacri C. O., Petitbon V., Mottier J., Caamaño M., Altstadt S., Andrzejewski J., Barbagallo M., Bécares V., Bečvář F., Belloni F., Berthoumieux E., Billowes J., Boccone V., Bosnar D., Brugger M., Calviani M., Calviño F., Cano-Ott D., Carrapiço C., Cerutti F., Chiaveri E., Chin M., Colonna N., Cortés G., Cortés-Giraldo M. A., Diakaki M., Domingo-Pardo C., Dzysiuk N., Eleftheriadis C., Ferrari A., Fraval K., Ganesan S., García A. R., Giubrone G., Gómez-Hornillos M. B., Gonçalves I. F., González-Romero E., Griesmayer E., Guerrero C., Gunsing F., Gurusamy P., Jenkins D. G., Jericha E., Kadi Y., Käppeler F., Karadimos D., Koehler P., Kokkoris M., Krtička M., Kroll J., Langer C., Lederer C., Leeb H., Losito R., Manousos A., Marganiec J., Martìnez T., Massimi C., Mastinu P. F., Mastromarco M., Meaze M., Mendoza E., Mengoni A., Milazzo P. M., Mingrone F., Mirea M., Mondalaers W., Pavlik A., Perkowski J., Plompen A., Praena J., Quesada J. M., Rauscher T., Reifarth R., Riego A., Roman F., Rubbia C., Sarmento R., Schillebeeckx P., Schmidt S., Tagliente G., Tain J. L., Tsinganis A., Valenta S., Vannini G., Variale V., Vaz P., Ventura A., Versaci R., Vermeulen M. J., Vlachoudis V., Vlastou R., Wallner A., Ware T., Weigand M., Weiß C., Wright T. J., **Žugec Petar**; ***Measurement of the angular distribution of fission fragments using a PPAC assembly at CERN n_TOF***, Nuclear Instruments and Methods in Physics Research A 743, 79 (2014)

7. Barbagallo M., Guerrero C., Tsinganis A., Tarrío D., Altstadt S., Andriamonje S., Andrzejewski J., Audouin L., Bécares V., Bečvář F., Belloni F., Berthoumieux E., Billowes J., Boccone V., Bosnar D., Brugger M., Calviani M., Calviño F., Cano-Ott D., Carrapiço C., Cerutti F., Chiaveri E., Chin M., Colonna N., Cortés G., Cortés-Giraldo M. A., Diakaki M., Domingo-Pardo C., Duran I., Dressler R., Dzysiuk N.,

Eleftheriadis C., Ferrari A., Fraval K., Ganesan S., Garcìa A. R., Giubrone G., Göbel K., Gómez-Hornillos M. B., Gonçalves I. F., González-Romero E., Griesmayer E., Gunsing F., Gurusamy P., Hernández-Prieto A., Jenkins D. G., Jericha E., Kadi Y., Käppeler F., Karadimos D., Kivel N., Koehler P., Kokkoris M., Krtička M., Kroll J., Lampoudis C., Langer C., Leal-Cidoncha E., Lederer C., Leeb H., Leong L. S., Losito R., Manousos A., Marganiec J., Martìnez T., Massimi C., Mastinu P. F., Mastromarco M., Meaze M., Mendoza E., Mengoni A., Milazzo P. M., Mingrone F., Mirea M., Mondalaers W., Papaevangelou, T., Paradela C., Pavlik A., Perkowski J., Plompen A., Praena J., Quesada J. M., Rauscher T., Reifarth R., Riego A., Roman F., Rubbia C., Sabate-Gilarte M., Sarmento R., Saxena A., Schillebeeckx P., Schmidt S., Schumann D., Steinegger P., Tagliente G., Tain J. L., Tassan-Got L., Valenta S., Vannini G., Variale V., Vaz P., Ventura A., Versaci R., Vermeulen M. J., Vlachoudis V., Vlastou R., Wallner A., Ware T., Weigand M., Weiß C., Wright T. J., **Žugec Petar**; ***High-accuracy determination of the neutron flux at n_TOF***, European Physical Journal A 49, 156 (2013)

8. Guerrero C., Tsinganis C. A., Berthoumieux E., Barbagallo M., Belloni F., Gunsing F., Weiß C., Chiaveri E., Calviani M., Vlachoudis V., Altstadt S., Andriamonje S., Andrzejewski J., Audouin L., Bécares V., Bečvář F., Billowes J., Boccone V., Bosnar D., Brugger D., Calviño F., Cano-Ott D., Carrapiço C., Cerutti F., Chin M., Colonna N., Cortés G., Cortés-Giraldo M. A., Diakaki M., Domingo-Pardo C., Duran I., Dressler R., Dzysiuk N., Eleftheriadis C., Ferrari A., Fraval K., Ganesan S., García A. R., Giubrone G., Göbel K., Gómez-Hornillos M. B., Gonçalves I. F., González-Romero E., Griesmayer E., Gurusamy P., Hernández-Prieto A., Jenkins D. G., Jericha E., Kadi Y., Käppeler F., Karadimos D., Kivel N., Koehler P., Kokkoris M., Krtička M., Kroll J., Lampoudis C., Langer C., Leal-Cidoncha E., Lederer C., Leeb H., Leong L. S., Losito R., Manousos A., Marganiec J., Martínez T., Massimi C., Mastinu P. F., Mastromarco M., Meaze M., Mendoza E., Mengoni A., Milazzo P. M., Mingrone F., Mirea M., Mondalaers W., Papaevangelou T., Paradela C., Pavlik A., Perkowski J., Plompen A., Praena J., Quesada J. M., Rauscher T., Reifarth R., Riego A., Roman F., Rubbia C., Sabate-Gilarte M., Sarmento R., Saxena A., Schillebeeckx P., Schmidt S., Schumann D., Steinegger P., Tagliente G., Tain J. L., Tarrío D., Tassan-Got L., Valenta S., Vannini G., Variale V., Vaz P., Ventura A., Versaci R., Vermeulen M. J., Vlastou R., Wallner A., Ware T., Weigand M., Wright T., **Žugec Petar**; ***Performance of the neutron time-of-flight facility n_TOF at CERN***, European Physical Journal A 49, 27 (2013)

9. Lederer C., Massimi C., Altstadt S., Andrzejewski J., Audouin L., Barbagallo M., Bécares V., Bečvář F., Belloni F., Berthoumieux E., Billowes J., Boccone V., Bosnar D., Brugger M., Calviani M., Calviño F., Cano-Ott D., Carrapiço C., Cerutti F., Chiaveri E., Chin M., Colonna N., Cortés G., Cortés-Giraldo M. A., Diakaki M., Domingo-Pardo C., Duran I., Dressler R., Dzysiuk N., Eleftheriadis C., Ferrari A., Fraval K., Ganesan S., Garcìa A. R., Giubrone G., Gómez-Hornillos M. B., Gonçalves I. F., González-Romero E., Griesmayer E., Guerrero C., Gunsing F., Gurusamy P., Jenkins D. G., Jericha E., Kadi Y., Käppeler F., Karadimos D., Kivel N., Koehler P., Kokkoris M., Korschinek G., Krtička M., Kroll J., Langer C., Leeb H., Leong L. S., Losito R., Manousos A., Marganiec J., Martìnez T., Mastinu P. F., Mastromarco M., Meaze M., Mendoza E., Mengoni A., Milazzo P. M., Mingrone F., Mirea M., Mondalaers W., Paradela C., Pavlik A., Perkowski J., Pignatari M., Plompen A., Praena J., Quesada J. M., Rauscher T., Reifarth R., Riego A., Roman

F., Rubbia C., Sarmento R., Schillebeeckx P., Schmidt S., Schumann D., Tagliente G., Tain J. L., Tarrío D., Tassan-Got L., Tsinganis A., Valenta S., Vannini G., Variale V., Vaz P., Ventura A., Versaci R., Vermeulen M. J., Vlachoudis V., Vlastou R., Wallner A., Ware T., Weigand M., Weiß C., Wright T. J., **Žugec Petar**; ***Neutron capture cross section of unstable ^{63}Ni: implications for stellar nucleosynthesis***, Physical Review Letters 110, 022501 (2013)

10. Weiß C., Griesmayer E., Guerrero C., Altstadt S., Andrzejewski J., Audouin L., Badurek G., Barbagallo M., Bécares V., Bečvář F., Belloni F., Berthoumieux E., Billowes J., Boccone V., Bosnar D., Brugger M., Calviani M., Calviño F., Cano-Ott D., Carrapiço C., Cerutti F., Chiaveri E., Chin M., Colonna N., Cortés G., Cortés-Giraldo M. A., Diakaki M., Domingo-Pardo C., Duran I., Dressler R., Dzysiuk N., Eleftheriadis C., Ferrari A., Fraval K., Ganesan S., Garcìa A. R., Giubrone G., Gómez-Hornillos M. B., Gonçalves I. F., González-Romero E., Gunsing F., Gurusamy P., Hernández-Prieto A., Jenkins D. G., Jericha E., Kadi Y., Käppeler F., Karadimos D., Kivel N., Koehler P., Kokkoris M., Krtička M., Kroll J., Lampoudis C., Langer C., Leal-Cidoncha E., Lederer C., Leeb H., Leong L. S., Losito R., Mallick A., Manousos A., Marganiec J., Martìnez T., Massimi C., Mastinu P. F., Mastromarco M., Meaze M., Mendoza E., Mengoni A., Milazzo P. M., Mingrone F., Mirea M., Mondalaers W., Paradela C., Pavlik A., Perkowski J., Plompen A., Praena J., Quesada J. M., Rauscher T., Reifarth R., Riego A., Robles M. S., Roman F., Rubbia C., Sabaté-Giralte M., Sarmento R., Saxena A., Schillebeeckx P., Schmidt S., Schumann D., Tagliente G., Tain J. L., Tarrío D., Tassan-Got L., Tsinganis A., Valenta S., Vannini G., Variale V., Vaz P., Ventura A., Versaci R., Vermeulen M. J., Vlachoudis V., Vlastou R., Wallner A., Ware T., Weigand M., Wright T. J., **Žugec Petar**; ***A new CVD diamond mosaic-detector for (n, α) cross-section measurements at the n_TOF experiment at CERN***, Nuclear Instruments and Methods in Physics Research A 732, 190 (2013)

11. **Žugec Petar**; ***A coincidental timing model for the scintillating fibers***, Nuclear Instruments and Methods in Physics Research A 659, 307 (2011)